Cooperative Manipulation and Formation Control using Multiple Aerial Vehicles

by

ULUHAN CEM KAYA

Presented to the Faculty of the Graduate School of

The University of Texas at Arlington in Partial Fulfillment

of the Requirements

for the Degree of

DOCTOR OF PHILOSOPHY

THE UNIVERSITY OF TEXAS AT ARLINGTON

December 2023

To my dear family and beloved friends,

and

to all those who have enriched my journey of learning and discovery

- this work is a tribute to the wisdom you've generously given.

Acknowledgements

This dissertation marks the end of my PhD journey, a transformative phase in my life. Its completion would not have been possible without the support and guidance of many individuals.

First and foremost, I express my deepest gratitude to my advisor, Dr.Kamesh Subbarao, for his faith in me and invaluable academic guidance. He has truly been a mentor in every sense, with his patience and support playing a crucial role in my work. He was always there for us, not just academically but also personally, uplifting, motivating, and serving as a moral compass guiding us through tough times. I will definitely miss our lab group meetings and cheerful dinners together. I am deeply thankful for the warm, supportive, and dynamic environment he created, which has been instrumental in our growth and success.

I am grateful to my committee members, Dr.Animesh Chakravarthy, Dr.Manfred Huber, Dr.Alan Bowling, and Dr.Bo Wang, for their academic insights and guidance all along. Engaging in fun and educational project meetings with Dr. Chakravarthy, and visiting Dr. Huber's lab to immerse myself in his profound knowledge and wisdom, have significantly broadened my knowledge and perspective. I feel incredibly fortunate to have been surrounded by such exceptional individuals who have taught me countless lessons. Additionally, I would like to express my gratitude to Tony White and Jason White, joint managing partners of Galaxy Unmanned Systems, for their project support and funding through the AFWERX STTR efforts. Their assistance has been instrumental in my research, enabling me to explore enriching paths and acquire numerous skills.

A special thanks goes to the administrative staff of the Mechanical&Aerospace Engineering Department, particularly Ayesha, Flora, Wendy, and Lanie, for their constant support, help and understandings. Their assistance in navigating complex university processes has been indispensable, making daunting tasks seem manageable and straightforward.

To my colleagues and friends at the Aerospace Systems Laboratory (ASL) – Ameya, Saina, Edward (Tsung-Liang), Shobhit, Jinay, Aakarshan, and Suguru – I owe a debt of gratitude for their collaborative spirit, enriching discussions, and lasting friendships. My dear friends Rajnish, Baris, and Diganta deserve a special mention for their endless laughter, encouragement, and reality checks. I am grateful for your unwavering support and willingness to listen to my rants and ramblings at any hour of day or night. I also extend my thanks to my colleague, Abhishek, for his close companionship and assistance in countless occasions helped me in countless occasions in the latter stages of my journey, and to Dr. Chakravarthy for the access to the Vicon Lab, which significantly fueled my curiosity. I thank all of you for the great times we shared together, making this experience enjoyable.

Finally, I owe a huge thanks to my family, who have been a constant source of encouragement and motivation. The unconditional love and support from my parents, Yasemin and Cemal, along with my siblings, Dilara and Ulas, have been the backbone and solid foundation upon which I leaned throughout my journey. A special mention goes to my nephew, Kuzey Mete, whose birth in my home during the challenging times of a pandemic brought a unique joy and light into our lives. His presence has been a cheerful and uplifting influence, leaving a lasting memory that I will always cherish. In particular, I extend special thanks to my father for his assistance in designing the CAD models of the simulated vehicles used in this research and for sharing his invaluable expertise.

This dissertation stands as a testament to the collective effort and kindness of all of you, and for that, I am eternally grateful.

December 04, 2023

Abstract

Cooperative Manipulation and Formation Control using Multiple Aerial Vehicles

Uluhan Cem Kaya, Ph.D.

The University of Texas at Arlington, 2023

Supervising Professor: Kamesh Subbarao

Recent advancements in autonomous systems have significantly impacted both academia and industry, opening new research avenues. One of them is the collaboration of multiple systems to achieve a common goal, which is known as a cooperative system. In the lack of human intelligence, decision making and perception capabilities, uncrewed autonomous systems could mutually benefit from each other's capabilities when they are deployed and utilized together. This research tackles the collaboration of group of uncrewed aerial systems (UASs) where the constraint on individual vehicles requires a varying level of coordination and cooperation. Such cooperation can be in the form of a physical support, where the task demands beyond the physical capabilities of a single system, and in the form of an intelligence level support, where a better perception, processing, or decision-making capability is needed in general. The objective of this study is the development and integration of cooperative guidance and control algorithms for a selected set of UASs and constrained mission scenarios which include the cooperative aerial payload manipulation task via multi-rotors with suspension cables and the cooperative formation task utilizing a team of airship and multi-rotors. Additionally, this research aims to integrate the developed algorithms

for both individual and cooperative models in high fidelity simulations so that the effectiveness of multi-agent collaboration can be studied over realistic flight tasks.

The first part of the research focuses on the modeling and simulation of individual aerial systems. Systems considered in this research for the case studies include multi-rotors with a flexible-cable suspended payload and an airship. In this part, the mathematical models of these systems are derived by employing Euler-Lagrangian and Newton-Euler methods, respectively. The dynamics of flexible cable model are analyzed and compared with analytical catenary solutions. Furthermore, to improve the simulation accuracy, a momentum- and geometrical structure-preserving variational integrator is implemented for multi-rotors with flexible-cable suspended payload systems.

In the second part, guidance and control laws are designed for each individual system to provide attitude stabilization and trajectory tracking. Initially, a game-theoretic approach based on a linearized system model is investigated for attenuating the swing of the suspended payload. This approach considers various state feedback scenarios for the multi-rotor with a slung load system. Building upon the insights gained from these linear analyses, a catenary shape-informed geometric control approach is developed for the attitude and trajectory tracking control of this system. For the airship, both linear and nonlinear control methods are developed. These include a gain-scheduling based linear quadratic control and a nonlinear dynamic inversion (NDI) method, respectively. Both approaches are then compared against each other, focusing on their advantages and implementation ease.

Finally, cooperative guidance and control laws are developed for realistic scenarios with constrained mission objectives, requiring either physical or intelligence-level cooperation among a group of UASs. Drawing on the catenary analysis of flexible cables, a cooperative control scenario is constructed. This scenario demonstrates co-

operation between vehicles for aerial manipulation of a suspended rigid payload using multi-rotors, where constraints stem from the payload capacity of a single vehicle and the physical connection of vehicles via flexible cables. Secondly, a leader-follower communication graph topology is employed in formation control scenarios involving a team of multi-rotors, highlighting the integration of an extended state observer (ESO) based total disturbance estimation model. This model significantly enhances the robustness of the system against external disturbances and unmodeled dynamics. Finally, we demonstrate the practical application of these studies in an illustrative scenario where cooperative formation support via UASs is needed in a search-and-rescue mission. In this scenario, we also utilize an airship to transport and deploy the multi-rotors to the mission destination where formation tasks are carried out adapting to various formation shapes and graph topologies. This scenario demands both physical and information level collaboration for enhanced area coverage, improved perception, and situational awareness. The constraints here arise from the physical limitations of individual vehicles (such as size, endurance, payload capacity, and operating environment) and information-level constraints (like processing power, sensing, and communication capabilities). This scenario forms a baseline that has practical applications in real life.

Table of Contents

List of Illustrations

List of Tables

Chapter 1

Introduction

Current technological advancements favor approaches that utilize multiple dynamical systems with various constraints over deploying a single, more advanced, and complex system in autonomous flight missions. This preference is driven by factors such as cost-effectiveness, robustness to failures, flexibility, scalability, and specific mission requirements. Consequently, the use of less advanced multi-vehicle systems, subject to physical or information-gathering limitations, has become more common. These constraints often require coordination and collaboration among the systems to successfully achieve mission objectives. This research delves into the cooperative behavior of groups of Unmanned Aerial Systems (UAS) vehicles. It focuses on their physical and information-level cooperation for tasks such as aerial payload manipulation and cooperative formation. The study includes developing corresponding system models, guidance and control methods, and conducting necessary analyses.

1.1 Objectives of the Research

The objectives of this research are summarized as follows:

1. **Development of Mathematical Models:** The first objective is to develop mathematical models for selected aerial systems, specifically a multi-rotor with a flexible-cable suspended payload and an airship, respectively. To achieve this, Euler-Lagrangian and Newton-Euler methods are employed for deriving the equations of motion for each system. Furthermore, this work presents the analytical solution of catenary equations and compares the precision of

the developed flexible cable model. It also addresses challenges in simulating highly nonlinear multi-body dynamics, such as those in flexible suspension cables. To enhance stability and accuracy in simulations, a momentum and structure-preserving integration method is introduced.

2. **Synthesis of Controllers for Individual Systems:** The second objective involves synthesizing low-level stabilizing and trajectory tracking controllers for each system. This includes developing and comparing the effectiveness and implementation ease of linear and nonlinear controllers. For the multi-rotor system, a linear quadratic tracker (LQT) and a nonlinear geometric controller are implemented, while the airship uses gain-scheduling based LQTs and nonlinear dynamic inversion (NDI) controllers. Additionally, various autonomous guidance laws are implemented for airship autopilot modes, including landing, take-off, and waypoint navigation.
3. **Cooperative Control Law Synthesis:** The third objective focuses on synthesizing cooperative control laws among multiple UAS vehicles. This involves constructing various scenarios for groups of vehicles and integrating distributed cooperative control laws. Scenarios include catenary-informed aerial manipulation of a suspended rigid payload via cooperative multi-rotors and multi-agent formations among multiple multi-rotors.
4. **Simulation of Realistic Cooperative Flight Scenarios:** The final objective is to construct and simulate realistic cooperative flight scenarios, such as UAS-supported search-and-rescue missions. This involves using formation control among collaborating vehicles while addressing other mission objectives. This step integrates previous results and algorithms to tackle a practical multi-vehicle autonomous UAS flight.

Figure 1.1: Illustration of an aerial payload manipulation mission by cooperative multi-rotors carrying an emergency bag suspended via cables

1.2 Problem Specification and Requirements

The specifications of cooperative aerial payload manipulation and cooperative formation problems with required sub-tasks are outlined below by illustrating the problems over representative mission scenarios that are also reflecting the purpose and significance of this research work well.

Firstly, Figure 1.1 illustrates an aerial payload manipulation scenario where a group of multi-rotors are designated to transport an emergency supply via suspension cables. In this scenario, although the maneuverability of individual vehicles is constrained due to the physical limits of cable and payload dynamics, the group can accomplish crucial missions with an increased payload capacity and controllability while still retaining a certain level of agility which can be especially decisive in time critical missions.

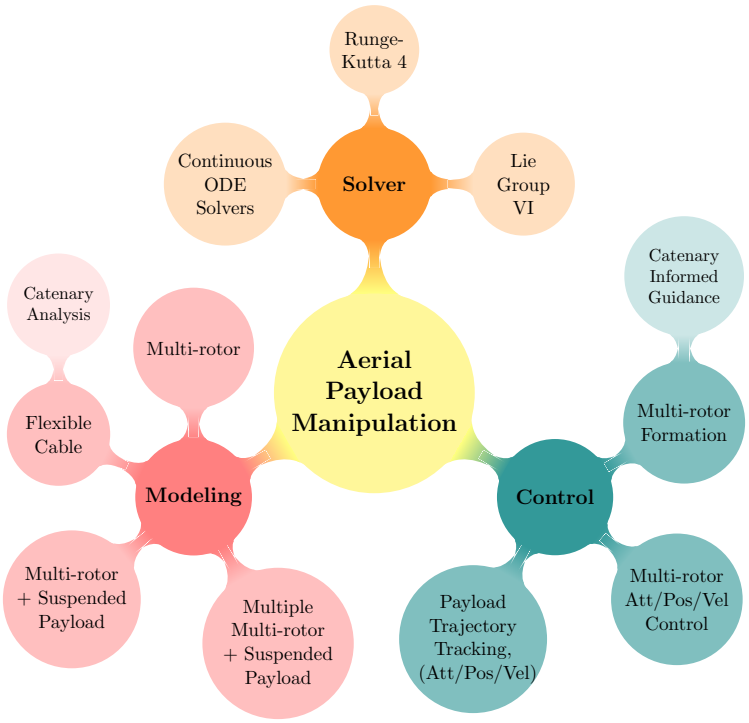

Figure 1.2: Aerial payload manipulation task work items

Figure 1.2 outlines the essential components of the aerial payload manipulation task, divided into three primary categories: modeling, control, and solver design. In the modeling phase, the process starts with individual elements, like the flexible suspension cable and multi-rotor, and progresses to modeling the entire multi-vehicle system. Control efforts are similarly divided, encompassing both payload and individual multi-rotor trajectory tracking, as well as the overall system formation control. The solver design addresses the complexities and constraints inherent in accurately solving the configuration manifold of the system.

Secondly, Figure 1.3 presents a cooperative formation task, where teams of multi-rotors engage in formation flight while being assisted by the corresponding airships. In this scenario, airships play a dual role: they act as leader nodes providing reference guidance to their respective multi-rotor team, and as surrogate aircraft,

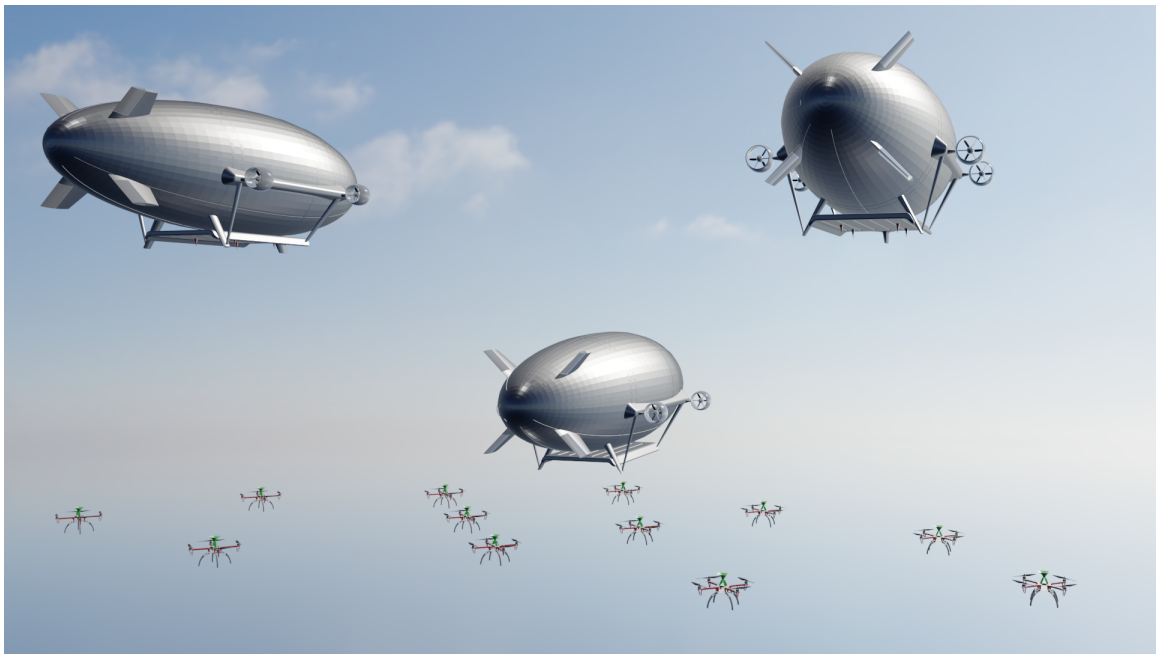

Figure 1.3: Illustration of a cooperative formation flight mission with teams of multi-rotors assisted by airships guiding the formations as leader nodes

facilitating the transportation of multi-rotors to the designated destination prior to the formation mission. This approach significantly enhances operational range and endurance by leveraging airships for long-distance transport, conserving multi-rotor energy for critical tasks. The synergy of airships and multi-rotors brings forth an increased payload capacity, providing a platform for comprehensive mission execution, and ensures improved stability and safety. The utility of this combination extends across various domains: from extensive area surveillance in environmental research and border control to critical roles in disaster response and humanitarian aid, where rapid deployment and supply delivery are paramount. Particularly, in search and rescue operations, the rapid transportation of multi-rotors to remote locations can be a game-changer. Agricultural monitoring benefits from the extensive coverage and detailed data collection, and urban planning and infrastructure inspection access the ability to conduct large-scale surveys and structural inspections. This innovative in-

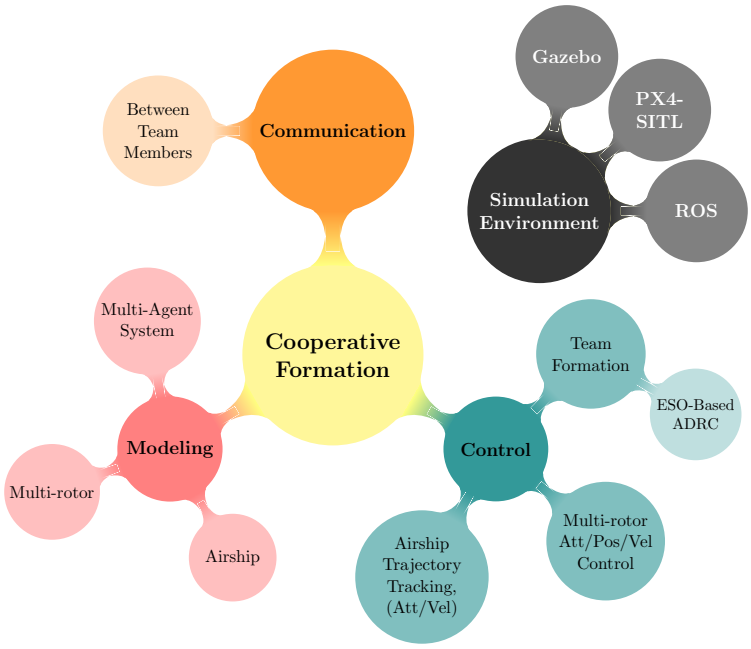

Figure 1.4: Cooperative formation task work items

tegration of airships and multi-rotors not only broadens the scope of aerial operations but also introduces efficiency and effectiveness for aerial tasks.

Figure 1.4 details the essential components of the cooperative formation task, categorized into three primary branches. In the modeling phase, attention is given to creating individual vehicle models for the multi-rotor and airship. The control aspect involves devising control systems tailored to both individual vehicles and the collective group formation. Additionally, the team formation benefits from an ESO-based active disturbance rejection control (ADRC) method for team members to accurately assess external disturbances like wind and unmodeled dynamics such as rotational dynamics, air drag and parameter uncertainties as total disturbance, which are critical for mitigating resultant adverse effects of these factors on the formation. Communication among team members is another crucial element where various graph topologies are employed to examine its significant influence on formation dynamics. Alongside these

efforts, the development and integration of necessary modules within the simulation environment, particularly for the formation task, are pursued in parallel.

1.3 Background and Motivation

This section provides a comprehensive overview of the background and relevant literature related to the key components of this research. It aims to contextualize the study within the existing body of knowledge and highlight how this work builds upon and differentiates from prior studies in the field.

1.3.1 Modeling and Simulation of Constrained Aerial Vehicles

This research utilizes two distinct systems: a multi-rotor with a flexible cable-suspended payload and an airship. When these systems operate independently, without cooperation, they encounter specific physical constraints. The multi-rotor is affected by the dynamics of the attached cable and payload, particularly its swinging motion. In contrast, the airship faces control-level physical constraints due to its under-actuated design. Additionally, the slung load system of the multi-rotor struggles with limited knowledge of the cable's shape and related states in practical applications. The following subsections provide a summary of existing literature on these individual systems, highlighting previous research and developments in this field.

1.3.1.1 Mathematical Model of Multi-rotors with a Cable Suspended Payload

The problem of transporting suspended payloads via uncrewed aerial vehicles has taken considerable amount of attention among researchers for more than two decades, and even longer if the root of this problem is considered to be the manipulation of a suspended payload. Literature provides numerous work done in this very topic tackling the problem with various approaches. This field has seen a variety

of approaches, with a notable increase in research following the demonstration of the differential flatness of a multi-rotor with a slung load system in Ref. [1], which simplified the relationship between the states of the multi-rotor and its load. There are two main approaches adopted by the researchers to model the multi-rotor with a slung load system. In the first approach, which has seen more attention due to its simplicity in the implementation, the suspension cable is considered to be a massless single rigid link with a payload attached at the end. Refs. [1, 2] derive the equations of motion for the system with this assumption utilizing Lagrange-d'Alembert principle and Euler-Lagrange mechanics. On the other hand, the second approach adopts various flexible cable models. One of the early work contributing to the development of a flexible cable is actually studied the dynamics of a chain pendulum on a planar cart in Ref. [3], where the chain pendulum is modeled as serially connected rigid links with individual masses concentrated at their outboard end. Similarly, Refs. [4, 5] extend this work to the aerial manipulation of the flexible cable with serially connected rigid links suspended under a quad-rotor without an additional payload. Apart from serially connected rigid link representations of a flexible cable, the other works investigate the varying length cable models in aerial payload manipulation scenarios. In Refs. [6, 7], the deliberately extendable single massless rigid link cable is modeled for the payload transportation via a quad-rotor. In Ref. [8], the cable's flexibility and elasticity are modeled using springs and dampers to more accurately depict the cable dynamics for cooperative payload manipulation tasks. In a similar fashion, Ref. [9] utilizes a spring-damper mechanism to model a single link massless elastic cable suspended under a quad-rotor with a point load attached. In addition to these two approaches tackling the cable models, several studies have adopted a hybrid modeling technique, using cable tautness to determine the treatment of the multi-rotor and payload as either a single system or separate entities. Refs. [2, 10] apply a switching

between these two models keeping track of tension in the cable calculated from the payload acceleration and the distance between the multi-rotor and payload. Likewise, in Ref. [9] non-negative tension constraint is employed to obtain a hybrid model considering only the simultaneous length of the cable from mass-spring-damper system. By taking the adopted modeling approaches including hybrid systems into account, it can be concluded that flexible cable approaches can address the deformations in cable shape without an explicit analysis of tension force along the cable yielding a more accurate approximation of actual continuous cable dynamics. However, due to the complexity of flexible cable models and their highly nonlinear configuration manifolds, the multi-vehicle aerial manipulation scenarios majorly adopt more simplified models as in the first approach with a single massless rigid link assumption.

The aerial suspended payload manipulation via multi-vehicle cooperation has also been a productive research avenue that is studied extensively. Several studies, such as Refs. [11, 12], employ simplified models with single massless rigid link cable and point load assumptions for the cooperative transportation of a common cable suspended payload via quad-rotors. Slightly improved approaches incorporating the dynamics of a rigid body payload are also present in the literature as can be seen in Refs. [13, 14]. In addition, despite the challenges in simulation and control method development processes, Refs. [15, 16] utilize the flexible cable model with serially connected rigid links supporting a rectangular rigid payload in their cooperative scheme.

All of these aforementioned studies rely on the simulations of adopted models under the assumption that the actual behavior of the real system is captured reasonably well by the developed dynamical models. Leaving aside the accuracy of models capturing the underlying physical phenomena, it is known that the majority of numerical integration methods, including the Runge-Kutta based ODE solvers, do not preserve the symmetries (invariants) and geometrical properties of the system, where

even slight deviations might substantially affect the overall simulation accuracy, especially for the systems under consideration here. Inherently, the conclusions drawn from inaccurate simulations of such complex physical systems may cause unexpected results in practice. These are particularly important in systems that involve flexible components, and a simple rigid body assumption does not capture the interactions between the components accurately. To address described numerical integration inaccuracies, a special class of geometric integration scheme, called variational integrators (VI), is introduced in the literature, Ref. [17]. VI approach, instead of discretizing continuous equations of motion as the most general-purpose integrators do, directly utilizes the discrete variational principle obtaining the discrete dynamics as a result of the discrete Hamilton's principle. Therefore, the derived discrete dynamics exactly preserves the momentum and the symplectic form of the system, as presented in great detail by Refs. [18,19] and [20]. In addition, Lee and his team in Refs. [21,22] put forward an enhancement for variational integrators to preserve the geometric structure of the configuration manifold, which is represented as a Lie group, in rigid-body problems. Along with the symplecticity and momentum conservation, the exact preservation of the structure of the manifold ensures an exponentially long-term stability with a good energy behavior, which makes VI methods an ideal candidate for the simulation of complex or highly nonlinear systems.

Motivation. It is essential to propose a sufficiently accurate model of cooperative multi-rotors with a suspended payload system that can closely approximate the actual dynamical behavior and at the same time, to establish a reliable numerical solver considering the structure of configuration manifold and geometrical constraints of the system such that the effect of numerical inaccuracies on the solutions can be minimized.

1.3.1.2 Mathematical Model of Airship

Research on airship dynamics modeling has a longstanding history in literature, though it has received less attention compared to heavier-than-air vehicles, primarily due to challenges in accurately representing the dynamic forces and moments arising from interactions between air particles and the non-rigid airship hull, which forms the aerodynamic properties of airship. One of the foundational works by Lamb in Ref. [23], introduces the mathematical model of added moment of inertia in terms of geometrical parameters of a general ellipsoidal shape that is immersed into moving fluid, where the dynamic displacement of fluid particles due to this immersion causes an increase in the overall moment of inertia of the body. Following that Munk in Ref. [24] provides a mathematical method to calculate axial and lateral forces and moments acting on the airship hull by unifying previous results from Lamb's work and the final equations are given as a function of dynamic pressure, angle of attack and the change in the cross-sectional area of the hull. Later, Ref. [25] improves the steady-state model based on previous studies by including the effect of fins and the interaction between airship hull and fins, and it introduces an estimation technique utilizing the developed model and wind tunnel experimental data to predict the aerodynamic coefficients and stability derivatives for the dynamic model. Another work contributing to the modeling effort is carried out in Ref. [26] where the propulsion and actuation systems with thrust vectoring and control surfaces are also integrated with a full 6DOF airship dynamical model. In addition, handling, control mode responses, and several factors causing non-intuitive effects are discussed in this work, where further details about these effects can be found in Ref. [27]. The study in Ref. [28] focuses on the modeling of a high altitude airship in several aspects, also offering an analytical procedure to obtain aerodynamic coefficients of the airship for

model derived in Ref. [25] by using only the airship's sizing and geometry. Similarly, a comprehensive characterization of the aerodynamic model of a low altitude airship is carried out in Ref. [29] and the derived aerodynamic model is refined by using wind tunnel experiments and actual flight tests. Additionally, the effect of varying mass on the airship dynamics is modeled and studied in Ref. [29]. On the other hand, Ref. [30] employs an Extended Kalman Filter (EKF) based method to estimate aerodynamic forces and moments acting on the airship from sensor data and vehicle model assuming that the aerodynamic model is unknown.

Motivation. For effective guidance and control of autonomous airship systems, it's crucial to develop a dynamical model that accurately approximates forces, moments, and other phenomena, considering the airship's full flight envelope. This model is essential for predicting the airship's behavior under various operational conditions and enabling precise control and maneuverability.

1.3.2 Guidance and Control Law Design

1.3.2.1 Autonomous Control of a Multi-rotor with Cable Suspended Payload

A multi-rotor with cable suspended slung load constitutes an under-actuated dynamical system. Arising needs for the aerial payload transportation via UAV systems require the careful considerations of control strategies to be implemented for these systems since the unaccounted disturbances resulted from the swing motion of the payload and cable could destabilize the overall system. In literature, two main approaches can be found with opposing objectives: one aims to suppress the swinging of the suspended load, and the other designs motion controllers that accommodate large swings. The first approach, focusing on swing elimination, often employs active feedback control and swing-free trajectory generation methods, analogous to overhead

crane load manipulation. Ref. [31] employs input shaping feed-forward and robust delayed feedback controllers to achieve simultaneous minimization of the swing excitation and active damping of the oscillations for helicopter slung load operations. In Ref. [32], dynamic programming method is utilized to obtain swing-free trajectories for a quad-rotor carrying suspended load by finding optimal sequence of control inputs to a quadratic cost function. Also, an adaptive control method is proposed for the compensation of unbalanced center of gravity shift due to the asymmetric placement of suspended load on quad-rotor. The passivity based controllers, which exploit a special structure of certain under-actuated systems, are commonly encountered for this topic, as well. The work in Ref. [33] introduces a special class of passivity-based control by modifying Hamiltonian of the system with a desired energy function minimizing the swinging of slung load. Further, Ref. [34] compares the swing mitigation performance of a passivity-based controller and an extended state observer-based active disturbance rejection controller (ADRC) for the system's response to an initially deflected suspended load scenario. Conversely, in the second approach, instead of suppressing the payload dynamics, the study aims to leverage it for obtaining more optimal performance in terms of energy and agility. In Ref. [1], a nonlinear geometric control approach with an almost global attractiveness is developed to track the desired flat outputs of the system including an arbitrary configuration of desired cable and payload attitude. This geometric method relies on the fast and accurate tracking of desired quad-rotor attitude, where it is computed from the geometric interpretation of commanded force vector and thrust direction of the quad-rotor. Work done in Ref. [35] provides a variation-based linearization of SO(3) and $\mathbb{S}^2$ configuration manifolds where the multi-rotor with a suspended load system evolves in the product of these two manifolds. After linearization, it also develops a finite-time horizon linear quadratic tracker (LQT) by considering the system as linear time varying (LTV) and

shows the stable tracking performance of the controller for various scenarios. Another linear control method with a linear model predictive controller (MPC) is developed for this system in Ref. [36]. Unlike the previous LQT method, this method can directly incorporate the limits and saturation on system states, inputs, and outputs by constructing a convex optimization problem with various constraints, which also provides robustness to modeling errors. Ref. [10] introduces a trajectory generation method with obstacle avoidance capability by considering an hybrid quad-rotor and slung load system model and utilizing a mixed integer quadratic programming formulation to account for convex polygonal obstacles and switching dynamics as well as the polynomial trajectory constraints in terms of continuity and waypoint states. In Ref. [37], a navigation through narrow windows for a cable suspended payload via quad-rotor is experimentally demonstrated successfully, where a pair of optimization based trajectory generation and a PD trajectory tracking control methods are utilized while employing an online system identification technique to approximate the parameters of a simplified system model. Majority of the studies assume that cable and payload states are known by the control system, and so, the developed feedback laws can utilize them to achieve a desired behavior without providing the methodology for how to obtain these state information. Several studies have tackled the extraction of slung load information for practical systems such as Refs. [31, 38] and [39] where a downward-facing camera is integrated to estimate the payload position and velocity using filtering methods and certain constraints of the cable and quad-rotor geometries.

All of above studies assume a massless rigid single link cable model for their multi-rotor with suspended load system and develop control laws accordingly. Whereas, a few works exist in the literature, where either varying length or flexible cable models are considered as well. Ref. [7] modifies the geometric control method developed

in Ref. [1] by integrating a pulley mechanism to introduce an additional control capability on the cable length so that the scenarios, where the multi-rotor with an adjustable-length cable suspended load system is expected to pass through narrow windows, can be successfully demonstrated. The work presented in Ref. [4] implements the geometric control method to stabilize the hover equilibrium condition for the flexible cable suspended load model carried by a quad-rotor, where the cable consists of a serially connected rigid links with concentrated point loads at the end of each link. The same system is controlled by a finite time horizon LQR approach in Ref. [5] as well. Furthermore, in Ref. [40], an adaptive control law compensating the uncertainty on cable and payload masses is integrated for the same system along with the geometric attitude control.

Motivation. Various linear and nonlinear control methods have been developed and integrated for the multi-rotor with slung load system. Among these methods, the geometric control approaches stand out for majority of the implementations lately due to its intuitiveness, adaptability, and almost global convergence properties as can be seen from the several of aforementioned reference studies with versatility.

1.3.2.2 Autonomous Control of Airship

Highly nonlinear and under-actuated dynamics of the airships have to be addressed by developing appropriate guidance and control systems. Moreover, transitions between low airspeed and aerodynamic flight regimes, which often require the utilization of additional separate actuation mechanisms, need to be handled by the control scheme. Literature has numerous work tackling this problem proposing diverse linear and nonlinear approaches. Due to their well established methodologies and design techniques, the solutions employing classical control methods with linearized system models are commonly practiced for airships. One of the early works,

given in Ref. [41], introduces a robust heading hold autopilot for an airship within H_∞ control framework. Similarly, Ref. [42] obtains the transfer functions from each inputs to airship states for certain trim conditions and proposes separate PI designs with varying design considerations according to specific autopilot modes such as altitude hold, velocity hold, and constant bank. However, the linearization at a specific trim point can only approximate the behavior of the actual system around this point, which necessitates the design of corresponding controllers for each trim condition and transition between them to cover full flight envelope of the airship. Therefore, several gain scheduling based control methods are developed, such as [43] and [44], where a single scheduling variable, airspeed and yaw rate states respectively, is used for smoothly switching between LQR controllers while the airship is being guided through waypoints. Further, Ref. [45] utilizes a continuous function of both forward and vertical speed states to adjust scheduling gains. On the other hand, nonlinear approaches focus on constructing a control scheme satisfying global stability instead of tackling local flight trim conditions individually. Compared to linear techniques, nonlinear methods are more flexible and they provide more powerful results since a better representation of highly complex and nonlinear nature of involved dynamics are achieved by utilizing actual nonlinear forms instead of linearized versions. One of the early work implementing a nonlinear control approach based on a backstepping (BS) method for airship hover stabilization achieving a global asymptotic stability under the actuator saturations is introduced in Ref. [46]. This reference work also investigates the robustness of proposed solution to the wind and turbulence disturbances during hover where the lateral under-actuation is observed for the airship. Another commonly used approach with nonlinear dynamic inversion (NDI) method, also known as feedback linearization where the system's undesirable nonlinearities are canceled out and the overall system is replaced with a desired dynamics, is de-

veloped for an autonomous airship of AURORA project in Ref. [47]. Moreover, the stability and robustness tests are carried out for various disturbance cases and model parameter errors, where an insightful analysis of the effect of aerodynamic parameter errors on the control stability is presented. Ref. [48] implements an incremental NDI method, which aims to reduce the model dependency of the controller by relying on measurements such as accelerometer data to obtain forces and moments approximately, instead of system model to eliminate the undesirable system dynamics, is implemented as well. The performance, sensitivity, and robustness comparisons of LQR based gain scheduling, BS, and NDI methods for the autonomous airship flight control considering its full flight envelope are given in Ref. [49]. In Ref. [50], the path following problem of an autonomous airship is tackled by employing a multi-input multi-output sliding mode control (SMC) technique which is a variable structure method via switching mechanisms and it yields high robustness to model uncertainty and external disturbances. Combining the advantages of BS and SMC methods, Ref. [51] introduces a unified method, BS-SMC, to position control of the airship under parametric uncertainties and disturbances. Similarly, Ref. [52] derives a unified BS-SMC framework and presents the comparison of these three methods, i.e., BS, SMC, and BS-SMC. Another method that demonstrates tolerance to model uncertainties and has relatively less complex design with intuitive parameter adjustments is the fuzzy logic control technique, where Ref. [53] utilizes it to design speed, heading, and altitude controllers for an airship. Apart from previous examples given here, there are several studies in the literature aiming for the integration of intelligent control techniques to propose better solutions to challenges in airship control framework. One of the example work, given in Ref. [54], integrates neural network layers with an NDI control method to compensate the model uncertainties in the system during feedback linearization process where the NDI method by itself is known to be highly

sensitive to the model discrepancies. Another good example to intelligent algorithm that aims to learn how a controlled airship flies from pilot demonstrations by utilizing a multi-state multi-action reinforcement learning (RL) method is introduced in Ref. [55]. In addition, there are other approaches employing the estimation techniques to minimize the effect of unknown dynamics, parameter uncertainties, and external disturbances. Ref. [56] integrates a nonlinear disturbance observer, similar to the work done in Ref. [57], with a backstepping controller to estimate the total disturbance on the airship including all the factors such as unmodeled dynamics, parameter uncertainty, and external disturbances for a planar path following control problem of an autonomous airship considering actuator dynamics, saturation, parameter variation, and wind.

Motivation. Existing control techniques for autonomous airships have distinct characteristics. While the classical control approaches provide insightful analysis and a well established design process, the challenges in proposing a controller for full available motion domain, especially in highly nonlinear flight regimes, significantly increase the required effort to design such controllers. However, advanced control methods hold an advantage of applying full nonlinear solutions to the underlying complex problems globally, which eliminates the partial analysis of the whole system. Nevertheless, in order to gain a better knowledge of stability and flight characteristics of the system, linear trim analyses and globally asymptotic control design process can be used complementarily.

1.3.3 Cooperative Control of Multiple Aerial Vehicles

1.3.3.1 Cooperative Aerial Manipulation of a Slung Load with Multiple Multi-rotors

Literature on the aerial payload manipulation via multi-rotors tackles this problem under two categories. In the first one, the solution is proposed by cooperative grasping and transporting of a rigid payload via aerial vehicles, which essentially simplifies the overall system to a single composite system with redundant force generation mechanisms. The other category considers the utilization of suspension cables to manipulate and transport the payload. Although the latter approach increases the level of under-actuation and disturbance in the system due to the cable dynamics, it recovers a portion of individual multi-rotor's agility comparing to the former category where the vehicles rigidly attached to a payload experience an increased inertia and constraints on the attitude control. The work in Ref. [58] constructs several cooperative grasping scenarios using quad-rotors rigidly attached to variously oriented rigid beams and it experiments hover stabilization and trajectory control employing a weighted pseudo-inverse technique to find the desired force component for each vehicle. Moreover, since the vehicles are rigidly attached to the payload and all vehicles and payload essentially share the same states, the overall control mechanism is decentralized in this work. A similar work considering a grasping scenario and trajectory control is introduced in Ref. [59] where instead of the rigid payload assumption, a flexible payload modeled by an arbitrary number of deformation modes via harmonic functions between the payload center of gravity and each attachment position of multi-rotors. On the other hand, there are more diverse studies tackling payload manipulation problem via suspension cables. Well known parallel manipulators concept that searches for both direct and inverse kinematics solutions to find desired robot pose and cable attitudes satisfying static payload equilibrium, cable

tension and kinematic constraints are investigated for an aerial manipulation task via multiple multi-rotors in Ref. [60, 61]. A similar approach without changing cable lengths, a fly-crane model, is implemented by incorporating an optimization-based robust full payload pose control technique in [62]. Another work employing kinematic relations to derive a feedback control law for the formation of two helicopters carrying a slung load via flexible cables is given in [63]. This work also integrates task prioritization through a null space projection method where the tasks are relative formation control, obstacle avoidance, payload stabilization, and orientation control. A passivity-based approach for the formation control of an arbitrary number of multi-rotors suspending a point load via massless rigid links is introduced in [12] where a graph topology is used to represent the virtual spring forces controlling the formation, and the payload-induced suspension forces are compensated. In Ref. [64], a nonlinear uncertainty and disturbance observer is developed to estimate the total disturbance on the cooperative cable suspended payload system leading to a robust control method, where overall stability of the system is proven by utilizing Lyapunov's direct method and validated by experimental demonstrations. Further, several studies propose optimization-based approaches, such as the nonlinear model predictive control (MPC) methods that consider vehicle collision constraints while transporting a rigid suspended payload with full pose control, developed in Refs. [65, 66]. Another investigation into convex and non-convex optimizations that ensure vehicle separation and prevent cable crossing by imposing cable angle, tension, and other constraints is presented in [67], which also showcases hardware demonstrations for indoor and outdoor environments, demonstrating real-time computational capabilities and some level of disturbance rejection. Papers extending the geometric control method for multi-rotors to cooperative payload manipulation tasks are also prevalent in literature. For instance, Ref. [11] integrates a geometric trajectory tracking control ap-

proach for cooperating multi-rotors suspending a point load via rigid massless links. Additionally, the study in [68] models the cooperative payload transportation as a hybrid system model utilizing switching dynamics due to the tension constraint and demonstrates the system behavior with a suspended rigid payload in both simulation and hardware experiments. Refs. [13, 14] consider a rigid payload in an aerial manipulation task and apply the pseudo-inverse method to distribute the desired forces and moments required to control the payload position and attitude via suspension cables. These studies also make use of a geometric control method to control the trajectory of individual vehicles while compensating the parallel and orthogonal components of required forces for adjusting cable tension and attitude. So far, aforementioned studies assume massless rigid link cables. However, in general, the actual suspension cable has certain mass and flexibility, and as the cable length increases, the effect of these properties on the overall system becomes non-negligible. Therefore, in order to propose a better solution to the actual system behavior, the control approach should also take the cable dynamics into account. Refs. [15, 16] incorporate the flexible suspension cable modeled by serially attached point masses into the cooperative aerial manipulation of a rigid payload, where a variation based linearization of the system and equilibrium control inputs along desired trajectories are used along with a geometric control approach and the developed method is demonstrated in both simulation and hardware demonstration, respectively. Another study employing the same flexible cable model is given in [69] that addresses the transport of a flexible hose supported by multiple multi-rotors at specific locations along the hose and it uses finite-time LQR control method for hover stabilization and trajectory tracking. In Ref. [8], the cable's flexibility and elasticity are modeled using springs and dampers to more accurately depict the cable dynamics for cooperative payload manipulation tasks. Finally, a more advanced and challenging aerial manipulation scenario with

the objective of stabilizing the ball location on a plate suspended by cables under multi-rotors while tracking a desired trajectory is considered in Ref. [70]. This work utilizes partial feedback linearization to cope with additional degrees of freedom resulting from the integration of a ball constrained on a planar motion on the plate and a backstepping technique with time scale separation for the control design.

Motivation. The cooperative payload manipulation of a suspended payload is a complex and highly under-actuated system with a delayed behavior with inherent oscillations. By taking aforementioned work into account, although flexible cable approaches can address the deformations in cable shape and resulting dynamical behavior yielding a more accurate approximation of actual continuous cable dynamics, it is obvious that the consideration of flexible nature of suspension system introduces an additional complexity to the system and required control strategies. Therefore, the effect of flexible cable and suspended load dynamics has not been captured in the vast majority of these studies due to adopted simplified approaches. Moreover, those few studies that do incorporate flexible models often investigate the linearized system behavior, which prevents effectively capturing the actual system behavior. However, an already existing methodology for representing the flexible cable structure and its characteristics through catenary formulation can be employed efficiently to capture the actual behavior of the cable and inform the control system for a faster response.

1.3.3.2 Cooperative Formation of Aerial Vehicles

Multi-agent formation control, a vital aspect of cooperative control theory, finds wide application ranging from uncrewed aerial vehicles and autonomous underwater vehicles to robotic swarms. Its primary appeal lies in coordinating autonomous agents to efficiently achieve collective goals, hence, reducing operational complexity and cost. This approach, inspired by natural systems like flocks of birds, is versatile in various

tasks, ranging from search-and-rescue missions to complex military operations, due to its coordinated and distributed nature.

Consensus protocols are fundamental to multi-agent formation control. They are algorithms that enable agents to reach an agreement on states or objectives, despite initial condition differences. The basic idea is that each agent updates its state based on the states of its local neighbors, ensuring that all agents eventually converge to a common value or a dynamic state. These protocols, inspired by decentralized decision-making seen in natural phenomena, enhance scalability and robustness compared to centralized control systems. In Ref. [71], focusing on fixed and switching topologies, the consensus problem in networks of dynamic agents is explored. This study introduces key results and establishes critical relationships between graph topology and formation dynamics.

However, applying the basic principles of multi-agent formation control and consensus protocols to real-life applications presents certain challenges. These primarily stem from unmodeled vehicle dynamics, parameter uncertainties, and external disturbances. In response, there is growing interest in integrating robust control systems with the consensus protocols of multi-agent systems (MAS). The literature has developed various approaches to this. Refs. [72, 73] explore H_∞-based consensus protocols for MAS with nonlinear dynamics, addressing parameter uncertainties and external disturbances, and investigating their global convergence. Other works adopt an adaptive framework. For instance, Ref. [74] integrates a neural-network based adaptive control technique to the consensus problem for second-order nonlinear dynamical systems with unknown dynamics. A similar approach for the formation tracking of quad-rotors with unknown parameters and external disturbances is developed in Ref. [75], where an adaptive backstepping design is integrated for robust formation in a consensus framework by considering only the translational dynam-

ics of the quad-rotors, while a separate adaptive disturbance rejection control based on the same backstepping technique is utilized as active disturbance rejection controller (ADRC) in the rotational dynamics of each agent. Various ADRC techniques, which are actually employed in numerous occasions in real-life systems, have found use cases for this topic as well. Techniques based on Disturbance Observer-Based Control (DOBC) and Extended State Observers (ESO) offer promising solutions to enhance the resilience of multi-agent formations against such external disturbances and uncertainties. DOBC focuses on direct disturbance estimation and rejection in the system. Ref. [76] proposes a DOBC-based ADRC approach for the consensus of LTI system with a deterministic disturbance using the relative state information obtained from the neighboring agents. Ref. [77] integrates an ADRC, based on a higher-order disturbance observer (DO), with an integral SMC for higher-order multi-agent systems, where numerically tested for a team of hypersonic vehicles in leader-follower scheme. Likewise, Ref. [78] implements a distributed fixed-time consensus observer-based robust SMC for aerial formation of quad-rotors. This method is experimentally tested along with Processor-in-the-loop and ROS/Gazebo simulations. Ref. [79] conducts a thorough investigation of input delayed consensus and formation, demonstrating DOBC-based implementations for a multi-agent system with unknown dynamics, time-varying formation shapes, and external disturbances. This study also provides an exhaustive analysis of various feedback control methods for both linear and nonlinear dynamics, such as observer-based, predictor-based, and H_∞ approaches for multi-agent consensus and formation. ESO, alternatively, estimates both the system states and the combined effect of system uncertainties and external disturbances, treating them as a total disturbance. This allows for real-time compensation, with its stability proven in Ref. [80]. In Ref. [81], an ESO-based ADRC method is investigated for the consensus of general LTI multi-agent systems with unknown external distur-

bance and uncertainty, using the estimates of both local agent states and disturbances in the consensus protocol, also showing tedious proofs of this ESO integrated system. Ref. [82] extends an ESO-based ADRC method to higher-order uncertain nonlinear multi-agent systems, where it assumes that there are unmeasurable agent states and unknown dynamics, and uses the output feedback in consensus protocol, which is further extended to the uncertain time delayed nonlinear systems in Ref. [83].

The integration of these advanced control methodologies with consensus protocols represents a significant step towards robustifying multi-agent formation control, ensuring that the coordinated behavior is maintained even under unpredictable environmental conditions and system dynamics. The current state of research indicates a growing convergence between advanced disturbance rejection techniques and multi-agent formation control.

Motivation. Traditional consensus protocols often rely on accurate models of the system dynamics and may not account for unmodeled dynamics or external disturbances effectively. Formation control of the aerial system due to highly dynamic operating environment and complex nature of the vehicles is susceptible to these effects, such as wind gusts, varying payloads, and other environmental factors. ESO-based methods' ability to estimate and compensate for both unmodeled dynamics and external disturbances in real-time ensures stable and reliable formation control, even in complex, nonlinear conditions typical to these systems. This approach aligns well with the decentralized nature of formation control, reducing communication overhead and enhancing scalability. Unlike other methods, which may rely heavily on accurate system models or complex control strategies, ESO provides a simpler yet effective solution for real-time active disturbance rejection control, making it an ideal choice for dynamic and uncertain operating conditions encountered in cooperative aerial formations.

1.4 Contributions of the Research

The major contributions of this research are summarized in this section along with the regarding publications.

1.4.1 Modeling and Simulation of Constrained Aerial Vehicles

The key contributions of the research in the context of modeling and simulation of dynamical systems are highlighted as follows:

1. This research provides the catenary shape analysis of a serially connected rigid links for the continuous suspension cable representation. It is shown that the analytical catenary equations can be utilized to approximate the steady-state shape and tension distribution of the suspension cable. From this analysis, a method is derived that establishes a relationship between the cable parameters, end-point locations, and the distribution of horizontal and vertical forces along its length.
2. The research also proposes a momentum and structure-preserving variational integrator for the long term accurate representation of the actual behavior of the multi-rotor and flexible suspension cable system. Due to the highly nonlinear configuration manifold that this system evolves in, conserving the system's momentum, manifold structure, and geometrical constraints achieves a long term stability and accuracy in the time evolution of the solution. Unlike traditional methods that integrate discretized continuous equations of motion, the variational integrator approach directly utilizes the discrete variational principle while obtaining the discrete Hamiltonian representation of the system, which provides a discrete dynamics as a pair of position and momentum states ensuring the conservation of momentum in consecutive time steps. Moreover, the

fulfillment of geometrical constraints is achieved by employing certain Lie group operations defined in the configuration manifold.

The publication based on the research above is listed below:

- Uluhan C. Kaya and Kamesh Subbarao, "Momentum Preserving Simulation of Cooperative Multirotors With Flexible-Cable Suspended Payload," ASME Journal of Dynamic Systems, Measurement, and Control, Vol. 144, No. 4, 2022, https://doi.org/10.1115/1.4053343 (Reference [84])

1.4.2 Guidance and Control Law Design

The key contributions of the research in the context of designing autonomous guidance and control laws for individual dynamical systems are highlighted as follows:

1. In this research, we analyzed the effect of available state feedback regarding the cable states on the swing attenuation of a multi-rotor with a flexible-cable suspended payload system by utilizing a game theoretic approach. In this approach, we constructed a quadratic differential game involving two players: the multi-rotor, aiming to minimize swing, and the suspended payload, representing the maximizing factor. This game is structured within a Linear-Quadratic-Tracking (LQT) framework, considering various scenarios of suspension cable state feedback available to the controller. These scenarios range from full state knowledge of the cable, to only having information about the relative attitude of the payload, or having no cable state information at all. The analysis from this work suggests that the controller with relative attitude information of the payload with respect to the multi-rotor can result in slower but more stable responses to disturbances caused by the initial deflection of the cable comparing to the case with full state knowledge of the cable segments.

2. Additionally, we introduced a method that incorporates catenary analysis of a flexible suspension cable into the guidance system of a single multi-rotor with a slung load. This approach enhances trajectory tracking accuracy by accounting for the shape and tension force along the flexible cable. It provides boundary conditions necessary to achieve the desired tension and cable shape, thereby offering a more refined understanding of the position and tension commands required by the multi-rotor. This improved knowledge assists in compensating for the swing dynamics of the cable and the resultant loads encountered in aerial payload transportation tasks. The method has been implemented in conjunction with a geometric control approach, further augmenting its effectiveness in precise trajectory management.
3. In this study, we propose a nonlinear dynamic inversion-based (NDI) approach for the attitude and trajectory tracking control of a medium-size, low altitude airship equipped with vertical takeoff and landing (VTOL) capabilities, thanks to its tiltable motor configuration. The research encompasses the design and integration of various autonomous guidance laws tailored for specific autopilot modes, including takeoff, landing, and waypoint navigation missions. Additionally, we developed a control allocation scheme utilizing the Moore-Penrose pseudo-inverse. This scheme facilitates transitioning between the airship's forward flight and hover flight control configurations. Consequently, our work presents a comprehensive control structure that enables autonomous navigation of the airship across its entire flight envelope.

The publications based on the research above are listed below:

- Uluhan C. Kaya and Kamesh Subbarao, "Simulation of Autonomous Airship Operations with Integrated Autopilot Modes for Practical Scenarios," AIAA Aviation Forum, Chicago, IL, June 2022. (Reference [85])

- Uluhan C. Kaya, Abhishek Kashyap, Kamesh Subbarao, and Animesh Chakravarthy, "Nonlinear Control of an Autonomous Airship with Collision Avoidance Capability," AIAA SciTech Forum, National Harbor, MD, January 2023. (Reference [86])
- Uluhan C. Kaya and Kamesh Subbarao, "Game Theoretic Approach for Swing Attenuation of a Multi-Rotor with Suspended Payload System," (To be submitted).

1.4.3 Cooperative Control of Multiple Aerial Vehicles

The research primarily contributes to the development of cooperative control laws in the following significant ways:

1. This research introduces a novel approach to cooperative aerial payload manipulation using multi-rotors, integrating catenary analysis for managing payloads suspended by flexible cables. The primary contribution is the use of catenary shape information to guide individual vehicles during trajectory tracking tasks. Building on our previous findings (referenced in [87]), this study also demonstrates the robustness of our approach against state uncertainties via Monte Carlo simulations where each multi-rotor system independently takes noise corrupted states for both payload and itself to implement necessary guidance and control for stabilization and trajectory tracking. Thus, these results essentially present a successful implementation of distributed control for the cooperative aerial payload manipulation task. This study exemplifies the cooperation between multiple UAS vehicles in physical level.
2. This study introduces the integration of an extended state observer (ESO) based total disturbance estimation model in cooperative formation control, which simplifies multi-agent system dynamics and enhances robustness against external

disturbances like wind, air drag, and parameter uncertainties. The research also investigates the impact of various graph topologies on formation control, which is crucial for coordinated and complex aerial tasks. A major focus of the study is on exploring how communication topology, external disturbances, and the application of ESO influence formation behavior, offering new insights into the dynamics of multi-agent aerial systems. A pivotal aspect of this work is the demonstration of its application in realistic scenarios, particularly in search and rescue missions, where an airship transports and deploys multi-rotors to the mission area. These multi-rotors then execute the tasks by forming various formations, adapting to different shapes and topologies, and following diverse trajectory commands. This practical demonstration underscores the effectiveness of the developed methods and models in real-world settings. Additionally, the integration of these algorithms and control systems into a simulation environment for formation tasks bridges the gap between theoretical development and practical application, ensuring operational viability of the proposed solutions in a range of applications, from emergency response to environmental monitoring.

The publications based on the research above is listed below:

- Uluhan C. Kaya and Kamesh Subbarao, "Catenary Guided Cooperative Aerial Manipulation of a Suspended Payload via Multi-Rotors," Journal of Guidance, Control, and Dynamics, 2024. (In Review).
- Uluhan C. Kaya and Kamesh Subbarao, "Catenary Guided Cooperative Aerial Manipulation of a Suspended Payload via Multi-Rotors," AIAA SciTech Forum, Orlando, FL, January 2024. (Reference [87]).

1.5 Outline of the Dissertation

This dissertation is divided into 5 chapters. In Chapter 2, the modeling of aerial vehicles and their associated subsystems that are employed in this research are carried out. Chapter 3 presents the development of linear and nonlinear control strategies for a single multi-rotor with a flexibly suspended payload and airship systems, respectively. Chapter 4 details the development of control strategies for both cooperative aerial manipulation and formation tasks involving multiple multi-rotors. Finally, the overall sumamry and concluding remarks of this dissertation is provided in Chapter 5.

Chapter 2

Modeling and Simulation of Constrained Aerial Systems

2.1 Modeling of Dynamical Systems

In this chapter, the modeling of aerial vehicles and their associated subsystems are carried out. For aerial payload manipulation, the focus is on modeling systems that include flexible cables, multi-rotors, and a suspended payload. On the other hand, the cooperative formation scenario employs an airship in conjunction with a team of multi-rotors.

2.1.1 Flexible Cable Modeling

In this research, the suspension cable is regarded as an inelastic yet flexible entity. This flexibility is represented by using a series of rigid links connected serially, which act as cable segments. The flexibility of the cable is achieved by the variations in the relative attitude of these links, illustrating the cable's deformation.

The simplifying assumptions for this model is given below.

Assumption 2.1.1.

- *Each cable segment is identical.*
- *Each segment has a lumped mass at its geometric center.*
- *Segments are constrained to prevent any twist motion along the link.*

Figure 2.1 illustrates a flexible cable consisting of N links, with one end supported and a force being applied at the opposite end.

Here, $\boldsymbol{q}_i \in \mathbb{R}^3$ corresponds to the unit vector along the i^{th} link through the cable and it lies on a manifold defined by a product of two spheres $\mathrm{S}^2 = \{\boldsymbol{q} \in \mathbb{R}^3 \mid \|\boldsymbol{q}\| = 1\}$,

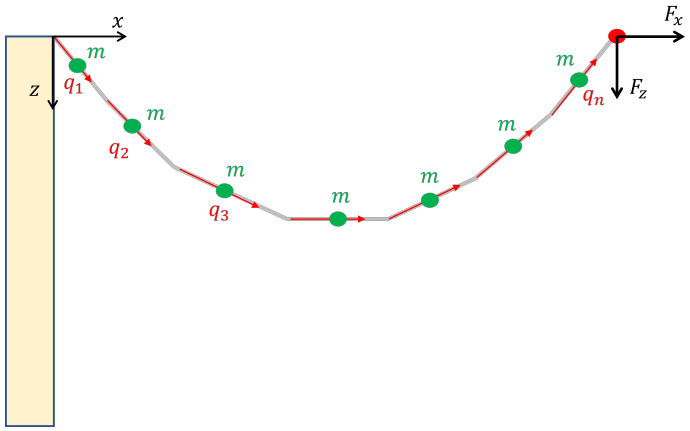

Figure 2.1: N-link cable supported at one end

which is a part of serially connected 2-sphere manifolds forming the complete cable. Also, $m_i = m$ for $(i = 1, 2, .., n)$ is the mass of each link. The overall system evolves in $(\mathrm{S}^2)^n = \mathrm{S}^2 \times \ldots \times \mathrm{S}^2$ configuration manifold.

The inertial positions of each segment and the final segment are found as follows,

$$\boldsymbol{x}_i = \sum_{j=1}^{i-1} l_j \boldsymbol{q}_j + \frac{l}{2}\boldsymbol{q}_i$$
$$\boldsymbol{x}_n = \sum_{i=1}^{n} l_i \boldsymbol{q}_i$$

where $l_i = l,\ (i = 1, 2, .., n)$ is the length of cable segments.

Lagrangian of this system is obtained below,

$$L = \frac{1}{2}\sum_{i,j=1}^{n} \dot{\boldsymbol{q}}_i^T \boldsymbol{M}_{ij} \dot{\boldsymbol{q}}_j + \sum_{i=1}^{n} \boldsymbol{q}_i^T \boldsymbol{M}_{0i} g \boldsymbol{e}_3 \tag{2.1}$$

where $\boldsymbol{e}_3 = [0\ 0\ 1]^T$ is the unit vector along the gravitational acceleration direction and the mass terms are defined as follows,

$$\boldsymbol{M}_{0i} = \Big(\frac{2(n-i)+1}{2} l_i m_i \boldsymbol{I}_3\Big)$$

$$\boldsymbol{M}_{ij} = \begin{cases} \frac{4(n-i)+1}{4} l_i^2 m_i \boldsymbol{I}_3, & \text{if } i = j \\ \frac{2(n-a)+1}{2} l_i^2 m_i \boldsymbol{I}_3, & \text{if } i \neq j,\ (a = \max(i,j)) \end{cases}$$

Kinematic relation between link attitude and angular velocity, $\boldsymbol{\omega} \in \mathbb{R}^3$, is defined by

$$\dot{\boldsymbol{q}} = \boldsymbol{\omega} \times \boldsymbol{q}$$

The variation on states is defined by

$$\delta \boldsymbol{q}_i = \boldsymbol{\xi}_i \times \boldsymbol{q}_i$$

$$\delta \dot{\boldsymbol{q}}_i = \dot{\boldsymbol{\xi}}_i \times \boldsymbol{q}_i + \boldsymbol{\xi}_i \times \dot{\boldsymbol{q}}_i$$

where $\boldsymbol{\xi}_i \in \mathbb{R}^3$ is an infinitesimal change in segment attitude.

Similarly, applying the variation, infinitesimal work done by the applied force is found by

$$\delta W = \boldsymbol{f} \cdot \delta \boldsymbol{x}_n = l \boldsymbol{f} \cdot \sum_{i=1}^{n} \delta \boldsymbol{q}_i$$

Using Lagrange d'Alembert formulation, we can obtain the minimum action principle below,

$$\begin{aligned} \delta \mathfrak{B} &= \int_0^T \left[\delta L + \delta W\right] dt = 0 \\ &= \sum_{i=1}^{n} \int_0^T \Big[\sum_{j=1}^{n} \delta \dot{\boldsymbol{q}}_i \cdot \boldsymbol{M}_{ij} \dot{\boldsymbol{q}}_j + \delta \boldsymbol{q}_i \cdot \boldsymbol{M}_{0i} g \boldsymbol{e}_3 + l \boldsymbol{f} \cdot \delta \boldsymbol{q}_i \Big] \, dt \end{aligned} \tag{2.2}$$

Employing vanishing boundary conditions and integration by parts, the equations of motion for this system are derived as follows,

$$\boldsymbol{M}_{ii} \dot{\boldsymbol{\omega}}_i = \boldsymbol{q}_i \times \sum_{j=1(j\neq i)}^{n} \big(\boldsymbol{M}_{ij} (\boldsymbol{q}_j \times \dot{\boldsymbol{\omega}}_j) + \boldsymbol{M}_{ij} (\boldsymbol{\omega}_j \cdot \boldsymbol{\omega}_j) \boldsymbol{q}_j + \boldsymbol{M}_{0i} g \boldsymbol{e}_3 + l \boldsymbol{f} \big) \tag{2.3}$$

where the identities, $\ddot{\boldsymbol{q}}_i = \dot{\boldsymbol{\omega}}_i \times \boldsymbol{q}_i + \boldsymbol{\omega}_i \times (\boldsymbol{\omega}_i \times \boldsymbol{q}_i) = \dot{\boldsymbol{\omega}}_i \times \boldsymbol{q}_i - (\boldsymbol{\omega}_i \cdot \boldsymbol{\omega}_i)\boldsymbol{q}_i$, $\boldsymbol{q}_i \cdot \boldsymbol{\omega}_i = 0$ and $\boldsymbol{q}_i \cdot \boldsymbol{q}_i = 1$ are used.

By transforming 2.3 into matrix form, $\boldsymbol{A}\dot{\boldsymbol{\omega}} = \boldsymbol{d}$,

$$\begin{bmatrix} \boldsymbol{M}_{11} & -\boldsymbol{M}_{12}\hat{\boldsymbol{q}}_1\hat{\boldsymbol{q}}_2 & \dots & -\boldsymbol{M}_{1n}\hat{\boldsymbol{q}}_1\hat{\boldsymbol{q}}_n \\ -\boldsymbol{M}_{21}\hat{\boldsymbol{q}}_2\hat{\boldsymbol{q}}_1 & \boldsymbol{M}_{22} & \dots & -\boldsymbol{M}_{2n}\hat{\boldsymbol{q}}_2\hat{\boldsymbol{q}}_n \\ \vdots & \vdots & & \vdots \\ -\boldsymbol{M}_{n1}\hat{\boldsymbol{q}}_n\hat{\boldsymbol{q}}_1 & -\boldsymbol{M}_{n2}\hat{\boldsymbol{q}}_n\hat{\boldsymbol{q}}_2 & \dots & \boldsymbol{M}_{nn} \end{bmatrix} \begin{bmatrix} \dot{\boldsymbol{\omega}}_1 \\ \dot{\boldsymbol{\omega}}_2 \\ \vdots \\ \dot{\boldsymbol{\omega}}_n \end{bmatrix}$$
$$= \begin{bmatrix} \sum_{j=2}^{n}(\boldsymbol{\omega}_j \cdot \boldsymbol{\omega}_j)\boldsymbol{M}_{1j}\hat{\boldsymbol{q}}_1\boldsymbol{q}_j + \hat{\boldsymbol{q}}_1\boldsymbol{M}_{01}g\boldsymbol{e}_3 + l\hat{\boldsymbol{q}}_1\boldsymbol{f} \\ \sum_{j=1(j\neq 2)}^{n}(\boldsymbol{\omega}_j \cdot \boldsymbol{\omega}_j)\boldsymbol{M}_{2j}\hat{\boldsymbol{q}}_2\boldsymbol{q}_j + \hat{\boldsymbol{q}}_2\boldsymbol{M}_{02}g\boldsymbol{e}_3 + l\hat{\boldsymbol{q}}_2\boldsymbol{f} \\ \vdots \\ \sum_{j=1}^{n-1}(\boldsymbol{\omega}_j \cdot \boldsymbol{\omega}_j)\boldsymbol{M}_{nj}\hat{\boldsymbol{q}}_n\boldsymbol{q}_j + \hat{\boldsymbol{q}}_n\boldsymbol{M}_{0n}g\boldsymbol{e}_3 + l\hat{\boldsymbol{q}}_n\boldsymbol{f} \end{bmatrix} \tag{2.4}$$

For the cable supported at both ends, $\boldsymbol{f} \in \mathbb{R}^3$ can be computed by the constraint equations. Figure 2.2 illustrates the constrained cable at the end points such that their positions are fixed.

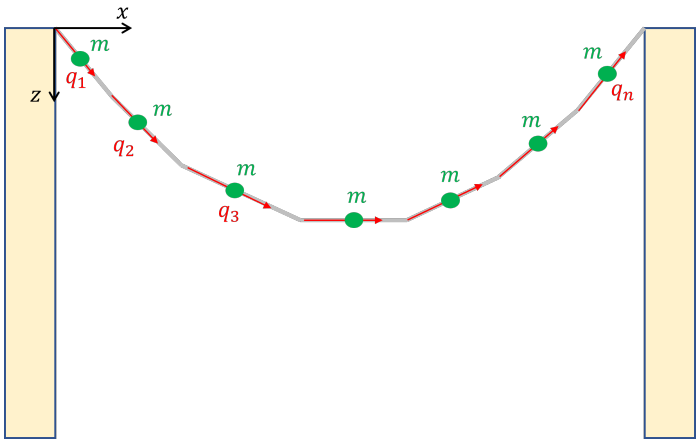

Figure 2.2: N-link cable supported at both ends

The constraint equation is defined below,

$$g(\boldsymbol{q}) \triangleq \sum_{i=1}^{n} l_i \boldsymbol{q}_i - \boldsymbol{x}_n = 0 \tag{2.5}$$

Using (2.5), the augmented Lagrangian can be obtained by

$$L_a = L(\boldsymbol{q}, \dot{\boldsymbol{q}}) + \boldsymbol{\lambda}^T g(\boldsymbol{q})$$

where $\boldsymbol{\lambda} \in \mathbb{R}^3$ is a vector of Lagrangian multipliers corresponding to the constraint forces.

The variation in the augmented Lagrangian is acquired by

$$\delta L_a = \sum_{i,j=1}^{n} \delta \dot{\boldsymbol{q}}_i \cdot \boldsymbol{M}_{ij} \dot{\boldsymbol{q}}_j + \sum_{i=1}^{n} \delta \boldsymbol{q}_i \cdot \boldsymbol{M}_{0i} g \boldsymbol{e}_3 + \sum_{i=1}^{n} l \boldsymbol{\lambda} \cdot \delta \boldsymbol{q}_i$$

Finally, the equations of motion for the constrained system are derived below,

$$\boldsymbol{M}_{ii} \dot{\boldsymbol{\omega}}_i = \boldsymbol{q}_i \times \sum_{j=1(j \neq i)}^{n} \left((\boldsymbol{q}_j \times \dot{\boldsymbol{\omega}}_j) \boldsymbol{M}_{ij} + (\boldsymbol{\omega}_j \cdot \boldsymbol{\omega}_j) \boldsymbol{M}_{ij} \boldsymbol{q}_j + \boldsymbol{M}_{0i} g \boldsymbol{e}_3 + l \boldsymbol{\lambda} \right)$$

which is the same as previous case. Here, instead of $\boldsymbol{f}$, unknown Lagrange multipliers, $\boldsymbol{\lambda}$, are introduced.

Constraint forces are

$$\boldsymbol{f}_{cons} = \boldsymbol{\lambda}$$

where $\boldsymbol{\lambda}$ represent the tension force at the end point, $\boldsymbol{x}_n$.

2.1.1.1 Catenary Analysis of the Flexible Cable Model

A catenary is defined as the curve formed by an inelastic chord hanging under its own weight, assuming uniform density and cross-sectional consistency throughout its length. Some of the examples[1] that we observe the catenary shape are given in Figure 2.3.

[1] https://en.wikipedia.org/wiki/Catenary

(a) Hanging chain

(b) Hanging bridge

(c) Hanging spider web

Figure 2.3: Examples of catenary shapes in structures and nature. [1]

The definition of the catenary curve aligns with the assumptions established in our flexible cable model. Thus, the analytical catenary equations can be utilized to assess the accuracy of the N-link flexible cable model, particularly in terms of its ability to replicate the actual shape of the cable under specified conditions.

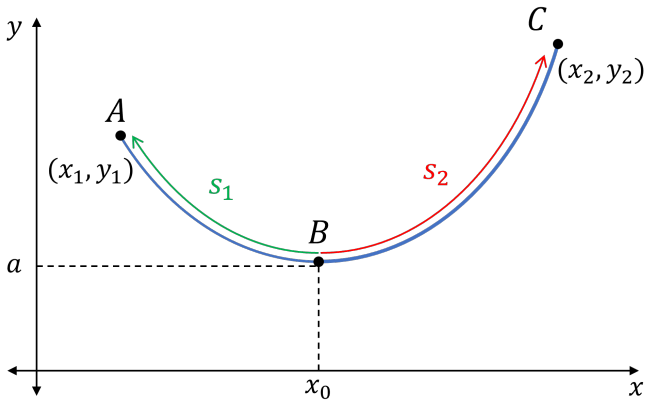

Figure 2.4: Illustration of catenary curve, parameters, and corresponding locations

The analytical catenary equations, which determine the relative height at any given horizontal position along the cable and the total length of the cable between two points, are given below,

$$y - y_0 = a \cosh\left(\frac{x - x_0}{a}\right) \tag{2.6}$$

$$s = s_1 + s_2 = 2a \sinh\left(\frac{x_2 - x_1}{2a}\right) \cosh\left(\frac{\frac{x_1+x_2}{2} - x_0}{a}\right) \tag{2.7}$$

where a is the parameter that defines the curvature of cable. Also, the other terms are illustrated in Figure 2.4.

Moreover, the free-body diagram of a cable segment, highlighting the acting forces, is depicted in Figure 2.5. In this diagram, T_0 symbolizes the tension force at the point where the cable is tangent to the horizontal plane, while T represents the general tension force along the cable. Additionally, w_0 denotes the unit weight per length of the cable.

Based on the force relations depicted in Figure 2.5, we can determine the angle, θ, which represents the angle between the horizontal plane and the tangent of the

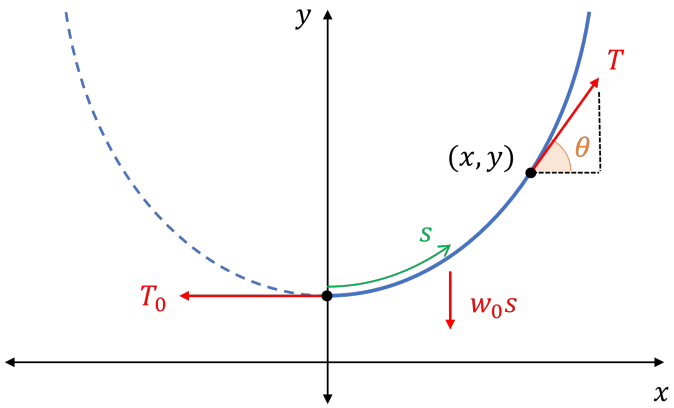

Figure 2.5: Illustration of free-body diagram of a cable segment with acting forces

curve at any point of the cable where tension force is applied, can be determined as follows,

$$\theta = \tan^{-1}\left(\frac{w_0 s}{T_0}\right)$$

To find the solution to catenary equations, provided in (2.6) and (2.7), for the given boundary conditions and constant cable length, an implicit solution can be used to determine the parameter a that defines the catenary curve. Solution procedure is outlined below,

- Guess a and solve $\hat{x}_0$ implicitly for given (x_1, y_1) and (x_2, y_2) pairs.
- Use $\hat{x}_0$ and update $\hat{a}$ using length equation.
- Repeat until the error between estimated and actual cable length is within the threshold.

Figure 2.6 displays a comparative analysis of the final shape and tension between the N-link flexible cable model and the catenary solutions under varying initial conditions and numbers of links. These plots distinctly reveal that with an increase in the number of links, the discrepancy between the analytical model and the N-link approximation of the flexible cable diminishes.

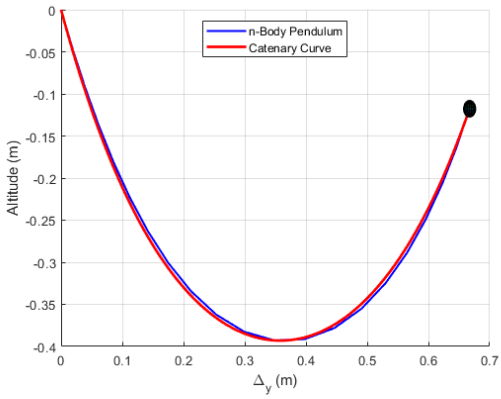

(a) 20-Link Cable vs Catenary Solution

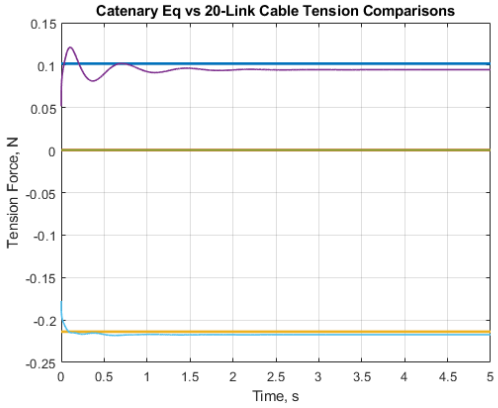

(b) Tension Force Comparison

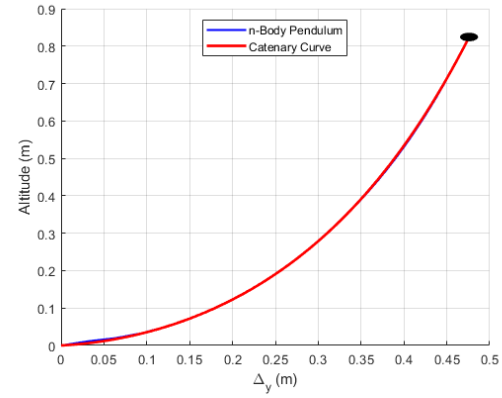

(c) 30-Link Cable vs Catenary Solution

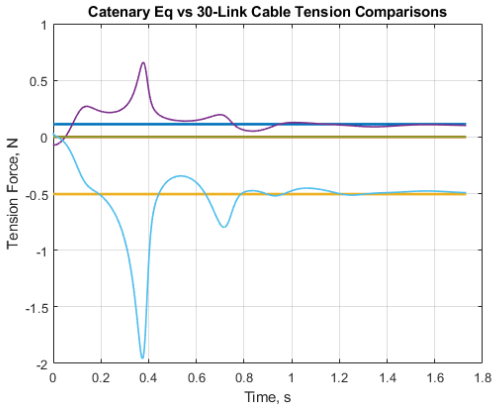

(d) Tension Force Comparison

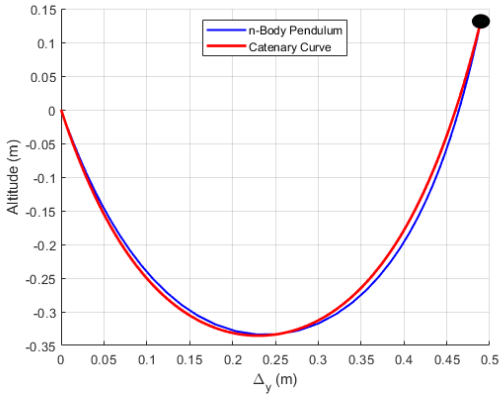

(e) 40-Link Cable vs Catenary Solution

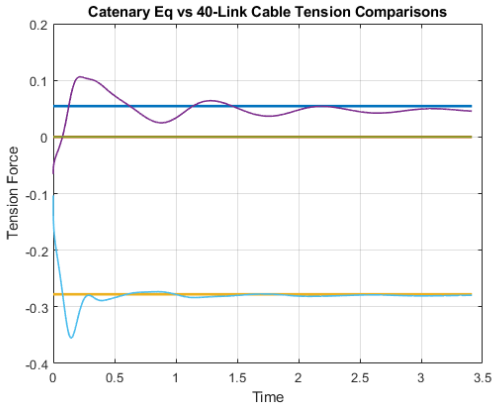

(f) Tension Force Comparison

Figure 2.6: The plots on the left column represents the comparison of steady-state shape of N-link cable with increased number of cable segments and the analytical catenary shape for various boundary conditions. The right column plots illustrate the end point tension force comparison.

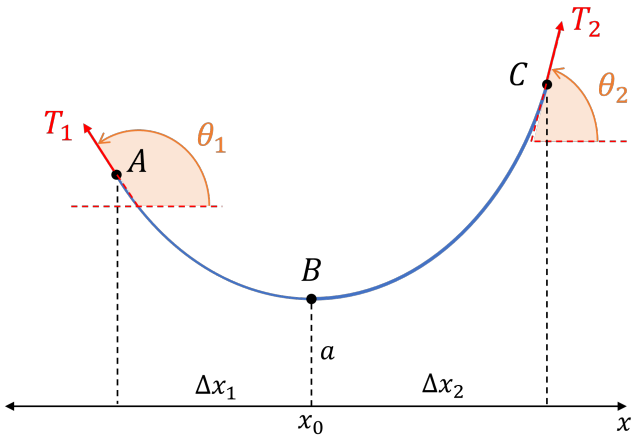

Figure 2.7: Illustration of catenary curve with end-point slopes and forces

Finding catenary curve given end-point slopes: Analytical solution of a catenary curve can be derived using Equations (2.6) and (2.7), provided that the end-point forces or slope of the angles are known. Figure 2.7 illustrates the curve with given boundary conditions. Equation for the slope of catenary curve is achieved by the differentiation of Equation (2.6),

$$\frac{dy}{dx} = \tan(\theta) = \sinh\left(\frac{\Delta x}{a}\right) \tag{2.8}$$

To find the curve parameter, a, Equation 2.7 is modified as follows,

$$s = 2a \sinh\left(\frac{\Delta x_2}{2a} - \frac{\Delta x_1}{2a}\right) \cosh\left(\frac{\Delta x_1}{2a} + \frac{\Delta x_2}{2a}\right) \tag{2.9}$$

By applying boundary conditions, the terms $\frac{\Delta x_1}{a}$ and $\frac{\Delta x_2}{a}$ can be obtained using the inverse hyperbolic sine function, $\sinh^{-1}(x) = \ln\left(x + \sqrt{x^2+1}\right)$.

$$\frac{\Delta x}{a} = \ln(\tan\theta + \sec\theta) \tag{2.10}$$

where θ is defined in an open interval of $\mathbb{R} \rightarrow \left(-\frac{\pi}{2}, \frac{\pi}{2}\right)$ and it can be computed given that the tension force at a desired location along the cable is known.

Finally, Equation (2.9) is utilized with the given and derived values to find a as follows,

$$a = \frac{s}{2\sinh\left(\frac{\Delta x_2}{2a} - \frac{\Delta x_1}{2a}\right)\cosh\left(\frac{\Delta x_1}{2a} + \frac{\Delta x_2}{2a}\right)} \tag{2.11}$$

Now, employing Equations (2.6) and (2.10), the catenary curve can be constructed. It is worth nothing that in case the angle θ approaches vertical line, resulting two conditions should be handled separately.

2.1.2 Single Multi-rotor with a Flexible Cable Suspended Payload

In this section, the modeling of a multi-rotor with a flexible cable suspended payload is performed as a multi-body dynamics problem, similar to Refs. [4] and [21]. To simplify the modeling of the actual flexible suspension cable, following assumptions are made accordingly.

Assumption 2.1.2.

1. *The cable is treated as the serial connection of multiple straight links with concentrated corresponding masses at the center of each link.*
2. *The cable segments are inelastic and they can carry the tension force only.*
3. *The cable links do not twist around its own length axis.*

Figure 2.8 illustrates the multi-rotor with the suspended payload system where the suspension cable is attached to the center of gravity of the multi-rotor.

Remark 2.1.1. *The model shown in Figure 2.8 is validated by comparing the results with the analytical catenary equations in the previous section. This comparison reveals that with an increasing number of cable segments, the static curve formed by the N-link cable—upon supporting its free end—gradually and asymptotically aligns with the catenary shape derived from the analytical equations.*

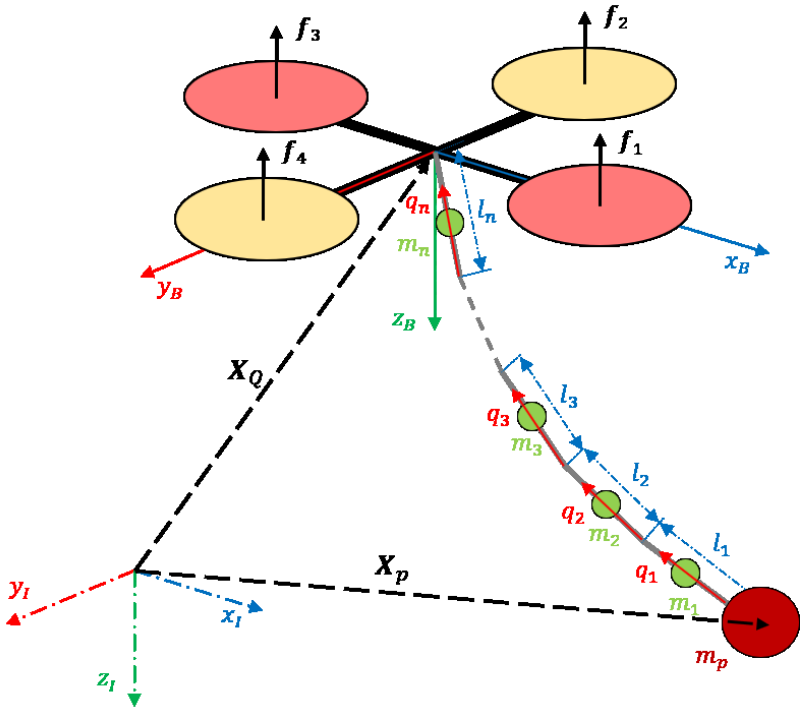

Figure 2.8: Illustration of a single multi-rotor with a flexibly suspended payload

The positions of the multi-rotor and the payload relative to the Inertial frame are represented by $\boldsymbol{x}_Q,\ \boldsymbol{x}_P \in \mathbb{R}^3$, respectively. Furthermore, the positions of the mass elements on each link, as well as the position of the multi-rotor itself, are expressed in terms of the payload's position and the unit directions along each link, as follows,

$$\boldsymbol{x}_i = \boldsymbol{x}_P + \sum_{a=1}^{i-1} l_a \boldsymbol{q}_a + \frac{1}{2} l_i \boldsymbol{q}_i$$

$$\boldsymbol{x}_Q = \boldsymbol{x}_P + \sum_{i=1}^{n} l_i \boldsymbol{q}_i$$

where $\boldsymbol{q}_i$ is the unit vector along the i^{th} link through the cable and it lies on a manifold defined by a product of two spheres $\mathrm{S}^2 = \{\boldsymbol{q} \in \mathbb{R}^3 \mid \|\boldsymbol{q}\| = 1\}$, which is a part of serially connected 2-sphere manifolds forming the complete cable. The links are assumed to be identical with length of $l_i = l$ and the mass of m_i for $i = 1, 2, .., n$. Moreover, the payload is modeled as a point mass with the magnitude of m_P.

The rate of change of unit vectors are expressed by a cross product as $\dot{\boldsymbol{q}}_i = \boldsymbol{\omega}_i \times \boldsymbol{q}_i$ where $\boldsymbol{\omega}_i$ is the angular velocity of the i^{th} link in its body-fixed frame. Considering the non-twisting cable link assumption made in Assumption 2.1.2, the orthogonality constraints on the link attitudes and angular velocities are introduced as $\boldsymbol{\omega}_i \cdot \boldsymbol{q}_i = 0$ and $\boldsymbol{q}_i \cdot \dot{\boldsymbol{q}}_i = 0$.

The mass and moment of inertia of the multi-rotor are denoted by m_Q and $\boldsymbol{J}_Q \in \mathbb{R}^{3\times 3}$ respectively, and its attitude is given by $\boldsymbol{R}_Q \in \mathrm{SO}(3)$ with the angular velocity of $\boldsymbol{\omega}_Q$ defined in the body-fixed coordinate frame. Thus, the configuration manifold of the complete system is $\mathbb{R}^3 \times \mathrm{SO}(3) \times (\mathrm{S}^2)^n$ where $(\mathrm{S}^2)^n = \mathrm{S}^2 \times \ldots \times \mathrm{S}^2$.

To construct the Lagrangian of the system, kinetic and potential energies are found as follows.

$$T = \frac{1}{2}\dot{\boldsymbol{x}}_Q^T m_Q \dot{\boldsymbol{x}}_Q + \frac{1}{2}\boldsymbol{\omega}_Q^T \boldsymbol{J}_Q \boldsymbol{\omega}_Q + \frac{1}{2}\sum_{i=1}^{n} \dot{\boldsymbol{x}}_i^T m_i \dot{\boldsymbol{x}}_i + \frac{1}{2}\dot{\boldsymbol{x}}_P^T m_P \dot{\boldsymbol{x}}_P \tag{2.12}$$

$$U = -m_Q g \boldsymbol{x}_Q \cdot \boldsymbol{e}_3 - \sum_{i=1}^{n} m_i g \boldsymbol{x}_i \cdot \boldsymbol{e}_3 - m_P g \boldsymbol{x}_P \cdot \boldsymbol{e}_3 \tag{2.13}$$

where $\boldsymbol{e}_3$ is the unit direction along the gravitational acceleration, g, i.e. $\boldsymbol{e}_3 = [0\ 0\ 1]^T$.

Substituting $\boldsymbol{x}_i$ and $\boldsymbol{x}_Q$ into (2.12)-(2.13), Lagrangian is obtained as

$$\begin{aligned} L(\boldsymbol{x}_P, \dot{\boldsymbol{x}}_P, \boldsymbol{R}_Q, \boldsymbol{\omega}_Q, \boldsymbol{q}_1, \dot{\boldsymbol{q}}_1, .., \boldsymbol{q}_n, \dot{\boldsymbol{q}}_n) &= T - U \\ &= \frac{1}{2}\dot{\boldsymbol{x}}_P^T \boldsymbol{M}_{00} \dot{\boldsymbol{x}}_P + \frac{1}{2}\boldsymbol{\omega}_Q^T \boldsymbol{J}_Q \boldsymbol{\omega}_Q + \boldsymbol{M}_{00} g \boldsymbol{x}_P \cdot \boldsymbol{e}_3 \\ &\quad + \dot{\boldsymbol{x}}_P^T \sum_{i=1}^{n} \boldsymbol{M}_{0i} \dot{\boldsymbol{q}}_i + \frac{1}{2}\sum_{i,j=1}^{n} \dot{\boldsymbol{q}}_i^T \boldsymbol{M}_{ij} \dot{\boldsymbol{q}}_j + \sum_{i=1}^{n} \boldsymbol{M}_{0i} g \boldsymbol{q}_i \cdot \boldsymbol{e}_3 \end{aligned}$$

where the mass terms are defined by

$$\boldsymbol{M}_{00} = \left(m_Q + \sum_{i=1}^{n} m_i + m_P \right) \boldsymbol{I}_3$$
$$\boldsymbol{M}_{0i} = \left(\frac{2(n-i)+1}{2} l m_i + l m_Q \right) \boldsymbol{I}_3$$
$$\boldsymbol{M}_{ij} = \begin{cases} \left(\frac{4(n-i)+1}{4} l^2 m_i + l^2 m_Q \right) \boldsymbol{I}_3, \text{ if } i = j \\ \left(\frac{2(n-a)+1}{2} l^2 m_i + l^2 m_Q \right) \boldsymbol{I}_3, \text{ if } i \neq j \ (a = \max(i,j)) \end{cases}$$

Using the variational principle on the Lagrangian, we obtain

$$\begin{aligned} \delta L =& \mathbf{D}_{\boldsymbol{x}_P} L \cdot \delta \boldsymbol{x}_P + \mathbf{D}_{\dot{\boldsymbol{x}}_P} L \cdot \delta \dot{\boldsymbol{x}}_P + \mathbf{D}_{\boldsymbol{R}_Q} L \cdot \delta \boldsymbol{R}_Q \\ &+ \mathbf{D}_{\boldsymbol{\omega}_Q} L \cdot \delta \boldsymbol{\omega}_Q + \sum_{i=1}^{n} \left(\mathbf{D}_{\boldsymbol{q}_i} L \cdot \delta \boldsymbol{q}_i + \mathbf{D}_{\dot{\boldsymbol{q}}_i} L \cdot \delta \dot{\boldsymbol{q}}_i \right) \end{aligned}$$

Variations on the states are derived as follows, [21]:

$$\begin{aligned} \delta \boldsymbol{R}_Q &= \boldsymbol{R}_Q \hat{\boldsymbol{\eta}}_Q \\ \delta \hat{\boldsymbol{\omega}}_Q &= (\delta \boldsymbol{R}_Q)^T \dot{\boldsymbol{R}}_Q + \boldsymbol{R}_Q^T \delta \dot{\boldsymbol{R}}_Q = \hat{\dot{\boldsymbol{\eta}}}_Q + \hat{\boldsymbol{\omega}}_Q \hat{\boldsymbol{\eta}}_Q - \hat{\boldsymbol{\eta}}_Q \hat{\boldsymbol{\omega}}_Q \\ &= \hat{\dot{\boldsymbol{\eta}}}_Q + \widehat{\boldsymbol{\omega}_Q \times \boldsymbol{\eta}_Q} = \hat{\dot{\boldsymbol{\eta}}}_Q + \mathrm{ad}_{\hat{\boldsymbol{\omega}}_Q} \hat{\boldsymbol{\eta}}_Q \\ \delta \boldsymbol{q}_i &= \boldsymbol{\xi}_i \times \boldsymbol{q}_i \\ \delta \dot{\boldsymbol{q}}_i &= \dot{\boldsymbol{\xi}}_i \times \boldsymbol{q}_i + \boldsymbol{\xi}_i \times \dot{\boldsymbol{q}}_i \end{aligned}$$

where $\boldsymbol{\eta}_Q, \boldsymbol{\xi} \in \mathbb{R}^3$. The hat operator $\widehat{(\cdot)} : \mathbb{R}^3 \to \mathfrak{so}(3)$ is the Lie algebra isomorphism between a vector $\in \mathbb{R}^3$ and its skew-symmetric form $\in \mathfrak{so}(3)$ as

$$\hat{\boldsymbol{a}} = \widehat{\begin{bmatrix} a_x \\ a_y \\ a_z \end{bmatrix}} = \begin{bmatrix} 0 & -a_z & a_y \\ a_z & 0 & -a_x \\ -a_y & a_x & 0 \end{bmatrix}$$

The adjoint action $\mathrm{ad}_x y : \mathfrak{g} \to \mathfrak{g}$, where $\mathfrak{g}$ is a Lie algebra over some arbitrary field and $x, y \in \mathfrak{g}$, is the group homomorphism providing a linear map as $\mathrm{ad}_x y = [x, y] =$

$xy - yx$. The co-adjoint action $\mathrm{ad}^*_x y : \mathfrak{g}^* \to \mathfrak{g}^*$ is the dual of the adjoint action defined as $\mathrm{ad}^*_x y = [y, x] = yx - xy$. Hence, for the $\mathfrak{so}(3)$, $\mathrm{ad}_{\hat{\boldsymbol{a}}}\hat{\boldsymbol{b}} = \hat{\boldsymbol{a}}\hat{\boldsymbol{b}} - \hat{\boldsymbol{b}}\hat{\boldsymbol{a}} = \widehat{\boldsymbol{a} \times \boldsymbol{b}}$ and $\mathrm{ad}^*_{\hat{\boldsymbol{a}}}\hat{\boldsymbol{b}} = \hat{\boldsymbol{b}}\hat{\boldsymbol{a}} - \hat{\boldsymbol{a}}\hat{\boldsymbol{b}} = \widehat{\boldsymbol{b} \times \boldsymbol{a}}$.

Equations below express the variations on the attitude states of multi-rotor and the cable links.

$$\begin{aligned}
\mathbf{D}_{\boldsymbol{R}_Q} L \cdot \delta \boldsymbol{R}_Q &= \mathbf{D}_{\boldsymbol{R}_Q} L \cdot (\boldsymbol{R}_Q \hat{\boldsymbol{\eta}}_Q) = \boldsymbol{R}_Q^T \mathbf{D}_{\boldsymbol{R}_Q} L \cdot \hat{\boldsymbol{\eta}}_Q \qquad (2.14)\\
\mathbf{D}_{\boldsymbol{\omega}_Q} L \cdot \delta \boldsymbol{\omega}_Q &= \mathbf{D}_{\boldsymbol{\omega}_Q} L \cdot (\dot{\boldsymbol{\eta}}_Q + \boldsymbol{\omega}_Q \times \boldsymbol{\eta}_Q)\\
&= \mathbf{D}_{\boldsymbol{\omega}_Q} L \cdot \dot{\boldsymbol{\eta}}_Q - (\boldsymbol{\omega}_Q \times \mathbf{D}_{\boldsymbol{\omega}_Q} L) \cdot \boldsymbol{\eta}_Q\\
\mathbf{D}_{\boldsymbol{q}_i} L \cdot \delta \boldsymbol{q}_i &= (\boldsymbol{q}_i \times \mathbf{D}_{\boldsymbol{q}_i} L) \cdot \boldsymbol{\xi}_i\\
\mathbf{D}_{\dot{\boldsymbol{q}}_i} L \cdot \delta \dot{\boldsymbol{q}}_i &= (\boldsymbol{q}_i \times \mathbf{D}_{\dot{\boldsymbol{q}}_i} L) \cdot \dot{\boldsymbol{\xi}}_i + (\dot{\boldsymbol{q}}_i \times \mathbf{D}_{\dot{\boldsymbol{q}}_i} L) \cdot \boldsymbol{\xi}_i \qquad (2.15)
\end{aligned}$$

The minimum action principle is formulated for the given system as

$$\delta \mathfrak{B} = \int_0^T \left[\delta L + \boldsymbol{f}_I \cdot \delta \boldsymbol{x}_Q + \boldsymbol{\tau} \cdot \boldsymbol{\eta}_Q \right] dt = 0$$

where the variation in multi-rotor position is $\delta \boldsymbol{x}_Q = \delta \boldsymbol{x}_P + \sum_{i=1}^n l \delta \boldsymbol{q}_i$. The total net force generated by the propellers is represented in the Inertial frame with $\boldsymbol{f}_I$, which can be obtained by utilizing the body frame representation $\boldsymbol{f}_B$ as $\boldsymbol{f}_I = \boldsymbol{R}_Q^T \boldsymbol{f}_B$. $\boldsymbol{\tau}$ is the net torque propellers generated, which is written in multi-rotor's body-fixed frame.

Continuous equations of motion for this single multi-rotor with a flexible cable suspended payload are derived below,

$$\mathbf{D}_{\boldsymbol{x}_P} L - \frac{d}{dt} \mathbf{D}_{\dot{\boldsymbol{x}}_P} L + \boldsymbol{f}_I = 0 \qquad (2.16)$$

$$\boldsymbol{q}_i \times \boldsymbol{q}_i \times (\mathbf{D}_{\boldsymbol{x}_i} L - \frac{d}{dt} \mathbf{D}_{\dot{\boldsymbol{q}}_i} L + l \boldsymbol{f}_I) = 0 \qquad (2.17)$$

$$\boldsymbol{R}_Q^T \mathbf{D}_{\boldsymbol{R}_Q} L - \frac{d}{dt} \mathbf{D}_{\hat{\omega}_Q} L + (\mathrm{ad}^*_{\hat{\omega}_Q} \cdot \mathbf{D}_{\hat{\omega}_Q} L) + \hat{\boldsymbol{\tau}} = 0 \qquad (2.18)$$

It is worth noting that the cable twist constraint $\boldsymbol{q}_i \cdot \boldsymbol{\xi}_i = 0$ is used in (2.17) as $(\boldsymbol{q}_i \times (\mathbf{D}_{\boldsymbol{q}_i} L - \frac{d}{dt}\mathbf{D}_{\dot{\boldsymbol{q}}_i} L)) \cdot \boldsymbol{\xi}_i = (c\boldsymbol{q}_i) \cdot \boldsymbol{\xi}_i$ for any arbitrary constant c.

Partial derivatives of Lagrangian are given below,

$$\begin{aligned}
\mathbf{D}_{\boldsymbol{x}_P} L &= \boldsymbol{M}_{00} g \boldsymbol{e}_3 \\
\mathbf{D}_{\dot{\boldsymbol{x}}_P} L &= \boldsymbol{M}_{00} \dot{\boldsymbol{x}}_P + \sum_{i=1}^{n} \boldsymbol{M}_{0i} \dot{\boldsymbol{q}}_i \\
\mathbf{D}_{\boldsymbol{R}_Q} L &= 0 \\
\mathbf{D}_{\boldsymbol{\omega}_Q} L &= \boldsymbol{J}_Q \boldsymbol{\omega}_Q \\
\mathbf{D}_{\boldsymbol{q}_i} L &= \boldsymbol{M}_{0i} g \boldsymbol{e}_3 \\
\mathbf{D}_{\dot{\boldsymbol{q}}_i} L &= \boldsymbol{M}_{0i} \dot{\boldsymbol{x}}_P + \sum_{j=1}^{n} \boldsymbol{M}_{ij} \dot{\boldsymbol{q}}_j
\end{aligned}$$

Substituting the partial derivatives and using the relation $\ddot{\boldsymbol{q}}_i = \dot{\boldsymbol{\omega}}_i \times \boldsymbol{q}_i + \boldsymbol{\omega}_i \times (\boldsymbol{\omega}_i \times \boldsymbol{q}_i) = \dot{\boldsymbol{\omega}}_i \times \boldsymbol{q}_i - (\boldsymbol{\omega}_i \cdot \boldsymbol{\omega}_i)\boldsymbol{q}_i$, continuous equations of motion become

$$\boldsymbol{M}_{00} \dot{\boldsymbol{v}}_P - \sum_{i=1}^{n} \boldsymbol{M}_{0i} \hat{\boldsymbol{q}}_i \dot{\boldsymbol{\omega}}_i = \sum_{i=1}^{n} (\boldsymbol{\omega}_i \cdot \boldsymbol{\omega}_i) \boldsymbol{M}_{0i} \boldsymbol{q}_i + \boldsymbol{M}_{00} g \boldsymbol{e}_3 + \boldsymbol{f}_I \tag{2.19}$$

$$\begin{aligned}
\boldsymbol{M}_{ii} \dot{\boldsymbol{\omega}}_i = \boldsymbol{q}_i \times \left(\sum_{j=1(j\neq i)}^{n} (\boldsymbol{M}_{ij} (\boldsymbol{q}_j \times \dot{\boldsymbol{\omega}}_j) + (\boldsymbol{\omega}_j \cdot \boldsymbol{\omega}_j) \boldsymbol{M}_{ij} \boldsymbol{q}_j) \right) \\
+ \boldsymbol{q}_i \times (\boldsymbol{M}_{0i} g \boldsymbol{e}_3 - \boldsymbol{M}_{0i} \dot{\boldsymbol{v}}_P + l \boldsymbol{f}_I)
\end{aligned} \tag{2.20}$$

$$\boldsymbol{J}_Q \dot{\boldsymbol{\omega}}_Q + \hat{\boldsymbol{\omega}}_Q (\boldsymbol{J}_Q \boldsymbol{\omega}_Q) = \boldsymbol{\tau} \tag{2.21}$$

Generalized momenta of the system are found by Legendre Transformation as

$$P_{\boldsymbol{v}_P} = \mathbf{D}_{\dot{\boldsymbol{x}}_P} L \tag{2.22}$$

$$P_{\boldsymbol{\omega}_Q} = \mathbf{D}_{\boldsymbol{\omega}_Q} L$$

$$P_{\boldsymbol{\omega}_i} = \boldsymbol{q}_i \times \mathbf{D}_{\dot{\boldsymbol{q}}_i} L \tag{2.23}$$

2.1.3 Multiple Multi-rotors with a Suspended Payload via Flexible Cables

2.1.3.1 For Lumped Mass Point Payload

In this section, the procedure explained previously is extended to involve cooperative multi-rotors transporting a common payload that are suspended via flexible cables. Figure 2.9 illustrates the proposed configuration.

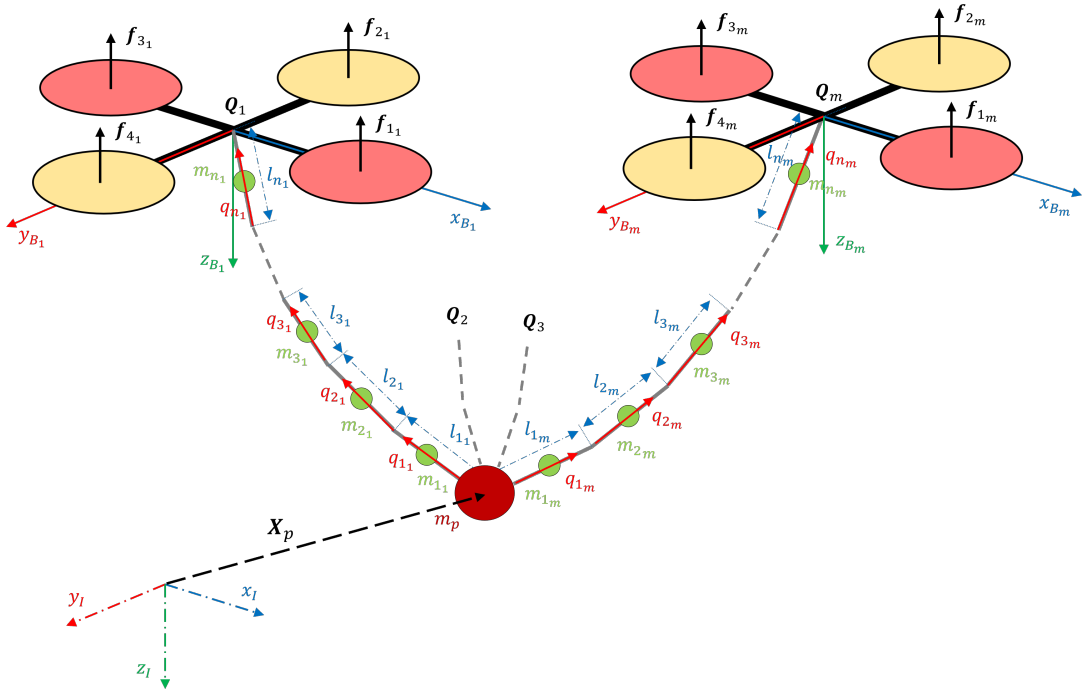

Figure 2.9: Illustration of cooperative multi-rotors with a flexibly suspended payload

In this configuration, the position vectors of each multi-rotor and their corresponding cable segments are represented in terms of the payload position, $\boldsymbol{x}_P$, and the unit vectors along cable links.

$$\boldsymbol{x}_{i_s} = \boldsymbol{x}_P + \sum_{r=1}^{i-1} l\boldsymbol{q}_{r_s} + \frac{1}{2} l\boldsymbol{q}_{i_s}$$

$$\boldsymbol{x}_{Q_s} = \boldsymbol{x}_P + \sum_{i=1}^{n} l\boldsymbol{q}_{i_s}$$

where $\boldsymbol{q}_{i_s}$ expresses the unit vector along the i^{th} link of the multi-rotor s. Without losing generality, suspension cables are assumed to be identical and consisting of the same number of segments.

Lagrangian of the cooperative multi-rotors with a slung-load system is constructed as

$$\begin{aligned}
&L(\boldsymbol{x}_P, \dot{\boldsymbol{x}}_P, \boldsymbol{R}_{Q_1}, \boldsymbol{\omega}_{Q_1}, \boldsymbol{R}_{Q_2}, \boldsymbol{\omega}_{Q_2}, .., \boldsymbol{R}_{Q_m}, \boldsymbol{\omega}_{Q_m}, \bar{\boldsymbol{q}}_1, \bar{\boldsymbol{q}}_2, .., \bar{\boldsymbol{q}}_m) \\
&= \frac{1}{2}\dot{\boldsymbol{x}}_P^T \boldsymbol{M}_{00} \dot{\boldsymbol{x}}_P + \boldsymbol{M}_{00} g \boldsymbol{x}_P \cdot \boldsymbol{e}_3 + \sum_{s=1}^{m}\sum_{i=1}^{n} \boldsymbol{M}_{0i_s} g \boldsymbol{q}_{i_s} \cdot \boldsymbol{e}_3 \\
&+ \sum_{s=1}^{m} \left[\frac{1}{2} {\boldsymbol{\omega}_{Q_s}}^T \boldsymbol{J}_{Q_s} \boldsymbol{\omega}_{Q_s} + \dot{\boldsymbol{x}}_P^T \sum_{i=1}^{n} \boldsymbol{M}_{0i_s} \dot{\boldsymbol{q}}_{i_s} + \frac{1}{2} \sum_{i,j=1}^{n} {\dot{\boldsymbol{q}}_{i_s}}^T \boldsymbol{M}_{ij_s} \dot{\boldsymbol{q}}_{j_s} \right]
\end{aligned}$$

where $\bar{\boldsymbol{q}}_s = [\boldsymbol{q}_{1_s}, \dot{\boldsymbol{q}}_{1_s}, .., \boldsymbol{q}_{n_s}, \dot{\boldsymbol{q}}_{n_s}]$ and the mass terms are

$$\begin{aligned}
\boldsymbol{M}_{00} &= \left(\sum_{s=1}^{m} (m_{Q_s} + \sum_{i=1}^{n} m_{i_s}) + m_P \right) \boldsymbol{I}_3 \\
\boldsymbol{M}_{0i_s} &= \left(\frac{2(n-i)+1}{2} l m_{i_s} + l m_{Q_s} \right) \boldsymbol{I}_3 \\
\boldsymbol{M}_{ij_s} &= \begin{cases} \left(\frac{4(n-i)+1}{4} l^2 m_{i_s} + l^2 m_{Q_s} \right) \boldsymbol{I}_3, \text{ if } i = j \\ \left(\frac{2(n-a)+1}{2} l^2 m_{i_s} + l^2 m_{Q_s} \right) \boldsymbol{I}_3, \text{ if } i \neq j, \quad (a = \max(i,j)) \end{cases}
\end{aligned}$$

The variational principle on Lagrangian gives us

$$\begin{aligned}
\delta L = &\mathbf{D}_{\boldsymbol{x}_P} L \cdot \delta \boldsymbol{x}_P + \mathbf{D}_{\dot{\boldsymbol{x}}_P} L \cdot \delta \dot{\boldsymbol{x}}_P + \sum_{s=1}^{m} \left[\mathbf{D}_{\boldsymbol{R}_{Q_s}} L \cdot \delta \boldsymbol{R}_{Q_s} + \mathbf{D}_{\boldsymbol{\omega}_{Q_s}} L \cdot \delta \boldsymbol{\omega}_{Q_s} \right] \\
&+ \sum_{s=1}^{m} \left[\mathbf{D}_{\boldsymbol{\omega}_{Q_s}} L \cdot \delta \boldsymbol{\omega}_{Q_s} + \sum_{i=1}^{n} \left(\mathbf{D}_{\boldsymbol{q}_{i_s}} L \cdot \delta \boldsymbol{q}_{i_s} + \mathbf{D}_{\dot{\boldsymbol{q}}_{i_s}} L \cdot \delta \dot{\boldsymbol{q}}_{i_s} \right) \right]
\end{aligned}$$

The variation on the work done by the forces and moments on each multi-rotor is

$$\delta W = \sum_{s=1}^{m} \left[\boldsymbol{f}_{I_s} \cdot \left(\delta \boldsymbol{x}_P + \sum_{i=1}^{n} l \delta \boldsymbol{q}_{i_s} \right) + \boldsymbol{\tau}_s \cdot \boldsymbol{\eta}_{Q_s} \right] \tag{2.24}$$

Using the relations given in (2.14)-(2.15), the variation on the action integral, $\delta\mathfrak{B} = \int_0^T (\delta L + \delta W)\, dt = 0$, is achieved as below,

$$\begin{aligned}
\delta\mathfrak{B} = \int_0^T \Bigg[& (\mathbf{D}_{\boldsymbol{x}_P} L - \frac{d}{dt}\mathbf{D}_{\dot{\boldsymbol{x}}_P} L + \sum_{s=1}^{m} \boldsymbol{f}_{I_s}) \cdot \delta\boldsymbol{x}_P \\
& + \sum_{s=1}^{m}\sum_{i=1}^{n} \boldsymbol{q}_{i_s} \times (\mathbf{D}_{\boldsymbol{q}_{i_s}} L - \frac{d}{dt}\mathbf{D}_{\dot{\boldsymbol{q}}_{i_s}} L + l\boldsymbol{f}_{I_s}) \cdot \boldsymbol{\xi}_{i_s} \\
& + \sum_{s=1}^{m} \Bigg[\boldsymbol{R}_{Q_s}{}^T \mathbf{D}_{\boldsymbol{R}_{Q_s}} L - \frac{d}{dt}\mathbf{D}_{\hat{\boldsymbol{\omega}}_{Q_s}} L + (\mathrm{ad}^*_{\hat{\boldsymbol{\omega}}_{Q_s}} \cdot \mathbf{D}_{\hat{\boldsymbol{\omega}}_{Q_s}} L) + \hat{\boldsymbol{\tau}}_s \Bigg] \cdot \hat{\boldsymbol{\eta}}_{Q_s} \Bigg]\, dt
\end{aligned}$$

which provides the continuous equations of motion for this cooperative system as follows:

$$\begin{aligned}
& \boldsymbol{M}_{00}\dot{\boldsymbol{v}}_P - \sum_{s=1}^{m}\sum_{i=1}^{n} \boldsymbol{M}_{0i_s} (\boldsymbol{q}_{i_s} \times \dot{\boldsymbol{\omega}}_{i_s}) \\
& \qquad = \sum_{s=1}^{m}\sum_{i=1}^{n} (\boldsymbol{\omega}_{i_s} \cdot \boldsymbol{\omega}_{i_s})\, \boldsymbol{M}_{0i_s}\boldsymbol{q}_{i_s} + \boldsymbol{M}_{00} g\boldsymbol{e}_3 + \sum_{s=1}^{m} \boldsymbol{f}_{I_s} \qquad (2.25) \\
& \boldsymbol{M}_{ii_s}\dot{\boldsymbol{\omega}}_{i_s} = \boldsymbol{q}_{i_s} \times \sum_{j=1(j\neq i)}^{n} (\boldsymbol{M}_{ij_s}(\boldsymbol{q}_{j_s} \times \dot{\boldsymbol{\omega}}_{j_s}) + (\boldsymbol{\omega}_{j_s} \cdot \boldsymbol{\omega}_{j_s})\boldsymbol{M}_{ij_s}\boldsymbol{q}_{j_s}) \\
& \qquad + \boldsymbol{x}_{i_s} \times (\boldsymbol{M}_{0i_s} g\boldsymbol{e}_3 - \boldsymbol{M}_{0i_s}\dot{\boldsymbol{v}}_P + l\boldsymbol{f}_{I_s}) \qquad (2.26) \\
& \boldsymbol{J}_{Q_s}\dot{\boldsymbol{\omega}}_{Q_s} + \hat{\boldsymbol{\omega}}_{Q_s}(\boldsymbol{J}_{Q_s}\boldsymbol{\omega}_{Q_s}) = \boldsymbol{\tau}_s \qquad (2.27)
\end{aligned}$$

One can deduce from (2.25)-(2.27) that the motion of the payload is affected by both the forces applied by multi-rotors and the dynamics of each flexible cable connected to it. On the other hand, Equation (2.26) indicates that each distinct suspension cable and the multi-rotor sub-system has its own separate dynamics, which are coupled by the whole system through the motion of the payload itself.

Generalized momentum states of the systems are derived by Legendre Transformation as follows,

$$P_{\boldsymbol{v}_P} = \mathbf{D}_{\dot{\boldsymbol{x}}_P} L \tag{2.28}$$

$$P_{\boldsymbol{\omega}_{Q_s}} = \mathbf{D}_{\boldsymbol{\omega}_{Q_s}} L$$

$$P_{\boldsymbol{\omega}_{i_s}} = \boldsymbol{q}_{i_s} \times \mathbf{D}_{\dot{\boldsymbol{q}}_{i_s}} L \tag{2.29}$$

These momentum states will be used in discrete Hamiltonian formalism in the next subsection.

2.1.3.2 For Rigid Body Payload

The previous model for the cooperative multi-rotors with a suspended load via flexible cables considers only a point mass payload. However, in this section, instead of a point load, a rigid body payload is incorporated with the model. Figure 2.10 illustrates the new model with a rectangular prism rigid slung payload with multi-rotors.

In this configuration, position vectors of each multi-rotor and their corresponding cable segments are represented in terms of the payload position, $\boldsymbol{x}_p$, and the unit vectors along cable links, $\boldsymbol{q}_{i_s}$, including the distance between attachment points and the center of mass of the payload, $\boldsymbol{\rho}_s$.

$$\boldsymbol{x}_{i_s} = \boldsymbol{x}_P + \boldsymbol{R}_P \boldsymbol{\rho}_s + \sum_{j=1}^{i-1} l\boldsymbol{q}_{j_s} + \frac{1}{2} l\boldsymbol{q}_{i_s}$$

$$\boldsymbol{x}_{Q_s} = \boldsymbol{x}_P + \boldsymbol{R}_P \boldsymbol{\rho}_s + \sum_{i=1}^{n} l\boldsymbol{q}_{i_s}$$

where $\boldsymbol{R}_P \in \mathbb{R}^{3\times 3}$ expresses the payload attitude with respect to the Inertial frame.

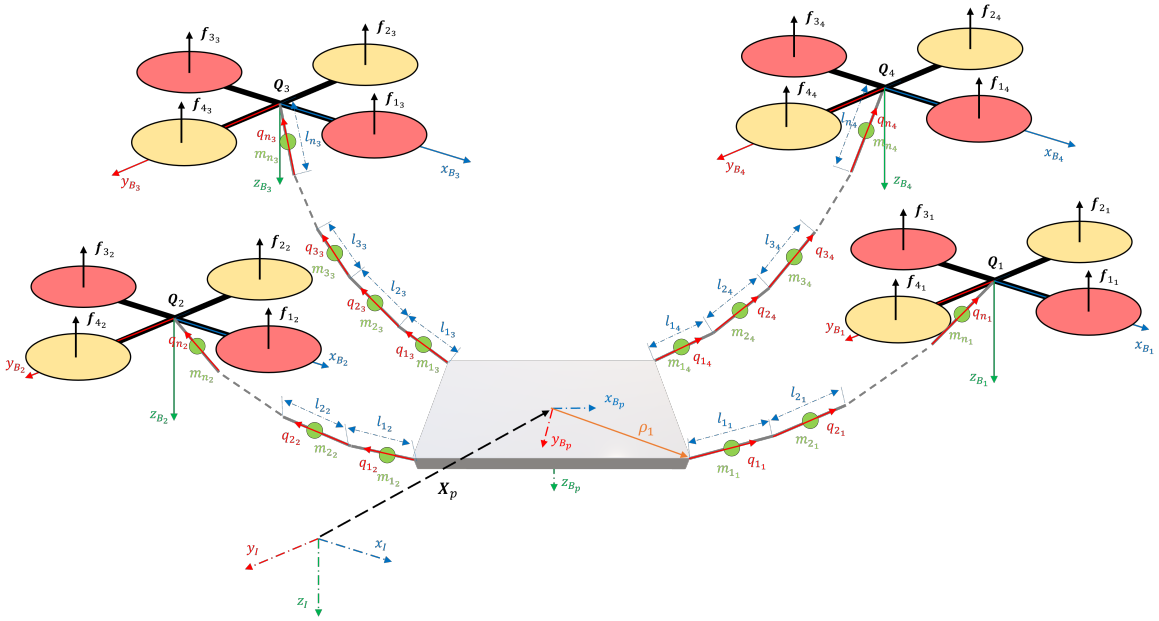

Figure 2.10: Illustration of cooperative multi-rotors with a flexibly suspended payload

Lagrangian of the system is derived as follows,

$$
\begin{aligned}
&L(\boldsymbol{x}_P, \dot{\boldsymbol{x}}_P, \boldsymbol{R}_P, \boldsymbol{\omega}_P, \boldsymbol{R}_{Q_1}, \boldsymbol{\omega}_{Q_1}, \boldsymbol{R}_{Q_2}, \boldsymbol{\omega}_{Q_2}, .., \boldsymbol{R}_{Q_m}, \boldsymbol{\omega}_{Q_m}, \bar{\boldsymbol{q}}_1, \bar{\boldsymbol{q}}_2, .., \bar{\boldsymbol{q}}_m) \\
&= \frac{1}{2}\left(\dot{\boldsymbol{x}}_P^T m_P \dot{\boldsymbol{x}}_P + \boldsymbol{\omega}_P^T \boldsymbol{J}_P \boldsymbol{\omega}_P\right) + \frac{1}{2}\sum_{s=1}^{m}\left(\dot{\boldsymbol{x}}_{Q_s}^T m_{Q_s} \dot{\boldsymbol{x}}_{Q_s} + \boldsymbol{\omega}_{Q_s}^T \boldsymbol{J}_{Q_s} \boldsymbol{\omega}_{Q_s} + \sum_{i=1}^{n} \dot{\boldsymbol{x}}_{i_s}^T m_{i_s} \dot{\boldsymbol{x}}_{i_s}\right) \\
&+ m_P g \boldsymbol{x}_P \cdot \boldsymbol{e}_3 + \sum_{s=1}^{m}\left(m_{Q_s} g \boldsymbol{x}_{Q_s} \cdot \boldsymbol{e}_3 + \sum_{i=1}^{n} m_{i_s} g \boldsymbol{x}_{i_s} \cdot \boldsymbol{e}_3\right) \\
&= \frac{1}{2}\left(\dot{\boldsymbol{x}}_P^T \boldsymbol{M}_{00} \dot{\boldsymbol{x}}_P + {\boldsymbol{\omega}_P}^T \boldsymbol{J}_P \boldsymbol{\omega}_P\right) + \sum_{s=1}^{m}\left[\frac{1}{2}{\boldsymbol{\omega}_{Q_s}}^T \boldsymbol{J}_{Q_s} \boldsymbol{\omega}_{Q_s} + \dot{\boldsymbol{x}}_P^T \sum_{i=1}^{n} \boldsymbol{M}_{0i_s} \dot{\boldsymbol{q}}_{i_s} + \frac{1}{2}\sum_{i,j=1}^{n} {\dot{\boldsymbol{q}}_{i_s}}^T \boldsymbol{M}_{ij_s} \dot{\boldsymbol{q}}_{j_s}\right] \\
&- \sum_{s=1}^{m} \boldsymbol{\rho}_s^T \hat{\boldsymbol{\omega}}_P \boldsymbol{R}_P^T \left[\boldsymbol{M}_{Q_s}\left(\dot{\boldsymbol{x}}_P + \frac{1}{2}\boldsymbol{R}_P \hat{\boldsymbol{\omega}}_P \boldsymbol{\rho}_s\right) + \sum_{i=1}^{n} \boldsymbol{M}_{0i_s} \dot{\boldsymbol{q}}_{i_s}\right] + \boldsymbol{M}_{00} g \boldsymbol{x}_P \cdot \boldsymbol{e}_3 \\
&+ \sum_{s=1}^{m}\left[\boldsymbol{M}_{Q_s} g \boldsymbol{R}_P \boldsymbol{\rho}_s + \sum_{i=1}^{n} \boldsymbol{M}_{0i_s} \boldsymbol{q}_{i_s}\right] \cdot \boldsymbol{e}_3
\end{aligned}
$$

where $\bar{\boldsymbol{q}}_s = [\boldsymbol{q}_{1s}, \dot{\boldsymbol{q}}_{1s}, .., \boldsymbol{q}_{ns}, \dot{\boldsymbol{q}}_{ns}]$ and the mass terms are

$$\boldsymbol{M}_{00} = \left(\sum_{s=1}^{m} (m_{Q_s} + \sum_{i=1}^{n} m_{i_s}) + m_P \right) \boldsymbol{I}_3$$

$$\boldsymbol{M}_{0i_s} = \left(\frac{2(n-i)+1}{2} l m_{i_s} + l m_{Q_s} \right) \boldsymbol{I}_3$$

$$\boldsymbol{M}_{ij_s} = \begin{cases} \left(\frac{4(n-i)+1}{4} l^2 m_{i_s} + l^2 m_{Q_s} \right) \boldsymbol{I}_3, \text{ if } i = j \\ \left(\frac{2(n-a)+1}{2} l^2 m_{i_s} + l^2 m_{Q_s} \right) \boldsymbol{I}_3, \text{ if } i \neq j, \quad (a = \max(i,j)) \end{cases}$$

$$\boldsymbol{M}_{Q_s} = m_{Q_s} + \sum_{i=1}^{n} m_{i_s}$$

The variational principle on Lagrangian is updated to include payload attitude as below,

$$\delta L = \mathbf{D}_{\boldsymbol{x}_P} L \cdot \delta \boldsymbol{x}_P + \mathbf{D}_{\dot{\boldsymbol{x}}_P} L \cdot \delta \dot{\boldsymbol{x}}_P + \mathbf{D}_{\boldsymbol{R}_P} L \cdot \delta \boldsymbol{R}_P + \mathbf{D}_{\boldsymbol{\omega}_P} L \cdot \delta \boldsymbol{\omega}_P$$
$$+ \sum_{s=1}^{m} \left[\mathbf{D}_{\boldsymbol{R}_{Q_s}} L \cdot \delta \boldsymbol{R}_{Q_s} + \mathbf{D}_{\boldsymbol{\omega}_{Q_s}} L \cdot \delta \boldsymbol{\omega}_{Q_s} \right] + \sum_{s=1}^{m} \left[\sum_{i=1}^{n} \left(\mathbf{D}_{\boldsymbol{q}_{i_s}} L \cdot \delta \boldsymbol{q}_{i_s} + \mathbf{D}_{\dot{\boldsymbol{q}}_{i_s}} L \cdot \delta \dot{\boldsymbol{q}}_{i_s} \right) \right]$$

The variation on the work done by the forces and moments on each multi-rotor is

$$\delta W = \sum_{s=1}^{m} \left[\boldsymbol{f}_{I_s} \cdot \left(\delta \boldsymbol{x}_P - \boldsymbol{R}_P \hat{\boldsymbol{\rho}}_s \boldsymbol{\eta}_P + \sum_{i=1}^{n} l \delta \boldsymbol{q}_{i_s} \right) + \boldsymbol{\tau}_s \cdot \boldsymbol{\eta}_{Q_s} \right] \tag{2.30}$$

Using the relations given in (2.14)-(2.15), the variation on the action integral, $\delta \mathfrak{B} = \int_0^T (\delta L + \delta W)\, dt = 0$, is achieved as below,

$$\delta \mathfrak{B} = \int_0^T \Bigg[\left(\mathbf{D}_{\boldsymbol{x}_P} L - \frac{d}{dt} \mathbf{D}_{\dot{\boldsymbol{x}}_P} L + \sum_{s=1}^{m} \boldsymbol{f}_{I_s} \right) \cdot \delta \boldsymbol{x}_P$$
$$+ \left(\boldsymbol{R}_P^T \mathbf{D}_{\boldsymbol{R}_P} L - \frac{d}{dt} \mathbf{D}_{\hat{\boldsymbol{\omega}}_P} L + \left(\mathrm{ad}^*_{\hat{\boldsymbol{\omega}}_P} \cdot \mathbf{D}_{\hat{\boldsymbol{\omega}}_P} L \right) + \sum_{s=1}^{m} \widehat{\hat{\boldsymbol{\rho}}_s \boldsymbol{R}_P^T \boldsymbol{f}_{I_s}} \right) \cdot \hat{\boldsymbol{\eta}}_P$$
$$+ \sum_{s=1}^{m} \left(\boldsymbol{R}_{Q_s}{}^T \mathbf{D}_{\boldsymbol{R}_{Q_s}} L - \frac{d}{dt} \mathbf{D}_{\hat{\boldsymbol{\omega}}_{Q_s}} L + \left(\mathrm{ad}^*_{\hat{\boldsymbol{\omega}}_{Q_s}} \cdot \mathbf{D}_{\hat{\boldsymbol{\omega}}_{Q_s}} L \right) + \hat{\boldsymbol{\tau}}_s \right) \cdot \hat{\boldsymbol{\eta}}_{Q_s}$$
$$+ \sum_{s=1}^{m} \sum_{i=1}^{n} \boldsymbol{q}_{i_s} \times \left(\mathbf{D}_{\boldsymbol{q}_{i_s}} L - \frac{d}{dt} \mathbf{D}_{\dot{\boldsymbol{q}}_{i_s}} L + l \boldsymbol{f}_{I_s} \right) \cdot \boldsymbol{\xi}_{i_s} \Bigg] \, dt$$

where the partial derivatives are as follows,

$$\mathbf{D}_{\boldsymbol{x}_P} L = \boldsymbol{M}_{00} g \boldsymbol{e}_3$$

$$\mathbf{D}_{\dot{\boldsymbol{x}}_P} L = \boldsymbol{M}_{00} \dot{\boldsymbol{x}}_P + \sum_{s=1}^{m} \sum_{i=1}^{n} \boldsymbol{M}_{0i_s} \dot{\boldsymbol{q}}_{i_s} + \sum_{s=1}^{m} \boldsymbol{M}_{Q_s} \boldsymbol{R}_P \hat{\boldsymbol{\omega}}_P \boldsymbol{\rho}_s$$

$$\mathbf{D}_{\boldsymbol{R}_P} L \cdot \delta \boldsymbol{R}_P = \mathbf{d}_{\boldsymbol{R}_P} \cdot \boldsymbol{\eta}_P$$

$$\mathbf{d}_{\boldsymbol{R}_P} = \sum_{s=1}^{m} \widehat{\hat{\boldsymbol{\omega}}_P \boldsymbol{\rho}_s} \boldsymbol{R}_P^T \left[\boldsymbol{M}_{Q_s} \dot{\boldsymbol{x}}_P + \sum_{i=1}^{n} \boldsymbol{M}_{0i_s} \dot{\boldsymbol{q}}_{i_s} \right] + \sum_{s=1}^{m} \boldsymbol{M}_{Q_s} \hat{\boldsymbol{\rho}}_s \boldsymbol{R}_P^T g \boldsymbol{e}_3$$

$$\mathbf{D}_{\boldsymbol{\omega}_P} L = \boldsymbol{J}_P \boldsymbol{\omega}_P + \sum_{s=1}^{m} \hat{\boldsymbol{\rho}}_s \boldsymbol{R}_P^T \left[\boldsymbol{M}_{Q_s} \dot{\boldsymbol{x}}_P + \sum_{i=1}^{n} \boldsymbol{M}_{0i_s} \dot{\boldsymbol{q}}_{i_s} \right] - \sum_{s=1}^{m} \boldsymbol{M}_{Q_s} \hat{\boldsymbol{\rho}}_s^2 \boldsymbol{\omega}_P$$

$$\mathbf{D}_{\boldsymbol{\omega}_{Q_s}} L = \boldsymbol{J}_{Q_s} \boldsymbol{\omega}_{Q_s}$$

$$\mathbf{D}_{\boldsymbol{R}_{Q_s}} L = 0$$

$$\mathbf{D}_{\boldsymbol{q}_{i_s}} L = \boldsymbol{M}_{0i_s} g \boldsymbol{e}_3$$

$$\mathbf{D}_{\dot{\boldsymbol{q}}_{i_s}} L = \boldsymbol{M}_{0i_s} \left(\dot{\boldsymbol{x}}_P + \boldsymbol{R}_P \hat{\boldsymbol{\omega}}_P \boldsymbol{\rho}_s \right) + \sum_{j=1}^{n} \boldsymbol{M}_{ij_s} \dot{\boldsymbol{q}}_{j_s}$$

The equations of motion for this cooperative system are obtained as below,

$$\boldsymbol{M}_{00} \dot{\boldsymbol{v}}_P - \sum_{s=1}^{m} \sum_{i=1}^{n} \boldsymbol{M}_{0i_s} \hat{\boldsymbol{q}}_{i_s} \dot{\boldsymbol{\omega}}_{i_s} - \sum_{s=1}^{m} \boldsymbol{M}_{Q_s} \boldsymbol{R}_P \hat{\boldsymbol{\rho}}_s \dot{\boldsymbol{\omega}}_P \tag{2.31}$$

$$= \sum_{s=1}^{m} \boldsymbol{M}_{Q_s} \boldsymbol{R}_P \hat{\boldsymbol{\omega}}_P \hat{\boldsymbol{\rho}}_s \boldsymbol{\omega}_P + \sum_{s=1}^{m} \sum_{i=1}^{n} \boldsymbol{M}_{0i_s} \left(\boldsymbol{\omega}_{i_s} \cdot \boldsymbol{\omega}_{i_s} \right) \boldsymbol{q}_{i_s} + \boldsymbol{M}_{00} g \boldsymbol{e}_3 - \sum_{s=1}^{m} f_{B_s} \boldsymbol{R}_{Q_s} \boldsymbol{e}_3$$

$$\bar{\boldsymbol{J}}_P \dot{\boldsymbol{\omega}}_P + \sum_{s=1}^{m} \hat{\boldsymbol{\rho}}_s \boldsymbol{R}_P^T \left(\boldsymbol{M}_{Q_s} \dot{\boldsymbol{v}}_P - \sum_{i=1}^{n} \boldsymbol{M}_{0i_s} \hat{\boldsymbol{q}}_{i_s} \dot{\boldsymbol{\omega}}_{i_s} \right) \tag{2.32}$$

$$= \sum_{s=1}^{m} \hat{\boldsymbol{\rho}}_s \boldsymbol{R}_P^T \sum_{i=1}^{n} \boldsymbol{M}_{0i_s} \left(\boldsymbol{\omega}_{i_s} \cdot \boldsymbol{\omega}_{i_s} \right) \boldsymbol{q}_{i_s} - \hat{\boldsymbol{\omega}}_P \bar{\boldsymbol{J}}_P \boldsymbol{\omega}_P + \sum_{s=1}^{m} \hat{\boldsymbol{\rho}}_s \boldsymbol{R}_P^T \left(\boldsymbol{M}_{Q_s} g \boldsymbol{e}_3 - f_{B_s} \boldsymbol{R}_{Q_s} \boldsymbol{e}_3 \right)$$

$$\boldsymbol{J}_{Q_s} \dot{\boldsymbol{\omega}}_{Q_s} + \hat{\boldsymbol{\omega}}_{Q_s} \left(\boldsymbol{J}_{Q_s} \boldsymbol{\omega}_{Q_s} \right) = \boldsymbol{\tau}_s \tag{2.33}$$

$$\boldsymbol{M}_{ii_s} \dot{\boldsymbol{\omega}}_{i_s} - \hat{\boldsymbol{q}}_{i_s} \sum_{j=1 (j \neq i)}^{n} \boldsymbol{M}_{ij_s} \hat{\boldsymbol{q}}_j \dot{\boldsymbol{\omega}}_j + \hat{\boldsymbol{x}}_{i_s} \boldsymbol{M}_{0i_s} \left(\dot{\boldsymbol{v}}_P - \boldsymbol{R}_P \hat{\boldsymbol{\rho}}_s \dot{\boldsymbol{\omega}}_P \right) \tag{2.34}$$

$$= \hat{\boldsymbol{q}}_{i_s} \left(\boldsymbol{M}_{0i_s} g \boldsymbol{e}_3 + \sum_{j=1 (j \neq i)}^{n} \boldsymbol{M}_{ij_s} \left(\boldsymbol{\omega}_j \cdot \boldsymbol{\omega}_j \right) \boldsymbol{q}_{j_s} \right) + \hat{\boldsymbol{q}}_{i_s} \left(-l f_{B_s} \boldsymbol{R}_{Q_s} \boldsymbol{e}_3 + \boldsymbol{M}_{0i_s} \boldsymbol{R}_P \hat{\boldsymbol{\omega}}_P \hat{\boldsymbol{\rho}}_s \boldsymbol{\omega}_P \right)$$

where $\widehat{\hat{\boldsymbol{\omega}}_P \boldsymbol{\rho}_s} = \widehat{\boldsymbol{\omega}_P \times \boldsymbol{\rho}_s} = \hat{\boldsymbol{\omega}}_P \hat{\boldsymbol{\rho}}_s - \hat{\boldsymbol{\rho}}_s \hat{\boldsymbol{\omega}}_P$ is used and the following grouping terms is applied,

$$\bar{\boldsymbol{J}}_P = \boldsymbol{J}_P - \sum_{s=1}^{m} \boldsymbol{M}_{Q_s} \hat{\boldsymbol{\rho}}_s^2$$

Generalized momentum states of the systems are derived by Legendre Transformation as

$$P_{\boldsymbol{v}_P} = \mathbf{D}_{\dot{\boldsymbol{x}}_P} L \tag{2.35}$$

$$P_{\boldsymbol{\omega}_P} = \mathbf{D}_{\boldsymbol{\omega}_p} L$$

$$P_{\boldsymbol{\omega}_{Q_s}} = \mathbf{D}_{\boldsymbol{\omega}_{Q_s}} L$$

$$P_{\boldsymbol{\omega}_{i_s}} = \boldsymbol{q}_{i_s} \times \mathbf{D}_{\dot{\boldsymbol{q}}_{i_s}} L \tag{2.36}$$

These momentum states will be used in discrete Hamiltonian formalism in the next subsection.

2.1.4 Airship

In this section, the mathematical modeling of the airship dynamics is carried out by deriving kinematic and dynamic equations for the translational and rotational motions along with the corresponding body forces, moments, and their mathematical models, respectively.

2.1.4.1 Airship Description

The airship that is considered for this study is a generic design constructed from a double ellipsoid geometry with common semi-minor axes for the hull envelope, as shown in Figure 2.11, similar to that in Ref. [28]. The design employs four tilt-able motors attached on the side supporters of the airship and four aerodynamic fins consisting of fixed and actuated control surface parts where they are installed at

the back of airship with a cross ('x') configuration. There is no internal pressure controlling ballonet considered in the design of this airship due to its length and volume restrictions, which also limits the flight envelope to only low altitude operations.

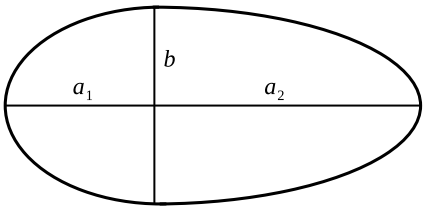

Figure 2.11: Double ellipsoid geometry that is used to construct the airship hull shape

Figure 2.12 displays the front and side views of the airship CAD model where the body fixed coordinate frame is shown as attached at the nose of hull.

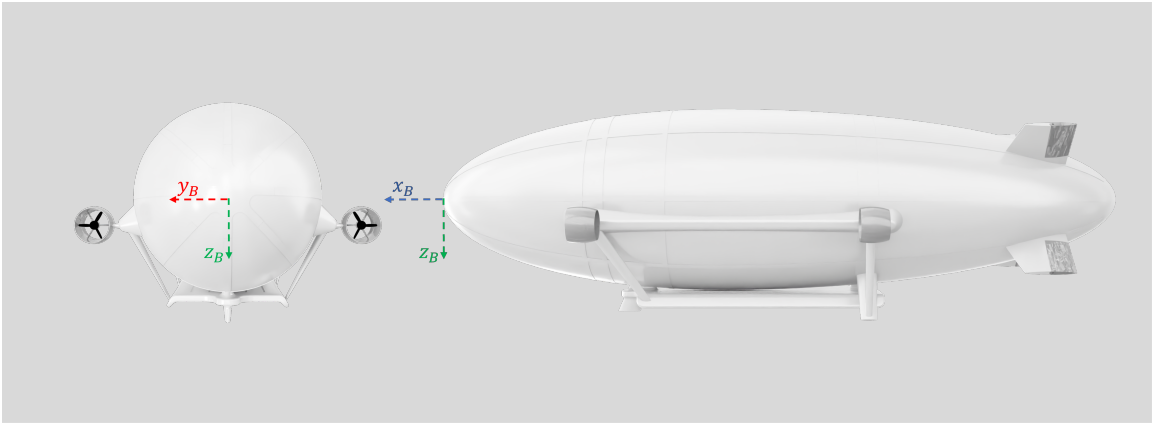

Figure 2.12: Illustration of the origin of airship body frame and the coordinate frame notation

The physical dimensions of the shape are tabulated in Table 2.1. Furthermore, the calculated total mass and the inertia of the airship is given in Table 2.2.

Parameter	Symbol	Value	Units	**Parameter**	Symbol	Value	Units
Hull Length	L	10.414	m	Hull Area ($V_{Hull}^{2/3}$)	S_H	10.7	m^2
Hull a1	a_1	4.318	m	Fin Area (fixed)	S_{F_f}	0.4	m^2
Hull a2	a_2	6.096	m	Fin Area (actuated)	S_{F_c}	0.3	m^2
Hull Radius	b	1.397	m	Gondola Area	S_G	1	m^2
Hull Volume	V_{Hull}	35	m^3				

Table 2.1: Airship dimensions

Parameter	Symbol	Value	Units	**Parameter**	Symbol	Value	Units
Total Mass	m_T	43.125	kg				
Total Inertia Ixx	I_{xx}	50	$kg.m^2$	Total Inertia Ixy	I_{xy}	0	$kg.m^2$
Total Inertia Iyy	I_{yy}	1400	$kg.m^2$	Total Inertia Ixz	I_{xz}	80	$kg.m^2$
Total Inertia Izz	I_{zz}	1350	$kg.m^2$	Total Inertia Iyz	I_{yz}	0	$kg.m^2$

Table 2.2: Airship mass and inertia parameters

2.1.4.2 Equations of Motion

The equations of motion for airship are derived by, first, defining the Inertial and body fixed coordinate frames. For the generality and the ease of modeling purposes, the body fixed frame is defined in North-East-Down (NED) convention and it is positioned at the tip of the hull envelope. Similarly, the Inertial reference frame is defined in NED convention and is attached to a reference position on the ground. Figure 2.13 illustrates both reference frames and the position vector of the airship.

For the rest of the derivations, assumptions that are made to simplify the modeling are listed below.

Assumption 2.1.3. *Total mass and inertia of the airship including the lifting gas stay constant.*

Assumption 2.1.4. *Rotation of Earth and the curvature of the surface of Earth are neglected (acceleration due to gravity is constant - low altitude operation).*

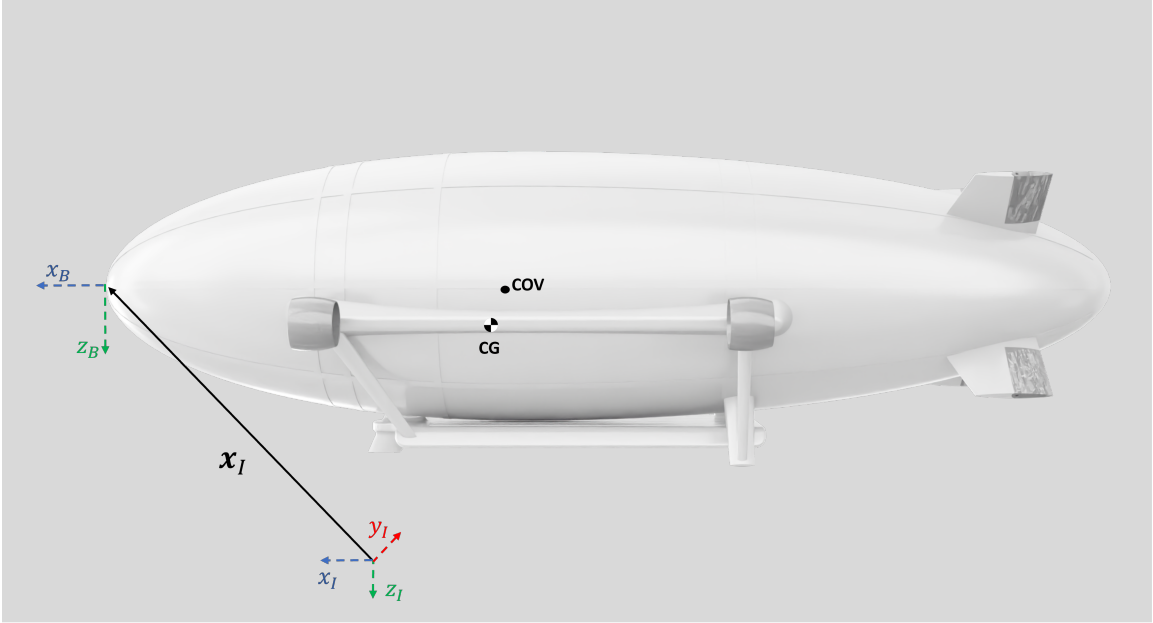

Figure 2.13: Illustration of the Inertial frame, body fixed frame and the airship position vector

2.1.4.2.1 Translational Kinematics The position vector of the body frame origin is defined in the Inertial frame as follows

$$\boldsymbol{x}_I = \begin{bmatrix} x \\ y \\ z \end{bmatrix}$$

Using the rotation matrix, $\boldsymbol{R}_{BI}$, from Inertial frame to the body frame, we obtain the body-fixed coordinate frame of reference as $[\hat{B}] = \boldsymbol{R}_{BI}[\hat{I}]$, where $[\hat{B}]$ and $[\hat{I}] = [\hat{i}\ \hat{j}\ \hat{k}]^T$ represent the orthogonal unit vectors for the body-fixed coordinate frame and the Inertial reference frame, respectively.

Differentiating the position vector with respect to the time, we obtain the relation below

$$\dot{\boldsymbol{x}}_I = \boldsymbol{v}_I = \boldsymbol{R}_{BI}^T \boldsymbol{v}_{B/W} + \boldsymbol{v}_W$$

where $\boldsymbol{v}_I = [\dot{x}\ \dot{y}\ \dot{z}]^T$ is the velocity of the origin of the body frame with respect to the Inertial frame represented in Inertial frame. $\boldsymbol{v}_{B/W} = [u\ v\ w]^T$ is the linear velocity of the body frame with respect to the surrounding air, and it is expressed in the body frame. $\boldsymbol{v}_W = [v_{W_x}\ v_{W_y}\ v_{W_z}]^T$ is the inertial velocity vector of the air (wind), with respect to the Inertial frame and it is expressed in the Inertial frame.

2.1.4.2.2 Rotational Kinematics The rotational kinematic equations are derived by utilizing the property of the rotation matrix, $\boldsymbol{R}_{BI}\boldsymbol{R}_{BI}^T = \boldsymbol{I}$, and the skew-symmetric matrix, $\hat{\boldsymbol{\omega}}^T + \hat{\boldsymbol{\omega}} = \boldsymbol{0}$. Time differentiation of $\boldsymbol{R}_{BI}\boldsymbol{R}_{BI}^T = \boldsymbol{I}$ yields

$$\dot{\boldsymbol{R}}_{BI}\boldsymbol{R}_{BI}^T + \boldsymbol{R}_{BI}\dot{\boldsymbol{R}}_{BI}^T = \boldsymbol{0}$$

where we define a skew-symmetric matrix, $\hat{\boldsymbol{\omega}} = \boldsymbol{R}_{BI}\dot{\boldsymbol{R}}_{BI}^T$, which represents the angular velocity of the body frame with respect to the Inertial frame represented in the body frame as $\boldsymbol{\omega} = [p\ q\ r]^T$.

The rate of change of attitude of the airship (rotational kinematic equations) is represented by

$$\dot{\boldsymbol{R}}_{BI} = -\hat{\boldsymbol{\omega}}\boldsymbol{R}_{BI} \tag{2.37}$$

which yields 9 differential equations to be solved simultaneously.

In this study, we utilize the 3-2-1 Euler angle representation of the attitude for simplicity. Therefore, the rotational kinematic equations are given in terms of roll, pitch and yaw rates as below

$$\begin{bmatrix} \dot{\phi} \\ \dot{\theta} \\ \dot{\psi} \end{bmatrix} = \begin{bmatrix} 1 & \sin(\phi)\tan(\theta) & \cos(\phi)\tan(\theta) \\ 0 & \cos(\phi) & -\sin(\phi) \\ 0 & \sin(\phi)\sec(\theta) & \cos(\phi)\sec(\theta) \end{bmatrix} \begin{bmatrix} p \\ q \\ r \end{bmatrix} \tag{2.38}$$

2.1.4.2.3 Translational Dynamics The dynamic equations for the translational motion are derived using Newton's second law of motion, which states that the net force acting on a body is equal to the rate of change of its linear momentum, $\sum \boldsymbol{f}_I = \frac{\mathbf{d}(m\boldsymbol{v}_I)}{dt}$. Firstly, the position vector of the center of the mass is defined as the sum of the body frame position and the relative position of the airship's cg point below

$$\boldsymbol{x}_{cg} = \boldsymbol{x}_I + \boldsymbol{R}_{BI}^T \boldsymbol{\rho}_{cg} \tag{2.39}$$

Afterwards, the time differentiation of (2.39) gives the velocity of the airship cg position as follows,

$$\dot{\boldsymbol{x}}_{cg} = \boldsymbol{R}_{BI}^T \boldsymbol{v}_{B/W} + \boldsymbol{v}_W + \boldsymbol{R}_{BI}^T \hat{\boldsymbol{\omega}} \boldsymbol{\rho}_{cg} \tag{2.40}$$

Finally, one more differentiation of (2.40) yields the second law of motion below

$$\begin{aligned} \ddot{\boldsymbol{x}}_{cg} &= \boldsymbol{R}_{BI}^T \hat{\boldsymbol{\omega}} \boldsymbol{v}_{B/W} + \boldsymbol{R}_{BI}^T \dot{\boldsymbol{v}}_{B/W} + \dot{\boldsymbol{v}}_W + \boldsymbol{R}_{BI}^T \hat{\boldsymbol{\omega}} (\boldsymbol{\omega} \times \boldsymbol{\rho}_{cg}) + \boldsymbol{R}_{BI}^T (\dot{\boldsymbol{\omega}} \times \boldsymbol{\rho}_{cg}) \\ &= \frac{\sum \boldsymbol{f}_I}{m_T} \end{aligned} \tag{2.41}$$

where $\sum \boldsymbol{f}_I$ is the total net force acting on the airship represented in the Inertial frame. Moreover, m_T is the total mass of the airship including the lifting gas.

Expressing the terms in the body-fixed frame by multiplying the both sides of the above equation by $\boldsymbol{R}_{BI}$, translational dynamic equations are obtained as

$$\dot{\boldsymbol{v}}_{B/W} + \boldsymbol{\omega} \times \boldsymbol{v}_{B/W} + \boldsymbol{R}_{BI} \dot{\boldsymbol{v}}_W + \boldsymbol{\omega} \times \boldsymbol{\omega} \times \boldsymbol{\rho}_{cg} + \dot{\boldsymbol{\omega}} \times \boldsymbol{\rho}_{cg} = \frac{\sum \boldsymbol{f}_B}{m_T}$$

The sum of external forces, which are represented in body frame, is given below

$$\sum \boldsymbol{f}_B = \boldsymbol{f}_{B_{buoy}} + \boldsymbol{f}_{B_w} + \boldsymbol{f}_{B_{aero}} + \boldsymbol{f}_{B_{mot}} + \boldsymbol{f}_{B_{fin}}$$

where $\boldsymbol{f}_{B_{buoy}}$ is the buoyancy force, $\boldsymbol{f}_{B_w}$ is the weight, $\boldsymbol{f}_{B_{aero}}$ are the hull aerodynamic forces, $\boldsymbol{f}_{B_{mot}}$ are the motor forces, and $\boldsymbol{f}_{B_{fin}}$ are the fin forces.

2.1.4.2.4 Rotational Dynamics The rate of change of angular momentum about a point is defined to be equal to the sum of moments acting on that point by Euler's law (the rotational analog of Newton's second law). The net moment acting on the airship center of mass in the Inertial frame is obtained from the following expression

$$\sum \boldsymbol{\tau}_I = \boldsymbol{x}_{cg} \times m_T \ddot{\boldsymbol{x}}_{cg} \tag{2.42}$$

Substituting (2.39) and (2.41) into (2.42), we find the relation between the net moment, net force and the linear acceleration as follows

$$\sum \boldsymbol{\tau}_I = \boldsymbol{x}_I \times \sum \boldsymbol{f}_I + \boldsymbol{R}_{BI}^T \boldsymbol{\rho}_{cg} \times m_T \ddot{\boldsymbol{x}}_{cg} \tag{2.43}$$

Knowing that the net moment acting on the center of mass has the following relation with the moment acting on the origin of the body frame due to the forces,

$$\sum \boldsymbol{\tau}_I = \sum \boldsymbol{\tau}_B + \boldsymbol{x}_I \times \sum \boldsymbol{f}_I$$

where $\sum \boldsymbol{\tau}_B$ is the sum of the moments acting on the origin of the body frame, the vector equation for the angular acceleration is found as follows,

$$\sum \boldsymbol{\tau}_B = \boldsymbol{\rho}_{cg} \times m_T \boldsymbol{R}_{BI}^T \ddot{\boldsymbol{x}}_{cg} \tag{2.44}$$

Substituting (2.41) into (2.44) and representing the vectors in the body frame, the net moment equation becomes

$$\begin{aligned} \sum \boldsymbol{\tau}_B = {} & \boldsymbol{\rho}_{cg} \times m_T (\dot{\boldsymbol{v}}_{B/W} + \boldsymbol{\omega} \times \boldsymbol{v}_{B/W} + \boldsymbol{R}_{BI} \dot{\boldsymbol{v}}_W) + \boldsymbol{\rho}_{cg} \times m_T (\boldsymbol{\omega} \times \boldsymbol{\omega} \times \boldsymbol{\rho}_{cg}) \\ & + \boldsymbol{\rho}_{cg} \times m_T (\dot{\boldsymbol{\omega}} \times \boldsymbol{\rho}_{cg}) \end{aligned} \tag{2.45}$$

Using $\mathbf{a} \times \mathbf{b} \times \mathbf{c} = (\mathbf{a} \cdot \mathbf{c})\mathbf{b} - (\mathbf{a} \cdot \mathbf{b})\mathbf{c}$ and $\mathbf{a}^T\mathbf{b}\mathbf{c} = \mathbf{c}\mathbf{a}^T\mathbf{b}$ for $\mathbf{a}, \mathbf{b}, \mathbf{c} \in \mathbb{R}^3$, the third term in (2.45) can be expanded as follows,

$$\begin{aligned}
\boldsymbol{\rho}_{cg} \times m_T \left(\dot{\boldsymbol{\omega}} \times \boldsymbol{\rho}_{cg}\right) &= m_T \left(\left(\boldsymbol{\rho}_{cg} \cdot \boldsymbol{\rho}_{cg}\right) \dot{\boldsymbol{\omega}} - \left(\boldsymbol{\rho}_{cg} \cdot \dot{\boldsymbol{\omega}}\right) \boldsymbol{\rho}_{cg}\right) \\
&= m_T \left(\boldsymbol{\rho}_{cg}^T \boldsymbol{\rho}_{cg} \dot{\boldsymbol{\omega}} - \boldsymbol{\rho}_{cg}^T \dot{\boldsymbol{\omega}} \boldsymbol{\rho}_{cg}\right) \\
&= m_T \left(\boldsymbol{\rho}_{cg}^T \boldsymbol{\rho}_{cg} \boldsymbol{I} - \boldsymbol{\rho}_{cg} \boldsymbol{\rho}_{cg}^T\right) \dot{\boldsymbol{\omega}} \\
&= \boldsymbol{J} \dot{\boldsymbol{\omega}}
\end{aligned}$$

where $\boldsymbol{J} = m_T \left(\boldsymbol{\rho}_{cg}^T \boldsymbol{\rho}_{cg} \boldsymbol{I} - \boldsymbol{\rho}_{cg} \boldsymbol{\rho}_{cg}^T\right)$, $\boldsymbol{J} \in \mathbb{R}^{3\times3}$ is defined to be the moment of inertia in the body frame.

Similarly, using $(\mathbf{a}^T\mathbf{b})\hat{\mathbf{a}} = -\hat{\mathbf{b}}(\mathbf{a}\mathbf{a}^T)$, the expansion of the second term in (2.45) is obtained by the following expression,

$$\begin{aligned}
\boldsymbol{\rho}_{cg} \times m_T(\boldsymbol{\omega} \times \boldsymbol{\omega} \times \boldsymbol{\rho}_{cg}) &= \boldsymbol{\rho}_{cg} \times m_T \left(\left(\boldsymbol{\omega} \cdot \boldsymbol{\rho}_{cg}\right) \boldsymbol{\omega} - \left(\boldsymbol{\omega} \cdot \boldsymbol{\omega}\right) \boldsymbol{\rho}_{cg}\right) \\
&= m_T \left(\boldsymbol{\rho}_{cg}^T \boldsymbol{\omega}\right) \hat{\boldsymbol{\rho}}_{cg} \boldsymbol{\omega} \\
&= -m_T \hat{\boldsymbol{\omega}} \left(\boldsymbol{\rho}_{cg} \boldsymbol{\rho}_{cg}^T\right) \boldsymbol{\omega} \\
&= m_T \boldsymbol{\omega} \times \left(\boldsymbol{\rho}_{cg}^T \boldsymbol{\rho}_{cg} \boldsymbol{I} - \boldsymbol{\rho}_{cg}^T \boldsymbol{\rho}_{cg} \boldsymbol{I} - \boldsymbol{\rho}_{cg} \boldsymbol{\rho}_{cg}^T\right) \boldsymbol{\omega} \\
&= \boldsymbol{\omega} \times (\boldsymbol{J}\boldsymbol{\omega}) \qquad (2.46)
\end{aligned}$$

Finally, the rotational dynamics equation is acquired as below,

$$\sum \boldsymbol{\tau}_B = \boldsymbol{J}\dot{\boldsymbol{\omega}} + \boldsymbol{\omega} \times (\boldsymbol{J}\boldsymbol{\omega}) + \boldsymbol{\rho}_{cg} \times m_T \left(\dot{\boldsymbol{v}}_{B/W} + \boldsymbol{\omega} \times \boldsymbol{v}_{B/W} + \boldsymbol{R}_{BI} \dot{\boldsymbol{v}}_W\right)$$

The sum of external moments acting on the origin of the body frame are represented in the body frame is given as

$$\sum \boldsymbol{\tau}_B = \boldsymbol{\tau}_{B_{buoy}} + \boldsymbol{\tau}_{B_w} + \boldsymbol{\tau}_{B_{aero}} + \boldsymbol{\tau}_{B_{mot}} + \boldsymbol{\tau}_{B_{fin}}$$

2.1.4.3 Modeling of Body Forces and Moments

2.1.4.3.1 Weight and Buoyancy Figure 2.14 illustrates the buoyancy and weight forces on the airship with their relative position vectors with respect to the airship's body frame. The buoyancy force due to the lifting gas, $\boldsymbol{f}_{buoy}$, is acting along the opposite direction of the gravitational acceleration, which is represented by the unit vector, $\boldsymbol{e}_3 = [0\ 0\ 1]^T$, in the negative z-axis of the Inertial frame. Similarly, the weight vector along the same direction with the gravitational acceleration is represented with $\boldsymbol{f}_w$.

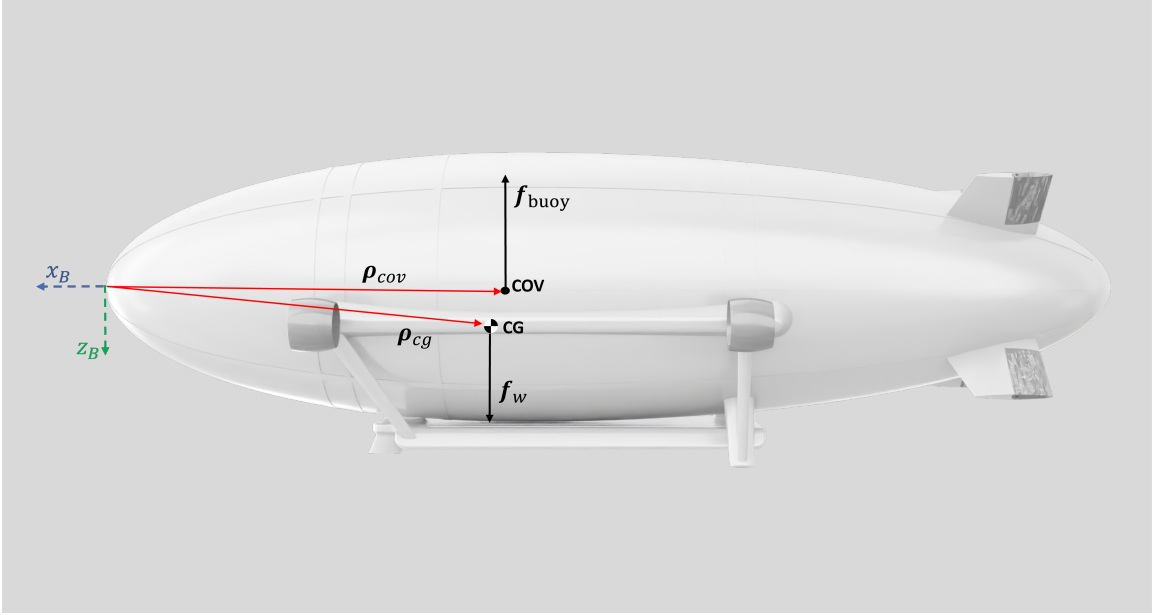

Figure 2.14: Illustration of buoyancy and weight force vectors with respect to the origin of the body frame

Assumption 2.1.5. *The center of gravity, CG, and the center of volume, COV, are assumed to be constant and located at* $\boldsymbol{\rho}_{cg}$ *and* $\boldsymbol{\rho}_{cov}$ *with respect to the origin of the body frame, respectively.*

Assumption 2.1.6. *The buoyancy force, $\boldsymbol{f}_{buoy}$, is assumed to be acting at the center of volume location.*

Buoyancy force and the resultant moment around the origin of the body frame, represented in the body frame, are given below,

$$\boldsymbol{f}_{buoy} = \boldsymbol{R}_{BI}^{T} \boldsymbol{f}_{B_{buoy}} = -f_{buoy} \boldsymbol{e}_3 \tag{2.47}$$

$$\boldsymbol{\tau}_{buoy} = \boldsymbol{R}_{BI}^{T} \boldsymbol{\tau}_{B_{buoy}} = \boldsymbol{R}_{BI}^{T} \left(\boldsymbol{\rho}_{cov} \times \boldsymbol{f}_{B_{buoy}} \right) \tag{2.48}$$

where $f_{buoy} \in \mathbb{R}$ is the magnitude of the buoyancy force, which is computed by $f_{buoy} = (\rho_{air} V_{Hull}) g$, corresponding to the mass of the air that has been displaced by the volume of the airship.

Similarly, the weight vector and the resultant moment around the origin of the body frame, represented in the body frame, are expressed below,

$$\boldsymbol{f}_{w} = \boldsymbol{R}_{BI}^{T} \boldsymbol{f}_{B_w} = m_T g \boldsymbol{e}_3 \tag{2.49}$$

$$\boldsymbol{\tau}_{w} = \boldsymbol{R}_{BI}^{T} \boldsymbol{\tau}_{B_w} = \boldsymbol{R}_{BI}^{T} \left(\boldsymbol{\rho}_{cg} \times \boldsymbol{f}_{B_w} \right) \tag{2.50}$$

2.1.4.3.2 Hull Aerodynamics The construction of high fidelity aerodynamic models demands a considerable amount of modeling and experimental validation efforts, and needs to be tailored specifically for a desired airship, which is not covered in this research. Instead, the previous modeling efforts are adopted to obtain the aerodynamic model of our airship. The aerodynamic modeling of the airship is based on the developments in Refs. [28] and [25], as well as Refs. [24] and [23]. However, instead of combining the aerodynamic effects of the hull and the fins in the same formulation, our approach further separates them as individual modules with the assumption that their interactions can be captured by the use of efficiency factors.

Assumption 2.1.7. *The aerodynamic effect of the fins on the back of the airship hull can be captured by the product of the efficiency factors for the hull, μ_H, and individ-*

ual fins, μ_F. Therefore, the superposition of these individual aerodynamic models is assumed to be sufficient for the hull-fin interaction modeling.

Figure 2.15 illustrates the hull aerodynamic force and moment, and the relative position of the aerodynamic center where the aerodynamic force and moment generated by the airship hull is assumed to be acting at.

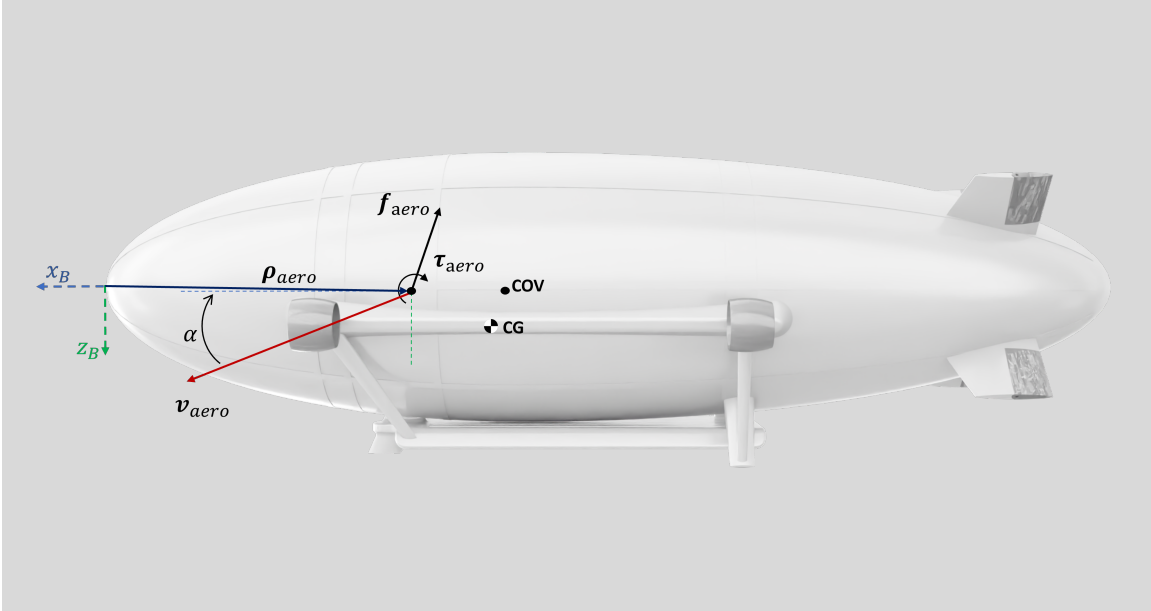

Figure 2.15: Illustration of the hull aerodynamic center on the airship and the acting aerodynamic force and moment

Assumption 2.1.8. *The aerodynamic center is assumed to be a fixed location on the airship hull. The forces and moments generated by the aerodynamic shape of the hull are assumed to be acting at this point.*

The hull aerodynamic force and moment equations are provided below in (2.51) and (2.52), represented in the body frame.

$$\boldsymbol{f}_{aero} = \boldsymbol{R}_{BI}^{T}\boldsymbol{f}_{B_{aero}} = \boldsymbol{R}_{BI}^{T} q_{0_{aero}} \begin{bmatrix} C_{X_1}\cos^2(\alpha)\cos^2(\beta) + C_{X_2}\sin(2\alpha)\sin(\frac{\alpha}{2}) \\ C_{Y_1}\cos(\frac{\beta}{2})\sin(2\beta) + C_{Y_2}\sin(\beta)\sin(|\beta|) \\ C_{Z_1}\cos(\frac{\alpha}{2})\sin(2\alpha) + C_{Z_2}\sin(\alpha)\sin(|\alpha|) \end{bmatrix} \tag{2.51}$$

$$\boldsymbol{\tau}_{aero} = \boldsymbol{R}_{BI}^{T} q_{0_{aero}} \begin{bmatrix} C_{L_1}\sin(\beta)\sin(|\beta|) \\ C_{M_1}\cos(\frac{\alpha}{2})\sin(2\alpha) + C_{M_2}\sin(\alpha)\sin(|\alpha|) \\ C_{N_1}\cos(\frac{\beta}{2})\sin(2\beta) + C_{N_2}\sin(\beta)\sin(|\beta|) \end{bmatrix}$$

$$\boldsymbol{\tau}_{B_{aero}} = \boldsymbol{R}_{BI}\boldsymbol{\tau}_{aero} + \boldsymbol{\rho}_{aero} \times \boldsymbol{f}_{B_{aero}} \tag{2.52}$$

where α and β are the angle of attack and the angle of side-slip measured at the aerodynamic center, respectively. In addition, C_X, C_Y, and C_Z are aerodynamic coefficients for the force calculation along the body axes, whereas C_L, C_M, and C_N are the aerodynamic coefficients used for aerodynamic moment calculations for the hull. Furthermore, the local velocity required for the calculation of the dynamic pressure measured at the aerodynamic center, $q_{0_{aero}} = \frac{1}{2}\rho_{air}\|\boldsymbol{v}_{aero}\|^2$, is found by the following expression,

$$\boldsymbol{v}_{aero} = \boldsymbol{v}_{B/W} + \boldsymbol{\omega} \times \boldsymbol{\rho}_{aero} = \begin{bmatrix} u_{aero} \\ v_{aero} \\ w_{aero} \end{bmatrix} \tag{2.53}$$

Angle of attack and angle of side-slip measured from the aerodynamic center of the hull can be expressed below, respectively.

$$\alpha = \tan^{-1}\left(\frac{w_{aero}}{u_{aero}}\right), \qquad \beta = \sin^{-1}\left(\frac{v_{aero}}{\|\boldsymbol{v}_{aero}\|}\right) \tag{2.54}$$

The components including $\sin(2\alpha)$ or $\sin(2\beta)$ in (2.51) and (2.52) represent the upsetting forces and moments due to an inclined ellipsoid moving through a fluid, as previously formulated by Munk, Ref. [24]. The other terms represent the normal and cross flow aerodynamic drag and resultant moments along the body axes. It is worth noting that cross flow terms play an important role as the restoring moments on the airship stability due to the shape of the airship and the location of the aerodynamic center.

The aerodynamic coefficients, which are derived in Ref. [28] as direct functions of airship geometry, are provided below,

Table 2.3: Aerodynamic Coefficient Formulations

Aerodynamic Force Coefficients	**Aerodynamic Moment Coefficients**
$C_{X_1} = -(C_{D_{H_0}} S_H + C_{D_{G_0}} S_G)$	$C_{L_1} = C_{D_{c_G}} S_G l_{G_z}$
$C_{X_2} = (k_1 - k_2)\mu_H I_1 S_H$	$C_{M_1} = (k_1 - k_2)\mu_H I_3 S_H L$
$C_{Y_1} = (k_1 - k_2)\mu_H I_1 S_H$	$C_{M_2} = -C_{D_{c_H}} J_2 S_H L$
$C_{Y_2} = -C_{D_{c_H}} J_1 S_H$	$C_{N_1} = (k_2 - k_1)\mu_H I_3 S_H L$
$C_{Z_1} = (k_1 - k_2)\mu_H I_1 S_H$	$C_{N_2} = C_{D_{c_H}} J_2 S_H L$
$C_{Z_2} = -C_{D_{c_H}} J_1 S_H$	

The coefficient definitions, parameters, and their values are tabulated in Table 2.4.

Table 2.4: Parameter Definitions and Values

Parameters	**Definition**	**Value**
$C_{D_{H_0}}$	Hull zero-angle drag coefficient, referenced to S_H	0.025
$C_{D_{G_0}}$	Gondola zero-angle drag coefficient, referenced to S_G	0.01
$C_{D_{c_H}}$	Hull cross flow drag coefficient, referenced to J_1	0.5
$C_{D_{c_G}}$	Gondola cross flow drag coefficient, referenced to S_G	1.0
l_h	Horizontal length from nose to trailing edge of the fins	8.89 m
l_{G_z}	Vertical distance of gondola from the aerodynamic center	1.0 m
μ_H	Hull efficiency factor	1.1
I_1	Non-dimensional cross-sectional reference area, $I_1 = \frac{1}{S_H}\int_{-a_1}^{l_h-a_1} \frac{dA}{dx} dx$	0.2518
I_3	Non-dimensional reference length along x, $I_3 = \frac{1}{S_H l_h}\int_{-a_1}^{l_h-a_1} x\frac{dA}{dx} dx$	-0.2973
J_1	Non-dimensional circular reference area, $J_1 = \frac{1}{S_H}\int_{-a_1}^{l_h-a_1} 2r(x)dx$	2.0915
J_2	Non-dimensional circular reference length, $J_2 = \frac{1}{S_H l_h}\int_{-a_1}^{l_h-a_1} 2r(x)xdx$	0.0762
k_1	axial added-mass coefficient	0.0904
k_2	transversal added-mass coefficient	0.8469
k_3	transversal added-mass coefficient (moment)	0.5743

The non-dimensional reference areas and the lengths, I_1, I_3, J_1 and J_2, are derived using the double ellipsoid geometry, as shown in Fig. 2.11, using the following expressions,

$$
\begin{aligned}
I_1 &= \pi \frac{b^2}{S_H}\left(1 - f^2\right) \\
I_3 &= -\frac{2\pi b^2}{3 S_H l_h}\left(a_1 + a_2 f^3\right) \\
J_1 &= \frac{b}{S_H}\left(\frac{\pi a_1}{2} + a_2 \sin^{-1}(f) + a_2\sqrt{1-f^2}\right) \\
J_2 &= \frac{2b}{3 S_H l_h}\left(a_2^2 - a_1^2 - a_2^2(1-f^2)^{3/2}\right)
\end{aligned}
$$

where $f = \frac{l_h - a_1}{a_2}$.

The calculation of the added-mass coefficients is detailed in Lamb's work in Ref. [23] as,

$$
\begin{aligned}
k_1 &= \frac{\Gamma}{2-\Gamma} \\
k_2 &= \frac{\Upsilon}{2-\Upsilon} \\
k_3 &= \frac{e^4(\Upsilon-\Gamma)}{(2-e^2)\big(2e^2-(2-e^2)(\Upsilon-\Gamma)\big)}
\end{aligned}
$$

where

$$
\begin{aligned}
e &= \sqrt{1-\frac{b^2}{(\frac{a_1+a_2}{2})^2}} \\
\Gamma &= \frac{2(1-e^2)}{e^3}\left(\frac{1}{2}\log\left(\frac{1+e}{1-e}\right)-e\right) \\
\Upsilon &= \frac{1}{e^2}-\frac{1-e^2}{2e^3}\log\left(\frac{1+e}{1-e}\right)
\end{aligned}
$$

2.1.4.3.3 Motors The motors of the airship in this study are attached to the end of their corresponding tilt servos, which brings the capability of changing the direction of the thrust they generate with respect to the body frame. Figure 2.16 illustrates the motor frame, body frame, the relative tilt angle of the motor, θ_{M_i}, and the force generated by the motor, f_{M_i}.

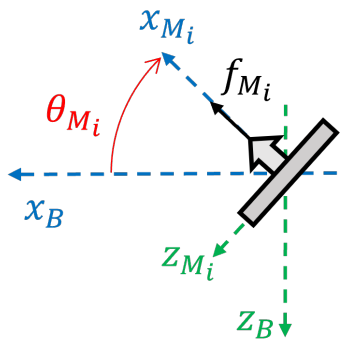

Figure 2.16: Illustration of motor frame with respect to the airship body frame

Assumption 2.1.9. *The motors are assumed to be generating forces only along their positive x-axis. Any moment about the motor axes due to the rotation of propellers is omitted for simplicity. In addition, any aerodynamic force and moment due to the shape of the motor pods are neglected.*

Assumption 2.1.10. *The force generated by a motor is assumed to have a linear relation with the square of the angular speed of the propellers as,* $f_{M_i} = k_F(\omega_{M_i})^2$.

Force and moment generated by the i^{th} motor represented in the body frame are given below,

$$\boldsymbol{f}_{mot} = \boldsymbol{R}_{BI}^T \boldsymbol{f}_{B_{mot}} = \boldsymbol{R}_{BI}^T \sum_{i=1}^{4} \boldsymbol{R}_{BM}(\theta_{M_i}) f_{M_i} \boldsymbol{e}_1$$

$$\boldsymbol{\tau}_{mot} = \boldsymbol{R}_{BI}^T \boldsymbol{\tau}_{B_{mot}} = \boldsymbol{R}_{BI}^T \sum_{i=1}^{4} \boldsymbol{\rho}_{M_i} \times \boldsymbol{R}_{BM}(\theta_{M_i}) f_{M_i} \boldsymbol{e}_1$$

where $[\hat{M}] = \boldsymbol{R}_{BM}^T[\hat{B}]$ are the orthogonal unit vectors representing the attitude of the motor frame with respect to the Inertial frame with $\boldsymbol{R}_{BM}$ as the rotation matrix from the motor frame to the body frame. Also, $\boldsymbol{\rho}_{M_i}$ is the relative position of the motor with respect to the origin of the body frame, represented in the body frame. The rotation matrix $\boldsymbol{R}_{BM}(\theta_{M_i})$ is defined as follows,

$$\boldsymbol{R}_{BM}(\theta_{M_i}) = \begin{bmatrix} \cos(\theta_{M_i}) & 0 & \sin(\theta_{M_i}) \\ 0 & 1 & 0 \\ -\sin(\theta_{M_i}) & 0 & \cos(\theta_{M_i}) \end{bmatrix}$$

2.1.4.3.4 Fins and Control Surfaces The airship in this study has four fins in a cross configuration to stabilize and control the attitude of the vehicle by generating necessary aerodynamic force and moment. Each fin consists of a fixed part, where it meets with the hull, and the controllable part, where it is attached to the fixed part with a revolute joint and used as a control surface by applying a deflection. Both parts are assigned to their individual reference frames. Figure 2.17 illustrates the

orientations of fins with respect to the body frame, where the subscripts of TL, TR, BL, and BR corresponds to the locations of fins as top-left, top-right, bottom-left, and bottom-right, respectively.

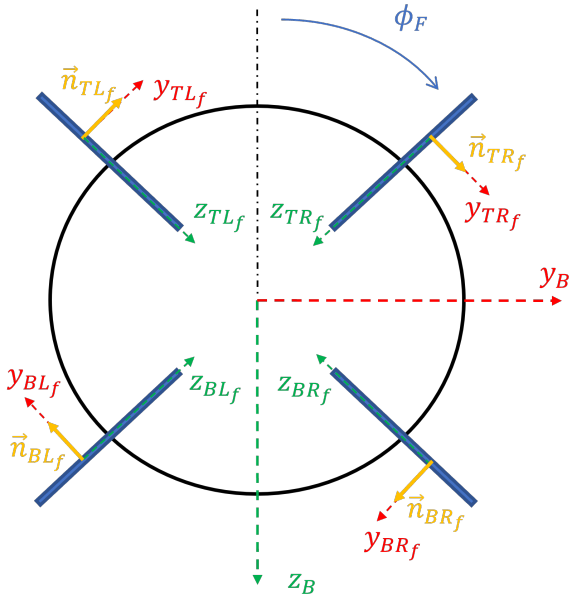

Figure 2.17: Illustration of the fin reference frames from the back view

Figure 2.18 shows the top view of a single fin with an attached control surface for both neutral and deflected configuration including mean chord lengths, respectively. Figure also displays the corresponding reference frames, where they also follow the right-hand-rule and NED convention.

In Figure 2.18, it can be seen that the effective chord length and orientation are changed by the deflection of control surface. The effective chord length can be calculated by applying triangle cosine rule as below,

$$\begin{aligned} c_{F_{i_{eff}}} &= \sqrt{c_{F_f}^2 + c_{F_c}^2 - 2c_{F_f}c_{F_c}\cos(\pi - \psi_{F_{i_c}})} \\ &= \sqrt{c_{F_f}^2 + c_{F_c}^2 + 2c_{F_f}c_{F_c}\cos(\psi_{F_{i_c}})} \end{aligned}$$

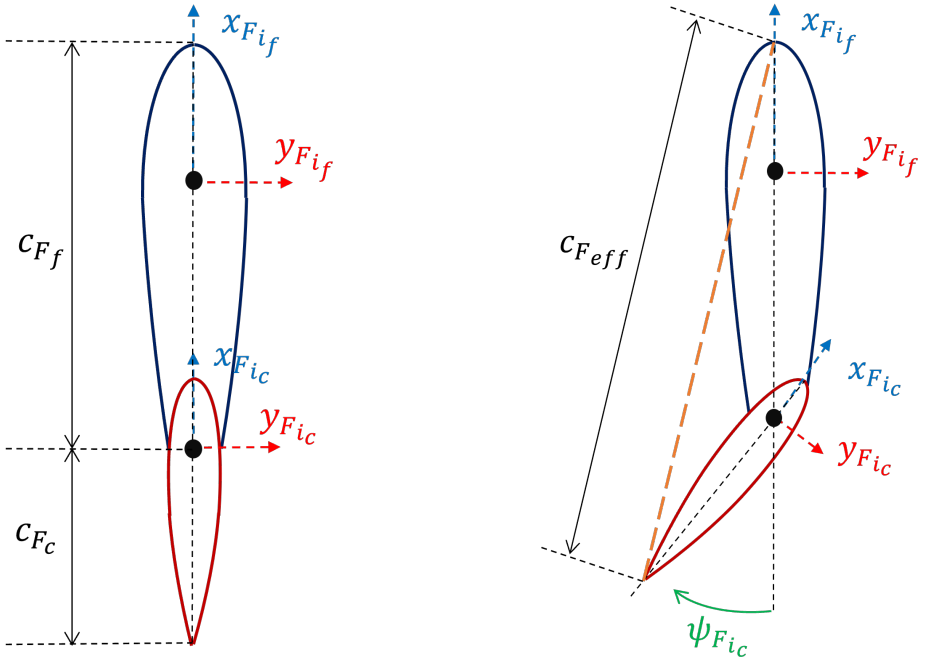

(a) Neutral Configuration (b) Deflected Configuration

Figure 2.18: Illustration of the fin and control surface from top view including mean chord length

Similarly, from the triangle geometry, the effective rotation of mean chord line from the fin frame, $\psi_{F_{eff}}$, can be found by

$$\psi_{F_{i_{eff}}} = \tan^{-1}\left(\frac{c_{F_c}\sin(\psi_{F_{i_c}})}{c_{F_f} + c_{F_c}\cos(\psi_{F_{i_c}})}\right)$$

In order to obtain relative velocity of the aerodynamic center of effective chord, where a quarter chord length from the leading edge is assumed to be the aerodynamic center, the following computation is required.

$$\boldsymbol{v}_{F_{i_{ac}}} = \boldsymbol{v}_{B/W} + \boldsymbol{\omega} \times \boldsymbol{\rho}_{F_{i_{ac}}} = \boldsymbol{R}_{BF} \begin{bmatrix} u_{F_{i_{ac}}} \\ v_{F_{i_{ac}}} \\ w_{F_{i_{ac}}} \end{bmatrix}$$

where a relative position of effective chord's aerodynamic center, $\boldsymbol{\rho}_{F_{i_{ac}}}$, is found by

$$\boldsymbol{\rho}_{F_{i_{ac}}} = \left(\boldsymbol{\rho}_{l_h} + \boldsymbol{R}_{BF}(\psi_{F_{i_{eff}}}) \left(-0.25 c_{F_{i_{eff}}} \boldsymbol{e}_1 - r_{fin_i} \boldsymbol{e}_3\right)\right)$$

and

$$\begin{aligned}
\boldsymbol{R}_{BF}(\psi_{F_{i_{eff}}}) &= \boldsymbol{R}_z(\psi_{F_{i_{eff}}}) \boldsymbol{R}_x(\phi_{F_i}) \\
&= \begin{bmatrix} \cos(\psi_{F_{i_{eff}}}) & -\sin(\psi_{F_{i_{eff}}})\cos(\phi_{F_i}) & \sin(\psi_{F_{i_{eff}}})\sin(\phi_{F_i}) \\ \sin(\psi_{F_{i_{eff}}}) & \cos(\psi_{F_{i_{eff}}})\cos(\phi_{F_i}) & -\cos(\psi_{F_{i_{eff}}})\sin(\phi_{F_i}) \\ 0 & \sin(\phi_{F_i}) & \cos(\phi_{F_i}) \end{bmatrix}
\end{aligned}$$

where $[\widehat{F_{i_{eff}}}]^T = \boldsymbol{R}_{BF}(\psi_{F_{i_{eff}}})^T [\hat{B}]$ are the orthogonal unit vectors representing the reference frame of the computed effective chord with respect to the Inertial frame. In addition, ϕ_{F_i} represents the roll orientation of the fins with respect to body frame and they are constant with values of 45, 135, 225 and 315 degrees for top-right, bottom-right, bottom-left and top-left fins from the back view, respectively. $\boldsymbol{\rho}_{l_h}$ denotes the relative position of the fin leading edge with respect to the CG. Finally, r_{fin_i} is the radial distance from root to fin aerodynamic center.

The aerodynamic force and moment generated by the i^{th} fin is calculated by the following equations, respectively.

$$\boldsymbol{f}_{B_{fin_i}} = \boldsymbol{R}_{BF}(\psi_{F_{i_{eff}}}) q_{0_{F_i}} \left(C_{L_{F_i}}\left(\alpha_{F_{i_f}}\right) S_{F_{i_{eff}}} \boldsymbol{u}_{L_{F_i}} + C_{D_{F_i}}\left(\alpha_{F_{i_f}}\right) S_{F_{i_{eff}}} \boldsymbol{u}_{D_{F_i}}\right) \quad (2.55)$$

$$\boldsymbol{\tau}_{B_{fin_i}} = \boldsymbol{R}_{BF}(\psi_{F_{i_{eff}}}) q_{0_{F_i}} C_{M_{F_i}}\left(\alpha_{F_{i_f}}\right) S_{F_{i_{eff}}} c_{F_{i_{eff}}} \boldsymbol{e}_3 + \boldsymbol{\rho}_{F_{i_{ac}}} \times \boldsymbol{f}_{B_{fin_i}} \quad (2.56)$$

where the variables regarding fin aerodynamics are given in Table 2.5 below.

Assumption 2.1.11. *The span-wise component of the fin's local velocity is neglected in the calculation of the lift and drag. Also, the side force due to the side-slip of fin is neglected.*

Table 2.5: Fin Variable Definitions and Expressions

Variable	Definition	Expression
$q_{0_{F_i}}$	Dynamic pressure at effective chord a.c.	$q_{0_{F_i}} = \frac{1}{2}\rho_{air}\|\boldsymbol{v}_{F_{iac}}\|^2$
α_{F_i}	Angle of attack for effective chord	$\alpha_{F_i} = \tan^{-1}\left(\frac{v_{i_f}}{u_{i_f}}\right)$
$\boldsymbol{u}_{D_{F_i}}$	Unit vector along drag force in effective chord frame	$\boldsymbol{u}_{D_{F_i}} = \frac{\left[-u_{F_{iac}}, -v_{F_{iac}}, 0\right]^T}{\sqrt{u^2_{F_{iac}} + v^2_{F_{iac}}}}$
$\boldsymbol{u}_{L_{F_i}}$	Unit vector along lift force in effective chord frame	$\boldsymbol{u}_{L_{F_i}} = \frac{\left[v_{F_{iac}}, -u_{F_{iac}}, 0\right]^T}{\sqrt{u^2_{F_{iac}} + v^2_{F_{iac}}}}$
$S_{F_{i_{eff}}}$	Effective reference area for the fin	$S_{F_{i_{eff}}} = c_{F_{i_{eff}}} \cdot (\text{fin span})$

Finally, the aerodynamic lift, drag and moment coefficients are modeled. The lift coefficient is approximated as a function of angle of attack using a fifth order polynomial as follows,

$$C_{L_{F_i}} = \sum_{k=0}^{5} c_k \alpha_{F_i}^k \tag{2.57}$$

where $c_k,\ k = 0, 1, .., 5$ coefficients are found by a polynomial fit function for the data generated by the red line in Figure 2.19, where $C_{L_{max}} = 1.2$ is chosen and the dashed line illustrates the polynomial fit line.

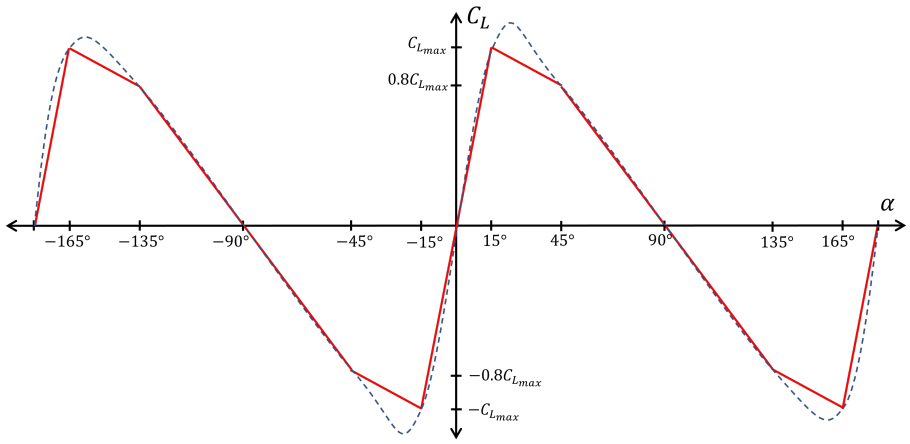

Figure 2.19: Lift vs angle of attack curve used to generate aerodynamic lift forces for the fins and control surfaces.

For the drag coefficient, the following model is used,

$$C_{D_{F_i}} = \begin{cases} C_{D_0} + kC_{L_{F_i}}^2, & \text{if } |\alpha_{F_i}| \leq 15\,\text{deg} \\ C_{D_0} + ... + C_{D_{\alpha_{F_i}}}\alpha_{F_i}, & \text{otherwise} \end{cases} \tag{2.58}$$

where the values of $C_{D_0} = 0.006$ and $k = 0.01$ are chosen for the simulations. Figure 2.20 illustrates the drag model.

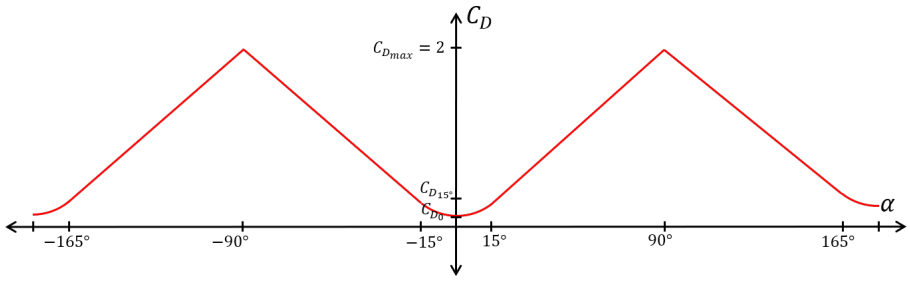

Figure 2.20: Drag vs angle of attack curve used to generate aerodynamic drag forces for the fins and control surfaces.

The aerodynamic moment modeling requires various other factors to be known for the full coverage of the flight envelope, which is out of scope for this study. However, for completeness, a simple linear model is chosen as follows,

$$C_{M_{F_i}} = C_{M_0} + C_{M_\alpha}\alpha_{F_i} + C_{M_q}q_{F_i}$$

2.2 Momentum/Structure Preserving Simulation of Suspended Payload Systems

The work and design decisions on the suspended payload systems in the literature are based on simulations or limited experimental verification under the assumption that the actual behavior of the real system is captured reasonably well by the developed dynamical models. Leaving aside the accuracy of models capturing the underlying physical phenomena, it is known that the majority of numerical integration methods, including the Runge-Kutta based ODE solvers, do not preserve

the symmetries (invariants) and the geometrical properties of the system, where even slight deviations might substantially affect the overall simulation accuracy, especially for the systems under consideration. Inherently, the conclusions drawn from inaccurate simulations of such complex physical systems may cause unexpected results in practice. These are particularly important in systems that involve flexible components, and a simple rigid body assumption does not capture the interactions between components accurately.

To overcome described integration inaccuracies, a special class of geometric integration scheme, called variational integrators (VI), is introduced in the literature, Ref. [17]. VI approach, instead of discretizing continuous equations of motion as the most general-purpose integrators do, directly utilizes the discrete variational principle obtaining the discrete dynamics as a result of the discrete Hamilton's principle. Therefore, derived discrete dynamics exactly preserves the momentum and symplectic form of the system, as presented in great detail by Refs. [18] and [20]. In addition, Lee and his team in Ref. [22] put forward an enhancement for variational integrators to preserve the geometric structure of the configuration manifold, which is represented as a Lie group, in rigid-body problems. Along with the symplecticity and momentum conservation, the exact preservation of the structure of the manifold ensures an exponentially long-term stability with a good energy behavior, which makes VI methods an ideal candidate for the simulation of complex or highly nonlinear systems.

As the precision and long-term numerical stability are detrimental for the simulations of space missions, VI methods are one of the natural choices in these missions. The spacecraft dynamics in Ref. [88] is tackled by developing a variant of variational integrators involving quaternions to represent the spacecraft attitude and demonstrates the superiority of VI simulation accuracy among the other continuous solvers. Various other work utilizing VI methods and discrete control systems have been pre-

sented by Lee et al., Refs. [21, 89], who have significant contributions in this area. Indeed, their representation of attitude dynamics via Lie group operations provides a basis for our N-Link cable model in this work as a series of spherical pendulums. Additionally, VI applications on a rigid-body dynamics of a quadrotor UAV in Ref. [90] and an underwater vehicle in Ref. [91] are among many other examples that led to our work. Apart from the aforementioned applications, Ref. [92] reveals another inspiring example of estimation and filtering for mechanical control systems, where multiple structure-preserving methods are incorporated with Kalman filters for higher accuracy in state estimations.

The main contribution of this work is the derivation and implementation of Lie group variational integrator method to the transportation of a suspended payload via flexible cables by either single or cooperative multi-rotors. This work is dedicated to accomplish more accurate simulations of cooperative multi-rotors transporting a slung load via flexible cables by employing a variational integrator approach. The physical system consists of multiple multi-rotors, serially attached cable segments with concentrated masses and a payload that is suspended via these cables. Hence, the described system defines a multi-body system with a complex geometry where the configuration manifold lies on a highly nonlinear space with geometrical constraints on each link, we benefited from Lie group VI approach in our work.

2.2.1 Overview of the Variational Integrator Procedure

In this section, a brief introduction to the formulation of variational integrator method is presented for general Lagrangian systems. In the first step, the continuous equations of motion of the system are derived by utilizing the variational principle, and then, the Hamiltonian representation of the system is obtained by Legendre transformation. Afterwards, the discrete equivalent of variational principle and Legendre

transformation are employed similarly to provide the discrete Hamiltonian formulation, which constitutes the basis of variational integrator. As a result, symplectic and momentum-preserving properties of Hamiltonian systems are benefited from while formulating the variational integration scheme.

2.2.1.1 Continuous Dynamics

General form of the Lagrangian of a dynamical system is expressed by

$$L(\boldsymbol{q}, \dot{\boldsymbol{q}}) = \frac{1}{2}\dot{\boldsymbol{q}}^T \boldsymbol{M} \dot{\boldsymbol{q}} - U(\boldsymbol{q}) \tag{2.59}$$

with the generalized coordinates, velocities, mass matrix and the coordinate dependent potential function are denoted with $\boldsymbol{q}$, $\dot{\boldsymbol{q}}$, $\boldsymbol{M}$ and U, respectively.

Applying the variational principle on Lagrangian and integrating it along time while holding the endpoints $\boldsymbol{q}(t)$, $t = t_0, t_f$ fixed, the least action principle yields the dynamics of the system, which is called Euler-Lagrange equations.

$$\mathbf{D}_{\boldsymbol{q}} L(\boldsymbol{q}, \dot{\boldsymbol{q}}) - \frac{d}{dt}\mathbf{D}_{\dot{\boldsymbol{q}}} L(\boldsymbol{q}, \dot{\boldsymbol{q}}) = 0 \tag{2.60}$$

where the partial derivatives are denoted by $\mathbf{D}_{\boldsymbol{q}} L(\boldsymbol{q}, \dot{\boldsymbol{q}}) = \partial L(\boldsymbol{q}, \dot{\boldsymbol{q}})/\partial \boldsymbol{q}$ and $\mathbf{D}_{\dot{\boldsymbol{q}}} L(\boldsymbol{q}, \dot{\boldsymbol{q}}) = \partial L(\boldsymbol{q}, \dot{\boldsymbol{q}})/\partial \dot{\boldsymbol{q}}$.

The motion evolves under a configuration-dependent potential in (2.59). However, the general forcing to the system can be included employing Lagrange d'Alembert principle as

$$\mathbf{D}_{\boldsymbol{q}} L(\boldsymbol{q}, \dot{\boldsymbol{q}}) - \frac{d}{dt}\mathbf{D}_{\dot{\boldsymbol{q}}} L(\boldsymbol{q}, \dot{\boldsymbol{q}}) + \boldsymbol{f} = 0 \tag{2.61}$$

Given the initial states, $(\boldsymbol{q}, \dot{\boldsymbol{q}})$, the time histories of the states are provided by the integration of (2.61), a second order ODE, along time. An alternate representation

of (2.61) can be achieved by Legendre Transformation, which yields Hamiltonian dynamics with the simpler first order equations of motion.

$$\dot{\boldsymbol{p}} - \mathbf{D}_{\boldsymbol{q}} L(\boldsymbol{q}, \boldsymbol{p}) = \boldsymbol{f} \tag{2.62}$$

where $\boldsymbol{p} = \mathbf{D}_{\dot{\boldsymbol{q}}} L(\boldsymbol{q}, \dot{\boldsymbol{q}})$ is called generalized momentum and it also establishes the symplectic form, $(\boldsymbol{q}, \boldsymbol{p})$.

2.2.1.2 Discrete Dynamics

Instead of directly discretizing the continuous equations of motion in (2.61) or (2.62), the discrete equivalent of continuous dynamics is derived applying the discrete version of calculus of variation and minimum action principle.

The first step is to attain the discrete linear approximation of the Lagrangian as

$$L_d(\boldsymbol{q}_k, \boldsymbol{q}_{k+1}) \approx L\Big((1-\alpha)\boldsymbol{q}_k + \alpha \boldsymbol{q}_{k+1}, \frac{\boldsymbol{q}_{k+1} - \boldsymbol{q}_k}{h}\Big) h \tag{2.63}$$

where the states are approximated by a linear interpolation as $\boldsymbol{q}(t) \approx (1-\alpha)\boldsymbol{q}_k + \alpha \boldsymbol{q}_{k+1}$ and $\dot{\boldsymbol{q}}(t) \approx \frac{\boldsymbol{q}_{k+1} - \boldsymbol{q}_k}{h}$ for $\alpha \in [0, 1]$ and $t = kh$ with time step of h. Many other linearization approaches are available in the literature with differing accuracy levels such as quadrature rules, $n-$point linear interpolation and so on. One of the most common approaches is to use the trapezoidal approximation of Lagrangian, midpoint rule, with the selection of $\alpha = 0.5$, where we also adopted in the rest of this work.

Then, applying the variational principle, discrete equivalent of the least action principle is formulated as a sum over time-steps, k.

$$\delta \mathfrak{B}_d = \sum_{k=0}^{N-1} \left[\mathbf{D}_{\boldsymbol{q}_k} L_d(\boldsymbol{q}_k, \boldsymbol{q}_{k+1}) \cdot \delta \boldsymbol{q}_k + \mathbf{D}_{\boldsymbol{q}_{k+1}} L_d(\boldsymbol{q}_k, \boldsymbol{q}_{k+1}) \cdot \delta \boldsymbol{q}_{k+1} \right]$$

where $\mathbf{D}_{\boldsymbol{q}_k} L_d$ is the partial differential of the discrete Lagrangian at time-step k with respect to the generalized coordinates at kth time-step, $\boldsymbol{q}_k$.

Knowing that the end points are held fixed, $\delta \boldsymbol{q}_k = 0$ for $k = 0, N$, discrete equations of motion are derived as:

$$\mathbf{D}_{\boldsymbol{q}_k} L_d(\boldsymbol{q}_k, \boldsymbol{q}_{k+1}) + \mathbf{D}_{\boldsymbol{q}_k} L_d(\boldsymbol{q}_{k-1}, \boldsymbol{q}_k) = 0$$

Employing the discrete version of Lagrange d'Alembert Principle, forced discrete Euler-Lagrange equations are acquired as follows:

$$\mathbf{D}_{\boldsymbol{q}_k} L_d(\boldsymbol{q}_k, \boldsymbol{q}_{k+1}) + \mathbf{D}_{\boldsymbol{q}_k} L_d(\boldsymbol{q}_{k-1}, \boldsymbol{q}_k) + \boldsymbol{f}_k^- + \boldsymbol{f}_{k-1}^+ = 0 \tag{2.64}$$

Discrete virtual work is again approximated by a linear combination of two consecutive states with the forcing as below:

$$\delta W = \int_{t_k}^{t_{k+1}} \boldsymbol{f} \cdot \delta \boldsymbol{x} \, dt \approx \boldsymbol{f}_k^- \cdot \delta \boldsymbol{x}_k + \boldsymbol{f}_k^+ \cdot \delta \boldsymbol{x}_{k+1} = \delta W_d$$

where $\boldsymbol{f}_k^- = (1-c)h\boldsymbol{f}_k$ and $\boldsymbol{f}_k^+ = ch\boldsymbol{f}_{k+1}$ with $c \in [0, 1]$. For midpoint (trapezoidal) approximation, parameter c is chosen to be 0.5.

Given the initial states of $(\boldsymbol{q}_0, \boldsymbol{q}_1)$, the next state, $\boldsymbol{q}_2$, can be computed from (2.64) and the integration progresses iteratively till the final state $\boldsymbol{q}_N$, i.e. $(\boldsymbol{q}_{k-1}, \boldsymbol{q}_k) \rightarrow (\boldsymbol{q}_k, \boldsymbol{q}_{k+1})$, $k = 1, .., N$. However, instead of working with the consecutive initial states in each integration step, it is more convenient and natural to utilize the initial position and velocity (or momentum) states of the system to define its motion. The conversion between the pair of consecutive positions to position-momentum pair can be established by discrete Legendre Transformation, which also yields the discrete Hamiltonian representation of the system as follows:

$$\boldsymbol{p}_k = -\mathbf{D}_{\boldsymbol{q}_k} L_d(\boldsymbol{q}_k, \boldsymbol{q}_{k+1}) - \boldsymbol{f}_k^- \tag{2.65}$$

$$\boldsymbol{p}_{k+1} = \mathbf{D}_{\boldsymbol{q}_{k+1}} L_d(\boldsymbol{q}_k, \boldsymbol{q}_{k+1}) + \boldsymbol{f}_k^+ \tag{2.66}$$

Given a pair of initial conditions, $(\boldsymbol{q}_0, \dot{\boldsymbol{q}}_0)$, the momentum state, $\boldsymbol{p}_0$, is assessed from $\boldsymbol{p}_k = \mathbf{D}_{\dot{\boldsymbol{q}}_k} L(\boldsymbol{q}_k, \dot{\boldsymbol{q}}_k)$ relation. Then, substituting $(\boldsymbol{q}_0, \boldsymbol{p}_0)$ pair into (2.65), $\boldsymbol{q}_1$ can

be solved implicitly. In the next step, (2.66) provides the next momentum state, $\boldsymbol{p}_{k+1}$, explicitly. Hence, the flow of the integration follows $(\boldsymbol{q}_k, \boldsymbol{p}_k) \rightarrow (\boldsymbol{q}_{k+1}, \boldsymbol{p}_{k+1}),\ k = 0, .., N-1$, as summarized in Algorithm 1.

Algorithm 1: Variational Integrator algorithm

IC: $(\boldsymbol{q}_0, \dot{\boldsymbol{q}}_0)$; `// Initial Pos and Vel`

Input: $(\boldsymbol{f}_k),\ k = 0 : N$; `// Command`

for $k = 0\ :\ N-1$ **do**

$\boldsymbol{p}_k \leftarrow \text{ComputeMomentum}(\boldsymbol{q}_k, \dot{\boldsymbol{q}}_k)$; `// Implicit Sol For Next Pos`

$\boldsymbol{q}_{k+1} \leftarrow \text{SolveForNextPos}(\boldsymbol{q}_k, \boldsymbol{p}_k, \boldsymbol{f}_k^-)$; `// Propagate Momentum Eq`

$\boldsymbol{p}_{k+1} \leftarrow \text{ComputeNextMomentum}(\boldsymbol{q}_k, \boldsymbol{q}_{k+1}, \boldsymbol{f}_k^+)$; `// Find Vel from Momentum`

$\dot{\boldsymbol{q}}_{k+1} \leftarrow \text{ExtractVelFromMomentum}(\boldsymbol{q}_{k+1}, \boldsymbol{p}_{k+1})$

end

Output: History of States $(\boldsymbol{q}_k, \dot{\boldsymbol{q}}_k),\ k = 0 : N$

2.2.2 Lie Group Variational Integrators on $SO(3)$ and S^2

2.2.2.1 Derivation of VI for Single Multi-rotor with Slung Load System

In the first step, Lagrangian of the system is approximated by employing the method described in (2.63) to the kinetic and potential energies given in (2.12)-(2.13).

$$L_d(\boldsymbol{x}_{P_k}, \boldsymbol{x}_{P_{k+1}}, \boldsymbol{R}_{Q_k}, \boldsymbol{\omega}_{Q_k}, \boldsymbol{q}_{1_k}, \boldsymbol{q}_{1_{k+1}}, .., \boldsymbol{q}_{n_k}, \boldsymbol{q}_{n_{k+1}}) = (T_k - U_k)h$$

One of the key advantages of the discrete dynamics over its continuous opponent is rooted from the way that the attitude dynamics of a body is represented. The attitude of a rigid body evolves in a nonlinear manifold such as SO(3) for the attitude

of the multi-rotor and S^2 for the attitude of the cable link for the cable suspended payload system. It is crucial for any numerical integration scheme to preserve the structure of the manifold to capture the actual behavior of the model. For this reason, the discrete system takes advantage of the structure preserving Lie group actions to approximate the attitude dynamics of the multi-rotor and the cable links.

The group action for SO(3) manifold is defined as the right matrix multiplication. The discrete update map of the multi-rotor attitude is given by $\boldsymbol{R}_{Q_{k+1}} = \boldsymbol{R}_{Q_k}\boldsymbol{F}_{Q_k}$ where $\boldsymbol{F}_{Q_k} \in \mathrm{SO}(3)$ is an infinitesimal rotation from $\boldsymbol{R}_{Q_k}$ to $\boldsymbol{R}_{Q_{k+1}}$. The group action for the configuration space in product of two spheres, S^2, is similarly defined but with the left matrix multiplication. The discrete update map of the cable link attitude is given by $\boldsymbol{q}_{k+1} = \boldsymbol{F}_{\boldsymbol{q}_k}\boldsymbol{q}_k$ where $\boldsymbol{F}_{\boldsymbol{q}_k} \in \mathrm{SO}(3)$ is an infinitesimal rotation from $\boldsymbol{q}_k$ to $\boldsymbol{q}_{k+1}$.

It is desired to approximate the continuous rotational kinematics of the multi-rotor, $\dot{\boldsymbol{R}}_{Q_k} = \boldsymbol{R}_{Q_k}\hat{\boldsymbol{\omega}}_{Q_k}$, in terms of discrete updates of infinitesimal rotations to preserve orthogonality and the structure of the manifold SO(3) during the evolution of the states. Hence, the need for additional manipulations to fix the deviations and accumulated errors on the orthogonality of the attitude representations can be eliminated since the group action in SO(3) preserves the manifold, i.e. $\boldsymbol{R}_{k+1}^T\boldsymbol{R}_{k+1} = \boldsymbol{I}_{3\times 3} = \boldsymbol{F}_k^T\boldsymbol{R}_k^T\boldsymbol{R}_k\boldsymbol{F}_k = \boldsymbol{F}_k^T\boldsymbol{F}_k$. Now, the approximation of the vehicle's angular velocity can be written as

$$\hat{\boldsymbol{\omega}}_{Q_k} = \boldsymbol{R}_{Q_k}^T\dot{\boldsymbol{R}}_{Q_k} \approx \boldsymbol{R}_{Q_k}^T\frac{\boldsymbol{R}_{Q_{k+1}} - \boldsymbol{R}_{Q_k}}{h} = \frac{\boldsymbol{F}_{Q_k} - \boldsymbol{I}_{3\times 3}}{h}$$

Using the trace identity, $\boldsymbol{\omega}_Q^T\boldsymbol{\omega}_Q = \mathrm{Tr}[\hat{\boldsymbol{\omega}}_Q\hat{\boldsymbol{\omega}}_Q^T]$, angular kinetic energy is rewritten by

$$\frac{1}{2}\boldsymbol{\omega}_Q^T\boldsymbol{J}_Q\boldsymbol{\omega}_Q = \frac{\mathrm{Tr}[(\boldsymbol{I} - \boldsymbol{F}_{Q_k})\boldsymbol{J}_{Q_d}]}{h^2} \tag{2.67}$$

where $\boldsymbol{J}_{Q_d}$ is the non-standard moment of inertia which can be obtained by $\boldsymbol{J}_{Q_d} = \frac{1}{2}\mathrm{Tr}[\boldsymbol{J}_Q]\boldsymbol{I}_{3\times 3} - \boldsymbol{J}_Q$.

Substituting (2.67), discrete Lagrangian becomes

$$\begin{aligned}
L_{d_k} &= L_d(\boldsymbol{x}_{P_k}, \boldsymbol{x}_{P_{k+1}}, \boldsymbol{R}_{Q_k}, \boldsymbol{F}_{Q_k}, \boldsymbol{q}_{1_k}, \boldsymbol{q}_{1_{k+1}}, .., \boldsymbol{q}_{n_k}, \boldsymbol{q}_{n_{k+1}}) \\
&= \frac{1}{2h}(\boldsymbol{x}_{P_{k+1}} - \boldsymbol{x}_{P_k})^T \boldsymbol{M}_{00}(\boldsymbol{x}_{P_{k+1}} - \boldsymbol{x}_{P_k}) + \frac{1}{h}\mathrm{Tr}[(\boldsymbol{I} - \boldsymbol{F}_{Q_k})\boldsymbol{J}_{Q_d}] \\
&\quad + \frac{1}{2h}\sum_{i,j=1}^{n}(\boldsymbol{q}_{i_{k+1}} - \boldsymbol{q}_{i_k})^T \boldsymbol{M}_{ij}(\boldsymbol{q}_{j_{k+1}} - \boldsymbol{q}_{j_k}) \\
&\quad + \frac{(\boldsymbol{x}_{P_{k+1}} - \boldsymbol{x}_{P_k})^T}{h}\sum_{i=1}^{n}\boldsymbol{M}_{0i}(\boldsymbol{q}_{i_{k+1}} - \boldsymbol{q}_{i_k}) \\
&\quad + \frac{h}{2}\left(\boldsymbol{M}_{00}g(\boldsymbol{x}_{P_k} + \boldsymbol{x}_{P_{k+1}}) + \sum_{i=1}^{n}\boldsymbol{M}_{0i}g(\boldsymbol{q}_{i_k} + \boldsymbol{q}_{i_{k+1}})\right)\cdot \boldsymbol{e}_3
\end{aligned}$$

Secondly, the variation on the discrete Lagrangian is assessed with

$$\begin{aligned}
\delta L_{d_k} &= \mathbf{D}_{\boldsymbol{x}_{P_k}} L_{d_k}\cdot \delta\boldsymbol{x}_{P_k} + \mathbf{D}_{\boldsymbol{x}_{P_{k+1}}} L_{d_k}\cdot \delta\boldsymbol{x}_{P_{k+1}} + \mathbf{D}_{\boldsymbol{R}_{Q_k}} L_{d_k}\cdot \delta\boldsymbol{R}_{Q_k} \\
&\quad + \mathbf{D}_{\boldsymbol{F}_{Q_k}} L_{d_k}\cdot \delta\boldsymbol{F}_{Q_k} + \sum_{i=1}^{n}\left(\mathbf{D}_{\boldsymbol{q}_{i_k}} L_{d_k}\cdot \delta\boldsymbol{q}_{i_k} + \mathbf{D}_{\boldsymbol{q}_{i_{k+1}}} L_{d_k}\cdot \delta\boldsymbol{q}_{i_{k+1}}\right)
\end{aligned}$$

and the variation on the states are expressed below

$$\begin{aligned}
\delta\boldsymbol{R}_{Q_k} &= \boldsymbol{R}_{Q_k}\hat{\boldsymbol{\eta}}_{Q_k} \\
\delta\boldsymbol{F}_{Q_k} &= (\delta\boldsymbol{R}_{Q_k})^T\boldsymbol{R}_{Q_{k+1}} + \boldsymbol{R}_{Q_k}^T\boldsymbol{R}_{Q_{k+1}}\hat{\boldsymbol{\eta}}_{Q_{k+1}} \\
&= -\hat{\boldsymbol{\eta}}_{Q_k}\boldsymbol{F}_{Q_k} + \boldsymbol{F}_{Q_k}\hat{\boldsymbol{\eta}}_{Q_{k+1}} = \boldsymbol{F}_{Q_k}(-\boldsymbol{F}_{Q_k}^T\hat{\boldsymbol{\eta}}_{Q_k}\boldsymbol{F}_{Q_k} + \hat{\boldsymbol{\eta}}_{Q_{k+1}}) \\
&= \boldsymbol{F}_{Q_k}(-\mathrm{Ad}_{\boldsymbol{F}_{Q_k}^T}\cdot\hat{\boldsymbol{\eta}}_{Q_k} + \hat{\boldsymbol{\eta}}_{Q_{k+1}}) \\
\delta\boldsymbol{q}_{i_k} &= \boldsymbol{\xi}_{i_k}\times\boldsymbol{q}_{i_k}
\end{aligned}$$

where the Adjoint group operations in SO(3) are defined as $\mathrm{Ad}_{\boldsymbol{F}_k^T}\cdot\hat{\boldsymbol{\eta}}_k = \boldsymbol{F}_k^T\hat{\boldsymbol{\eta}}_k\boldsymbol{F}_k$ and $\mathrm{Ad}^*_{\boldsymbol{F}_k^T}\cdot\hat{\boldsymbol{\eta}}_k = \boldsymbol{F}_k\hat{\boldsymbol{\eta}}_k\boldsymbol{F}_k^T$.

The terms regarding the variation on the attitude of the multi-rotor can be expressed as follows.

$$\begin{aligned}
\mathbf{D}_{\boldsymbol{R}_{Q_k}} L_{d_k} \cdot \delta \boldsymbol{R}_{Q_k} &= \mathbf{D}_{\boldsymbol{R}_{Q_k}} L_{d_k} \cdot (\boldsymbol{R}_{Q_k} \boldsymbol{R}_{Q_k}^T \delta \boldsymbol{R}_{Q_k}) = \boldsymbol{R}_{Q_k}^T \mathbf{D}_{\boldsymbol{R}_{Q_k}} L_{d_k} \cdot (\boldsymbol{R}_{Q_k}^T \delta \boldsymbol{R}_{Q_k}) \\
&= \boldsymbol{R}_{Q_k}^T \mathbf{D}_{\boldsymbol{R}_{Q_k}} L_{d_k} \cdot \hat{\boldsymbol{\eta}}_{Q_k} \\
\mathbf{D}_{\boldsymbol{F}_{Q_k}} L_{d_k} \cdot \delta \boldsymbol{F}_{Q_k} &= \mathbf{D}_{\boldsymbol{F}_{Q_k}} L_{d_k} \cdot (\boldsymbol{F}_{Q_k} \boldsymbol{F}_{Q_k}^T \delta \boldsymbol{F}_{Q_k}) = \boldsymbol{F}_{Q_k}^T \mathbf{D}_{\boldsymbol{F}_{Q_k}} L_{d_k} \cdot (\boldsymbol{F}_{Q_k}^T \delta \boldsymbol{F}_{Q_k}) \\
&= \boldsymbol{F}_{Q_k}^T \mathbf{D}_{\boldsymbol{F}_{Q_k}} L_{d_k} \cdot (-\mathrm{Ad}_{\boldsymbol{F}_{Q_k}^T} \cdot \hat{\boldsymbol{\eta}}_{Q_k} + \hat{\boldsymbol{\eta}}_{Q_{k+1}}) \\
&= -\mathrm{Ad}^*_{\boldsymbol{F}_{Q_k}^T} \cdot \boldsymbol{F}_{Q_k}^T \mathbf{D}_{\boldsymbol{F}_{Q_k}} L_{d_k} \cdot \hat{\boldsymbol{\eta}}_{Q_k} + \boldsymbol{F}_{Q_k}^T \mathbf{D}_{\boldsymbol{F}_{Q_k}} L_{d_k} \cdot \hat{\boldsymbol{\eta}}_{Q_{k+1}}
\end{aligned}$$

Minimum action principle is formulated with an action sum, including the forces and moments propellers exerted to the system.

$$\begin{aligned}
\delta \mathfrak{B}_k &= \sum_{k=0}^{N-1} [\delta L_{d_k} + \delta W_{d_k}] = 0 \\
\delta W_{d_k} &= \boldsymbol{f}_{I_k}^- \cdot (\delta \boldsymbol{x}_{P_k} + \sum_{i=1}^{n} l \delta \boldsymbol{q}_{i_k}) \\
&\quad + \boldsymbol{f}_{I_k}^+ \cdot (\delta \boldsymbol{x}_{P_{k+1}} + \sum_{i=1}^{n} l \delta \boldsymbol{q}_{i_{k+1}}) + \boldsymbol{\tau}_k^- \cdot \boldsymbol{\eta}_{Q_k} + \boldsymbol{\tau}_k^+ \cdot \boldsymbol{\eta}_{Q_{k+1}}
\end{aligned}$$

Finally, considering the vanishing end-point conditions, forced discrete Euler-Lagrange equations are obtained as

$$\mathbf{D}_{\boldsymbol{x}_{P_k}} L_{d_k} + \mathbf{D}_{\boldsymbol{x}_{P_k}} L_{d_{k-1}} + \boldsymbol{f}_{I_{k-1}}^+ + \boldsymbol{f}_{I_k}^- = 0 \tag{2.68}$$

$$\boldsymbol{R}_{Q_k}^T \mathbf{D}_{\boldsymbol{R}_{Q_k}} L_{d_k} - \mathrm{Ad}^*_{\boldsymbol{F}_{Q_k}^T} \cdot \boldsymbol{F}_{Q_k}^T \mathbf{D}_{\boldsymbol{F}_{Q_k}} L_{d_k} + \boldsymbol{F}_{Q_{k-1}}^T \mathbf{D}_{\boldsymbol{F}_{Q_{k-1}}} L_{d_{k-1}} + \hat{\boldsymbol{\tau}}_{k-1}^+ + \hat{\boldsymbol{\tau}}_k^- = 0$$

$$\boldsymbol{q}_{i_k} \times \boldsymbol{q}_{i_k} \times \left(\mathbf{D}_{\boldsymbol{q}_{i_k}} L_{d_k} + \mathbf{D}_{\boldsymbol{q}_{i_k}} L_{d_{k-1}} + l \boldsymbol{f}_{I_{k-1}}^+ + l \boldsymbol{f}_{I_k}^- \right) = 0 \tag{2.69}$$

where the partial derivatives of the discrete Lagrangian are derived as below.

For the position and attitude states of the multi-rotor:

$$\begin{aligned}
\mathbf{D}_{\boldsymbol{x}_{P_k}} L_{d_k} &= -\boldsymbol{M}_{00}\frac{(\boldsymbol{x}_{P_{k+1}} - \boldsymbol{x}_{P_k})}{h} + \frac{h}{2}\boldsymbol{M}_{00} g\boldsymbol{e}_3 - \sum_{i=1}^{n} \boldsymbol{M}_{0i}\frac{(\boldsymbol{q}_{i_{k+1}} - \boldsymbol{q}_{i_k})}{h} \\
\mathbf{D}_{\boldsymbol{x}_{P_k}} L_{d_{k-1}} &= \boldsymbol{M}_{00}\frac{(\boldsymbol{x}_{P_k} - \boldsymbol{x}_{P_{k-1}})}{h} + \frac{h}{2}\boldsymbol{M}_{00} g\boldsymbol{e}_3 + \sum_{i=1}^{n} \boldsymbol{M}_{0i}\frac{(\boldsymbol{q}_{i_k} - \boldsymbol{q}_{i_{k-1}})}{h} \\
\boldsymbol{F}_{Q_k}^T \mathbf{D}_{\boldsymbol{F}_{Q_k}} L_{d_k} &= \frac{1}{h}[\boldsymbol{J}_{Q_d}\boldsymbol{F}_{Q_k} - \boldsymbol{F}_{Q_k}^T \boldsymbol{J}_{Q_d}] \\
\boldsymbol{R}_{Q_k}^T \mathbf{D}_{\boldsymbol{R}_{Q_k}} L_{d_k} &= 0
\end{aligned} \tag{2.70}$$

For the attitude states of the suspension cable:

$$\begin{aligned}
\mathbf{D}_{\boldsymbol{q}_{i_k}} L_{d_k} &= -\boldsymbol{M}_{0i}\frac{(\boldsymbol{x}_{P_{k+1}} - \boldsymbol{x}_{P_k})}{h} - \sum_{j=1}^{n} \boldsymbol{M}_{ij}\frac{(\boldsymbol{q}_{j_{k+1}} - \boldsymbol{q}_{j_k})}{h} + \frac{h}{2}\boldsymbol{M}_{0i} g\boldsymbol{e}_3 \\
\mathbf{D}_{\boldsymbol{q}_{i_k}} L_{d_{k-1}} &= \boldsymbol{M}_{0i}\frac{(\boldsymbol{x}_{P_k} - \boldsymbol{x}_{P_{k-1}})}{h} + \sum_{j=1}^{n} \boldsymbol{M}_{ij}\frac{(\boldsymbol{q}_{j_k} - \boldsymbol{q}_{j_{k-1}})}{h} + \frac{h}{2}\boldsymbol{M}_{0i} g\boldsymbol{e}_3
\end{aligned}$$

Remark 2.2.1. *Equation (2.70) is derived utilizing the identities* $Tr[\boldsymbol{AB}] = Tr[\boldsymbol{BA}] = Tr[\boldsymbol{A}^T\boldsymbol{B}^T] = Tr[\boldsymbol{B}^T\boldsymbol{A}^T],\ \boldsymbol{A}, \boldsymbol{B} \in \mathbb{R}^{n\times n}$ *and* $\boldsymbol{y}^T\hat{\boldsymbol{x}}\boldsymbol{z} = -Tr[\boldsymbol{y}\boldsymbol{z}^T\hat{\boldsymbol{x}}] =< \boldsymbol{y}\boldsymbol{z}^T - \boldsymbol{z}\boldsymbol{y}^T, \hat{\boldsymbol{x}} >$.

Solution of the discrete Euler-Lagrange equations derived in (2.68)-(2.69) requires the initial conditions to include the states at consecutive time steps, i.e. $(\boldsymbol{x}_{P_0}, \boldsymbol{x}_{P_1}, \boldsymbol{R}_{Q_0}, \boldsymbol{F}_{Q_0}, \boldsymbol{q}_{1_0}, \boldsymbol{q}_{1_1}, ..., \boldsymbol{q}_{n_0}, \boldsymbol{q}_{n_1})$. However, specifying consecutive initial positions is not practical in general for most dynamical simulations, and will be avoided using the discrete Legendre Transformation, which yields position and velocity pair as defined below for the derived discrete system.

$$P_{\boldsymbol{v}_{P_k}} = -\mathbf{D}_{\boldsymbol{x}_{P_k}} L_{d_k} - \boldsymbol{f}_{I_k}^{-} \tag{2.71}$$

$$P_{\hat{\boldsymbol{\omega}}_{Q_k}} = -\boldsymbol{R}_{Q_k}^T \mathbf{D}_{\boldsymbol{R}_{Q_k}} L_{d_k} + \mathrm{Ad}^*_{\boldsymbol{F}_{Q_k}^T} \cdot (\boldsymbol{F}_{Q_k}^T \mathbf{D}_{\boldsymbol{F}_{Q_k}} L_{d_k}) - \hat{\boldsymbol{\tau}}_k^{-}$$

$$P_{\boldsymbol{\omega}_{i_k}} = -\boldsymbol{q}_{i_k} \times (\mathbf{D}_{\boldsymbol{q}_{i_k}} L_{d_k} + l \boldsymbol{f}_{I_k}^{-}) \tag{2.72}$$

$$P_{\boldsymbol{v}_{P_{k+1}}} = \mathbf{D}_{\boldsymbol{x}_{P_{k+1}}} L_{d_k} + \boldsymbol{f}_{I_k}^{+} \tag{2.73}$$

$$P_{\hat{\boldsymbol{\omega}}_{Q_{k+1}}} = \boldsymbol{F}_{Q_k}^T \mathbf{D}_{\boldsymbol{F}_{Q_k}} L_{d_k} + \hat{\boldsymbol{\tau}}_k^{+}$$

$$P_{\boldsymbol{\omega}_{i_{k+1}}} = \boldsymbol{q}_{i_{k+1}} \times (\mathbf{D}_{\boldsymbol{q}_{i_{k+1}}} L_{d_k} + l \boldsymbol{f}_{I_k}^{+}) \tag{2.74}$$

Solution Procedure for the Discrete Dynamics:

The solution procedure consists of four sequential stages and these stages are iterated till the final time step, $k = N$. The first stage involves computation of the momenta, $(P_{\boldsymbol{v}_{P_0}}, P_{\boldsymbol{\omega}_{Q_0}}, P_{\boldsymbol{\omega}_{i_0}})$, from the given initial states as $(\boldsymbol{x}_{P_0}, \boldsymbol{v}_{P_0}, \boldsymbol{R}_{Q_0}, \boldsymbol{\omega}_{Q_0}, \boldsymbol{q}_{i_0}, \boldsymbol{\omega}_{i_0})$. This is achieved by employing the relations derived in continuous Legendre Transformation (2.22)-(2.23). In the second stage, the computed momenta are used along with the states at the current time step to provide $(\boldsymbol{x}_{P_1}, \boldsymbol{R}_{Q_1}, \boldsymbol{q}_{i_1})$ by implicitly solving (2.71)-(2.72). Afterwards, substituting the consecutive states at both time steps into (2.73)-(2.74), the momenta at the next time step, $(P_{\boldsymbol{v}_{P_1}}, P_{\boldsymbol{\omega}_{Q_1}}, P_{\boldsymbol{\omega}_{i_1}})$, are computed in the third stage. Finally, the last stage returns the velocity states, $(\boldsymbol{v}_{P_1}, \boldsymbol{\omega}_{Q_1}, \boldsymbol{\omega}_{i_1})$, utilizing the same relations in (2.22)-(2.23) inversely, but by substituting $(P_{\boldsymbol{v}_{P_1}}, P_{\boldsymbol{\omega}_{Q_1}}, P_{\boldsymbol{\omega}_{i_1}})$. Thereby, the iteration repeats these sequential stages to propagate the states of the system in discrete time steps.

2.2.2.2 Derivation of VI for Multiple Multi-rotors with Slung Load System

Discrete Lagrangian for the cooperative system is constructed as below

$$
\begin{aligned}
&L_{d_k} = L_d(\boldsymbol{x}_{P_k}, \boldsymbol{x}_{P_{k+1}}, \bar{\boldsymbol{\xi}}_{1_k}, \bar{\boldsymbol{\xi}}_{2_k}, .., \bar{\boldsymbol{\xi}}_{m_k}) \\
&= \frac{1}{2h}(\boldsymbol{x}_{P_{k+1}} - \boldsymbol{x}_{P_k})^T \boldsymbol{M}_{00}(\boldsymbol{x}_{P_{k+1}} - \boldsymbol{x}_{P_k}) + \frac{h}{2}\boldsymbol{M}_{00} g(\boldsymbol{x}_{P_k} + \boldsymbol{x}_{P_{k+1}}) \cdot \boldsymbol{e}_3 \\
&+ \sum_{s=1}^{m} \left[\frac{1}{h}\mathrm{Tr}[(\boldsymbol{I} - \boldsymbol{F}_{Q_{s_k}})\boldsymbol{J}_{Q_{s_d}}] + \frac{h}{2}\sum_{i=1}^{n} \boldsymbol{M}_{0i_s} g(\boldsymbol{q}_{i_{s_k}} + \boldsymbol{q}_{i_{s_{k+1}}}) \cdot \boldsymbol{e}_3 \right. \\
&\quad \left. + \frac{1}{2h}\sum_{i,j=1}^{n} (\boldsymbol{q}_{i_{s_{k+1}}} - \boldsymbol{q}_{i_{s_k}})^T \boldsymbol{M}_{ij_s}(\boldsymbol{q}_{j_{s_{k+1}}} - \boldsymbol{q}_{j_{s_k}}) + \frac{(\boldsymbol{x}_{P_{k+1}} - \boldsymbol{x}_{P_k})^T}{h} \sum_{i=1}^{n} \boldsymbol{M}_{0i_s}(\boldsymbol{q}_{i_{s_{k+1}}} - \boldsymbol{q}_{i_{s_k}}) \right]
\end{aligned}
$$

where $\bar{\boldsymbol{\xi}}_s = [\boldsymbol{R}_{Q_{s_k}},\ \boldsymbol{F}_{Q_{s_k}},\ \boldsymbol{q}_{1_{s_k}}, \boldsymbol{q}_{1_{s_{k+1}}},\ ..\ , \boldsymbol{q}_{n_{s_k}}, \boldsymbol{q}_{n_{s_{k+1}}}]$.

Applying the variation principle on the discrete Lagrangian yields

$$
\begin{aligned}
\delta L_{d_k} &= \mathbf{D}_{\boldsymbol{x}_{P_k}} L_{d_k} \cdot \delta \boldsymbol{x}_{P_k} + \mathbf{D}_{\boldsymbol{x}_{P_{k+1}}} L_{d_k} \cdot \delta \boldsymbol{x}_{P_{k+1}} \\
&+ \sum_{s=1}^{m} \left[\mathbf{D}_{\boldsymbol{R}_{Q_{s_k}}} L_{d_k} \cdot \delta \boldsymbol{R}_{Q_{s_k}} + \mathbf{D}_{\boldsymbol{F}_{Q_{s_k}}} L_{d_k} \cdot \delta \boldsymbol{F}_{Q_{s_k}} + \sum_{i=1}^{n} \left(\mathbf{D}_{\boldsymbol{q}_{i_{s_k}}} L_{d_k} \cdot \delta \boldsymbol{q}_{i_{s_k}} + \mathbf{D}_{\boldsymbol{q}_{i_{s_{k+1}}}} L_{d_k} \cdot \delta \boldsymbol{q}_{i_{s_{k+1}}} \right) \right]
\end{aligned}
$$

Discrete equivalent of Equation (2.24) for the work done on the system by each multi-rotor is expressed as follows:

$$
\delta W_{d_k} = \sum_{s=1}^{m} \left[\boldsymbol{f}_{I_{s_k}}^{-} \cdot (\delta \boldsymbol{x}_{P_k} + \sum_{i=1}^{n} l \delta \boldsymbol{q}_{i_{s_k}}) + \boldsymbol{\tau}_{s_k}^{-} \cdot \boldsymbol{\eta}_{Q_{s_k}} + \boldsymbol{f}_{I_{s_k}}^{+} \cdot (\delta \boldsymbol{x}_{P_{k+1}} + \sum_{i=1}^{n} l \delta \boldsymbol{q}_{i_{s_{k+1}}}) + \boldsymbol{\tau}_{s_k}^{+} \cdot \boldsymbol{\eta}_{Q_{s_{k+1}}} \right]
$$

Ultimately, the minimization of the action provides discrete Euler-Lagrange equations for the cooperative system as

$$
\begin{aligned}
&\mathbf{D}_{\boldsymbol{x}_{P_k}} L_{d_k} + \mathbf{D}_{\boldsymbol{x}_{P_k}} L_{d_{k-1}} + \sum_{s=1}^{m} \left[\boldsymbol{f}_{I_{s_k}}^{-} + \boldsymbol{f}_{I_{s_{k-1}}}^{+} \right] = 0 \\
&\boldsymbol{R}_{Q_{s_k}}^T \mathbf{D}_{\boldsymbol{R}_{Q_{s_k}}} L_{d_k} - \mathrm{Ad}^*_{\boldsymbol{F}_{Q_{s_k}}^T} \cdot \boldsymbol{F}_{Q_{s_k}}^T \mathbf{D}_{\boldsymbol{F}_{Q_{s_k}}} L_{d_k} + \boldsymbol{F}_{Q_{s_{k-1}}}^T \mathbf{D}_{\boldsymbol{F}_{Q_{s_{k-1}}}} L_{d_{k-1}} + \hat{\boldsymbol{\tau}}_{s_{k-1}}^{+} + \hat{\boldsymbol{\tau}}_{s_k}^{-} = 0 \\
&\boldsymbol{q}_{i_{s_k}} \times \boldsymbol{q}_{i_{s_k}} \times \left(\mathbf{D}_{\boldsymbol{q}_{i_{s_k}}} L_{d_k} + \mathbf{D}_{\boldsymbol{q}_{i_{s_k}}} L_{d_{k-1}} + l \boldsymbol{f}_{I_{s_k}}^{-} + l \boldsymbol{f}_{I_{s_{k-1}}}^{+} \right) = 0
\end{aligned}
$$

for $s = 1, .., m$.

Substituting the partial derivatives of the discrete Lagrangian, which can be derived exactly as in the single multi-rotor case for the given cooperative system, discrete equations of motion become

$$\boldsymbol{M}_{00}\frac{\left(\boldsymbol{x}_{P_{k+1}}-2\boldsymbol{x}_{P_k}-\boldsymbol{x}_{P_{k-1}}\right)}{h}=h\boldsymbol{M}_{00}g\boldsymbol{e}_3+\sum_{s=1}^{m}\left(h\boldsymbol{f}_{I_{s_k}}+\sum_{i=1}^{n}\boldsymbol{M}_{0i_s}\frac{(-\boldsymbol{q}_{i_{s_{k+1}}}+2\boldsymbol{q}_{i_{s_k}}-\boldsymbol{q}_{i_{s_{k-1}}})}{h}\right)$$

$$\frac{1}{h}\left[\boldsymbol{F}_{Q_{s_{k-1}}}{}^{T}\boldsymbol{J}_{Q_{s_d}}-\boldsymbol{J}_{Q_{s_d}}\boldsymbol{F}_{Q_{s_{k-1}}}+\boldsymbol{F}_{Q_{s_k}}\boldsymbol{J}_{Q_{s_d}}-\boldsymbol{J}_{Q_{s_d}}\boldsymbol{F}_{Q_{s_k}}{}^{T}\right]^{\vee}=h\boldsymbol{\tau}_{s_k}$$

$$\boldsymbol{q}_{i_{s_k}}\times\sum_{j=1}^{n}\boldsymbol{M}_{ij_s}\frac{(-\boldsymbol{q}_{j_{s_{k+1}}}+2\boldsymbol{q}_{j_{s_k}}-\boldsymbol{q}_{j_{s_{k-1}}})}{h}=\boldsymbol{q}_{i_{s_k}}\times\left[\frac{\left(\boldsymbol{x}_{P_{k+1}}-2\boldsymbol{x}_{P_k}+\boldsymbol{x}_{P_{k-1}}\right)}{h}\boldsymbol{M}_{0i_s}-h\boldsymbol{M}_{0i_s}g\boldsymbol{e}_3-lh\boldsymbol{f}_{I_{s_k}}\right.$$

By applying discrete Legendre Transformation, discrete Hamiltonian form of the derived equations are obtained with discrete momenta as follows.

$$P_{\boldsymbol{v}_{P_k}}=-\mathbf{D}_{\boldsymbol{x}_{P_k}}L_{d_k}-\sum_{s=1}^{m}\boldsymbol{f}_{I_{s_k}}^{-} \tag{2.75}$$

$$P_{\hat{\boldsymbol{\omega}}_{Q_{s_k}}}=-\boldsymbol{R}_{Q_{s_k}}^{T}\mathbf{D}_{\boldsymbol{R}_{Q_{s_k}}}L_{d_k}+\mathrm{Ad}^{*}_{\boldsymbol{F}_{Q_{s_k}}^{T}}\cdot(\boldsymbol{F}_{Q_{s_k}}^{T}\mathbf{D}_{\boldsymbol{F}_{Q_{s_k}}}L_{d_k})-\hat{\boldsymbol{\tau}}_{s_k}^{-}$$

$$P_{\boldsymbol{\omega}_{i_{s_k}}}=-\boldsymbol{q}_{i_{s_k}}\times(\mathbf{D}_{\boldsymbol{q}_{i_{s_k}}}L_{d_k}+l\boldsymbol{f}_{I_{s_k}}^{-}) \tag{2.76}$$

$$P_{\boldsymbol{v}_{P_{k+1}}}=\mathbf{D}_{\boldsymbol{x}_{P_{k+1}}}L_{d_k}+\sum_{s=1}^{m}\boldsymbol{f}_{I_{s_k}}^{+} \tag{2.77}$$

$$P_{\hat{\boldsymbol{\omega}}_{Q_{s_{k+1}}}}=\boldsymbol{F}_{Q_{s_k}}^{T}\mathbf{D}_{\boldsymbol{F}_{Q_{s_k}}}L_{d_k}+\hat{\boldsymbol{\tau}}_{s_k}^{+}$$

$$P_{\boldsymbol{\omega}_{i_{s_{k+1}}}}=\boldsymbol{q}_{i_{s_{k+1}}}\times(\mathbf{D}_{\boldsymbol{q}_{i_{s_{k+1}}}}L_{d_k}+l\boldsymbol{f}_{I_{s_k}}^{+}) \tag{2.78}$$

Solution Procedure for the Discrete Dynamics:

The solution procedure follows the same stages as described in the discrete dynamics of a single multi-rotor with a slung load system. The momenta, $(P_{\boldsymbol{v}_{P_0}}, P_{\boldsymbol{\omega}_{Q_{s_0}}}, P_{\boldsymbol{\omega}_{i_{s_0}}})$, are calculated from the given initial states, $(\boldsymbol{x}_{P_0}, \boldsymbol{v}_{P_0}, \boldsymbol{R}_{Q_{s_0}}, \boldsymbol{\omega}_{Q_{s_0}}, \boldsymbol{q}_{i_{s_0}}, \boldsymbol{\omega}_{i_{s_0}})$ using (2.28)-(2.29) in the first stage. Following that, the implicit solution of (2.75)-(2.76) supplies the states at the next time step, $(\boldsymbol{x}_{P_1}, \boldsymbol{R}_{Q_{s_1}}, \boldsymbol{q}_{i_{s_1}})$. Then, the states at the consecutive steps are substituted into (2.77)-(2.78) to get the momenta at the next time step, $(P_{\boldsymbol{v}_{P_1}}, P_{\boldsymbol{\omega}_{Q_{s_1}}}, P_{\boldsymbol{\omega}_{i_{s_1}}})$, which are also used to compute the velocity states as

$(\boldsymbol{v}_{P_1}, \boldsymbol{\omega}_{s_1}, \boldsymbol{\omega}_{i_{s_1}})$ by the use of (2.28)-(2.29). These sequential stages form an integration flow to solve the discrete equations of the derived Hamiltonian system.

For a rigid body payload, the following discrete Lagrangian is utilized,

$$
\begin{aligned}
L_{d_k} &= L_d(\boldsymbol{x}_{P_k}, \boldsymbol{x}_{P_{k+1}}, \boldsymbol{R}_{P_k}, \boldsymbol{F}_{P_k}, \bar{\boldsymbol{\xi}}_{1_k}, \bar{\boldsymbol{\xi}}_{2_k}, .., \bar{\boldsymbol{\xi}}_{m_k}) \\
&= \frac{1}{2h}\left(\boldsymbol{x}_{P_{k+1}} - \boldsymbol{x}_{P_k}\right)^T \boldsymbol{M}_{00}\left(\boldsymbol{x}_{P_{k+1}} - \boldsymbol{x}_{P_k}\right) + \frac{1}{h}\mathrm{Tr}\left[\left(\boldsymbol{I} - \boldsymbol{F}_{P_k}\right)\boldsymbol{J}_{P_d}\right] \\
&+ \sum_{s=1}^{m}\left[\frac{1}{h}\mathrm{Tr}\left[\left(\boldsymbol{I} - \boldsymbol{F}_{Q_{s_k}}\right)\boldsymbol{J}_{Q_{s_d}}\right] + \frac{\left(\boldsymbol{x}_{P_{k+1}} - \boldsymbol{x}_{P_k}\right)^T}{h}\sum_{i=1}^{n}\boldsymbol{M}_{0i_s}\left(\boldsymbol{q}_{i_{s_{k+1}}} - \boldsymbol{q}_{i_{s_k}}\right)\right. \\
&\qquad \left. + \frac{1}{2h}\sum_{i,j=1}^{n}\left(\boldsymbol{q}_{i_{s_{k+1}}} - \boldsymbol{q}_{i_{s_k}}\right)^T \boldsymbol{M}_{ij_s}\left(\boldsymbol{q}_{j_{s_{k+1}}} - \boldsymbol{q}_{j_{s_k}}\right)\right] \\
&- \sum_{s=1}^{m}\boldsymbol{\rho}_s^T\frac{\boldsymbol{F}_{P_k} - \boldsymbol{I}}{h}\frac{\left(\boldsymbol{R}_{P_k} + \boldsymbol{R}_{P_k}\boldsymbol{F}_{P_k}\right)^T}{2}\boldsymbol{M}_{Q_s}\left(\left(\boldsymbol{x}_{P_{k+1}} - \boldsymbol{x}_{P_k}\right) + \frac{\left(\boldsymbol{R}_{P_k} + \boldsymbol{R}_{P_k}\boldsymbol{F}_{P_k}\right)}{4}\left(\boldsymbol{F}_{P_k} - \boldsymbol{I}\right)\boldsymbol{\rho}_s\right) \\
&- \sum_{s=1}^{m}\boldsymbol{\rho}_s^T\frac{\boldsymbol{F}_{P_k} - \boldsymbol{I}}{h}\frac{\left(\boldsymbol{R}_{P_k} + \boldsymbol{R}_{P_k}\boldsymbol{F}_{P_k}\right)^T}{2}\left[\sum_{i=1}^{n}\boldsymbol{M}_{0i_s}\left(\boldsymbol{q}_{i_{s_{k+1}}} - \boldsymbol{q}_{i_{s_k}}\right)\right] \\
&+ \frac{h}{2}\left(\boldsymbol{M}_{00}g\left(\boldsymbol{x}_{P_k} + \boldsymbol{x}_{P_{k+1}}\right) + \sum_{s=1}^{m}\left[\boldsymbol{M}_{Q_s}g\left(\boldsymbol{R}_{P_k} + \boldsymbol{R}_{P_k}\boldsymbol{F}_{P_k}\right)\boldsymbol{\rho}_s + \sum_{i=1}^{n}\boldsymbol{M}_{0i_s}g\left(\boldsymbol{q}_{i_{s_k}} + \boldsymbol{q}_{i_{s_{k+1}}}\right)\right]\right)\cdot\boldsymbol{e}_3
\end{aligned}
$$

Applying the variation principle on the discrete Lagrangian, we obtain

$$
\begin{aligned}
\delta L_{d_k} &= \mathbf{D}_{\boldsymbol{x}_{P_k}}L_{d_k}\cdot\delta\boldsymbol{x}_{P_k} + \mathbf{D}_{\boldsymbol{x}_{P_{k+1}}}L_{d_k}\cdot\delta\boldsymbol{x}_{P_{k+1}} + \mathbf{D}_{\boldsymbol{R}_{P_k}}L_{d_k}\cdot\delta\boldsymbol{R}_{P_k} + \mathbf{D}_{\boldsymbol{F}_{P_k}}L_{d_k}\cdot\delta\boldsymbol{F}_{P_k} \\
&+ \sum_{s=1}^{m}\left[\mathbf{D}_{\boldsymbol{R}_{Q_{s_k}}}L_{d_k}\cdot\delta\boldsymbol{R}_{Q_{s_k}} + \mathbf{D}_{\boldsymbol{F}_{Q_{s_k}}}L_{d_k}\cdot\delta\boldsymbol{F}_{Q_{s_k}}\right] \\
&+ \sum_{s=1}^{m}\left[\sum_{i=1}^{n}\left(\mathbf{D}_{\boldsymbol{q}_{i_{s_k}}}L_{d_k}\cdot\delta\boldsymbol{q}_{i_{s_k}} + \mathbf{D}_{\boldsymbol{q}_{i_{s_{k+1}}}}L_{d_k}\cdot\delta\boldsymbol{q}_{i_{s_{k+1}}}\right)\right]
\end{aligned}
$$

The work done on the system by each multi-rotor is expressed below,

$$
\begin{aligned}
\delta W_{d_k} = \sum_{s=1}^{m}\left[\boldsymbol{f}_{I_{s_k}}^{-}\cdot\left(\delta\boldsymbol{x}_{P_k} - \boldsymbol{R}_{P_k}\hat{\boldsymbol{\rho}}_s\boldsymbol{\eta}_{P_k} + \sum_{i=1}^{n}l\delta\boldsymbol{q}_{i_{s_k}}\right) + \boldsymbol{\tau}_{s_k}^{-}\cdot\boldsymbol{\eta}_{Q_{s_k}} + \boldsymbol{\tau}_{s_k}^{+}\cdot\boldsymbol{\eta}_{Q_{s_{k+1}}}\right. \\
\left. + \boldsymbol{f}_{I_{s_k}}^{+}\cdot\left(\delta\boldsymbol{x}_{P_{k+1}} - \boldsymbol{R}_{P_{k+1}}\hat{\boldsymbol{\rho}}_s\boldsymbol{\eta}_{P_{k+1}} + \sum_{i=1}^{n}l\delta\boldsymbol{q}_{i_{s_{k+1}}}\right)\right]
\end{aligned}
$$

The minimization of the action provides discrete Euler-Lagrange equations as follows,

$$\mathbf{D}_{\boldsymbol{x}_{P_k}} L_{d_k} + \mathbf{D}_{\boldsymbol{x}_{P_k}} L_{d_{k-1}} + \sum_{s=1}^{m} \left(\boldsymbol{f}_{I_{s_k}}^{-} + \boldsymbol{f}_{I_{s_{k-1}}}^{+} \right) = 0$$

$$\boldsymbol{R}_{P_k}^T \mathbf{D}_{\boldsymbol{R}_{P_k}} L_{d_k} - \mathrm{Ad}^*_{\boldsymbol{F}_{P_k}^T} \cdot \boldsymbol{F}_{P_k}^T \mathbf{D}_{\boldsymbol{F}_{P_k}} L_{d_k} + \widehat{\left(\hat{\boldsymbol{\rho}}_s \boldsymbol{R}_{P_k}^T \boldsymbol{f}_{I_{s_k}}^{-} \right)} + \boldsymbol{F}_{P_{k-1}}^T \mathbf{D}_{\boldsymbol{F}_{P_{k-1}}} L_{d_{k-1}} + \widehat{\left(\hat{\boldsymbol{\rho}}_s \boldsymbol{R}_{P_k}^T \boldsymbol{f}_{I_{s_{k-1}}}^{+} \right)} = 0$$

$$\boldsymbol{R}_{Q_{s_k}}^T \mathbf{D}_{\boldsymbol{R}_{Q_{s_k}}} L_{d_k} - \mathrm{Ad}^*_{\boldsymbol{F}_{Q_{s_k}}^T} \cdot \boldsymbol{F}_{Q_{s_k}}^T \mathbf{D}_{\boldsymbol{F}_{Q_{s_k}}} L_{d_k} + \boldsymbol{F}_{Q_{s_{k-1}}}^T \mathbf{D}_{\boldsymbol{F}_{Q_{s_{k-1}}}} L_{d_{k-1}} + \hat{\boldsymbol{\tau}}_{s_{k-1}}^{+} + \hat{\boldsymbol{\tau}}_{s_k}^{-} = 0$$

$$\boldsymbol{q}_{i_{s_k}} \times \boldsymbol{q}_{i_{s_k}} \times \left(\mathbf{D}_{\boldsymbol{q}_{i_{s_k}}} L_{d_k} + \mathbf{D}_{\boldsymbol{q}_{i_{s_k}}} L_{d_{k-1}} + l \boldsymbol{f}_{I_{s_{k-1}}}^{+} + l \boldsymbol{f}_{I_{s_k}}^{-} \right) = 0$$

for $s = 1, .., m$.

Partial derivatives are found as below,

$$\begin{aligned}
\mathbf{D}_{\boldsymbol{x}_{P_k}} L_{d_k} &= -\boldsymbol{M}_{00} \frac{\left(\boldsymbol{x}_{P_{k+1}} - \boldsymbol{x}_{P_k} \right)}{h} - \sum_{s=1}^{m} \sum_{i=1}^{n} \boldsymbol{M}_{0i_s} \frac{\left(\boldsymbol{q}_{i_{s_{k+1}}} - \boldsymbol{q}_{i_{s_k}} \right)}{h} \\
&\quad + \sum_{s=1}^{m} \frac{\left(\boldsymbol{R}_{P_k} + \boldsymbol{R}_{P_{k+1}} \right)}{2} \frac{\left(\boldsymbol{F}_{P_k}^T - \boldsymbol{I} \right)}{h} \boldsymbol{\rho}_s \boldsymbol{M}_{Q_s} + \frac{h}{2} \boldsymbol{M}_{00} g \boldsymbol{e}_3 \\
\mathbf{D}_{\boldsymbol{x}_{P_k}} L_{d_{k-1}} &= \boldsymbol{M}_{00} \frac{\left(\boldsymbol{x}_{P_k} - \boldsymbol{x}_{P_{k-1}} \right)}{h} + \sum_{s=1}^{m} \sum_{i=1}^{n} \boldsymbol{M}_{0i_s} \frac{\left(\boldsymbol{q}_{i_{s_k}} - \boldsymbol{q}_{i_{s_{k-1}}} \right)}{h} \\
&\quad - \sum_{s=1}^{m} \frac{\left(\boldsymbol{R}_{P_{k-1}} + \boldsymbol{R}_{P_k} \right)}{2} \frac{\left(\boldsymbol{F}_{P_{k-1}}^T - \boldsymbol{I} \right)}{h} \boldsymbol{\rho}_s \boldsymbol{M}_{Q_s} + \frac{h}{2} \boldsymbol{M}_{00} g \boldsymbol{e}_3
\end{aligned}$$

$$\begin{aligned}
\boldsymbol{F}_{P_k}^T \mathbf{D}_{\boldsymbol{F}_{P_k}} L_{d_k} &= \frac{1}{h} \left(\boldsymbol{A}_k \boldsymbol{F}_{P_k} - \boldsymbol{F}_{P_k}^T \boldsymbol{A}_k^T \right) \\
\boldsymbol{F}_{Q_{s_k}}^T \mathbf{D}_{\boldsymbol{F}_{Q_{s_k}}} L_{d_k} &= \frac{1}{h} \left(\boldsymbol{J}_{Q_{s_d}} \boldsymbol{F}_{Q_{s_k}} - \boldsymbol{F}_{Q_{s_k}}^T \boldsymbol{J}_{Q_{s_d}} \right) \\
\boldsymbol{R}_{Q_{s_k}}^T \mathbf{D}_{\boldsymbol{R}_{Q_{s_k}}} L_{d_k} &= 0
\end{aligned}$$

where

$$\boldsymbol{A}_k = \boldsymbol{J}_{P_d} + \frac{\boldsymbol{F}_{P_k} \boldsymbol{\rho}_s \boldsymbol{\rho}_s^T + \boldsymbol{\rho}_s \boldsymbol{\rho}_s^T \boldsymbol{F}_{P_k} - 2 \boldsymbol{\rho}_s \boldsymbol{\rho}_s^T}{8}$$

$$\boldsymbol{R}_{P_k}^T \mathbf{D}_{\boldsymbol{R}_{P_k}} L_{d_k} = -\frac{1}{2h} \sum_{s=1}^{m} \widehat{\left[\left(\boldsymbol{F}_{P_k}^T - \boldsymbol{F}_{P_k}\right)\boldsymbol{\rho}_s\right] \boldsymbol{R}_{P_k}^T \left[\boldsymbol{M}_{Q_s}\left(\boldsymbol{x}_{P_{k+1}} - \boldsymbol{x}_{P_k}\right) + \sum_{i=1}^{n} \boldsymbol{M}_{0i_s}\left(\boldsymbol{q}_{i_{s_{k+1}}} - \boldsymbol{q}_{i_{s_k}}\right)\right]}$$
$$+ \frac{h}{2} \sum_{s=1}^{m} \widehat{\left(\boldsymbol{I} + \boldsymbol{F}_{P_k}\right)\boldsymbol{\rho}_s \boldsymbol{M}_{Q_s} g \boldsymbol{R}_{P_k}^T \boldsymbol{e}_3}$$

$$\mathbf{D}_{\boldsymbol{q}_{i_{s_k}}} L_{d_k} = -\frac{\left(\boldsymbol{x}_{P_{k+1}} - \boldsymbol{x}_{P_k}\right)}{h} \boldsymbol{M}_{0i_s} - \sum_{j=1}^{n} \frac{\left(\boldsymbol{q}_{j_{s_{k+1}}} - \boldsymbol{q}_{j_{s_k}}\right)}{h} \boldsymbol{M}_{0i_s}$$
$$+ \boldsymbol{\rho}_s^T \frac{\boldsymbol{F}_{P_k} - \boldsymbol{F}_{P_k}^T}{2h} \boldsymbol{M}_{0i_s} + \frac{h}{2} \boldsymbol{M}_{0i_s} g \boldsymbol{e}_3$$
$$\mathbf{D}_{\boldsymbol{q}_{i_{s_k}}} L_{d_{k-1}} = \frac{\left(\boldsymbol{x}_{P_k} - \boldsymbol{x}_{P_{k-1}}\right)}{h} \boldsymbol{M}_{0i_s} + \sum_{j=1}^{n} \frac{\left(\boldsymbol{q}_{j_{s_k}} - \boldsymbol{q}_{j_{s_{k-1}}}\right)}{h} \boldsymbol{M}_{0i_s}$$
$$- \boldsymbol{\rho}_s^T \frac{\boldsymbol{F}_{P_{k-1}} - \boldsymbol{F}_{P_{k-1}}^T}{2h} \boldsymbol{M}_{0i_s} + \frac{h}{2} \boldsymbol{M}_{0i_s} g \boldsymbol{e}_3$$

2.2.3 Simulation Results and Comparison of VI and ODE Solvers

In this section, numerical simulations for the systems developed in Section 2.1.2 and 2.1.3.1 are provided to illustrate the effectiveness of variational integration scheme in these complex systems. Simulations are carried out in each scenario for both continuous and discrete dynamics, where the fourth order fixed-step Runge-Kutta (RK4) and variable-step ODE45 solvers are selected for the integration of continuous dynamics separately. Simulation results obtained from the implementation of variational integrator are compared with the results from selected continuous time integrators, RK4 and ODE45, in terms of their preservation of momentum, total energy and the geometrical constraints of the systems.

2.2.3.1 Simulation of a Single Multi-Rotor with a Flexible Cable Suspended Payload

In this example, the response of the continuous and discrete time models of the single multi-rotor with a flexible cable suspended payload system to an initial deflection of the suspension cable is analyzed to demonstrate the effectiveness of variational integrator solution comparing the fixed-step RK4 and the variable-step ODE45 integrator solutions of the continuous-time model.

The payload is initially located at the origin and it is suspended via a cable, which is constructed from 10 rigid links and it connects payload to the center of mass of the multi-rotor, such that the initial deflection of the cable makes 30 degree angle with the horizontal plane as illustrated in Figure 2.21. Multi-rotor applies a vertical force to compensate the total weight of the whole system. The system does not have an initial velocity and an acceleration except the gravity.

Remark 2.2.2. *It is known that in the case where the suspension cable is not straight initially, i.e. having relative displacements among cable links, simulated systems suffer from numerical instabilities due to the chaotic and unstable behavior of the undamped*

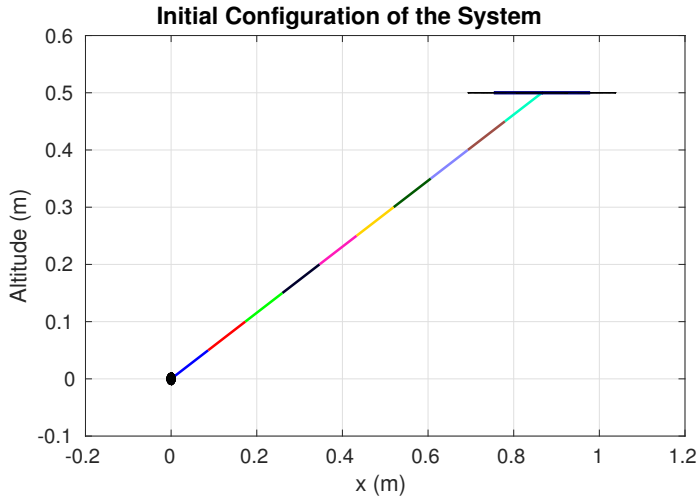

Figure 2.21: Initial configuration of the single multi-rotor with a flexibly suspended payload

dynamics regardless of the integration method utilized. A common approach to prevent such numerical instabilities is to introduce a damping into the system, such as torsional damping between the cable links in the form of $\boldsymbol{\tau}_{d_i} = -c_d(\boldsymbol{\omega}_{i-1/i} - \boldsymbol{\omega}_{i/i+1})$. *However, since the damping would prevent the preservation of the energy, the scenarios are simulated without any damping to illustrate the effectiveness of VI method.*

Parameters used in this simulation are chosen as below.

$$m_Q = 1.2 \text{ kg},\ m_P = 0.5 \text{ kg},\ m_i = 0.005 \text{ kg}$$

$$\boldsymbol{J}_Q = diag(1.367e-2,\ 1.367e-2,\ 2.586e-2)$$

$h = 0.001$sec (for both RK4 and VI)

$l_{cable} = 1$m (total cable length)

Simulation results are plotted in Figure 2.22. The left and middle columns correspond to the continuous-time model solution by RK4 and ODE45 integrators respectively, whereas the right column shows the discrete-time model solution by Lie group VI method. Since the system has zero net force in all axes, it is expected

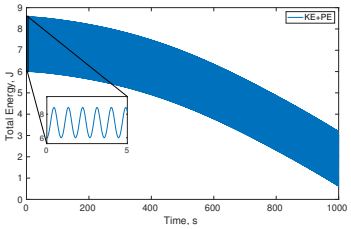

(a) Total energy of the system (RK4)

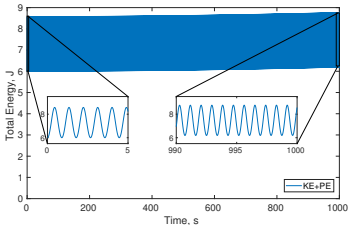

(b) Total energy of the system (ODE45)

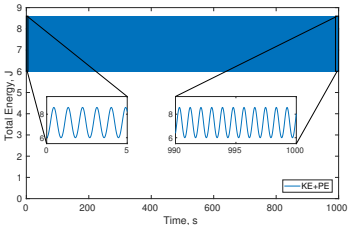

(c) Total energy of the system (VI)

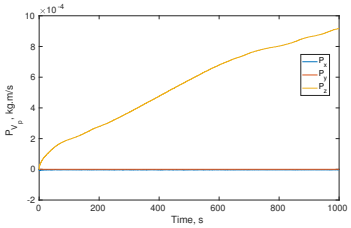

(d) Linear momenta of System (RK4)

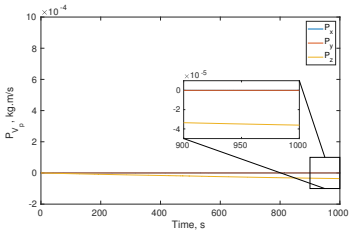

(e) Linear momenta of System (ODE45)

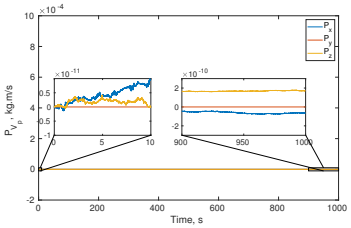

(f) Linear momenta of System (VI)

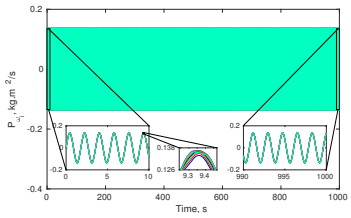

(g) Angular momenta of the cable links (RK4)

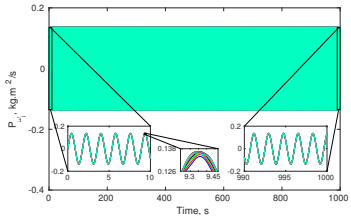

(h) Angular momenta of the cable links (ODE45)

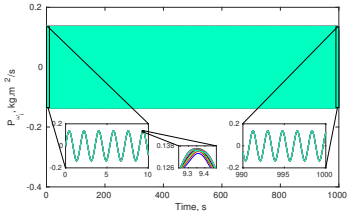

(i) Angular momenta of the cable links (VI)

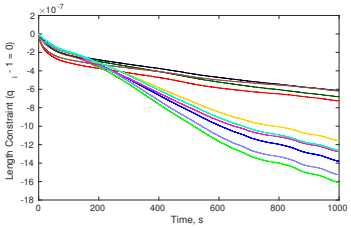

(j) Unit length constraints of the cable links (RK4)

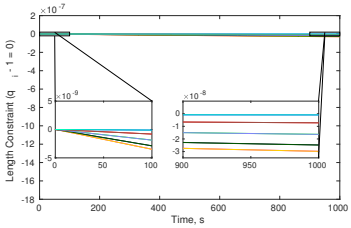

(k) Unit length constraints of the cable links (ODE45)

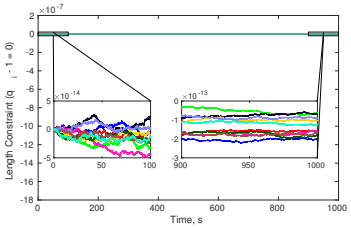

(l) Unit length constraints of the cable links (VI)

Figure 2.22: Comparison between the simulations by RK4, ODE45 and VI methods in terms of simulation accuracy for a single multi-rotor with a flexible cable suspended payload

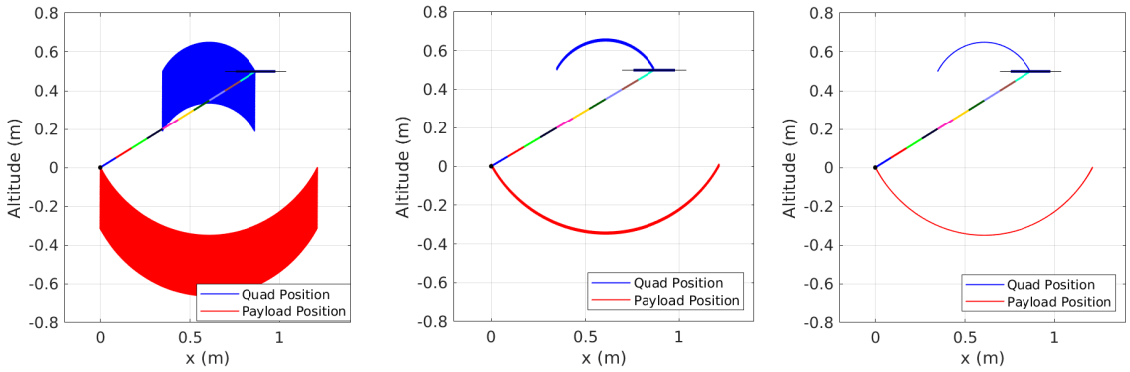

(a) Multi-rotor and payload trajectories (RK4)

(b) Multi-rotor and payload trajectories (ODE45)

(c) Multi-rotor and payload trajectories (VI)

Figure 2.23: Comparison between the simulated trajectories of the single multi-rotor with a flexible cable suspended payload system by RK4, ODE45 and VI integration methods

to undergo a stable oscillatory motion like a dumbbell due to the restoring moment around the center of gravity, which is resulting from the vertically applied force by the propellers. The time histories of the systems' total energies are plotted in Figures 2.22a-2.22c. Although the total energies follow a sinusoidal wave in all methods, as expected, an artificial change in system's total energy is noticed over time with the RK4 and ODE45 solutions, while the variational integrator successfully preserves the total energy over a thousand second without any sign of artificial variations.

Figures 2.22d-2.22f show the generalized linear momenta of the whole system during the motion. As the system rotates around the center of gravity, linear momenta should be preserved, which corresponds to zero linear momenta since the system initially starts from the rest. The VI method solution on the right graph displays the anticipated behavior with a relatively small numerical tolerance, whereas RK4 solution has a clear separation on the z component of the linear momentum from the origin. Similarly, the ODE45 solution demonstrates a constant drift apart from the numerical inaccuracy although it is significantly smaller than the deviation in RK4.

It can be inferred from these graphs that the conservation of linear momentum of the payload is achieved only in variational integrator solution. Likewise, the angular momenta of the cable links are plotted in Figures 2.22g-2.22i. In contrast to linear momenta results, the angular momenta of the links are preserved by each method along the expected trajectory due to the harmonic nature of total net torque on the system. Since the relative motion between the links are not substantial for the desired initial configuration of the system, the error in the angular motion is expected to be small.

Finally, Figures 2.22j-2.22l indicate how well the constraint of the constant cable length, which is enforced by the norm of the unit vectors, is satisfied over time. The deviation on the unit vector norm would also cause the warping on the configuration manifold, which is essentially what we see in the RK4 and ODE45 results. The consistent drift from the constraints affects the symplecticity and the other invariant properties on the system for the continuous-time model solution. The use of Lie group operations proves to be a substantial improvement for preserving the structure and constraints of the system as seen in VI method results, which seems to be affected by only the numerical truncation errors.

The resultant trajectories of multi-rotor and payload obtained from the simulations are plotted in Figure 2.23. Figure 2.23a evidently illustrates the effect of accumulation of the errors, especially in vertical position, over time on the simulated trajectories during the numerical integration process. The adaptive variable-step solution of ODE45 noticeably improves the solution in Figure 2.23b even though it does not eliminate the drift completely. Conversely, Figure 2.23c exhibits an achievement of a long-term stable response of the single multi-rotor with a flexible cable suspended payload system.

2.2.3.2 Simulation of a Cooperative Multi-Rotors with a Suspended Payload System via Flexible Cables

This example involves three multi-rotors cooperatively suspending a common payload via flexible cables as formulated in Section 2.1.3.1. The simulation scenario is extending the previous example for the three vehicles where each multi-rotor is 120 degree apart from the others and supports a common payload located at the origin initially as illustrated in Figure 2.24.

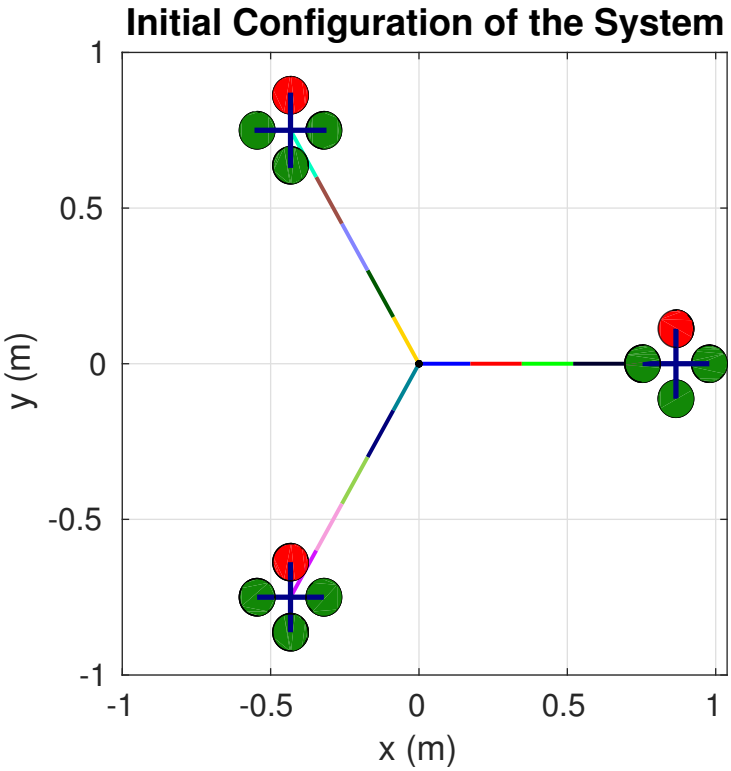

Figure 2.24: Initial configuration of the cooperative multi-rotors with a flexibly suspended payload

The parameters that are used in this simulation are identical to the previous example, except for the cable links. The continuous flexible cables of 1 meter in

length are represented with 5 links with a mass of 0.01 kg for each link. Similarly, the step-size of 0.001 second is chosen for both continuous time and discrete time solvers.

The expected behavior from the simulation of the cooperative system slightly differs from the results of the single multi-rotor and payload system. In this configuration, since the multi-rotors are evenly spread, the motion of the payload is constrained to the z axis only. Considering each multi-rotor and the corresponding suspension cable as an individual subsystem, one can see that each subsystem again has a dumbbell like oscillatory motion around the center of gravity of the whole system, which is a constant location on the z axis above the payload.

Remark 2.2.3. *It is worth noting here that due to the coupled constraints between the individual subsystems, the numerical inaccuracies of simulation is significantly amplified regardless of the integration method.*

Figure 2.26 presents the result of the simulation for the cooperative system. Figures on the left column correspond to the solution by RK4 integrator, where we see a quick divergent behavior after around 400 seconds. It can be deduced that for the given parameters and the configuration, the continuous-time model solution by RK4 does not preserve any of the system's invariants, which inherently yields inaccurate simulation results. In the middle column, the adaptive variable-step ODE45 solver slows down the rate of deviation from the actual states, but it cannot eliminate the main factor contributing the fast divergence since the continuous time equations of motion do not strongly enforce the constraint and structure preservation. However, the figures on the right column, corresponding to the Lie group VI method, demonstrates the predicted behavior for over a long time. Despite that the VI method also suffers from the chaotic nature of the model and the amplified numerical inaccuracies, it manages to maintain the acceptable level of accuracy on the preservation of total energy, the momentum and the constraints. It can also be inferred from these results

that one can minimize the artificial control command effort to mitigate the numerical errors introduced by the solver instabilities by just adopting a suitable numerical solver that complies with the physical properties and geometrical constraints of the actual system such as the family of variational integrators.

The payload trajectories plotted in Figure 2.25. Figure 2.25c clearly draws conclusion in favor of the VI method for the solution of cooperative multi-rotors with a flexibly suspended payload system. It is worth mentioning here that the considered simulations in this work are open-loop and uncontrolled free dynamics of the systems, and it is seen that the VI method minimizes the drifts on the constraints and overall invariants of the system, which makes it superior comparing to the other implemented solver methods. However, the most dynamic simulations are carried out with closed-loop feedback controls preventing large drifts from the desired states, yielding the stability and dampening to the system dynamics. Therefore, the accumulation of the errors due the deviations from the system invariants can be slowed down for the simulations with relatively shorther time periods by the RK4 and ODE45 methods, although the drifts are still present, and so, the complexities involved with designing a VI solver can be avoided while sacrificing the accuracy. Nevertheless, the simulations requiring stable energy behavior and the conservation of the system invariants over a long period should be carefully handled by putting enough attention on the selection of the numerical solver as well.

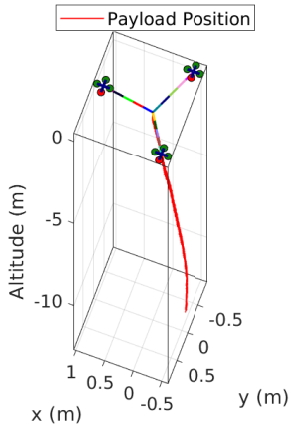

(a) Payload trajectory (RK4)

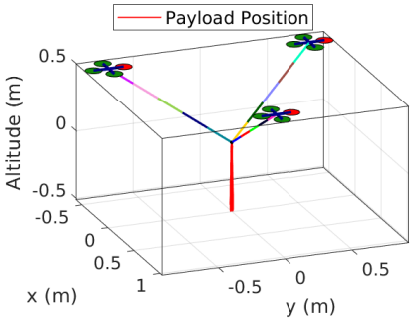

(b) Payload trajectory (ODE45)

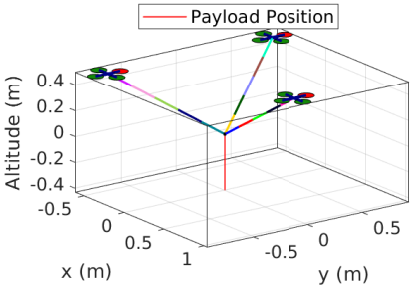

(c) Payload trajectory (VI)

Figure 2.25: Comparison between the simulated trajectories of the cooperative multi-rotors with a flexible cable suspended payload system by RK4, ODE45 and VI integration methods

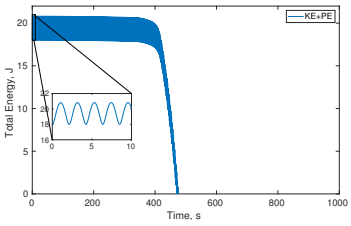

(a) Total energy of the system (RK4)

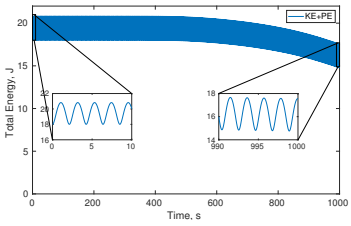

(b) Total energy of the system (ODE45)

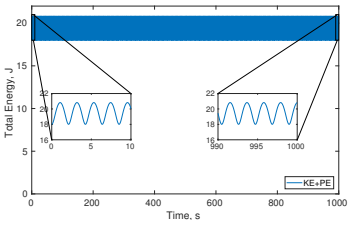

(c) Total energy of the system (VI)

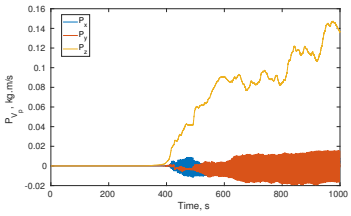

(d) Linear momenta of System (RK4)

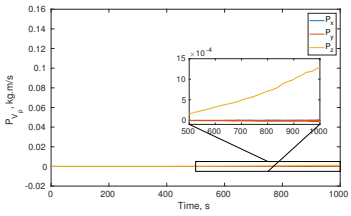

(e) Linear momenta of System (ODE45)

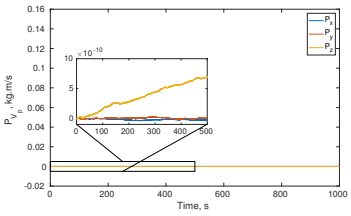

(f) Linear momenta of System (VI)

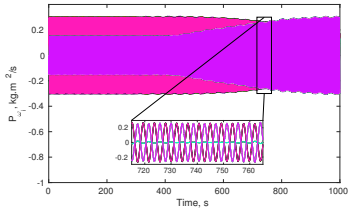

(g) Angular momenta of the cable links (RK4)

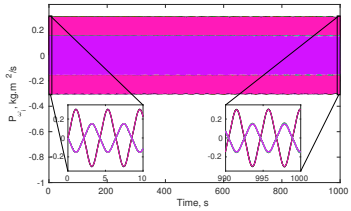

(h) Angular momenta of the cable links (ODE45)

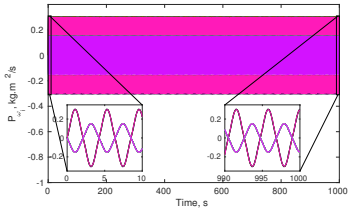

(i) Angular momenta of the cable links (VI)

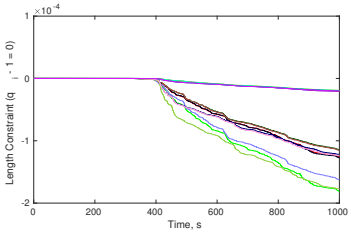

(j) Unit length constraints of the cable links (RK4)

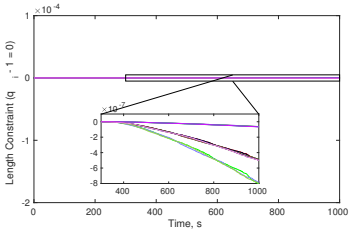

(k) Unit length constraints of the cable links (ODE45)

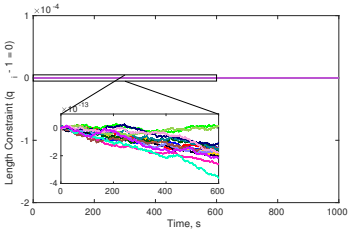

(l) Unit length constraints of the cable links (VI)

Figure 2.26: Comparison between the simulations by RK4 and VI methods in terms of simulation accuracy for three cooperative multi-rotors with a suspended payload via flexible cables

2.3 Chapter Summary

This chapter presented the mathematical modeling of aerial manipulation using suspended payloads with multi-rotor and airship systems. Initially, the chapter derived a flexible cable model consisting of serially attached rigid links with centered point loads. This model is then compared to the analytical formulation of catenary curves, focusing on the accuracy of tension distribution and cable shape representation. The findings reveal that with an increasing number of discrete links, the cable's shape and tension distribution asymptotically converge to the results obtained from the analytical catenary solution.

Subsequently, the chapter derived models for a suspended point load using a flexible cable, both for single and multiple multi-rotors, developed using the Euler-Lagrange approach. Additionally, a cooperative model involving multiple vehicles carrying a flexibly suspended rigid payload is introduced, applicable in cooperative aerial payload manipulation scenarios. This is followed by a detailed modeling of airship dynamics, including the acting forces, moments and their mathematical expressions, utilizing the Newton-Euler method.

The latter part of the chapter demonstrated the development of a momentum and structure-preserving Lie group variational integrator for the suspended load systems previously discussed. Simulations of these systems using common ODE solvers showed that overall momentum and energy states are not conserved, and slight deviations in geometric constraints lead to rapid divergent behaviors due to the complex and nonlinear nature of the system's configuration manifold. To address this, the variational integrator (VI) method, which ensures exact mapping of momentum states between consecutive time steps, was employed to enhance the long-term stability and accuracy of the simulations. Moreover, incorporating Lie group actions in the attitude dynamics of multi-rotors and cable segments achieved exact preservation of geomet-

ric constraints. The effectiveness of this approach is validated through comparative simulations, highlighting its superiority over other solvers in representative scenarios.

Chapter 3

Guidance and Control Law Design

3.1 Autonomous Control of Multi-rotor with a Flexible Cable Suspended Payload

In this section, linear and nonlinear control methods for a slung load system suspended via flexible cable under a multi-rotor are introduced, respectively.

3.1.1 Linear Control

This work addresses the attenuation of payload swing motion in a system where the payload is suspended by a flexible cable under a multi-rotor, using a game-theoretic approach. In this approach, the system is modeled as a two-player zero-sum game. Here, the impact of the cable and payload swing on the multi-rotor is considered a maximizing factor, while the multi-rotor's control strategy aims to minimize this effect, treating it as an external disturbance. The problem is represented as a linear quadratic (LQ) differential game, following the linearization of the system around a desired trajectory. An optimal control law, derived from this model, is tested in three different scenarios based on the available feedback regarding the cable and payload states to stabilize hovering.

The first scenario involves no feedback from the cable and payload states, representing a situation with minimal information. In the second scenario, the control strategy is based on the instantaneous knowledge of the payload's relative direction to the attachment point of the cable on the multi-rotor, which is utilized to approximate the cable as an imaginary single rigid link of constant length extended along this direction. Finally, to evaluate the effectiveness of these control methods under varying

levels of state feedback, a finite-time LQ controller with comprehensive state feedback, including all cable segments and payload states, is developed. This controller is implemented in the same simulation setup for baseline comparison.

For further analyses on the effect of cable state knowledge, the model derived in Section 2.1.2 is modified by utilizing the differential flatness property such that the payload states are written in terms of multi-rotor states. Figure 3.1 illustrates the modified system.

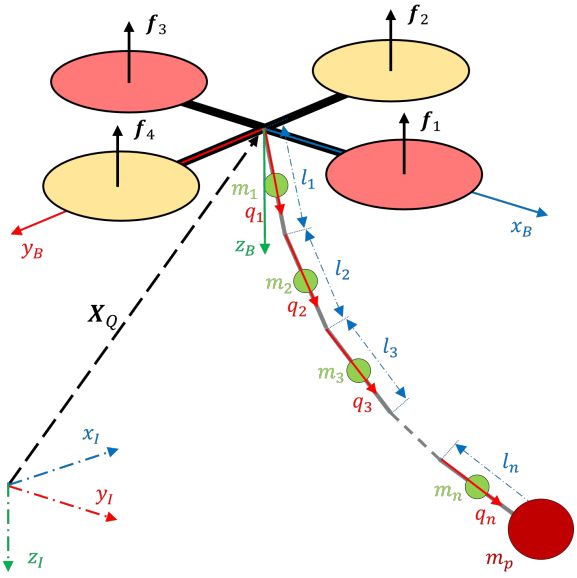

Figure 3.1: Illustration of a multi-rotor with a flexibly suspended point load

The position of the multi-rotor with respect to an inertial frame is denoted by $\boldsymbol{x}_Q \in \mathbb{R}^3$. Similarly, the position of the mass elements on each link and the payload itself are written in terms of the position of the multi-rotor and the unit directions along each link, respectively, as

$$\boldsymbol{x}_i = \boldsymbol{x}_Q + \sum_{j=1}^{i-1} l_j \boldsymbol{q}_j + \frac{1}{2} l_i \boldsymbol{q}_i$$

$$\boldsymbol{x}_P = \boldsymbol{x}_Q + \sum_{i=1}^{n} l_i \boldsymbol{q}_i$$

Complete equations of motion for the nonlinear model of the system are given below,

$$\dot{\boldsymbol{x}}_Q = \boldsymbol{v}_Q \tag{3.1}$$

$$\boldsymbol{M}_{00}\dot{\boldsymbol{v}}_Q - \sum_{i=1}^{n} \boldsymbol{M}_{0i}\hat{\boldsymbol{q}}_i\dot{\boldsymbol{\omega}}_i = \sum_{i=1}^{n} \boldsymbol{M}_{0i}(\boldsymbol{\omega}_i \cdot \boldsymbol{\omega}_i)\boldsymbol{q}_i + \boldsymbol{M}_{00} g \boldsymbol{e}_3 - f_B \boldsymbol{R}_Q \boldsymbol{e}_3 \tag{3.2}$$

$$\dot{\boldsymbol{R}}_Q = \boldsymbol{R}_Q \hat{\boldsymbol{\omega}}_Q \tag{3.3}$$

$$\boldsymbol{J}_Q \dot{\boldsymbol{\omega}}_Q + \hat{\boldsymbol{\omega}}_Q (\boldsymbol{J}_Q \boldsymbol{\omega}_Q) = \boldsymbol{\tau} \tag{3.4}$$

$$\dot{\boldsymbol{q}}_i = \boldsymbol{\omega}_i \times \boldsymbol{q}_i \tag{3.5}$$

$$\boldsymbol{M}_{ii}\dot{\boldsymbol{\omega}}_i = \boldsymbol{q}_i \times \left(\sum_{j=1(j\neq i)}^{n} (\boldsymbol{M}_{ij}(\boldsymbol{q}_j \times \dot{\boldsymbol{\omega}}_j) + (\boldsymbol{\omega}_j \cdot \boldsymbol{\omega}_j)\boldsymbol{M}_{ij}\boldsymbol{q}_j) + \boldsymbol{M}_{0i}\left(g\boldsymbol{e}_3 - \dot{\boldsymbol{v}}_Q\right) \right) \tag{3.6}$$

where $f_B \in \mathbb{R}^1$ and $\boldsymbol{\tau} = [\tau_x \ \tau_y \ \tau_z]^T \in \mathbb{R}^3$ are the thrust and moment inputs, respectively. The mass terms are redefined by

$$\boldsymbol{M}_{00} = \left(m_Q + \sum_{i=1}^{n} m_i + m_P \right) \boldsymbol{I}_3$$

$$\boldsymbol{M}_{0i} = \left(\frac{2(n-i)+1}{2} l m_i + l m_P \right) \boldsymbol{I}_3$$

$$\boldsymbol{M}_{ij} = \begin{cases} \left(\frac{4(n-i)+1}{4} l^2 m_i + l^2 m_P \right) \boldsymbol{I}_3, \text{ if } i = j \\ \left(\frac{2(n-a)+1}{2} l^2 m_i + l^2 m_P \right) \boldsymbol{I}_3, \text{ if } i \neq j, \quad (a = \max(i,j)) \end{cases}$$

3.1.1.1 Various Scenarios

Using Equations (3.1)-(3.6), the linear systems with respect to the available state feedback are constructed below.

3.1.1.1.1 Without Cable and Payload State Feedback

This scenario corresponds to situations where information about the cable and payload states is unavailable to the controller. Consequently, any impact on the multi-rotor is treated as an unknown external disturbance, with no further information into its dynamics.

The variations on multi-rotor states is obtained as follows,

$$\begin{aligned}
\delta\dot{\boldsymbol{x}}_Q &= \delta\boldsymbol{v}_Q \\
\boldsymbol{M}_{00}\delta\dot{\boldsymbol{v}}_Q &= f_{B_d}\boldsymbol{R}_{Q_d}\hat{\boldsymbol{e}}_3\boldsymbol{\eta}_Q - \boldsymbol{R}_{Q_d}\boldsymbol{e}_3\delta f_B + \delta\boldsymbol{f}_{w_Q} \\
\dot{\boldsymbol{\eta}}_Q &= \delta\boldsymbol{\omega}_Q - \hat{\boldsymbol{\omega}}_{Q_d}\boldsymbol{\eta}_Q \\
\boldsymbol{J}_Q\delta\dot{\boldsymbol{\omega}}_Q &= (\widehat{\boldsymbol{J}_Q\boldsymbol{\omega}_{Q_d}} - \hat{\boldsymbol{\omega}}_{Q_d}\boldsymbol{J}_Q)\delta\boldsymbol{\omega}_Q + \delta\boldsymbol{\tau}
\end{aligned}$$

where $\boldsymbol{\eta}_Q \in \mathbb{R}^3$ is an infinitesimal multi-rotor attitude error and $\boldsymbol{f}_{w_Q} \in \mathbb{R}^3$ is the external disturbance on the linear motion of the multi-rotor. Variables with the subscript d refer to the time-varying desired trajectory states.

These equations can be put in a linear matrix form as below,

$$\dot{\boldsymbol{s}}(t) = \boldsymbol{A}(t)\boldsymbol{s}(t) + \boldsymbol{B}_Q(t)\delta\boldsymbol{u}_Q(t) + \boldsymbol{B}_w(t)\delta\boldsymbol{u}_w(t)$$

where the linear states and the inputs are

$\boldsymbol{s} = [\delta\boldsymbol{x}_Q^T\ \delta\boldsymbol{v}_Q^T\ \boldsymbol{\eta}_Q^T\ \delta\boldsymbol{\omega}_Q^T]^T\ \in \mathbb{R}^{12}$

$\delta\boldsymbol{u}_Q = [\delta f_B\ \delta\boldsymbol{\tau}^T]^T\ \in \mathbb{R}^4$

$\delta\boldsymbol{u}_w = \delta\boldsymbol{f}_{w_Q}\ \in \mathbb{R}^3$

3.1.1.1.2 Only Relative Direction of the Payload

This scenario represents practical situations where only the relative direction of the payload is known in the cable and payload subsystem. Estimating the states of the

cable is challenging in real-world applications. However, the relative direction of the payload concerning the multi-rotor can be determined using various methods, such as downward-facing cameras, RFID object tracking, etc.

In this case, since the cable states are unknown, we utilize the known relative direction of the payload, attached at the one end of the cable, to make an approximation. It is assumed that an imaginary single link, with a length of L, oriented along the payload's relative direction can approximate the combined effect of the cable and payload dynamics on the system. The payload direction is defined as follows,

$$\boldsymbol{q}_P = \frac{\boldsymbol{x}_P - \boldsymbol{x}_Q}{||\boldsymbol{x}_P - \boldsymbol{x}_Q||}$$

The effects arising from cable and payload dynamics, which are not captured by this approximation, are assumed to be unknown external disturbances affecting both the multi-rotor and the dynamics of the imaginary link. The modified equations of motion, incorporating these assumptions, are presented below,

$$\boldsymbol{M}_{00}\left(\dot{\boldsymbol{v}}_Q - g\boldsymbol{e}_3\right) = \boldsymbol{M}_{01}^{*}\left(\hat{\boldsymbol{q}}_P\dot{\boldsymbol{\omega}}_P + (\boldsymbol{\omega}_P \cdot \boldsymbol{\omega}_P)\boldsymbol{q}_P\right) - f_B\boldsymbol{R}_Q\boldsymbol{e}_3 + \boldsymbol{f}_{w_Q}$$

$$\dot{\boldsymbol{q}}_P = \boldsymbol{\omega}_P \times \boldsymbol{q}_P$$

$$\boldsymbol{M}_{11}^{*}\dot{\boldsymbol{\omega}}_P = \boldsymbol{q}_P \times \boldsymbol{M}_{01}^{*}(g\boldsymbol{e}_3 - \dot{\boldsymbol{v}}_Q) + \boldsymbol{f}_{w_C}$$

where $\boldsymbol{\omega}_P$ represents the angular velocity of the imaginary link and the external disturbances on the multi-rotor and cable are defined by $\boldsymbol{f}_{w_Q} \in \mathbb{R}^3$ and $\boldsymbol{f}_{w_C} \in \mathbb{R}^3$, respectively. Also, the mass matrices are modified according to the single imaginary link assumption as

$$\boldsymbol{M}_{01}^{*} = \left(\frac{nm_iL}{2} + m_PL\right)\boldsymbol{I}_3 \quad , \quad \boldsymbol{M}_{11}^{*} = \left(\frac{nm_iL^2}{4} + m_PL^2\right)\boldsymbol{I}_3$$

Following the linearization procedure outlined in Refs. [5] and [35], variation on the equations of motion yields the following equations,

$$
\begin{aligned}
\delta\dot{\boldsymbol{x}}_Q &= \delta\boldsymbol{v}_Q \\
\boldsymbol{M}_{00}\delta\dot{\boldsymbol{v}}_Q &= \boldsymbol{M}_{01}^*\hat{\boldsymbol{q}}_{P_d}\delta\dot{\boldsymbol{\omega}}_P + \boldsymbol{M}_{01}^*\left(\hat{\dot{\boldsymbol{\omega}}}_{P_d}\hat{\boldsymbol{q}}_{P_d} - ||\boldsymbol{\omega}_{P_d}||^2\hat{\boldsymbol{q}}_{P_d}\right)\boldsymbol{\xi}_P \\
&\quad + 2\boldsymbol{M}_{01}^*\boldsymbol{q}_{P_d}\boldsymbol{\omega}_{P_d}^T\delta\boldsymbol{\omega}_P + f_{B_d}\boldsymbol{R}_{Q_d}\hat{\boldsymbol{e}}_3\boldsymbol{\eta}_Q - \boldsymbol{R}_{Q_d}\boldsymbol{e}_3\delta f_B + \delta\boldsymbol{f}_{w_Q} \\
\dot{\boldsymbol{\eta}}_Q &= \delta\boldsymbol{\omega}_Q - \hat{\boldsymbol{\omega}}_{Q_d}\boldsymbol{\eta}_Q \\
\boldsymbol{J}_Q\delta\dot{\boldsymbol{\omega}}_Q &= (\widehat{\boldsymbol{J}_Q\boldsymbol{\omega}_{Q_d}} - \hat{\boldsymbol{\omega}}_{Q_d}\boldsymbol{J}_Q)\delta\boldsymbol{\omega}_Q + \delta\boldsymbol{\tau} \\
\dot{\boldsymbol{\xi}}_P &= \left(\boldsymbol{q}_{P_d}\boldsymbol{q}_{P_d}^T\hat{\boldsymbol{\omega}}_{P_d}\right)\boldsymbol{\xi}_P + (\boldsymbol{I}_3 - \boldsymbol{q}_{P_d}\boldsymbol{q}_{P_d}^T)\delta\boldsymbol{\omega}_P \\
\boldsymbol{M}_{11}^*\delta\dot{\boldsymbol{\omega}}_P &= -\boldsymbol{M}_{01}^*\hat{\boldsymbol{q}}_{P_d}\left(\delta\dot{\boldsymbol{v}}_Q + \left(g\hat{\boldsymbol{e}}_3 - \hat{\dot{\boldsymbol{v}}}_{Q_d}\right)\boldsymbol{\xi}_P\right) + \delta\boldsymbol{f}_{w_C}
\end{aligned}
$$

The linear states and the inputs are reconstructed for this scenario as follows,

$$\boldsymbol{s} = [\delta\boldsymbol{x}_Q^T\ \delta\boldsymbol{v}_Q^T\ \boldsymbol{\eta}_Q^T\ \delta\boldsymbol{\omega}_Q^T\ \boldsymbol{\xi}_P^T\ \delta\boldsymbol{\omega}_P^T]^T\ \in \mathbb{R}^{18}$$

$$\delta\boldsymbol{u}_Q = [\delta f_B\ \delta\boldsymbol{\tau}^T]^T\ \in \mathbb{R}^4$$

$$\delta\boldsymbol{u}_w = [\delta\boldsymbol{f}_{w_Q}^T\ \delta\boldsymbol{f}_{w_C}^T]^T\ \in \mathbb{R}^6$$

3.1.1.1.3 Full State Feedback

Unlike the previous scenarios, this scenario deviates from the two-player differential game approach. It operates under the assumption that complete information, including cable and payload states, is known. This eliminates the need for the maximizing player in the game, allowing for the use of the same solution method without considering the disturbance. Consequently, this scenario provides a baseline performance for comparison with other scenarios, assuming full knowledge of the system states.

The linearized model of the complete system is provided below,

$$
\begin{aligned}
\delta\dot{\boldsymbol{x}}_Q &= \delta\boldsymbol{v}_Q \\
\boldsymbol{M}_{00}\delta\dot{\boldsymbol{v}}_Q &= \sum_{i=1}^{n}\boldsymbol{M}_{0i}\left(\hat{\boldsymbol{q}}_{i_d}\delta\dot{\boldsymbol{\omega}}_i + \left(\hat{\dot{\boldsymbol{\omega}}}_{i_d}\hat{\boldsymbol{q}}_{i_d} - ||\boldsymbol{\omega}_{i_d}||^2\hat{\boldsymbol{q}}_{i_d}\right)\boldsymbol{\xi}_i\right) + 2\sum_{i=1}^{n}\boldsymbol{M}_{0i}\boldsymbol{q}_{i_d}\boldsymbol{\omega}_{i_d}^T\delta\boldsymbol{\omega}_i \\
&\quad + f_{B_d}\boldsymbol{R}_{Q_d}\hat{\boldsymbol{e}}_3\boldsymbol{\eta}_Q - \boldsymbol{R}_{Q_d}\boldsymbol{e}_3\delta f_B \\
\dot{\boldsymbol{\eta}}_Q &= \delta\boldsymbol{\omega}_Q - \hat{\boldsymbol{\omega}}_{Q_d}\boldsymbol{\eta}_Q \\
\boldsymbol{J}_Q\delta\dot{\boldsymbol{\omega}}_Q &= (\widehat{\boldsymbol{J}_Q\boldsymbol{\omega}_{Q_d}} - \hat{\boldsymbol{\omega}}_{Q_d}\boldsymbol{J}_Q)\delta\boldsymbol{\omega}_Q + \delta\boldsymbol{\tau} \\
\dot{\boldsymbol{\xi}}_i &= \left(\boldsymbol{q}_{i_d}\boldsymbol{q}_{i_d}^T\hat{\boldsymbol{\omega}}_{i_d}\right)\boldsymbol{\xi}_i + (\boldsymbol{I}_3 - \boldsymbol{q}_{i_d}\boldsymbol{q}_{i_d}^T)\delta\boldsymbol{\omega}_i \\
\boldsymbol{M}_{ii}\delta\dot{\boldsymbol{\omega}}_i &= \hat{\boldsymbol{q}}_{i_d}\sum_{\substack{j=1\\(j\neq i)}}^{n}\hat{\boldsymbol{q}}_{j_d}\boldsymbol{M}_{ij}\delta\dot{\boldsymbol{\omega}}_j - \hat{\boldsymbol{q}}_{i_d}\boldsymbol{M}_{0i}\delta\dot{\boldsymbol{v}}_Q + \sum_{\substack{j=1\\(j\neq i)}}^{n}\left(\boldsymbol{M}_{ij}\widehat{\hat{\boldsymbol{q}}_{j_d}\dot{\boldsymbol{\omega}}_{j_d}} + \boldsymbol{\omega}_{j_d}^T\boldsymbol{\omega}_{j_d}\boldsymbol{M}_{ij}\hat{\boldsymbol{q}}_{j_d}\right)\hat{\boldsymbol{q}}_{i_d}\boldsymbol{\xi}_i \\
&\quad + \left(\boldsymbol{M}_{0i}\hat{\dot{\boldsymbol{v}}}_{Q_d} - \boldsymbol{M}_{0i}g\hat{\boldsymbol{e}}_3\right)\hat{\boldsymbol{q}}_{i_d}\boldsymbol{\xi}_i + \hat{\boldsymbol{q}}_{i_d}\sum_{\substack{j=1\\(j\neq i)}}^{n}\left(\boldsymbol{M}_{ij}\hat{\dot{\boldsymbol{\omega}}}_{j_d}\hat{\boldsymbol{q}}_{j_d} - \boldsymbol{M}_{ij}\boldsymbol{\omega}_{j_d}^T\boldsymbol{\omega}_{j_d}\hat{\boldsymbol{q}}_{j_d}\right)\boldsymbol{\xi}_j \\
&\quad + 2\hat{\boldsymbol{q}}_{i_d}\sum_{\substack{j=1\\(j\neq i)}}^{n}\boldsymbol{M}_{ij}\boldsymbol{q}_{j_d}\boldsymbol{\omega}_{j_d}^T\delta\boldsymbol{\omega}_j
\end{aligned}
$$

where the linear state and the inputs are

$$\boldsymbol{s} = [\delta\boldsymbol{x}_Q^T\ \delta\boldsymbol{v}_Q^T\ \boldsymbol{\eta}_Q^T\ \delta\boldsymbol{\omega}_Q^T\ \bar{\boldsymbol{\xi}}^T\ \delta\bar{\boldsymbol{\omega}}^T]^T\ \in \mathbb{R}^{12+6n}$$

$$\delta\boldsymbol{u}_Q = [\delta f_B\ \delta\boldsymbol{\tau}^T]^T\ \in \mathbb{R}^4$$

$$\bar{\boldsymbol{\xi}} = [\boldsymbol{\xi}_1^T\ \boldsymbol{\xi}_2^T\ ...\ \boldsymbol{\xi}_n^T]^T\ \in \mathbb{R}^{3n}$$

$$\delta\bar{\boldsymbol{\omega}} = [\delta\boldsymbol{\omega}_1^T\ \delta\boldsymbol{\omega}_2^T\ ...\ \delta\boldsymbol{\omega}_n^T]^T\ \in \mathbb{R}^{3n}$$

Linear error states for the scenarios are computed as follows, [35],

$$\begin{aligned}
\delta \boldsymbol{x}_Q &= \boldsymbol{x}_Q - \boldsymbol{x}_{Q_d} \\
\delta \boldsymbol{v}_Q &= \boldsymbol{v}_Q - \boldsymbol{v}_{Q_d} \\
\boldsymbol{\eta}_Q \approx \boldsymbol{e}_{\boldsymbol{R}_Q} &= \frac{1}{2}(\boldsymbol{R}_{Q_d}^T \boldsymbol{R}_Q - \boldsymbol{R}_Q^T \boldsymbol{R}_{Q_d})^\vee \\
\delta \boldsymbol{\omega}_Q \approx \boldsymbol{e}_{\boldsymbol{\omega}_Q} &= \boldsymbol{\omega}_Q - (\boldsymbol{R}_Q^T \boldsymbol{R}_{Q_d})\boldsymbol{\omega}_{Q_d} \\
\boldsymbol{\xi}_i \approx \boldsymbol{e}_{\boldsymbol{q}} &= \hat{\boldsymbol{q}}_{i_d} \boldsymbol{q}_i \\
\delta \boldsymbol{\omega}_i \approx \boldsymbol{e}_{\boldsymbol{\omega}_i} &= \boldsymbol{\omega}_i + (\hat{\boldsymbol{q}}_i^2)\boldsymbol{\omega}_{i_d}
\end{aligned}$$

In addition, the configuration error between the desired and actual attitude of the multi-rotor is given by

$$\psi_{\boldsymbol{R}} = \text{trace}(\boldsymbol{I}_3 - \boldsymbol{R}_{Q_d}^T \boldsymbol{R}_Q)/2$$

3.1.1.2 Controller Design

The cost function for the differential game is given in a quadratic form by

$$\begin{aligned}
C = &\frac{1}{2}\boldsymbol{s}(t_f)^T \boldsymbol{Q_f} \boldsymbol{s}(t_f) \\
&+ \frac{1}{2}\int_0^{t_f} \left[\boldsymbol{s}(t)^T \boldsymbol{Q} \boldsymbol{s}(t) + \delta \boldsymbol{u}_Q^T \boldsymbol{R_Q} \delta \boldsymbol{u}_Q - \gamma^2 \delta \boldsymbol{u}_w^T \boldsymbol{R_w} \delta \boldsymbol{u}_w\right] dt
\end{aligned}$$

where $\boldsymbol{Q_f}$ and $\boldsymbol{Q}$ are positive semi-definite symmetric weighting matrices corresponding to the error states, $\boldsymbol{s}(t)$, at the final time, t_f, and along the trajectory, respectively. $\boldsymbol{R_Q}$ and $\boldsymbol{R_w}$ are positive definite symmetric weighting matrices for the multi-rotor control inputs and disturbance force caused by the swing motion of the cable and payload along the trajectory, respectively. Moreover, γ represents the relative ratio between $\delta \boldsymbol{u}_Q$ and $\delta \boldsymbol{u}_w$.

Hamiltonian of the derived game is obtain as below,

$$H = \frac{1}{2}\left[\boldsymbol{s}^T\boldsymbol{Q}\boldsymbol{s} + \delta\boldsymbol{u}_Q^T\boldsymbol{R}_{\boldsymbol{Q}}\delta\boldsymbol{u}_Q - \gamma^2\delta\boldsymbol{u}_w^T\boldsymbol{R}_{\boldsymbol{w}}\delta\boldsymbol{u}_w\right] + \boldsymbol{\lambda}^T\left(\boldsymbol{A}\boldsymbol{s} + \boldsymbol{B}_Q\delta\boldsymbol{u}_Q + \boldsymbol{B}_w\delta\boldsymbol{u}_w\right)$$

where $\boldsymbol{\lambda}$ is the Lagrange multipliers for the satisfaction of the dynamical constraints.

In this work, there is no limit enforced on the player inputs. Therefore, the stationarity condition for the optimality can be found directly by differentiating the Hamiltonian with respect to the corresponding input variables as follows.

Optimal control input for the multi-rotor, $\delta\boldsymbol{u}_Q^*$,

$$\frac{\partial H}{\partial \delta\boldsymbol{u}_Q} = 0 = \boldsymbol{R}_{\boldsymbol{Q}}\delta\boldsymbol{u}_Q + \boldsymbol{B}_Q^T\boldsymbol{\lambda}(t)$$
$$\delta\boldsymbol{u}_Q^* = -\boldsymbol{R}_{\boldsymbol{Q}}^{-1}\boldsymbol{B}_Q^T\boldsymbol{\lambda}(t) \tag{3.7}$$

Similarly, the optimal disturbance maximizing the cost, $\delta\boldsymbol{u}_w^*$,

$$\frac{\partial H}{\partial \delta\boldsymbol{u}_w} = 0 = -\gamma^2\boldsymbol{R}_{\boldsymbol{w}}\delta\boldsymbol{u}_w + \boldsymbol{B}_w^T\boldsymbol{\lambda}(t)$$
$$\delta\boldsymbol{u}_w^* = \frac{1}{\gamma^2}\boldsymbol{R}_{\boldsymbol{w}}^{-1}\boldsymbol{B}_w^T\boldsymbol{\lambda}(t) \tag{3.8}$$

From the necessary conditions of optimality, the co-state equation is obtained by

$$-\frac{\partial H}{\partial \boldsymbol{s}} = \dot{\boldsymbol{\lambda}} = -\boldsymbol{Q}\boldsymbol{s} - \boldsymbol{A}^T\boldsymbol{\lambda} \tag{3.9}$$

Assuming that the co-state equation has a linear relation with the states in the form of $\boldsymbol{\lambda}(t) = \boldsymbol{P}(t)\boldsymbol{s}(t)$ with a time varying matrix $\boldsymbol{P}(t)$ and the boundary condition of $\boldsymbol{P}(t_f) = \boldsymbol{Q}_{\boldsymbol{f}}$, which is derived from the cost function. Differentiating

$\boldsymbol{\lambda}$ and equating it to Equation (3.9), the differential Riccati equation providing the optimal solution to the given problem is derived.

$$\begin{aligned}\dot{\boldsymbol{\lambda}} &= \dot{\boldsymbol{P}}\boldsymbol{s} + \boldsymbol{P}\dot{\boldsymbol{s}} \\ &= \dot{\boldsymbol{P}}\boldsymbol{s} + \boldsymbol{P}\left(\boldsymbol{A}\boldsymbol{s} + \boldsymbol{B}_Q\delta\boldsymbol{u}_Q + \boldsymbol{B}_w\delta\boldsymbol{u}_w\right) \\ &= -\boldsymbol{Q}\boldsymbol{s} - \boldsymbol{A}^T(\boldsymbol{P}\boldsymbol{s})\end{aligned}$$

Substituting the optimal control inputs for both players from Equations (3.7)-(3.8) and arranging the terms,

$$-\dot{\boldsymbol{P}} = \boldsymbol{A}^T\boldsymbol{P} + \boldsymbol{P}\boldsymbol{A} - \boldsymbol{P}\boldsymbol{B}_Q\boldsymbol{R}_{\boldsymbol{Q}}^{-1}\boldsymbol{B}_Q^T\boldsymbol{P} + \frac{1}{\gamma^2}\boldsymbol{P}\boldsymbol{B}_w\boldsymbol{R}_{\boldsymbol{w}}^{-1}\boldsymbol{B}_w^T\boldsymbol{P} + \boldsymbol{Q} \tag{3.10}$$

$$\boldsymbol{P}(t_f) = \boldsymbol{Q}_{\boldsymbol{f}}$$

Differential Riccati equation given in Equations (3.10) is solved backward in time starting from time t_f, and the solution of $\boldsymbol{P}$ matrices along time instances are saved as a multi-dimensional array. Using $\boldsymbol{P}(t)$, the control input of the multi-rotor is found for each time segment and applied to the actual non-linear system to simulate the response. Since the disturbance is not controlled by any means, the game essentially has only one active player playing its strategy optimally, which results in a behavior favoring the minimizing player while reducing the disturbance effect. Control input attenuating the swing motion caused by the flexible cable suspended payload for the linear system is found to be

$$\begin{bmatrix}\delta f_B \\ \delta\boldsymbol{\tau}\end{bmatrix} = -\boldsymbol{R}_{\boldsymbol{Q}}^{-1}\boldsymbol{B}_Q^T\boldsymbol{P}(t)\boldsymbol{s}(t) \tag{3.11}$$

The required change in the control inputs of the multi-rotor providing a stable tracking response for the linearized system is found in Equation (3.11). Total input applied to the system is given by

$$f_B = f_{B_d} + \delta f_B$$

$$\boldsymbol{\tau} = \boldsymbol{\tau}_d + \delta \boldsymbol{\tau}$$

3.1.1.3 Simulation Results

In this section, the simulation of derived swing attenuating controller is demonstrated for the hover stabilization of the multi-rotor with a 10-link cable suspended payload considering the scenarios described previously.

3.1.1.3.1 Simulation Parameters

System Parameters: Physical parameters of the multi-rotor with N-link flexible cable suspended system is provided below

$$n = 10,\ l = 0.1 \text{ m},\ m_Q = 1.2 \text{ kg},\ m_i = 0.01 \text{ kg},$$

$$m_P = 0.3 \text{ kg},\ \boldsymbol{J}_Q = \text{diag}([1.367e-2, 1.367e-2, 2.586e-2])$$

Motor Dynamics: A first order dynamics with the time constant of 0.005 second is implemented to model the actuator dynamics on rotors.

Control allocation matrix is given below

$$\begin{bmatrix} f_B \\ \boldsymbol{\tau} \end{bmatrix} = \begin{bmatrix} 1 & 1 & 1 & 1 \\ 0 & L & 0 & -L \\ -L & 0 & L & 0 \\ k_M & -k_M & k_M & -k_M \end{bmatrix} \begin{bmatrix} f_1 \\ f_2 \\ f_3 \\ f_4 \end{bmatrix} \tag{3.12}$$

where the force and moment due to the rotational speed of an individual rotor, Ω_{M_i}, are calculated by the following equations

$$f_i = k_F \Omega_{M_i}^2 \boldsymbol{\tau}_z = k_M f_i \tag{3.13}$$

where k_F and k_M represent the coefficients relating the rotor speed to the force and moment, respectively.

$$k_F = 9.12 \times 10^{-6} \frac{N}{rad^2},\ k_M = 10^{-2} m,\ L = 0.3m$$

L is the arm length of the multi-rotor in this work. These coefficients are chosen to provide maximum thrust of 10 Newtons for each motor with full rotational speed of 10000 rpm.

Trajectory: The desired trajectory for the hover condition is defined by the following states

$$\boldsymbol{x}_{Q_d} = \boldsymbol{v}_{Q_d} = \dot{\boldsymbol{v}}_{Q_d} = \boldsymbol{\omega}_{Q_d} = [0\ 0\ 0]^T, \boldsymbol{R}_{Q_d} = \boldsymbol{I}_3,$$

$$\boldsymbol{q}_{i_d} = \boldsymbol{e}_3,\ \boldsymbol{\omega}_{i_d} = \dot{\boldsymbol{\omega}}_{i_d} = [0\ 0\ 0]^T \ \text{ for } i = 1, .., n, p$$

$$f_{B_d} = (m_Q + m_P + n m_i) g,\ \boldsymbol{\tau}_d = [0\ 0\ 0]^T$$

Cost Function: Below weighting matrices and parameters are used in the cost function of the scenarios.

The common matrices and parameters among the scenarios are as follows,

$$\boldsymbol{Q_Q} = \text{blckdiag}([100\boldsymbol{I}_3,\ 25\boldsymbol{I}_3,\ 40\boldsymbol{I}_3,\ 5\boldsymbol{I}_3])$$

$$\boldsymbol{Q_{fQ}} = \text{blckdiag}([100\boldsymbol{I}_3,\ 50\boldsymbol{I}_3,\ 50\boldsymbol{I}_3,\ 50\boldsymbol{I}_3]),$$

$$\boldsymbol{R_Q} = \boldsymbol{I}_4,\ \gamma = 1.5,\ t_f = 5\text{sec}$$

where $\boldsymbol{Q_Q}$ and $\boldsymbol{Q_{fQ}}$ represents the error state weighting of the multi-rotor states for the running cost and the terminal cost, respectively.

The cost matrices regarding the cable attitude and angular velocity are provided below for the corresponding scenarios.

For the scenario with full state knowledge:

$$\boldsymbol{Q_{f_{q_i}}} = 100\boldsymbol{I}_3,\ \boldsymbol{Q_{f_{\omega_i}}} = \boldsymbol{I}_3$$
$$\boldsymbol{Q_{q_i}} = 5\boldsymbol{I}_3,\ \boldsymbol{Q_{\omega_i}} = 0.05\boldsymbol{I}_3$$

For the scenario with only relative orientation of the payload is known:

$$\boldsymbol{Q_{f_{qp}}} = 10\boldsymbol{I}_3,\ \boldsymbol{Q_{f_{\omega_p}}} = 10\boldsymbol{I}_3$$
$$\boldsymbol{Q_{q_p}} = 5\boldsymbol{I}_3,\ \boldsymbol{Q_{\omega_p}} = 5\boldsymbol{I}_3$$

Initial Condition: Initially, the system starts from the rest with a given initial deflection of the cable as shown in Figure 3.2.

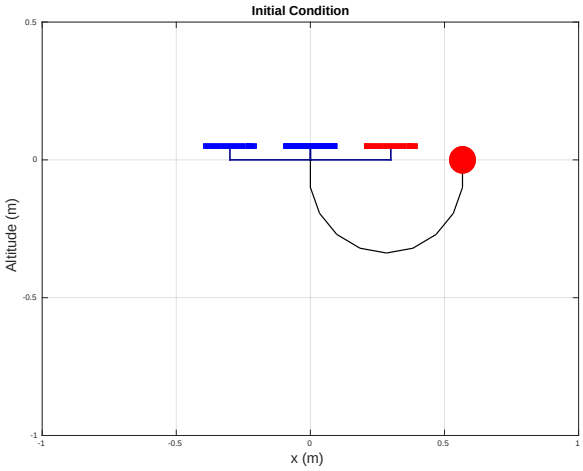

Figure 3.2: Initial condition of the multi-rotor and suspension cable

3.1.1.3.2 Comparison Metrics

In order to compare the performance of swing attenuation and control strategies implemented on the scenarios, we have constructed various comparison metrics. The first metric is designed to provide information on the transient response of the cable segments during the control maneuver where the root mean square (RMS) of cable segment attitude error from the desired configuration is utilized as follows,

$$C_{\boldsymbol{\xi}}(t) = \sqrt{\frac{1}{n}\sum_{i=1}^{n} ||\boldsymbol{\xi}_i(t)||^2}$$

Additionally, a cumulative metric accounting for cable segment attitude error along the duration of motion is introduced by

$$C_{\int \boldsymbol{\xi}} = \int_0^{t_f} C_{\boldsymbol{\xi}}(t)dt$$

which provides a scalar value for clearer comparison.

On the other hand, instantaneous and cumulative control effort during the stabilization are also considered in comparison. The following metric, employing RMS of instantaneous rotor speed, gives an insight on the control history of the multi-rotor during the stabilization.

$$C_{\Omega_M}(t) = \sqrt{\frac{1}{4}\sum_{i=1}^{4} ||\Omega_{M_i}(t)||^2}$$

Moreover, a cumulative metric is constructed to quantify the additional effort required to reach out the desired configuration from the given initial condition employing the integration of absolute difference between the nominal desired and RMS of instantaneous rotor speed, which is provided below,

$$C_{\int \Omega_M} = \int_0^{t_f} \|\Omega_{\bar{M}} - C_{\Omega_M}(t)\|\, dt$$

where $\Omega_{\bar{M}}$ is the average value of rotor speed in desired multi-rotor configuration during hover.

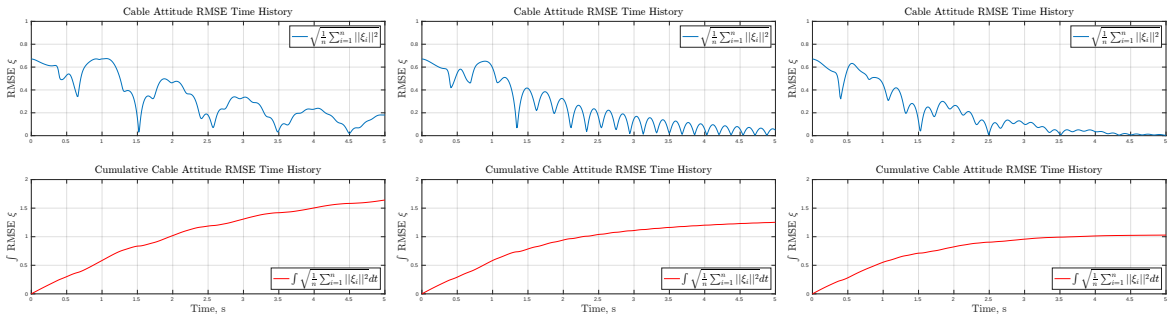

(a) Scenario 1 (b) Scenario 2 (c) Scenario 3

Figure 3.3: Time history plots of root mean square of cable attitude error the stable hover condition and the cumulative sum of the error in time for the simulated scenarios.

3.1.1.3.3 Results and Discussion

The simulation results for each scenario and their comparisons are provided in this section.

Swing Attenuation Comparison: Time history plots of transient and cumulative cable segment attitude errors for each scenario are illustrated in Figure 3.3.

Considering the transient responses, the oscillations due to inter-link interactions and overall exponential decay with varying speeds in cable attitude error can be clearly observed. As expected, the first scenario without any knowledge on the cable states has the slowest damped behavior and the longest oscillation periods for overall cable swing since it is not explicitly accounted for. However, the attenuation of an imaginary rigid link in the second scenario significantly improves the overall decay speed although the inter-link oscillations continue even after the imaginary link settles in the desired configuration. This result is also expected because the imaginary link assumption can only partially capture the effect of actual flexible cable shape. Finally, the third scenario, where the full cable state feedback is utilized in

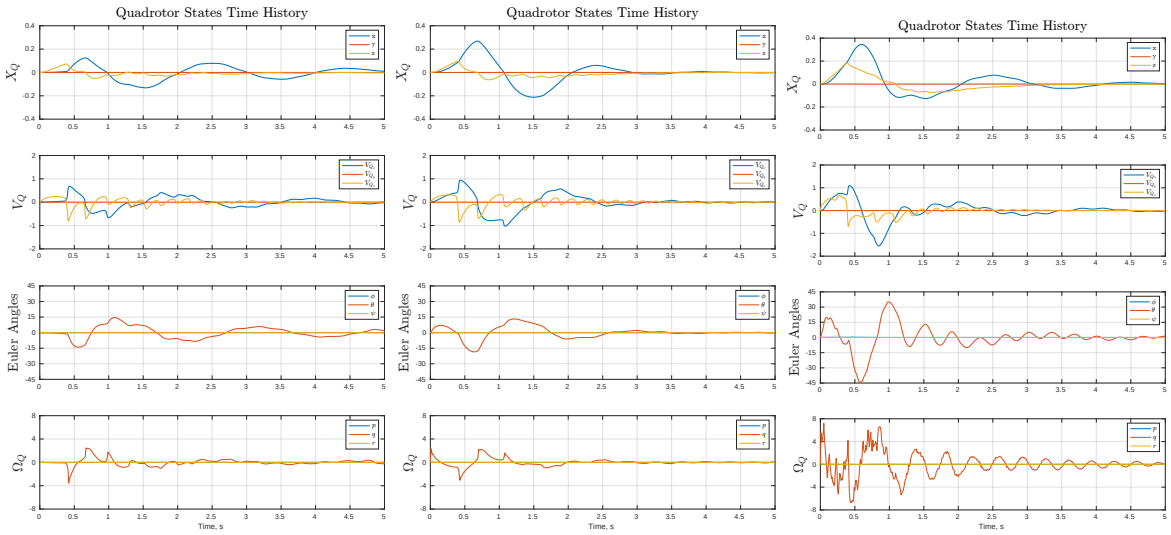

(a) Scenario 1 (b) Scenario 2 (c) Scenario 3

Figure 3.4: Time history plots of multi-rotor states for the simulated scenarios.

the control strategy, outperforms the previous scenario by improving the mitigation of overall cable attitude and inter-link oscillations. The cumulative cable segment attitude error plots for each scenario under the transient response plots demonstrate individual performances where the lower final value corresponds a better attenuation characteristic overall.

Multi-rotor States and Control Comparison: Time histories of multi-rotor states are plotted for the scenarios in Figure 3.4.

Comparing the vehicles states, it can be seen that the first scenario corresponding no cable information during the control yields the least damped oscillatory behavior with lowest peak values in multi-rotor motion. Since the cable itself behaves similar to a perturbed pendulum, the swing motion introduces a periodic disturbance on the multi-rotor, which cannot be effectively accounted for by control strategy in the absence of any cable information. Therefore, the multi-rotor only compensates error in the vehicle hover configuration without an explicit cable swing attenuation

effort. However, the second scenario, involving explicit swing attenuation of a single imaginary link, improves the decay in vehicle state oscillations considerably despite a larger initial response comparing the first scenario. Finally, although the last scenario shows a similar damped response with the second scenario, the response to the oscillations between cable segments are obvious in the multi-rotor attitude. This means that any slight error from desired cable attitude configurations is actively compensated in this scenario, and thus, the response is less smooth and takes longer to settle than the one in the second scenario.

Figure 3.5 illustrates the time history plots of root mean square of multi-rotor rotor speeds and cumulative sum of absolute difference between rotor speed RMS value and desired value for hover, which is shown with dashed black lines in the figures. Plots indicate the instantaneous and cumulative effort to bring the multi-rotor and suspended payload system into the desired hover configuration. Comparing the RMS rotor speed plots in the first and second scenario, even though they have similar trends, the latter case is observed to have less rotor speed deviation from the hover condition, which is also quantified by the cumulative plots. According to these two plots, it can be inferred that the amount of additional effort required to bring the system into the desired configuration is less for the second scenario. On the other hand, the last scenario demonstrates significantly larger spikes for the first 0.5 seconds where the cable attitude error is the largest at and it accumulates more control effort initially. However, after the initial correction phase, the remaining section displays a quickly diminishing additional effort and it settles down almost completely after 3 seconds. Despite the initial agile corrections, the overall cumulative additional control effort spent for the last scenario is the least among the other scenario results, which is expected due to the full knowledge of the system states. Nevertheless, the difference

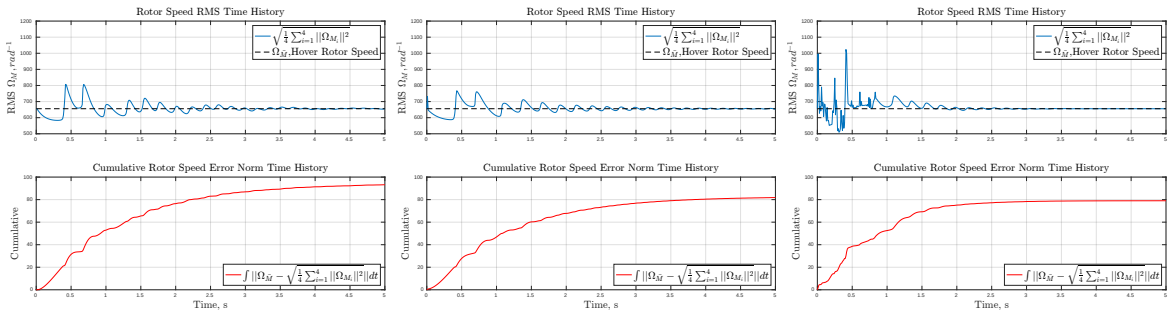

(a) Scenario 1 (b) Scenario 2 (c) Scenario 3

Figure 3.5: Time history plots of root mean square of rotor speeds multi-rotor experienced and the cumulative sum of absolute difference from the desired rotor speed for the simulated scenarios.

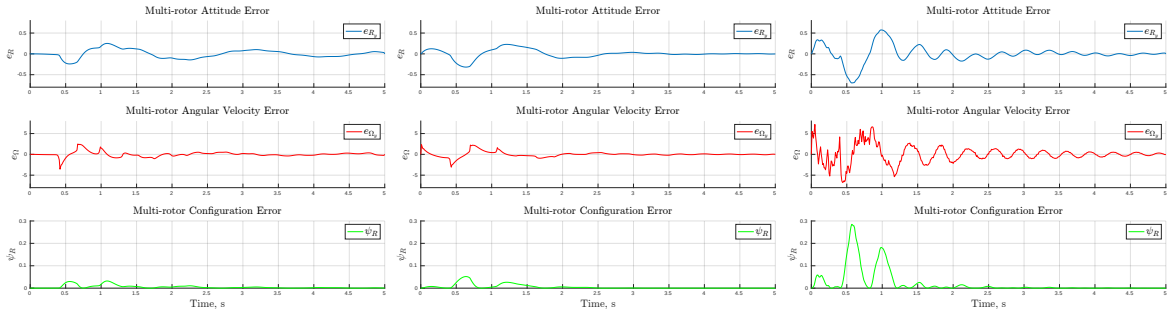

(a) Scenario 1 (b) Scenario 2 (c) Scenario 3

Figure 3.6: Time history plots of multi-rotor attitude error, angular velocity error, and configuration error from the hover condition for the simulated scenarios.

in the final cumulative result between the second and third scenarios is comparable and it should be noted for the further discussion.

Finally, Figure 3.6 presents the errors in multi-rotor attitude, angular velocity, and configuration from the desired values for each scenario. In these plots, it is seen that as the information about cable and payload dynamics increases, the multi-rotor deviates more from the desired configuration transiently to compensate cable configuration errors.

Alongside with the implementation of game theoretic approach on the swing attenuation of multi-rotor with suspended payload system, this work aimed to in-

vestigate the effectiveness of incorporating either full or partial knowledge about the suspension cable and payload subsystem in control synthesis with specifically constructed scenarios. The scenarios with no information and full state information on the cable are expected to constitute the lower and upper end in the performance comparisons, respectively, while the scenario with single imaginary link assumption is designed to provide a more effective solution than the first scenario and practically applicable approach comparing the full cable state feedback scenario.

The results from these scenarios also follow the expectations from constructed strategies. In the first scenario, the control effort for multi-rotor to stay in the hover condition is not able to mitigate the swing motion as effective as the other scenarios as expected from the worst case response since no information about either cable or payload dynamics is known. In fact, the compensation of unknown disturbance for the multi-rotor can produce additional excitation on the cable and payload, which could result in unstable behavior. Yet, with a simple but practical assumption where the relative direction information of the payload is known, the attenuation of an instantaneous imaginary rigid cable link demonstrated a considerable improvement in the stabilization performance. Lastly, the final scenario illustrated how much more the full system knowledge can be benefited for this task, and it established a performance level that we qualitatively and quantitatively used to compare the results against.

3.1.2 Nonlinear Control

In this section, a nonlinear geometric control approach is developed to stabilize the system and ensure smooth tracking of the desired payload trajectory. This approach integrates a catenary-informed guidance strategy. Additionally, insights from the linear control analysis are utilized, particularly the concept of approximating the actual flexible cable with an imaginary single rigid cable, to enhance the system's oscillation damping characteristics.

The geometric control method, as presented in Ref. [13], is modified and adapted in this work. This adaptation incorporates both the flexible cable model and catenary analysis discussed in previous sections. The specific system model applied in this approach is detailed in Section 2.1.2. The sequential steps followed in this control approach are outlined below,

1. **Desired Payload Acceleration Determination:** The desired payload acceleration (net force) is calculated based on the given trajectory and the current state of the payload.
2. **Catenary Analysis for Commanded Tension Force:** Using the desired payload acceleration, catenary analysis is employed to determine the commanded tension force at the cable's multi-rotor side end-point. This also corresponds to the desired position of the multi-rotor relative to the payload's instantaneous location.
3. **Assumption of a Virtual Rigid Link:** To adequately capture transient cable dynamics, a virtual rigid link is assumed between the payload's instantaneous position and the multi-rotor. This assumption aids in improving the damping of cable oscillations. The unit vector along this virtual link, as illustrated in Figure 3.7, and the instantaneous angular velocity are continuously estimated.

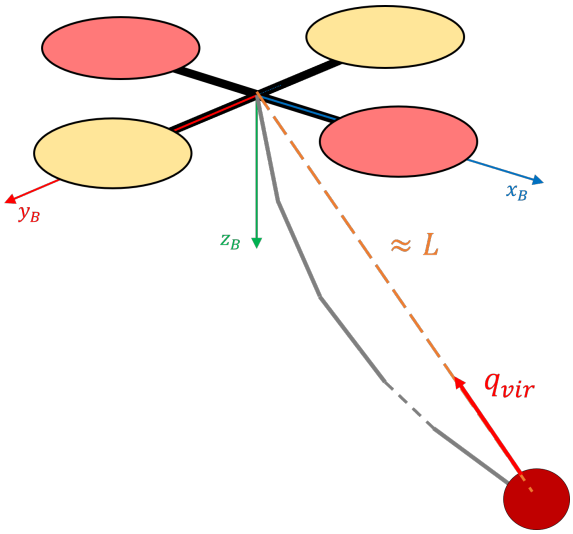

Figure 3.7: Illustration of the virtual rigid link cable connecting multi-rotor to the payload

4. **Calculation of Corrective Force Components:** The necessary orthogonal and parallel force components to be applied at the link's vehicle side end-point are calculated based on the error between the current virtual link and the commanded cable attitude. This calculation considers the payload and cable system as a whole.
5. **Implementation of Geometric Control Approach:** With the desired tension force determined, which provides the necessary payload acceleration, and the corrective forces ensuring cable attitude control, as well as the catenary-guided reference for vehicle relative position and payload trajectory, a geometric control approach is implemented for the attitude and trajectory tracking control of the multi-rotor.

The force required to provide the necessary acceleration for payload to track the specified trajectory can be found by

$$\boldsymbol{\mu}_d = -\boldsymbol{K}_{\boldsymbol{x}_P}\boldsymbol{e}_{\boldsymbol{x}_P} - \boldsymbol{K}_{\boldsymbol{v}_P}\boldsymbol{e}_{\boldsymbol{v}_P} + m_P\left(\dot{\boldsymbol{v}}_{P_d} - g\boldsymbol{e}_3\right) \tag{3.14}$$

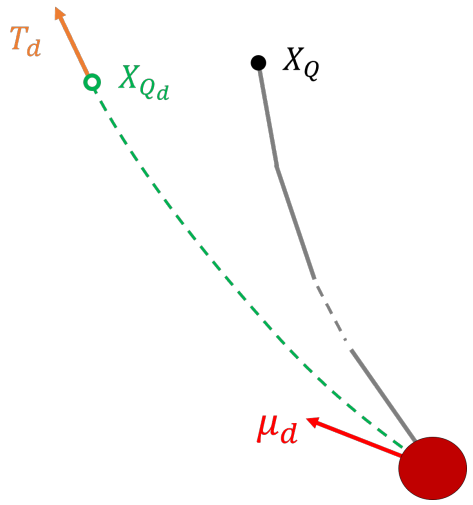

Figure 3.8: Illustration of the desired catenary shape and cable tension computed from desired force vector

where $\boldsymbol{K}_{\boldsymbol{x}_P}$ and $\boldsymbol{K}_{\boldsymbol{v}_P}$ are feedback gains for the payload position and velocity errors, which are defined as follows,

$$\boldsymbol{e}_{\boldsymbol{x}_P} = \boldsymbol{x}_P - \boldsymbol{x}_{P_d}$$

$$\boldsymbol{e}_{\boldsymbol{v}_P} = \boldsymbol{v}_P - \boldsymbol{v}_{P_d}$$

After obtaining the desired force vector $\boldsymbol{\mu}_d$ for the payload, catenary analysis, introduced in Section 2.1.1.1, is employed to acquire the end-point cable tension and desired catenary shape to sustain the calculated force, which also yields the desired position of the multi-rotor. Figure 3.8 illustrates the required catenary shape to realize the desired payload acceleration.

The virtual link states can be estimated using derivative filters provided that the instantaneous relative position or unit vector along that vector is available. In this work, a second order critically damped filter is utilized to estimate virtual link states, $\boldsymbol{q}_{vir}$ and $\dot{\boldsymbol{q}}_{vir}$. $\boldsymbol{q}_{vir}$ is the unit vector along the virtual link pointing towards

the multi-rotor position and $\dot{\boldsymbol{q}}_{vir}$ is the rate of change of this vector in time. From these two states, the angular velocity of the virtual link can be computed by

$$\boldsymbol{\omega}_{vir} = \boldsymbol{q}_{vir} \times \dot{\boldsymbol{q}}_{vir} \tag{3.15}$$

where $\boldsymbol{q} \times (\boldsymbol{\omega} \times \boldsymbol{q}) = \boldsymbol{\omega}$ and $\boldsymbol{q} \cdot \boldsymbol{\omega} = 0$ identities are used.

In order to reduce the swing motion of the cable and track the desired cable attitude, the control has to take virtual link states into account. Essentially, there are two goals in this part. The first goal is to eliminate the error between desired and current virtual link attitudes, whereas, the second one aims for the compensation of resulting centripetal forces due to the pendulum swing motion of the payload and cable. The former goal can be achieved by implementing a simple PD control method that calculates a necessary force vector, which is orthogonal to $\boldsymbol{q}_{vir}$, to drive the virtual cable to the desired attitude as given in Equation 3.16,

$$\boldsymbol{f}_{\boldsymbol{q}}^{\perp} = (m_Q + m_L)\, L\hat{\boldsymbol{q}}_{vir} \left(\boldsymbol{K}_{\boldsymbol{q}} \boldsymbol{e}_{\boldsymbol{q}_{vir}} + \boldsymbol{K}_{\boldsymbol{\omega}} \boldsymbol{e}_{\boldsymbol{\omega}_{vir}}\right) \tag{3.16}$$

where m_L is the total mass of the cable, $\boldsymbol{K}_{\boldsymbol{q}}$ and $\boldsymbol{K}_{\boldsymbol{\omega}}$ are the feedback gains for the attitude and angular velocity errors for the virtual link, respectively. The error terms are calculated as follows, Ref. [13],

$$\boldsymbol{e}_{\boldsymbol{q}_{vir}} = \boldsymbol{q}_{vir_d} \times \boldsymbol{q}_{vir}$$

$$\boldsymbol{e}_{\boldsymbol{\omega}_{vir}} = \boldsymbol{\omega}_{vir} + \hat{\boldsymbol{q}}_{vir}^2 \boldsymbol{\omega}_{vir_d}$$

and provided that desired multi-rotor position is found, the unit vector along desired virtual link can be obtained by

$$\boldsymbol{q}_{vir_d} = \frac{\boldsymbol{x}_{Q_d} - \boldsymbol{x}_P}{||\boldsymbol{x}_{Q_d} - \boldsymbol{x}_P||}$$

For compensation of the resultant centripetal force, which is parallel to $\boldsymbol{q}_{vir}$, the following correction force is calculated in Equation (3.17),

$$\boldsymbol{f}_{\boldsymbol{q}}^{\parallel} = \left(m_Q + \frac{m_L}{2}\right) L \left(\boldsymbol{\omega}_{vir} \cdot \boldsymbol{\omega}_{vir}\right) \boldsymbol{q}_{vir} \tag{3.17}$$

Finally, including all the findings from previous steps, an overall desired force vector is obtained and a nonlinear geometric control method for the multi-rotor attitude and trajectory tracking control, based on Refs. [1, 4, 13, 93], is employed.

Total net desired force that achieves the satisfactory payload trajectory tracking while compensating resultant forces including the weight of the multi-rotor is found below,

$$\boldsymbol{f}_d = \boldsymbol{T}_d + \boldsymbol{f}_{\boldsymbol{q}}^{\perp} + \boldsymbol{f}_{\boldsymbol{q}}^{\parallel} - \boldsymbol{K}_{\boldsymbol{x}_Q} \boldsymbol{e}_{\boldsymbol{x}_Q} - \boldsymbol{K}_{\boldsymbol{v}_Q} \boldsymbol{e}_{\boldsymbol{v}_Q} + m_Q \left(\dot{\boldsymbol{v}}_{Q_d} - g\boldsymbol{e}_3\right)$$

where the desired tension force is $\boldsymbol{T}_d = \boldsymbol{\mu}_d - m_L g \boldsymbol{e}_3$. $\boldsymbol{K}_{\boldsymbol{x}_Q}$ and $\boldsymbol{K}_{\boldsymbol{v}_Q}$ are the feedback gains for multi-rotor position and velocity errors, which are calculated as below,

$$\boldsymbol{e}_{\boldsymbol{x}_Q} = \boldsymbol{x}_Q - \boldsymbol{x}_{Q_d}$$

$$\boldsymbol{e}_{\boldsymbol{v}_Q} = \boldsymbol{v}_Q - \boldsymbol{v}_{Q_d}$$

Almost globally asymptotically convergent attitude control of the multi-rotor is satisfied by the following control law,

$$f_B = -\boldsymbol{f}_d \cdot \boldsymbol{R}_Q \boldsymbol{e}_3$$

$$\boldsymbol{\tau} = -\boldsymbol{K}_{\boldsymbol{R}_Q} \boldsymbol{e}_{\boldsymbol{R}_Q} - \boldsymbol{K}_{\boldsymbol{\omega}_Q} \boldsymbol{e}_{\boldsymbol{\omega}_Q} + \boldsymbol{\omega}_Q \times \boldsymbol{J}_Q \boldsymbol{\omega}_Q - \boldsymbol{J}_Q \left(\hat{\boldsymbol{\omega}}_Q \boldsymbol{R}_Q^T \boldsymbol{R}_{Q_c} \boldsymbol{\omega}_{Q_c} - \boldsymbol{R}_Q^T \boldsymbol{R}_{Q_c} \dot{\boldsymbol{\omega}}_{Q_c}\right)$$

where the error terms are found by

$$\boldsymbol{e}_{\boldsymbol{R}_Q} = \frac{1}{2}\left(\boldsymbol{R}_{Q_c}^T \boldsymbol{R}_Q - \boldsymbol{R}_Q^T \boldsymbol{R}_{Q_c}\right)$$

$$\boldsymbol{e}_{\boldsymbol{\omega}_Q} = \boldsymbol{\omega}_Q - \boldsymbol{R}_Q^T \boldsymbol{R}_{Q_c} \boldsymbol{\omega}_{Q_c}$$

and the commanded multi-rotor attitude $\boldsymbol{R}_{Q_c}$ is computed as follows,

$$\boldsymbol{R}_{Q_c} = \begin{bmatrix} -\frac{\boldsymbol{b}_{3_c} \times \boldsymbol{b}_{2_c}}{||\boldsymbol{b}_{3_c} \times \boldsymbol{b}_{2_c}||}, & \frac{\boldsymbol{b}_{3_c} \times \boldsymbol{b}_{1_d}}{||\boldsymbol{b}_{3_c} \times \boldsymbol{b}_{1_d}||}, & \boldsymbol{b}_{3_c} \end{bmatrix}$$

where

$$\boldsymbol{b}_{3_c} = -\frac{\boldsymbol{f}_d}{||\boldsymbol{f}_d||}, \qquad \boldsymbol{b}_{2_c} = \frac{\boldsymbol{b}_{3_c} \times \boldsymbol{b}_{1_d}}{||\boldsymbol{b}_{3_c} \times \boldsymbol{b}_{1_d}||}$$

and the desired orientation of the multi-rotor can be arbitrarily set by $\boldsymbol{b}_{1_d}$ unit vector which is used to find the desired projection of body-x axis on the xy-plane.

3.1.2.1 Simulation Results

In order to test the derived control law for the same multi-rotor with a flexible cable suspended load system as shown in the linear control section, a smooth trajectory for the payload is commanded.

Trajectory: The desired time-parameterized payload trajectory is defined by the following equations

$$\boldsymbol{x}_{P_d}(t) = \begin{bmatrix} r_x \sin(\omega_x t) & r_y \cos(\omega_y) - r_y & 0 \end{bmatrix}^T$$

where r_x and r_y correspond to the radius of a curve in x and y directions while ω_x and ω_y refer the angular speed in these axes, respectively. This trajectory defines an infinity (∞) shape in xy-plane.

$$r_x = 1 \text{ m},\ r_y = -2 \text{ m},\ \omega_x = 0.2\pi \text{ rad/s},\ \omega_y = 0.1\pi \text{ rad/s}$$

Feedback Control Gains: The following values for the feedback control gains are used in the simulation.

$$\boldsymbol{K}_{\boldsymbol{x}_Q} = 5,\ \boldsymbol{K}_{\boldsymbol{v}_Q} = 8,\ \boldsymbol{K}_{\boldsymbol{R}_Q} = 10,\ \boldsymbol{K}_{\boldsymbol{\omega}_Q} = 4,\ \boldsymbol{K}_{\boldsymbol{x}_P} = 9,\ \boldsymbol{K}_{\boldsymbol{v}_P} = 1,\ \boldsymbol{K}_{\boldsymbol{q}} = 1,\ \boldsymbol{K}_{\boldsymbol{\omega}} = 0.5$$

Figure 3.9 shows the snapshots of simulated trajectory with the system components at specific time instances. In these plots, desired payload force, $\boldsymbol{\mu}_d$, commanded multi-rotor position, $\boldsymbol{x}_{Q_d}$, and the overall history of the trajectory tracking are displayed. Since the system starts from a stable hover initial condition, in the first 4 seconds it tries to swiftly catch the desired velocity profile. Therefore, quick acceleration and deceleration segments and resultant path deviations can be spotted in this period. However, after reaching to the desired velocity profile, the system demonstrates a smooth tracking of the trajectory while keeping the cable and payload swing almost unnoticeable.

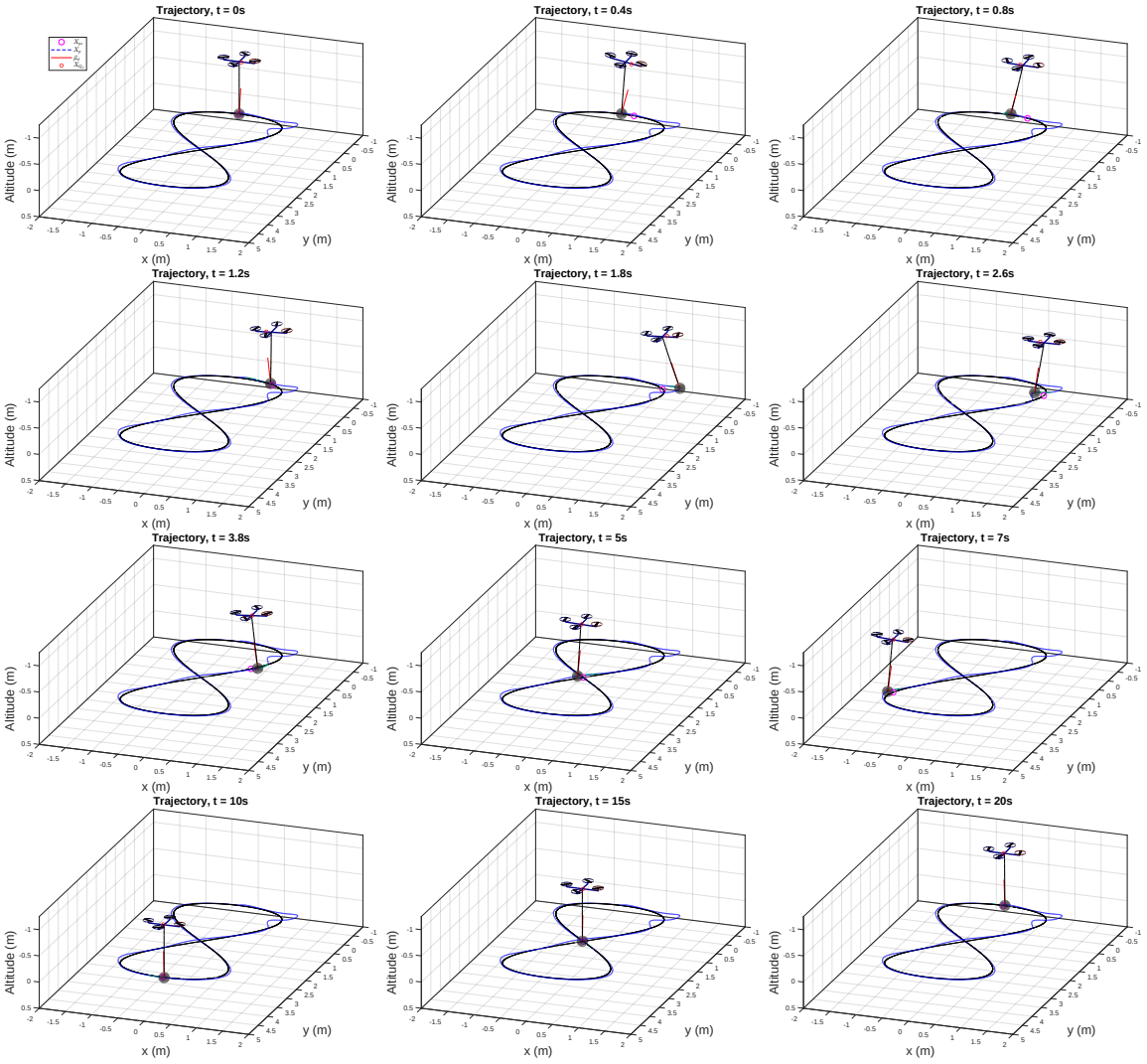

Figure 3.9: Snapshots of the simulation during an infinity shape trajectory tracking for 20 seconds

3.2 Autonomous Control of Airship

This section introduces both linear and nonlinear autonomous control of the airship model developed in Section 2.1.4. The linear approach utilizes a linear quadratic (LQ) control method in a gain scheduling framework, whereas the nonlinear approach employs a nonlinear dynamic inversion (NDI) based control method for the attitude and trajectory control of the airship.

3.2.1 Linear Control

The narrow flight envelope of the desired airship limited by its dimensions and the expected near constant, or slowly-varying, system parameters, makes the linear control approach an ideal starting point for stabilizing and controlling the airship states to track desired trajectories. For this purpose, an LQ control and linear interpolating gain scheduling methods are developed due to their relative ease of development and implementation. In addition, the linear analyses of the desired trim conditions and intuitive selection of weight matrices to design an effective controller capturing the desired performance are aimed in this work.

Firstly, the trim conditions for the desired flight regimes are found and the linearization of nonlinear 6-DOF equations about these trim conditions is carried out. Afterwards, two separate LQ controllers are designed for the longitudinal and lateral-directional motions of the airship. Finally, a linear interpolating gain scheduling method is integrated to utilize these flight trim conditions to satisfy the piece-wise continuity of the airship flight envelope so that the linearization assumptions of the designed controllers can still be hold.

3.2.1.1 Linearization of the Airship Model

The compact form of the nonlinear equations for the airship model can be represented by

$$\dot{\boldsymbol{\xi}} = f(\boldsymbol{\xi}, \boldsymbol{\eta})$$

where the state and control vectors are as follows

$$\boldsymbol{\xi} = [x\ y\ z\ u\ v\ w\ \phi\ \theta\ \psi\ p\ q\ r]^T$$
$$\boldsymbol{\eta} = [f_{M_{FL}}\ f_{M_{FR}}\ f_{M_{BL}}\ f_{M_{BR}}\ \theta_{M_{FL}}\ \theta_{M_{FR}}\ \theta_{M_{BL}}\ \theta_{M_{BR}}\ \psi_{F_{TL}}\ \psi_{F_{TR}}\ \psi_{F_{BL}}\ \psi_{F_{BR}}]^T$$

where the subscripts for motor forces, f_M, and motor pod tilt angles, θ_M, are defined as FL for forward-left, FR for forward-right, BL for backward-left, and BR for backward-right. Similarly, the convention for fin deflection (ψ_F) subscripts are TL for top-left, TR for top-right, BL for bottom-left, and BR for bottom-right.

To obtain and work on a more generalized representation, control inputs are normalized as $f_M = \tau f_{M_{max}}$, $\theta_M = \mu\theta_{M_{max}}$, and $\psi_F = \delta\psi_{F_{max}}$ where the normalized quantities are defined to be $\tau : [0, 1]$, $\mu : [-1, 1]$, and $\delta : [-1, 1]$. Furthermore, individual mixing strategies are applied to the motor thrust, tilt angles and the fin deflections. From the main and differential thrust, and tilt angles, the mixers are constructed as below,

$$\begin{bmatrix} \tau_{FL} \\ \tau_{FR} \\ \tau_{BL} \\ \tau_{BR} \end{bmatrix} = \begin{bmatrix} +0.5 & +0.25 & +0.25 \\ +0.5 & -0.25 & +0.25 \\ +0.5 & +0.25 & -0.25 \\ +0.5 & -0.25 & -0.25 \end{bmatrix} \begin{bmatrix} \tau_M \\ \tau_{D_{LR}} \\ \tau_{D_{FB}} \end{bmatrix}, \quad \begin{bmatrix} \mu_{FL} \\ \mu_{FR} \\ \mu_{BL} \\ \mu_{BR} \end{bmatrix} = \begin{bmatrix} +0.5 & +0.25 & +0.25 \\ +0.5 & -0.25 & +0.25 \\ +0.5 & +0.25 & -0.25 \\ +0.5 & -0.25 & -0.25 \end{bmatrix} \begin{bmatrix} \mu_M \\ \mu_{D_{LR}} \\ \mu_{D_{FB}} \end{bmatrix}$$

where the subscript M corresponds to the main cumulative value while D_{LR} and D_{FB} refer to the differential inputs for the left-right and forward-backward sets.

The mapping from aileron, elevator and rudder deflections to individual control surface deflections is achieved by the following mixer,

$$\begin{bmatrix} \delta_{TL} \\ \delta_{TR} \\ \delta_{BL} \\ \delta_{BR} \end{bmatrix} = \begin{bmatrix} +\frac{1}{3} & -\frac{1}{3} & -\frac{1}{3} \\ +\frac{1}{3} & +\frac{1}{3} & -\frac{1}{3} \\ +\frac{1}{3} & -\frac{1}{3} & +\frac{1}{3} \\ +\frac{1}{3} & +\frac{1}{3} & +\frac{1}{3} \end{bmatrix} \begin{bmatrix} \delta_a \\ \delta_e \\ \delta_r \end{bmatrix}$$

Employing the mixer relations and the normalized controls, the new normalized control input vector becomes

$$\bar{\boldsymbol{\eta}} = [\tau_M \ \tau_{D_{LR}} \ \tau_{D_{FB}} \ \mu_M \ \mu_{D_{LR}} \ \mu_{D_{FB}} \ \delta_a \ \delta_e \ \delta_r]^T$$

The linearization of the 6-DOF airship nonlinear model is obtained by utilizing small perturbation theory about a generic trim condition denoted as $(\boldsymbol{\xi}_0, \ \bar{\boldsymbol{\eta}}_0)$. The perturbation on the states and control vectors are defined by their nominal values with small perturbations as follows

$$\boldsymbol{\xi} = \boldsymbol{\xi}_0 + \Delta\boldsymbol{\xi}$$

$$\bar{\boldsymbol{\eta}} = \bar{\boldsymbol{\eta}}_0 + \Delta\bar{\boldsymbol{\eta}}$$

Substituting the perturbed values into the nonlinear equation form yields

$$\dot{\boldsymbol{\xi}}_0 + \Delta\dot{\boldsymbol{\xi}} = f(\boldsymbol{\xi}_0 + \Delta\boldsymbol{\xi}, \bar{\boldsymbol{\eta}}_0 + \Delta\bar{\boldsymbol{\eta}})$$

Using the first order linear approximation by Taylor series expansion, we attain the linearized model around the nominal value as

$$\dot{\boldsymbol{\xi}}_0 + \Delta\dot{\boldsymbol{\xi}} = f(\boldsymbol{\xi}_0, \bar{\boldsymbol{\eta}}_0) + \sum_{i=1}^{12} \left(\frac{\partial f}{\partial \boldsymbol{\xi}_i} \right) \Big|_{\boldsymbol{\xi}=\boldsymbol{\xi}_0} \Delta\boldsymbol{\xi}_i + \sum_{j=1}^{9} \left(\frac{\partial f}{\partial \bar{\boldsymbol{\eta}}_j} \right) \Big|_{\bar{\boldsymbol{\eta}}=\bar{\boldsymbol{\eta}}_0} \Delta\bar{\boldsymbol{\eta}}_j + \text{H.O.T.}$$

where H.O.T. stands for higher order terms that are not included in the linear expansion.

Since it is known that $\dot{\boldsymbol{\xi}}_0 = f(\boldsymbol{\xi}_0, \bar{\boldsymbol{\eta}}_0)$ holds from the substitution of the nominal values into the nonlinear equation, after removing these terms from the equation, the linear time-invariant system is obtained as below

$$\begin{aligned}\Delta\dot{\boldsymbol{\xi}} &= \sum_{i=1}^{12}\left(\frac{\partial f}{\partial \boldsymbol{\xi}_i}\right)\Big|_{(\boldsymbol{\xi}_0,\bar{\boldsymbol{\eta}}_0)}\Delta\boldsymbol{\xi}_i + \sum_{j=1}^{9}\left(\frac{\partial f}{\partial \bar{\boldsymbol{\eta}}_j}\right)\Big|_{(\boldsymbol{\xi}_0,\bar{\boldsymbol{\eta}}_0)}\Delta\bar{\boldsymbol{\eta}}_j \\ &= \boldsymbol{A}\Delta\boldsymbol{\xi} + \boldsymbol{B}\Delta\bar{\boldsymbol{\eta}}\end{aligned}$$

where $\boldsymbol{A} \in \mathbb{R}^{12\times 12}$ and $\boldsymbol{B} \in \mathbb{R}^{12\times 9}$ Jacobian matrices are given below

$$\boldsymbol{A} = \begin{bmatrix}
\frac{\partial \dot{x}}{\partial x} & \frac{\partial \dot{x}}{\partial y} & \frac{\partial \dot{x}}{\partial z} & \frac{\partial \dot{x}}{\partial u} & \frac{\partial \dot{x}}{\partial v} & \frac{\partial \dot{x}}{\partial w} & \frac{\partial \dot{x}}{\partial \phi} & \frac{\partial \dot{x}}{\partial \theta} & \frac{\partial \dot{x}}{\partial \psi} & \frac{\partial \dot{x}}{\partial p} & \frac{\partial \dot{x}}{\partial q} & \frac{\partial \dot{x}}{\partial r} \\
\frac{\partial \dot{y}}{\partial x} & \frac{\partial \dot{y}}{\partial y} & \frac{\partial \dot{y}}{\partial z} & \frac{\partial \dot{y}}{\partial u} & \frac{\partial \dot{y}}{\partial v} & \frac{\partial \dot{y}}{\partial w} & \frac{\partial \dot{y}}{\partial \phi} & \frac{\partial \dot{y}}{\partial \theta} & \frac{\partial \dot{y}}{\partial \psi} & \frac{\partial \dot{y}}{\partial p} & \frac{\partial \dot{y}}{\partial q} & \frac{\partial \dot{y}}{\partial r} \\
\frac{\partial \dot{z}}{\partial x} & \frac{\partial \dot{z}}{\partial y} & \frac{\partial \dot{z}}{\partial z} & \frac{\partial \dot{z}}{\partial u} & \frac{\partial \dot{z}}{\partial v} & \frac{\partial \dot{z}}{\partial w} & \frac{\partial \dot{z}}{\partial \phi} & \frac{\partial \dot{z}}{\partial \theta} & \frac{\partial \dot{z}}{\partial \psi} & \frac{\partial \dot{z}}{\partial p} & \frac{\partial \dot{z}}{\partial q} & \frac{\partial \dot{z}}{\partial r} \\
\frac{\partial \dot{u}}{\partial x} & \frac{\partial \dot{u}}{\partial y} & \frac{\partial \dot{u}}{\partial z} & \frac{\partial \dot{u}}{\partial u} & \frac{\partial \dot{u}}{\partial v} & \frac{\partial \dot{u}}{\partial w} & \frac{\partial \dot{u}}{\partial \phi} & \frac{\partial \dot{u}}{\partial \theta} & \frac{\partial \dot{u}}{\partial \psi} & \frac{\partial \dot{u}}{\partial p} & \frac{\partial \dot{u}}{\partial q} & \frac{\partial \dot{u}}{\partial r} \\
\frac{\partial \dot{v}}{\partial x} & \frac{\partial \dot{v}}{\partial y} & \frac{\partial \dot{v}}{\partial z} & \frac{\partial \dot{v}}{\partial u} & \frac{\partial \dot{v}}{\partial v} & \frac{\partial \dot{v}}{\partial w} & \frac{\partial \dot{v}}{\partial \phi} & \frac{\partial \dot{v}}{\partial \theta} & \frac{\partial \dot{v}}{\partial \psi} & \frac{\partial \dot{v}}{\partial p} & \frac{\partial \dot{v}}{\partial q} & \frac{\partial \dot{v}}{\partial r} \\
\frac{\partial \dot{w}}{\partial x} & \frac{\partial \dot{w}}{\partial y} & \frac{\partial \dot{w}}{\partial z} & \frac{\partial \dot{w}}{\partial u} & \frac{\partial \dot{w}}{\partial v} & \frac{\partial \dot{w}}{\partial w} & \frac{\partial \dot{w}}{\partial \phi} & \frac{\partial \dot{w}}{\partial \theta} & \frac{\partial \dot{w}}{\partial \psi} & \frac{\partial \dot{w}}{\partial p} & \frac{\partial \dot{w}}{\partial q} & \frac{\partial \dot{w}}{\partial r} \\
\frac{\partial \dot{\phi}}{\partial x} & \frac{\partial \dot{\phi}}{\partial y} & \frac{\partial \dot{\phi}}{\partial z} & \frac{\partial \dot{\phi}}{\partial u} & \frac{\partial \dot{\phi}}{\partial v} & \frac{\partial \dot{\phi}}{\partial w} & \frac{\partial \dot{\phi}}{\partial \phi} & \frac{\partial \dot{\phi}}{\partial \theta} & \frac{\partial \dot{\phi}}{\partial \psi} & \frac{\partial \dot{\phi}}{\partial p} & \frac{\partial \dot{\phi}}{\partial q} & \frac{\partial \dot{\phi}}{\partial r} \\
\frac{\partial \dot{\theta}}{\partial x} & \frac{\partial \dot{\theta}}{\partial y} & \frac{\partial \dot{\theta}}{\partial z} & \frac{\partial \dot{\theta}}{\partial u} & \frac{\partial \dot{\theta}}{\partial v} & \frac{\partial \dot{\theta}}{\partial w} & \frac{\partial \dot{\theta}}{\partial \phi} & \frac{\partial \dot{\theta}}{\partial \theta} & \frac{\partial \dot{\theta}}{\partial \psi} & \frac{\partial \dot{\theta}}{\partial p} & \frac{\partial \dot{\theta}}{\partial q} & \frac{\partial \dot{\theta}}{\partial r} \\
\frac{\partial \dot{\psi}}{\partial x} & \frac{\partial \dot{\psi}}{\partial y} & \frac{\partial \dot{\psi}}{\partial z} & \frac{\partial \dot{\psi}}{\partial u} & \frac{\partial \dot{\psi}}{\partial v} & \frac{\partial \dot{\psi}}{\partial w} & \frac{\partial \dot{\psi}}{\partial \phi} & \frac{\partial \dot{\psi}}{\partial \theta} & \frac{\partial \dot{\psi}}{\partial \psi} & \frac{\partial \dot{\psi}}{\partial p} & \frac{\partial \dot{\psi}}{\partial q} & \frac{\partial \dot{\psi}}{\partial r} \\
\frac{\partial \dot{p}}{\partial x} & \frac{\partial \dot{p}}{\partial y} & \frac{\partial \dot{p}}{\partial z} & \frac{\partial \dot{p}}{\partial u} & \frac{\partial \dot{p}}{\partial v} & \frac{\partial \dot{p}}{\partial w} & \frac{\partial \dot{p}}{\partial \phi} & \frac{\partial \dot{p}}{\partial \theta} & \frac{\partial \dot{p}}{\partial \psi} & \frac{\partial \dot{p}}{\partial p} & \frac{\partial \dot{p}}{\partial q} & \frac{\partial \dot{p}}{\partial r} \\
\frac{\partial \dot{q}}{\partial x} & \frac{\partial \dot{q}}{\partial y} & \frac{\partial \dot{q}}{\partial z} & \frac{\partial \dot{q}}{\partial u} & \frac{\partial \dot{q}}{\partial v} & \frac{\partial \dot{q}}{\partial w} & \frac{\partial \dot{q}}{\partial \phi} & \frac{\partial \dot{q}}{\partial \theta} & \frac{\partial \dot{q}}{\partial \psi} & \frac{\partial \dot{q}}{\partial p} & \frac{\partial \dot{q}}{\partial q} & \frac{\partial \dot{q}}{\partial r} \\
\frac{\partial \dot{r}}{\partial x} & \frac{\partial \dot{r}}{\partial y} & \frac{\partial \dot{r}}{\partial z} & \frac{\partial \dot{r}}{\partial u} & \frac{\partial \dot{r}}{\partial v} & \frac{\partial \dot{r}}{\partial w} & \frac{\partial \dot{r}}{\partial \phi} & \frac{\partial \dot{r}}{\partial \theta} & \frac{\partial \dot{r}}{\partial \psi} & \frac{\partial \dot{r}}{\partial p} & \frac{\partial \dot{r}}{\partial q} & \frac{\partial \dot{r}}{\partial r}
\end{bmatrix}_{(\boldsymbol{\xi}_0,\bar{\boldsymbol{\eta}}_0)}$$

$$\boldsymbol{B} = \begin{bmatrix} \frac{\partial \dot{x}}{\partial \tau_M} & \frac{\partial \dot{x}}{\partial \tau_{D_{LR}}} & \frac{\partial \dot{x}}{\partial \tau_{D_{FB}}} & \frac{\partial \dot{x}}{\partial \mu_M} & \frac{\partial \dot{x}}{\partial \mu_{D_{LR}}} & \frac{\partial \dot{x}}{\partial \mu_{D_{FB}}} & \frac{\partial \dot{x}}{\partial \delta_a} & \frac{\partial \dot{x}}{\partial \delta_e} & \frac{\partial \dot{x}}{\partial \delta_r} \\ \frac{\partial \dot{y}}{\partial \tau_M} & \frac{\partial \dot{y}}{\partial \tau_{D_{LR}}} & \frac{\partial \dot{y}}{\partial \tau_{D_{FB}}} & \frac{\partial \dot{y}}{\partial \mu_M} & \frac{\partial \dot{y}}{\partial \mu_{D_{LR}}} & \frac{\partial \dot{y}}{\partial \mu_{D_{FB}}} & \frac{\partial \dot{y}}{\partial \delta_a} & \frac{\partial \dot{y}}{\partial \delta_e} & \frac{\partial \dot{y}}{\partial \delta_r} \\ \frac{\partial \dot{z}}{\partial \tau_M} & \frac{\partial \dot{z}}{\partial \tau_{D_{LR}}} & \frac{\partial \dot{z}}{\partial \tau_{D_{FB}}} & \frac{\partial \dot{z}}{\partial \mu_M} & \frac{\partial \dot{z}}{\partial \mu_{D_{LR}}} & \frac{\partial \dot{z}}{\partial \mu_{D_{FB}}} & \frac{\partial \dot{z}}{\partial \delta_a} & \frac{\partial \dot{z}}{\partial \delta_e} & \frac{\partial \dot{z}}{\partial \delta_r} \\ \frac{\partial \dot{u}}{\partial \tau_M} & \frac{\partial \dot{u}}{\partial \tau_{D_{LR}}} & \frac{\partial \dot{u}}{\partial \tau_{D_{FB}}} & \frac{\partial \dot{u}}{\partial \mu_M} & \frac{\partial \dot{u}}{\partial \mu_{D_{LR}}} & \frac{\partial \dot{u}}{\partial \mu_{D_{FB}}} & \frac{\partial \dot{u}}{\partial \delta_a} & \frac{\partial \dot{u}}{\partial \delta_e} & \frac{\partial \dot{u}}{\partial \delta_r} \\ \frac{\partial \dot{v}}{\partial \tau_M} & \frac{\partial \dot{v}}{\partial \tau_{D_{LR}}} & \frac{\partial \dot{v}}{\partial \tau_{D_{FB}}} & \frac{\partial \dot{v}}{\partial \mu_M} & \frac{\partial \dot{v}}{\partial \mu_{D_{LR}}} & \frac{\partial \dot{v}}{\partial \mu_{D_{FB}}} & \frac{\partial \dot{v}}{\partial \delta_a} & \frac{\partial \dot{v}}{\partial \delta_e} & \frac{\partial \dot{v}}{\partial \delta_r} \\ \frac{\partial \dot{w}}{\partial \tau_M} & \frac{\partial \dot{w}}{\partial \tau_{D_{LR}}} & \frac{\partial \dot{w}}{\partial \tau_{D_{FB}}} & \frac{\partial \dot{w}}{\partial \mu_M} & \frac{\partial \dot{w}}{\partial \mu_{D_{LR}}} & \frac{\partial \dot{w}}{\partial \mu_{D_{FB}}} & \frac{\partial \dot{w}}{\partial \delta_a} & \frac{\partial \dot{w}}{\partial \delta_e} & \frac{\partial \dot{w}}{\partial \delta_r} \\ \frac{\partial \dot{\phi}}{\partial \tau_M} & \frac{\partial \dot{\phi}}{\partial \tau_{D_{LR}}} & \frac{\partial \dot{\phi}}{\partial \tau_{D_{FB}}} & \frac{\partial \dot{\phi}}{\partial \mu_M} & \frac{\partial \dot{\phi}}{\partial \mu_{D_{LR}}} & \frac{\partial \dot{\phi}}{\partial \mu_{D_{FB}}} & \frac{\partial \dot{\phi}}{\partial \delta_a} & \frac{\partial \dot{\phi}}{\partial \delta_e} & \frac{\partial \dot{\phi}}{\partial \delta_r} \\ \frac{\partial \dot{\theta}}{\partial \tau_M} & \frac{\partial \dot{\theta}}{\partial \tau_{D_{LR}}} & \frac{\partial \dot{\theta}}{\partial \tau_{D_{FB}}} & \frac{\partial \dot{\theta}}{\partial \mu_M} & \frac{\partial \dot{\theta}}{\partial \mu_{D_{LR}}} & \frac{\partial \dot{\theta}}{\partial \mu_{D_{FB}}} & \frac{\partial \dot{\theta}}{\partial \delta_a} & \frac{\partial \dot{\theta}}{\partial \delta_e} & \frac{\partial \dot{\theta}}{\partial \delta_r} \\ \frac{\partial \dot{\psi}}{\partial \tau_M} & \frac{\partial \dot{\psi}}{\partial \tau_{D_{LR}}} & \frac{\partial \dot{\psi}}{\partial \tau_{D_{FB}}} & \frac{\partial \dot{\psi}}{\partial \mu_M} & \frac{\partial \dot{\psi}}{\partial \mu_{D_{LR}}} & \frac{\partial \dot{\psi}}{\partial \mu_{D_{FB}}} & \frac{\partial \dot{\psi}}{\partial \delta_a} & \frac{\partial \dot{\psi}}{\partial \delta_e} & \frac{\partial \dot{\psi}}{\partial \delta_r} \\ \frac{\partial \dot{p}}{\partial \tau_M} & \frac{\partial \dot{p}}{\partial \tau_{D_{LR}}} & \frac{\partial \dot{p}}{\partial \tau_{D_{FB}}} & \frac{\partial \dot{p}}{\partial \mu_M} & \frac{\partial \dot{p}}{\partial \mu_{D_{LR}}} & \frac{\partial \dot{p}}{\partial \mu_{D_{FB}}} & \frac{\partial \dot{p}}{\partial \delta_a} & \frac{\partial \dot{p}}{\partial \delta_e} & \frac{\partial \dot{p}}{\partial \delta_r} \\ \frac{\partial \dot{q}}{\partial \tau_M} & \frac{\partial \dot{q}}{\partial \tau_{D_{LR}}} & \frac{\partial \dot{q}}{\partial \tau_{D_{FB}}} & \frac{\partial \dot{q}}{\partial \mu_M} & \frac{\partial \dot{q}}{\partial \mu_{D_{LR}}} & \frac{\partial \dot{q}}{\partial \mu_{D_{FB}}} & \frac{\partial \dot{q}}{\partial \delta_a} & \frac{\partial \dot{q}}{\partial \delta_e} & \frac{\partial \dot{q}}{\partial \delta_r} \\ \frac{\partial \dot{r}}{\partial \tau_M} & \frac{\partial \dot{r}}{\partial \tau_{D_{LR}}} & \frac{\partial \dot{r}}{\partial \tau_{D_{FB}}} & \frac{\partial \dot{r}}{\partial \mu_M} & \frac{\partial \dot{r}}{\partial \mu_{D_{LR}}} & \frac{\partial \dot{r}}{\partial \mu_{D_{FB}}} & \frac{\partial \dot{r}}{\partial \delta_a} & \frac{\partial \dot{r}}{\partial \delta_e} & \frac{\partial \dot{r}}{\partial \delta_r} \end{bmatrix}_{(\boldsymbol{\xi}_0, \bar{\boldsymbol{\eta}}_0)}$$

The partial derivatives required for the linearization process are listed in four categories as follows.

3.2.1.1.1 Linearization of Translational Kinematics

$$\frac{\partial \dot{\boldsymbol{x}}_I}{\partial \boldsymbol{x}_I} = 0_{3\times 3}, \quad \frac{\partial \dot{\boldsymbol{x}}_I}{\partial \boldsymbol{v}_{B/W}} = \boldsymbol{R}_{BI}^T, \quad \frac{\partial \dot{\boldsymbol{x}}_I}{\partial \boldsymbol{\omega}} = 0_{3\times 3}, \quad \frac{\partial \dot{\boldsymbol{x}}_I}{\partial \bar{\boldsymbol{\eta}}} = 0_{3\times 9}$$

$$\frac{\partial \dot{x}}{\partial \phi} = v(\sin\phi\sin\psi + \cos\phi\sin\theta\cos\psi) + w(\cos\phi\sin\psi - \sin\phi\sin\theta\cos\psi)$$
$$\frac{\partial \dot{x}}{\partial \theta} = -u\sin\theta\cos\psi + v\sin\phi\cos\theta\cos\psi + w\cos\phi\cos\theta\cos\psi$$
$$\frac{\partial \dot{x}}{\partial \psi} = -u\cos\theta\sin\psi - v(\cos\phi\cos\psi + \sin\phi\sin\theta\sin\psi) + w(\sin\phi\cos\psi - \cos\phi\sin\theta\sin\psi)$$

$$\frac{\partial \dot{y}}{\partial \phi} = v(-\sin\phi\cos\psi + \cos\phi\sin\theta\sin\psi) - w(\cos\phi\cos\psi + \sin\phi\sin\theta\sin\psi)$$
$$\frac{\partial \dot{y}}{\partial \theta} = -u\sin\theta\sin\psi + v\sin\phi\cos\theta\sin\psi + w\cos\phi\cos\theta\sin\psi$$
$$\frac{\partial \dot{y}}{\partial \psi} = u\cos\theta\cos\psi - v(\cos\phi\sin\psi - \sin\phi\sin\theta\cos\psi) + w(\sin\phi\sin\psi + \cos\phi\sin\theta\cos\psi)$$
$$\frac{\partial \dot{z}}{\partial \phi} = v\cos\phi\cos\theta - w\sin\phi\cos\theta$$
$$\frac{\partial \dot{z}}{\partial \theta} = -u\cos\theta - v\sin\phi\sin\theta - w\cos\phi\sin\theta$$
$$\frac{\partial \dot{z}}{\partial \psi} = 0$$

3.2.1.1.2 Linearization of Rotational Kinematics:

Defining $\boldsymbol{\pi} = [\phi\ \theta\ \psi]^T$ for Euler angle states, the following derivations are obtained,

$$\frac{\partial \dot{\boldsymbol{\pi}}}{\partial \boldsymbol{x}_I} = 0_{3\times 3}, \quad \frac{\partial \dot{\boldsymbol{\pi}}}{\partial \boldsymbol{v}_{B/W}} = 0_{3\times 3}, \quad \frac{\partial \dot{\boldsymbol{\pi}}}{\partial \bar{\boldsymbol{\eta}}} = 0_{3\times 9}$$

$$\frac{\partial \dot{\phi}}{\partial \phi} = (q\cos\phi - r\sin\phi)\tan\theta, \quad \frac{\partial \dot{\phi}}{\partial \theta} = (q\sin\phi + r\cos\phi)\sec^2\theta, \quad \frac{\partial \dot{\phi}}{\partial \psi} = 0$$
$$\frac{\partial \dot{\theta}}{\partial \phi} = -q\sin\phi - r\cos\phi, \quad \frac{\partial \dot{\theta}}{\partial \theta} = 0, \quad \frac{\partial \dot{\theta}}{\partial \psi} = 0$$
$$\frac{\partial \dot{\psi}}{\partial \phi} = (q\cos\phi - r\sin\phi)\sec\theta, \quad \frac{\partial \dot{\psi}}{\partial \theta} = (q\sin\phi + r\cos\phi)\tan\theta\sec\theta, \quad \frac{\partial \dot{\psi}}{\partial \psi} = 0$$
$$\frac{\partial \dot{\phi}}{\partial p} = 1, \quad \frac{\partial \dot{\phi}}{\partial q} = \sin\phi\tan\theta, \quad \frac{\partial \dot{\phi}}{\partial r} = \cos\phi\tan\theta$$
$$\frac{\partial \dot{\theta}}{\partial p} = 0, \quad \frac{\partial \dot{\theta}}{\partial q} = \cos\phi, \quad \frac{\partial \dot{\theta}}{\partial r} = -\sin\phi$$
$$\frac{\partial \dot{\psi}}{\partial p} = 0, \quad \frac{\partial \dot{\psi}}{\partial q} = \sin\phi\sec\theta, \quad \frac{\partial \dot{\psi}}{\partial r} = \cos\phi\sec\theta$$

3.2.1.1.3 Linearization of Translational Dynamics:

$$\frac{\partial \dot{\boldsymbol{v}}_{B/W}}{\partial \boldsymbol{x}_I} = 0, \quad \frac{\partial \dot{\boldsymbol{v}}_{B/W}}{\partial \boldsymbol{v}_{B/W}} = \frac{\partial\left(\frac{\sum \boldsymbol{f}_B}{m_T}\right)}{\partial \boldsymbol{v}_{B/W}} - \hat{\boldsymbol{\omega}}, \quad \frac{\partial \dot{\boldsymbol{v}}_{B/W}}{\partial \boldsymbol{\omega}} = \frac{\partial\left(\frac{\sum \boldsymbol{f}_B}{m_T}\right)}{\partial \boldsymbol{\omega}} + \hat{\boldsymbol{v}}_{B/W} - (\boldsymbol{\omega}^T\boldsymbol{\rho}_{cg}\boldsymbol{I} + \boldsymbol{\omega}\boldsymbol{\rho}_{cg}^T - 2\boldsymbol{\rho}_{cg}\boldsymbol{\omega}^T)$$

$$\frac{\partial \dot{\boldsymbol{v}}_{B/W}}{\partial \phi} = \frac{\partial\left(\frac{\sum \boldsymbol{f}_B}{m_T}\right)}{\partial \phi}, \quad \frac{\partial \dot{\boldsymbol{v}}_{B/W}}{\partial \theta} = \frac{\partial\left(\frac{\sum \boldsymbol{f}_B}{m_T}\right)}{\partial \theta}, \quad \frac{\partial \dot{\boldsymbol{v}}_{B/W}}{\partial \psi} = 0, \quad \frac{\partial \dot{\boldsymbol{v}}_{B/W}}{\partial \bar{\boldsymbol{\eta}}} = \frac{\partial\left(\frac{\sum \boldsymbol{f}_B}{m_T}\right)}{\partial \bar{\boldsymbol{\eta}}}$$

3.2.1.1.4 Linearization of Rotational Dynamics:

$$\frac{\partial \dot{\boldsymbol{\omega}}}{\partial \boldsymbol{x}_I} = 0_{3\times 3}, \quad \frac{\partial \dot{\boldsymbol{\omega}}}{\partial \boldsymbol{v}_{B/W}} = \boldsymbol{J}^{-1}\left(\frac{\partial \sum \boldsymbol{\tau}_B}{\partial \boldsymbol{v}_{B/W}} - m_T \hat{\boldsymbol{\rho}}_{cg}\hat{\boldsymbol{\omega}}\right)$$
$$\frac{\partial \dot{\boldsymbol{\omega}}}{\partial \boldsymbol{\omega}} = \boldsymbol{J}^{-1}\left(\frac{\partial \sum \boldsymbol{\tau}_B}{\partial \boldsymbol{\omega}} + \left(\widehat{\boldsymbol{J}\boldsymbol{\omega}} - \hat{\boldsymbol{\omega}}\boldsymbol{J}\right) + m_T \hat{\boldsymbol{\rho}}_{cg}\hat{\boldsymbol{v}}_{B/W}\right)$$

$$\frac{\partial \dot{\boldsymbol{\omega}}}{\partial \phi} = \boldsymbol{J}^{-1}\left(\frac{\partial \sum \boldsymbol{\tau}_B}{\partial \phi}\right), \quad \frac{\partial \dot{\boldsymbol{\omega}}}{\partial \theta} = \boldsymbol{J}^{-1}\left(\frac{\partial \sum \boldsymbol{\tau}_B}{\partial \theta}\right), \frac{\partial \dot{\boldsymbol{\omega}}}{\partial \psi} = 0, \quad \frac{\partial \dot{\boldsymbol{\omega}}}{\partial \bar{\boldsymbol{\eta}}} = \boldsymbol{J}^{-1}\left(\frac{\partial \sum \boldsymbol{\tau}_B}{\partial \bar{\boldsymbol{\eta}}}\right)$$

Partial derivatives of the body forces and moments involve tedious derivation steps, which are not explicitly provided in this work. However, the state and control variable dependencies of the individual forces and moments are listed in Table 3.1 as a guide to the reader below.

Table 3.1: State and Control Variable Dependencies of Body Forces and Moments

Name	**State Variables**	**Control Variables**
Buoyancy	$\phi,\ \theta$	
Weight	$\phi,\ \theta$	
Hull Aerodynamics	$u,\ v,\ w,\ p,\ q,\ r$	
Motors		$\tau_M,\ \tau_{D_{LR}},\ \tau_{D_{FB}},\ \mu_M,\ \mu_{D_{LR}},\ \mu_{D_{FB}}$
Fins	$u,\ v,\ w,\ p,\ q,\ r$	$\delta_a,\ \delta_e,\ \delta_r$

3.2.1.2 Linear Quadratic Control Design

Linear quadratic control is an optimal feedback control method that utilizes the minimization of a cost function penalizing the states and control inputs according to the user defined weight matrices for optimal state and control input trajectories. In this work, an infinite horizon LQ method is utilized to stabilize the linear systems derived in previous section to stay near their defined nominal values.

The cost function to be minimized is in the following form,

$$J = \frac{1}{2}\int_0^\infty \left(\Delta\boldsymbol{\xi}^T\boldsymbol{Q}\Delta\boldsymbol{\xi} + \Delta\bar{\boldsymbol{\eta}}^T\boldsymbol{R}\Delta\bar{\boldsymbol{\eta}}\right)\ dt$$

where $\boldsymbol{Q} \geq 0$ (positive semi-definite) and $\boldsymbol{R} > 0$ (positive definite) are the weighting matrices for the state errors, $\Delta\boldsymbol{\xi} = \boldsymbol{\xi} - \boldsymbol{\xi}_0$, and control input errors, $\Delta\bar{\boldsymbol{\eta}} = \bar{\boldsymbol{\eta}} - \bar{\boldsymbol{\eta}}_0$, respectively.

The optimal feedback control law is given as below,

$$\Delta\bar{\boldsymbol{\eta}} = -\boldsymbol{K}\Delta\boldsymbol{\xi}$$

where $\boldsymbol{K}$ is the feedback gain matrix that multiplies the state errors and it is found as follows,

$$\boldsymbol{K} = \boldsymbol{R}^{-1}\boldsymbol{B}^T\boldsymbol{P}$$

where $\boldsymbol{P}$ is obtained by solving the Algebraic Riccati equation below.

$$\boldsymbol{P}\boldsymbol{A}^T + \boldsymbol{A}^T\boldsymbol{P} - \boldsymbol{P}\boldsymbol{B}\boldsymbol{R}^{-1}\boldsymbol{B}^T\boldsymbol{P} + \boldsymbol{Q} = 0$$

The motion of airship is decoupled into the longitudinal and lateral-directional motions and they are tackled individually as two separate control subsystems. The states and control inputs for the longitudinal motion are given below,

$$\boldsymbol{\xi}_{LONG} = \begin{bmatrix} u \\ w \\ \theta \\ q \end{bmatrix}, \qquad \bar{\boldsymbol{\eta}}_{LONG} = \begin{bmatrix} \tau_M \\ \tau_{D_{FB}} \\ \mu_M \\ \mu_{D_{FB}} \\ \delta_e \end{bmatrix}$$

In general, longitudinal motion involves the forward and vertical speed, and the pitching of the airship utilizing collective main thrust, main tilt angles of the motor

pods, differential thrust and tilt angles for forward and backward motor sets, and the elevator commands. For a controlled flight around various trim conditions, the change in longitudinal states and controls is expected to be slower comparing the lateral-directional states, which are given as follows,

$$\boldsymbol{\xi}_{LAT} = \begin{bmatrix} v \\ \phi \\ p \\ r \end{bmatrix}, \qquad \bar{\boldsymbol{\eta}}_{LAT} = \begin{bmatrix} \tau_{D_{LR}} \\ \mu_{D_{LR}} \\ \delta_a \\ \delta_r \end{bmatrix}$$

where the lateral-directional stability is achieved by the use of differential thrust, differential tilt angles on the motor pods, ailerons and rudders to control the lateral velocity, roll and yaw attitudes. The change in lateral states of the airship has a dominant effect on other states, as in the case with most vehicles. Therefore, faster, robust, and tight control is desired for the lateral-directional subsystem.

Figure 3.10 summarizes the overall control structure of the airship, where the longitudinal and lateral-directional subsystems and their feedback loops can be seen clearly.

After designing the control input feedback relation with the state errors, the actual control inputs are mapped back into their scale by applying the previously defined mixer logic to obtain $\boldsymbol{u}_0, \delta\boldsymbol{u}_{LONG}$, and $\delta\boldsymbol{u}_{LAT}$ from $\bar{\boldsymbol{\eta}}_0, \Delta\bar{\boldsymbol{\eta}}_{LONG}$, and $\Delta\bar{\boldsymbol{\eta}}_{LAT}$, respectively.

Remark 3.2.1. *The selection of effective weighting matrices, $\boldsymbol{Q}$ and $\boldsymbol{R}$, requires information about the behavior of the linear system around specific nominal conditions. Hence, varying weightings might be required for systems having varying system dynamics over the defined range of states and control inputs. A good example for this scenario would be an airship flying at a low airspeed which has significantly different flight characteristics and control allocation requirements comparing to the case with*

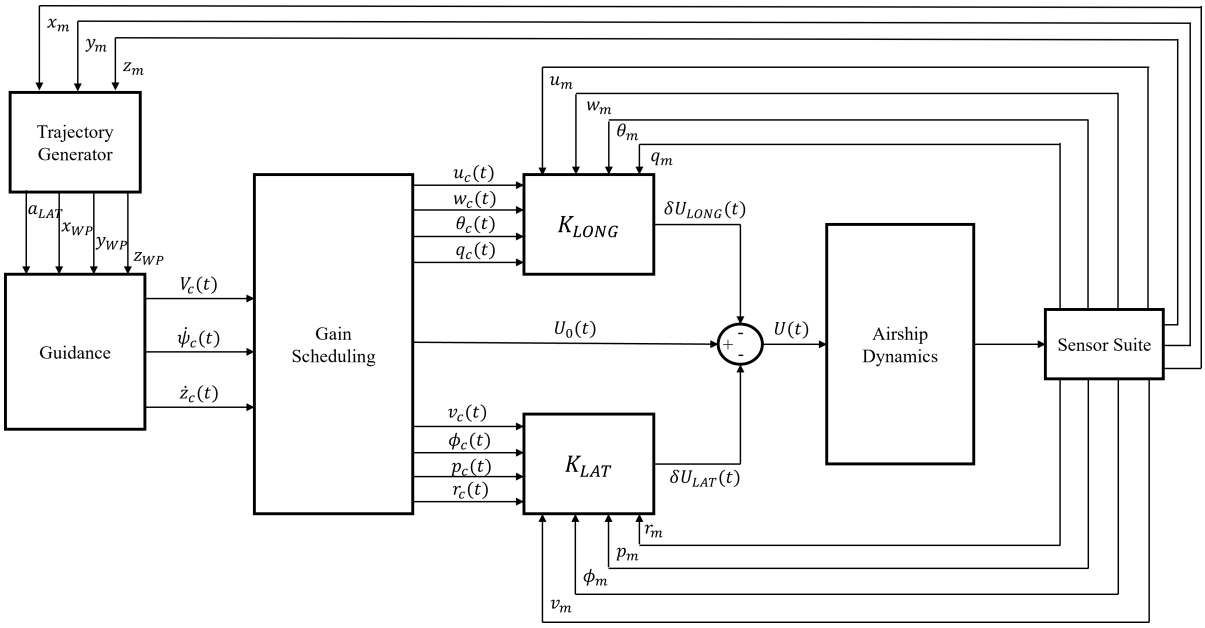

Figure 3.10: The overall linear control system of the airship

a relatively high airspeed. This is due to the aerodynamic ineffectiveness of the hull and fins in low airspeed conditions.

3.2.1.3 Gain Scheduling

The controllers previously designed are valid in the vicinity of the designated nominal (trim) flight condition, and as the conditions differ from that point, their control effectiveness changes significantly. However, for a useful flight mission, various trim conditions that requires different airspeed, attitude, or maneuvers have to be utilized consistently with a smooth transition. A potential but not practical solution is to find as many trim conditions as possible with a very tight tolerance to cover full flight envelope and switch between them as necessary. Instead, an interpolating gain scheduling technique, which is adopted in this work, can be effectively proposed to connect a subset of distant trim conditions by employing the interpolation so that continuously smooth transitions between various flight regimes can be achieved

without numerous discrete switches. The latter method eliminates finding and storing a large number of trim points and the switching mechanism between them, especially for the flight regimes where the state and control transitions occur approximately linearly.

Remark 3.2.2. *To capture the curvature of trim state and control transitions, highly nonlinear flight regimes have to be sampled more densely for an effective gain scheduling implementation. These regimes mostly correspond to the low airspeed flight and turning maneuvers for the airship vehicle.*

Remark 3.2.3. *It is worth noting that finding trim conditions utilizing various combinations of available control actuation is possible and there could be several heuristics that can be implemented to aid finding these trim conditions. However, this process requires more exhaustive and in depth studies, which falls outside the scope of this research. Therefore, during the linear control design, we only focused on forward flight regime where all the motor tilt angles align with the body-x direction and kept stationary without utilizing differential tilt commands. Moreover, the individual thrusters are combined as left and right sets, and operated together.*

The gain-scheduling technique requires scheduling variables to establish two end-points of a multi-dimensional line for interpolation. In this work, airspeed, yaw rate and climb rate of the airship are chosen to be scheduling variables so that various trajectories in the airship's flight envelope can be achieved by scheduling these variables.

Using the scheduling variables, the gain scheduling hyperspace is constructed with multiple trim conditions for three essential maneuvers which are airspeed change, heading change, and the altitude change commands. Individual considerations of these commands, their trim conditions and the relation with scheduling variables are examined and illustrated in the subsequent figures.

3.2.1.3.1 Trim Conditions for Airspeed Change Maneuver During the airspeed change maneuver, heading and altitude of the airship are kept constant in a straight and level flight. Figure 3.11 demonstrates how the trim conditions change for varying airspeed from 3 m/s to 15 m/s.

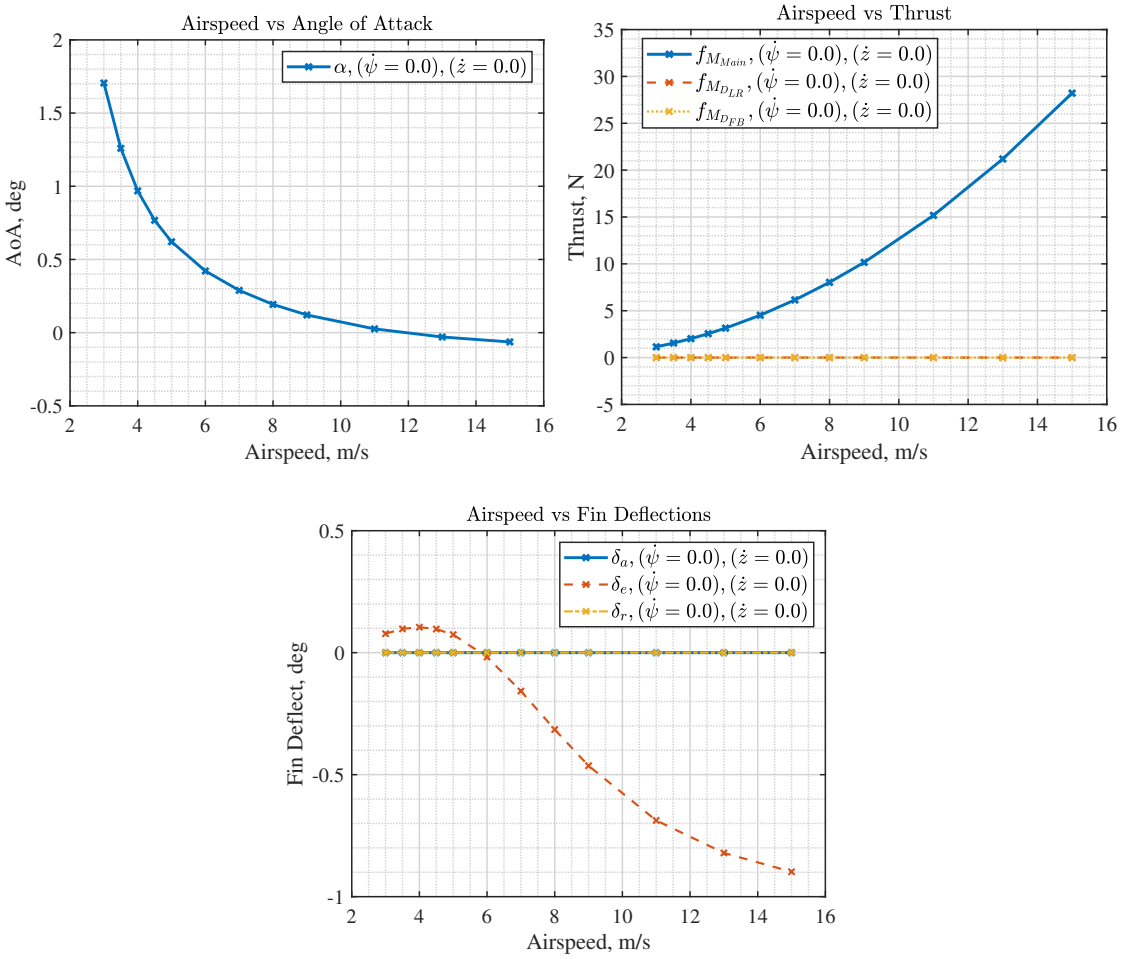

Figure 3.11: Trim conditions for control inputs during airspeed change maneuver from 3 m/s to 15 m/s

As the airspeed increase, the thrust required for the equilibrium increases quadratically due to the quadratic relation between velocity and air drag. Similarly,

it is also seen that for low airspeed flight, airship requires higher angle of attack to generate necessary lift to overcome weight and drag while positive elevator deflection is used to balance the pitching moment for a straight and level flight. In addition, it is worth noting that observing the angle of attack and elevator deflection graphs, the nonlinearity of motion becomes dominant below 6 m/s of airspeed, which we determined it to be the minimum speed of the forward flight regimes.

The variation of open loop poles of the longitudinal and lateral-directional subsystems is illustrated in Figure 3.12. The black crosses represent the eigenvalues for the minimum airspeed scenario, which is for 3 m/s, and as the airspeed increases, the size of red crosses, representing the varying eigenvalues, decrease. As seen from the graphs, although both subsystems have the eigenvalues on the left half-plane, for low airspeed scenarios, longitudinal subsystem has a set of poles close to the origin and as the airspeed increases, one of the poles coincides with the imaginary axis which indicates the marginal stability.

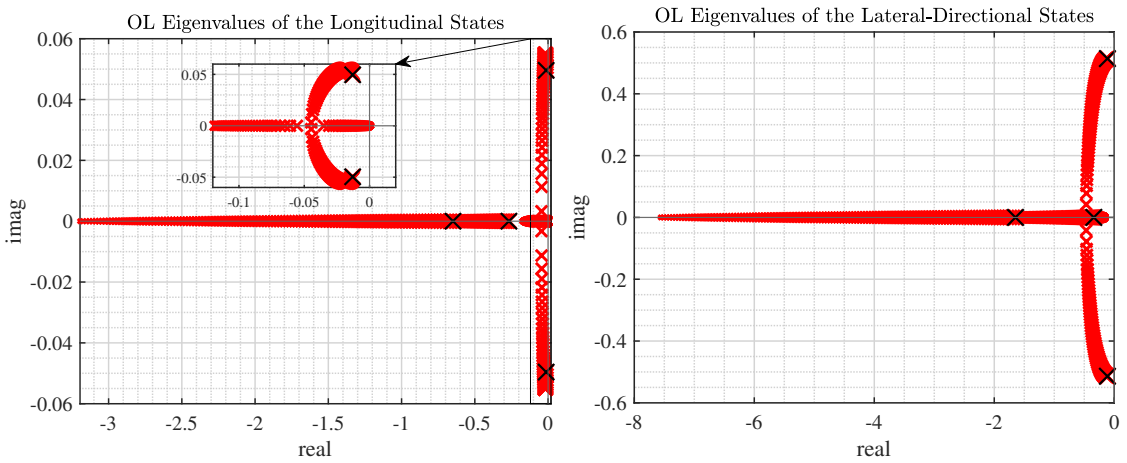

Figure 3.12: The variation on open loop eigenvalues during airspeed change maneuver from 3 m/s to 15 m/s

Similarly, the variation on closed loop poles of the longitudinal and lateral-directional subsystems with the implemented LQ controllers while keeping $\boldsymbol{Q}$ and $\boldsymbol{R}$ weighting matrices constant is plotted in Figure 3.13. From the plots, it can be inferred that increasing the airspeed provides more stability to the longitudinal and lateral-directional subsystem in general, which is expected since the control effectiveness of the fins increases with the increase in airspeed.

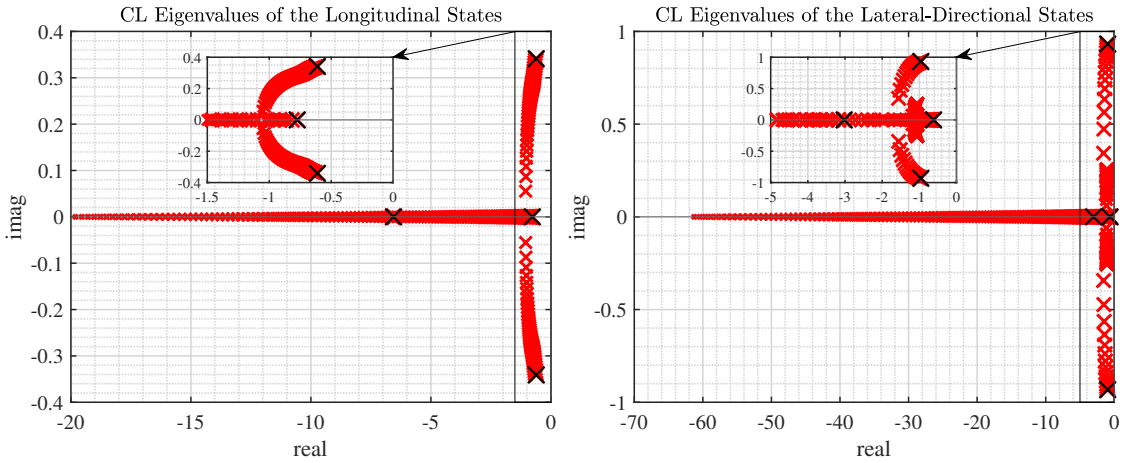

Figure 3.13: The variation on closed loop eigenvalues during airspeed change maneuver from 3 m/s to 15 m/s

3.2.1.3.2 Trim Conditions for Heading Change Maneuver In heading change maneuver, airspeed and altitude of the airship are kept stationary while implementing a yaw rate command. The turning maneuver in an airship requires a combined effort of all control inputs and the side-slip to provide necessary lateral force, which differentiates the airships from the conventional fixed-wing aircraft. As opposed to the most fixed-wing aircraft, lift is generated by lifting gas in airships and there is no control over the main lift vector magnitude and direction, which are constant in Inertial frame. Therefore, the side-slip angle and the rudder deflections with

the support of other control inputs are employed for the turn maneuvers. Figure 3.14 presents the change in control inputs and side-slip angle for various yaw rate trim conditions with the cruise airspeed, which is determined to be 10 m/s for the rest of this study.

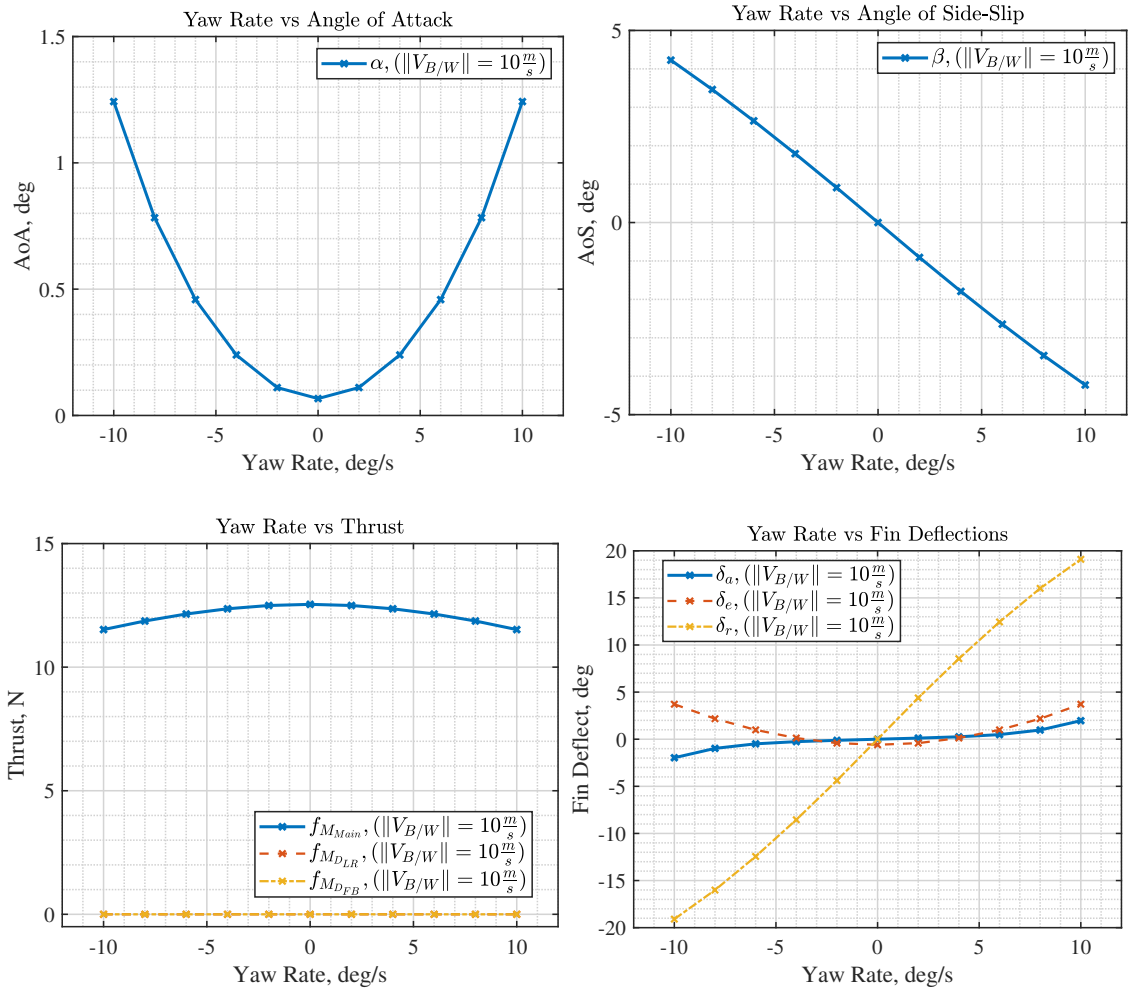

Figure 3.14: Trim conditions during heading change maneuver from -10 to 10 deg/s

As seen from the figures, to sustain higher yaw rates, larger side-slip and rudder deflections are required. The other control inputs, motor thrusts, aileron and elevator deflections, are adjusted to satisfy force and moment equilibrium for the desired trim condition.

In Figure 3.15, the variation on open loop eigenvalues of the subsystems during yaw rate commands are illustrated. Although the lateral-directional subsystem demonstrates a stable response, the longitudinal subsystem has poles close to the marginal stability for this maneuver.

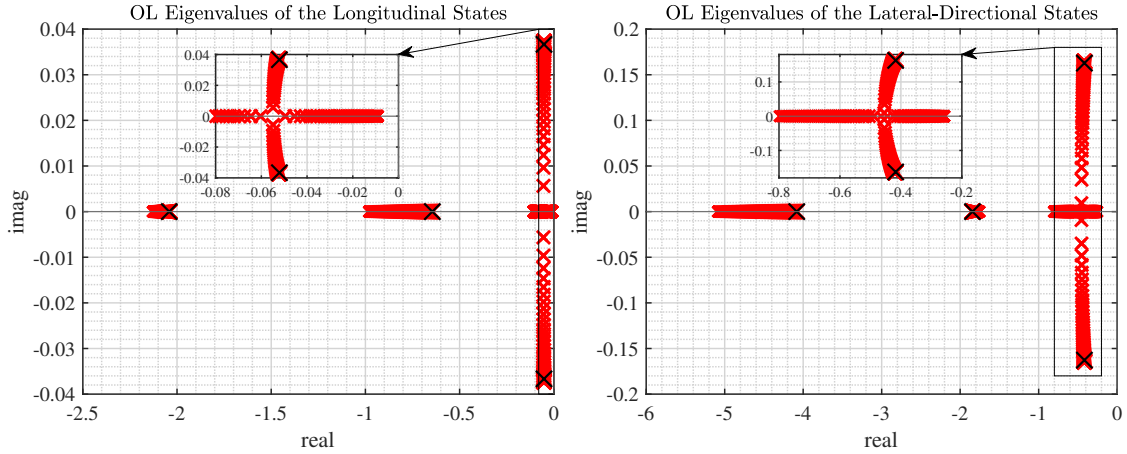

Figure 3.15: The variation on open loop eigenvalues during heading change maneuver from -10 to 10 deg/s

Figure 3.16 illustrates the variation on closed loop poles of the longitudinal and lateral subsystem in trim for various yaw rate commands. After control implementation, both subsystem demonstrates sufficiently stable behaviors.

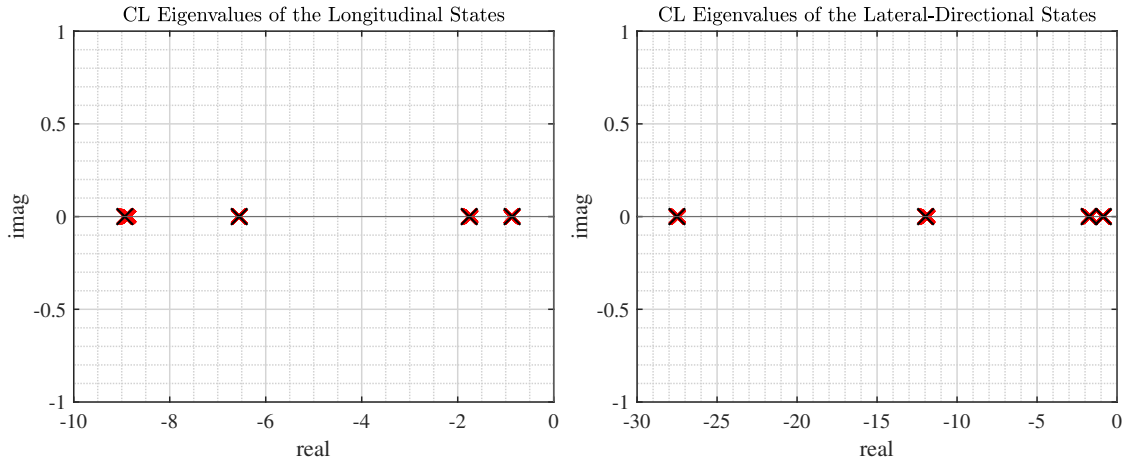

Figure 3.16: The variation on closed loop eigenvalues during heading change maneuver from -10 to 10 deg/s

3.2.1.3.3 Trim Conditions for Altitude Change Maneuver The altitude change maneuver is achieved by adjusting the angle of attack and pitch angle of the airship while keeping constant airspeed and heading. Only the longitudinal states and control inputs are expected to be involved in this maneuver. Figure 3.17 shows the change in these angles and control inputs for various climb rate commands in trim with the cruise airspeed.

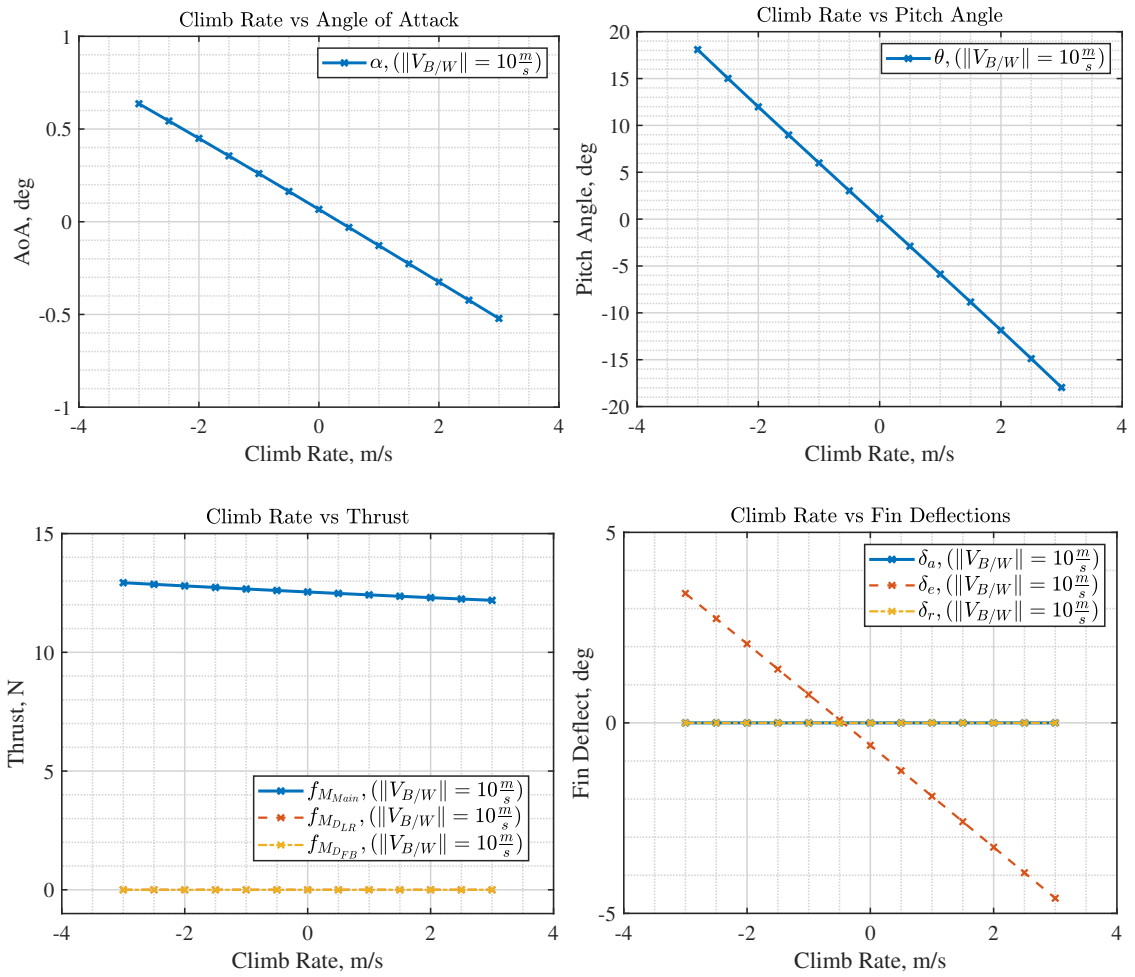

Figure 3.17: Trim conditions during altitude change maneuver from -3 m/s to 3 m/s where negative sign indicates the increasing altitude

In Figure 3.18, the open loop eigenvalues of the subsystems for different climb rate commands are plotted. As can be seen, one of the poles of longitudinal subsystem shifts to the right half-plane without control command.

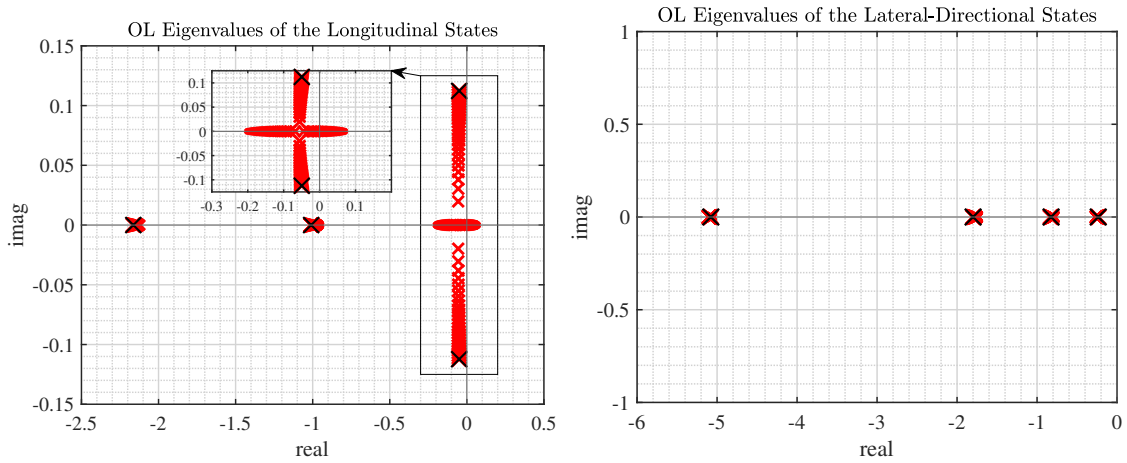

Figure 3.18: The variation on open loop eigenvalues during altitude change maneuver from -3 m/s to 3 m/s

The variation on closed loop eigenvalues of the subsystems for increasing climb rate command is given in Figure 3.19.

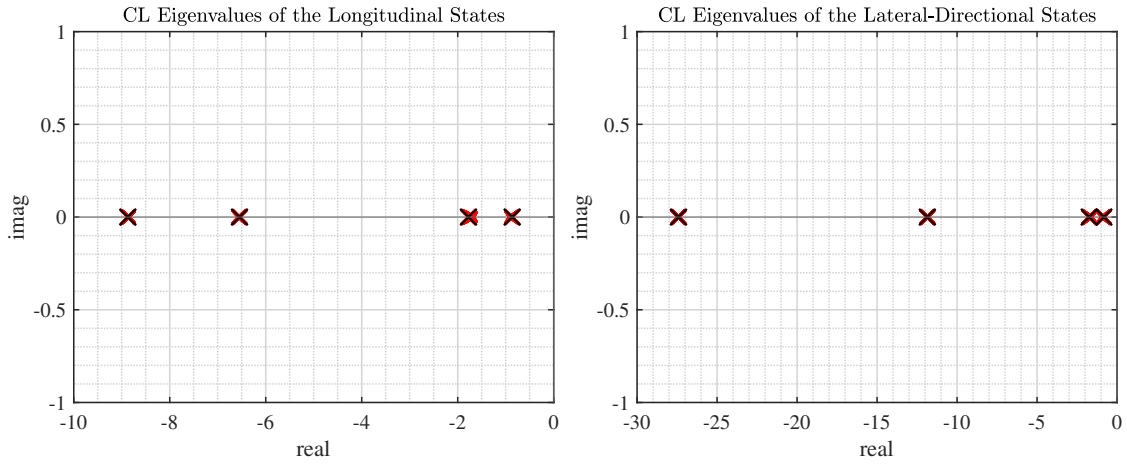

Figure 3.19: The variation on closed loop eigenvalues during altitude change maneuver from -3 m/s to 3 m/s

3.2.1.3.4 Representation of Trim Conditions as 3D Surface Plots

In order to visualize the trim conditions for combined airspeed and climb rate commands, 3D surface plots of corresponding states and control inputs are constructed in Figure 3.20.

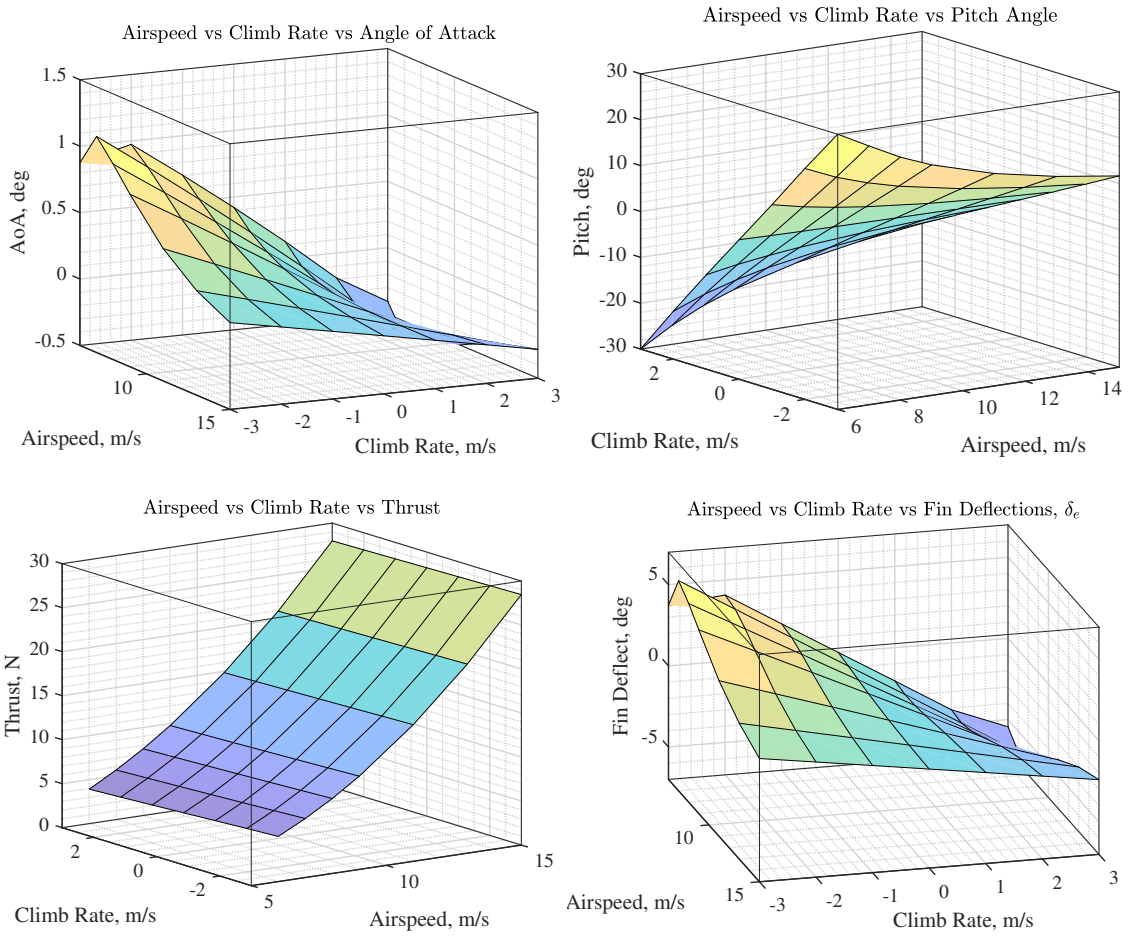

Figure 3.20: 3D illustration of trim conditions for airspeed and climb rate commands between 6 m/s to 15 m/s and -3 m/s to 3 m/s, respectively.

Likewise, the trim conditions for varying airspeed and yaw rate commands are illustrated in Figure 3.21.

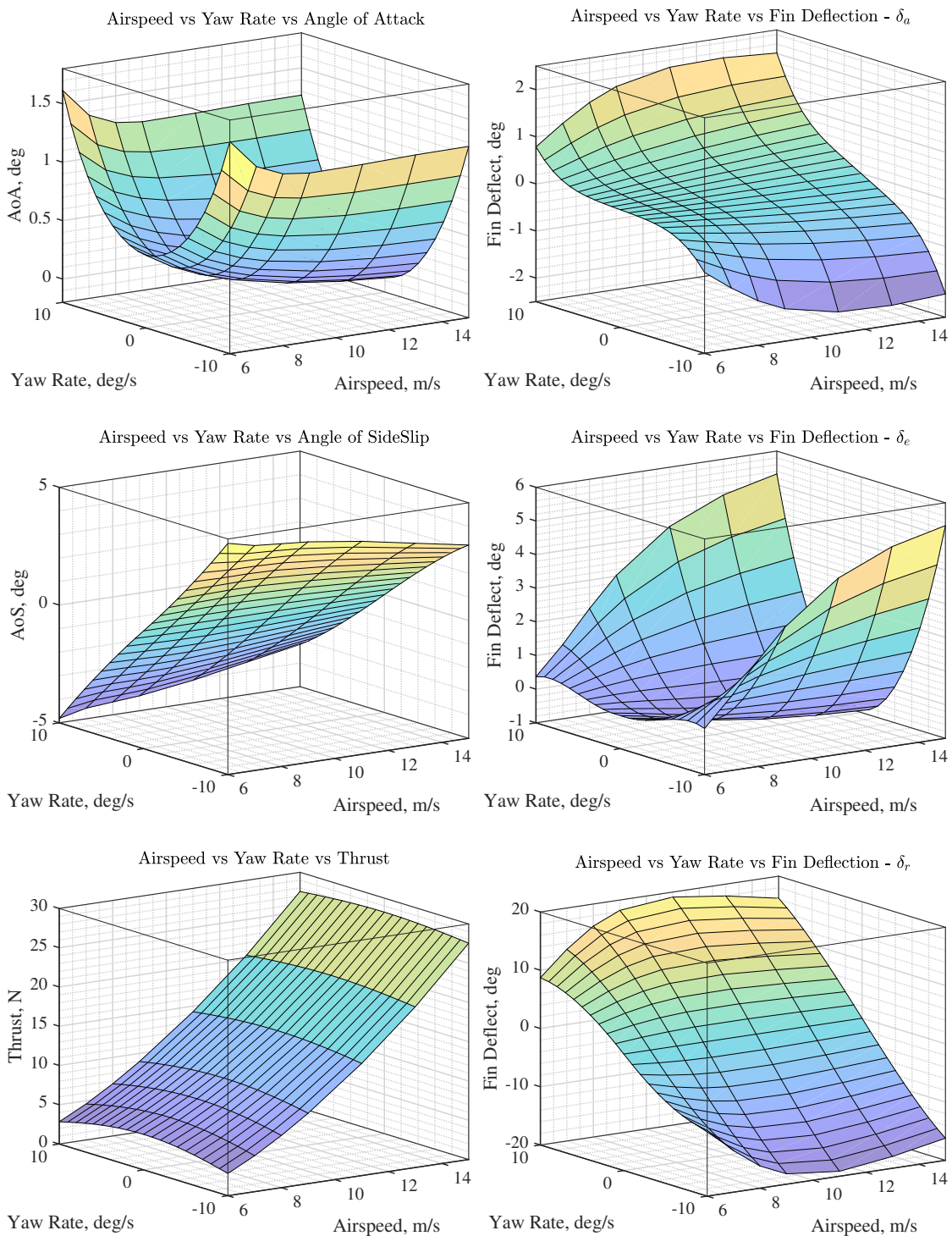

Figure 3.21: 3D illustration of trim conditions for airspeed and yaw rate commands between 6 m/s to 15 m/s and -10 deg/s to 10 deg/s, respectively.

3.2.1.4 Guidance Laws and Autopilot Modes

In this section, various autopilot modes required for a successful flight mission are introduced and their corresponding guidance laws are formulated. Starting with basic commands, such as change airspeed, heading and altitude, more complex mission level commands, such as waypoint navigation and return-to-base, are constructed. Table 3.2 presents the details of implemented autopilot modes with their descriptions, input parameters, stationary states and the formulations.

3.2.1.4.1 Constant Yaw Rate Turn Turn maneuvers in heading change and loiter modes assume a circular path with zero wind condition, as shown in Figure 3.22.

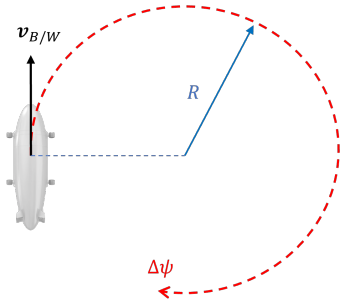

Figure 3.22: Illustration of heading change maneuver in a circular path

Given the turn radius and the desired airspeed, the rate of turn, which gives the commanded yaw rate for the vehicle, can be found by,

$$\dot{\psi}_{comm} = \mathrm{d}\frac{\|\boldsymbol{v}_{B/W}\|_d}{R_d}$$

where d indicates the direction of turn. The clock-wise turns are assigned to +1 while the counter clock-wise ones to -1.

Table 3.2: Various Autopilot Modes Implemented for Airship

Mode Name	**Input Parameters**	**Hold States**	**Description**
Hold		$\|\boldsymbol{v}_{B/W}\|$, ψ, z	Obtain the current airspeed, heading, and altitude at the time of switching and keep them constant
Airspeed Change	$\|\boldsymbol{v}_{B/W}\|_d$, τ_d	ψ, z	Obtain the current heading and altitude at the time of switching and keep them constant while adjusting commanded airspeed. Simple sigmoid function with desired time constant, τ_d, is implemented to smoothly adjust the commanded airspeed for gain scheduling as follows, $$\boldsymbol{v}_{comm} = \|\boldsymbol{v}_{B/W}\| + \Delta\|\boldsymbol{v}_{B/W}\| \left(\frac{1}{1 + e^{-\frac{t - t_s - 5\tau_d}{\tau_d}}} \right)$$
Heading Change	ψ_d, R_d, d	$\|\boldsymbol{v}_{B/W}\|$, z	Obtain the current airspeed and altitude at the time of switching and keep them constant while adjusting commanded yaw rate. Yaw rate command is found from a circular path with current airspeed, $\|\boldsymbol{v}_{B/W}\|$, desired turn radius, R_d, and direction, d, as follows, $$\dot{\psi}_{comm} = \begin{cases} \mathrm{d}\frac{\|\boldsymbol{v}_{B/W}\|}{R_d}, \text{ if } \|\psi_d - \psi\| \geq 15\,\mathrm{deg} \\ k_p(\psi_d - \psi) + k_d(\dot{\psi}_d - \dot{\psi}), \text{ else} \end{cases}$$
Altitude Change	z_d	$\|\boldsymbol{v}_{B/W}\|$, ψ	Obtain the current airspeed and heading at the time of switching and keep them constant while adjusting commanded climb rate. Climb rate command is found by a PD controller as follows, $$\dot{z}_{comm} = k_p(z_d - z) + k_d(\dot{z}_d - \dot{z})$$
Loiter	R_d, d	$\|\boldsymbol{v}_{B/W}\|$, z	Obtain the current airspeed and altitude at the time of switching and keep them constant while adjusting commanded yaw rate. Yaw rate command is found from a circular path formula as follows, $$\dot{\psi}_{comm} = \mathrm{d}\frac{\|\boldsymbol{v}_{B/W}\|}{R_d}$$
Mission	$\|\boldsymbol{v}_{B/W}\|_d$, WPs		Start waypoint following mission with desired airspeed. Utilize Proportional Navigation algorithm for heading guidance and PD controller for altitude control.
Return To Base	$\|\boldsymbol{v}_{B/W}\|_d$, WP_0		Special case of mission mode with a single waypoint where the home position is located.

Remark 3.2.4. *Heading change and loiter modes assume zero wind condition for constant yaw rate turn with respect to the Inertial frame. However, a strong wind condition would have disrupted the shape of circular path in the assumption if only the airspeed is taken into account. Therefore, for better turning characteristics, one should implement varying airspeed turns with constant ground speed for the airship.*

3.2.1.4.2 Proportional Navigation Guidance Law Mission and return-to-base modes employs the proportional navigation (PN) like guidance law to guide the heading of airship to the waypoint directions in horizontal plane. PN law, which has many practical implementations for missile guidance, finds the necessary lateral acceleration to adjust the heading of the airship so that the approaching velocity to the waypoint is maximized, which dictates a non-rotating line-of-sight (LOS) vector. Figure 3.23 illustrates the vectors and angles involved in PN guidance law.

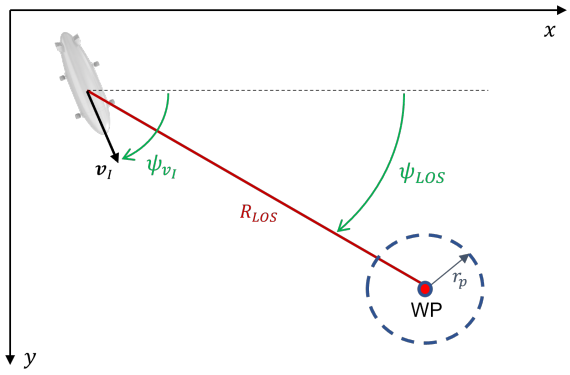

Figure 3.23: Illustration of proportional navigation guidance for waypoint navigation

The PN guidance law that provides the necessary yaw rate command for waypoint navigation is given as follows,

$$\dot{\psi}_{comm} = -N \frac{\|\boldsymbol{v}_I\|_d \sin(\psi_{\boldsymbol{v}_I} - \psi_{LOS})}{\|R_{LOS_{xy}}\|}$$

where N is the navigation constant, which is chosen to be 5 in this study. In addition, $R_{LOS_{xy}}$ is the projection of LOS vector to the horizontal plane. It is worth noting that this formulation provides a heading guidance in horizontal plane. The altitude difference between the waypoint and current location of the airship is handled by the altitude controller.

3.2.1.5 Simulation Results

This section summarizes the results of the implemented autonomous flight scenarios with integrated autopilot modes for the airship detailed in previous sections. To demonstrate the effectiveness of the developed autopilot modes, guidance, and control strategies, two practical scenarios, where patrolling and survey missions of an area are constructed, are considered. Constructed missions require the utilization of multiple autopilot modes and smooth transitions between them during the flight.

3.2.1.5.1 Patrolling Mission In this mission, patrolling of an area with the waypoint navigation is demonstrated. The mission consists of acceleration, climb, waypoint following, loiter, descent, and deceleration steps as shown with the mission profile of the flight in Figure 3.24. These steps are chosen to mimic a typical patrolling mission except the take-off and landing steps which are excluded in this study since they require a considerable amount of effort to find low airspeed trim conditions and to synthesize specifically designed controllers which are operating in highly nonlinear flight regime.

The mission starts with the airship having a forward speed of 6 m/s at the origin of Inertial frame. In the first step, airspeed change mode is employed to accelerate the airship to its designated cruise speed of 10 m/s. Afterwards, the altitude change is commanded to climb to 100 meters. Then, the mission mode is turned on for

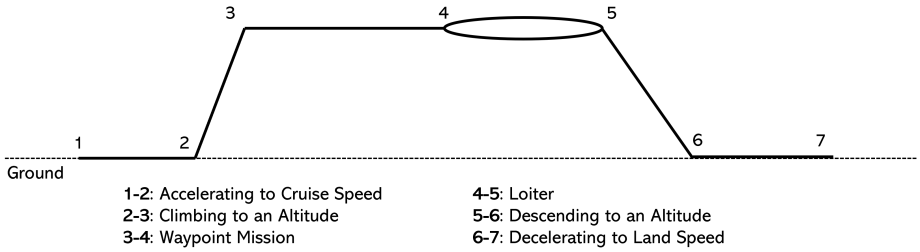

Figure 3.24: Illustration of the patrolling mission profile

the navigation of a series of predefined waypoints with the cruise speed. At the last waypoint of the mission, loiter command is called for a certain amount of time. In the last two steps of the mission, descending to the ground altitude and decelerating to the minimum speed of 6 m/s are performed. The trajectory of simulated vehicle is plotted from the isometric and top views in Figure 3.25.

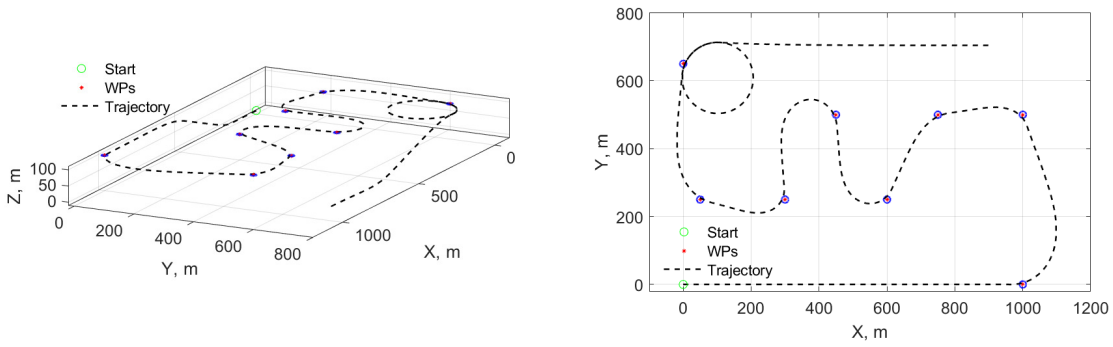

Figure 3.25: Isometric and top views of the patrolling mission trajectory

The time histories of the airship control inputs and states during the patrolling mission are presented in Figures 3.26 and 3.27. The acceleration to cruise speed at a constant altitude (can be seen in the first 20 seconds) is achieved by a smooth thrust command while keeping a constant pitch angle. The transition to altitude change

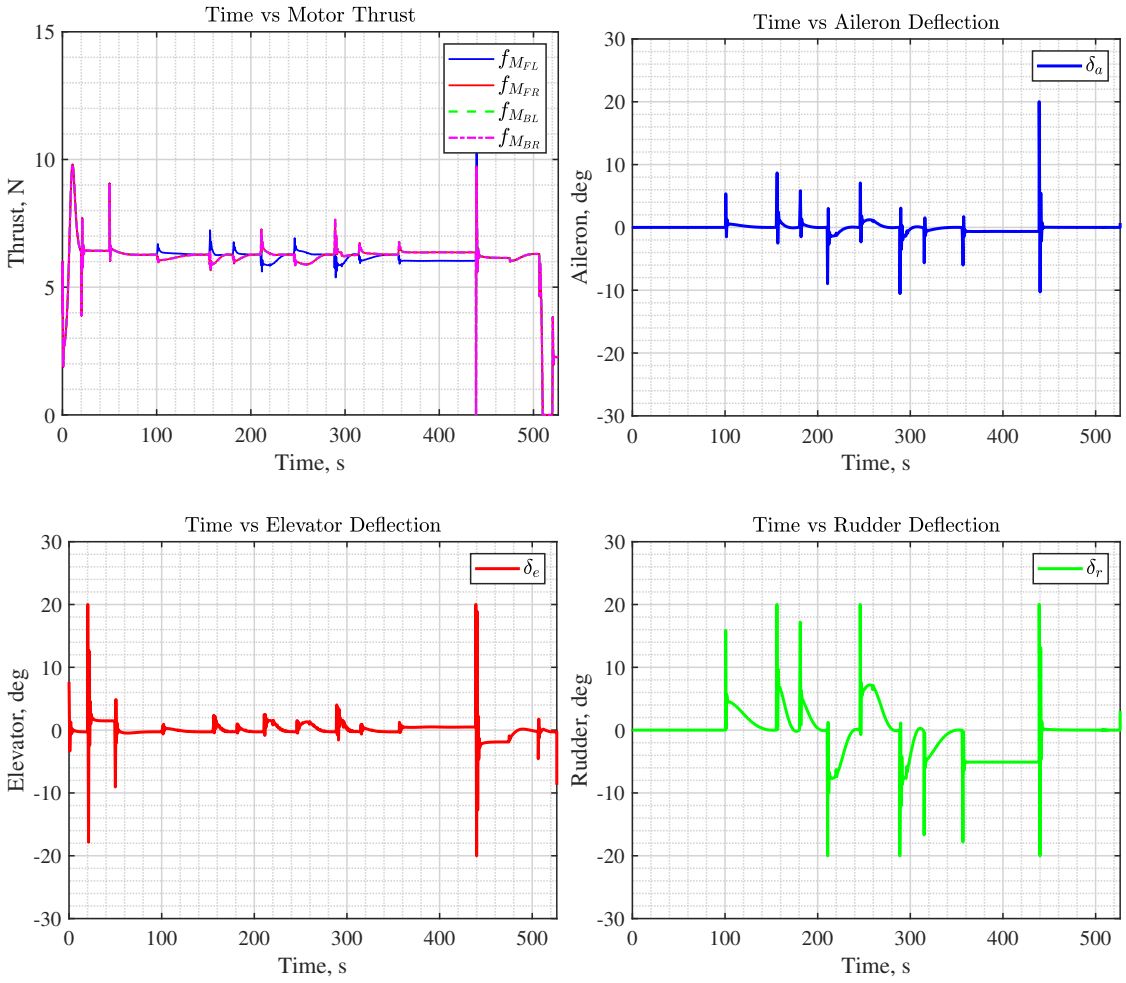

Figure 3.26: Time histories of the airship control inputs for patrolling mission

mode seems to require a quick change in angle of attack and pitch attitude, which results in sharp thrust and elevator inputs. Then, a smooth transition to the mission mode, which constitutes a large portion of the mission, occurs. It is clearly seen that the PN guidance law at the cruise speed provides satisfactorily smooth and consistent behavior while traversing the waypoints at a constant altitude. Following that the transition to loiter mode also takes place fluently by the help of swift and constant aileron and rudder deflections. Afterwards, the descent phase happens with relatively large pitch control similar to the climb. At the last step, the deceleration command

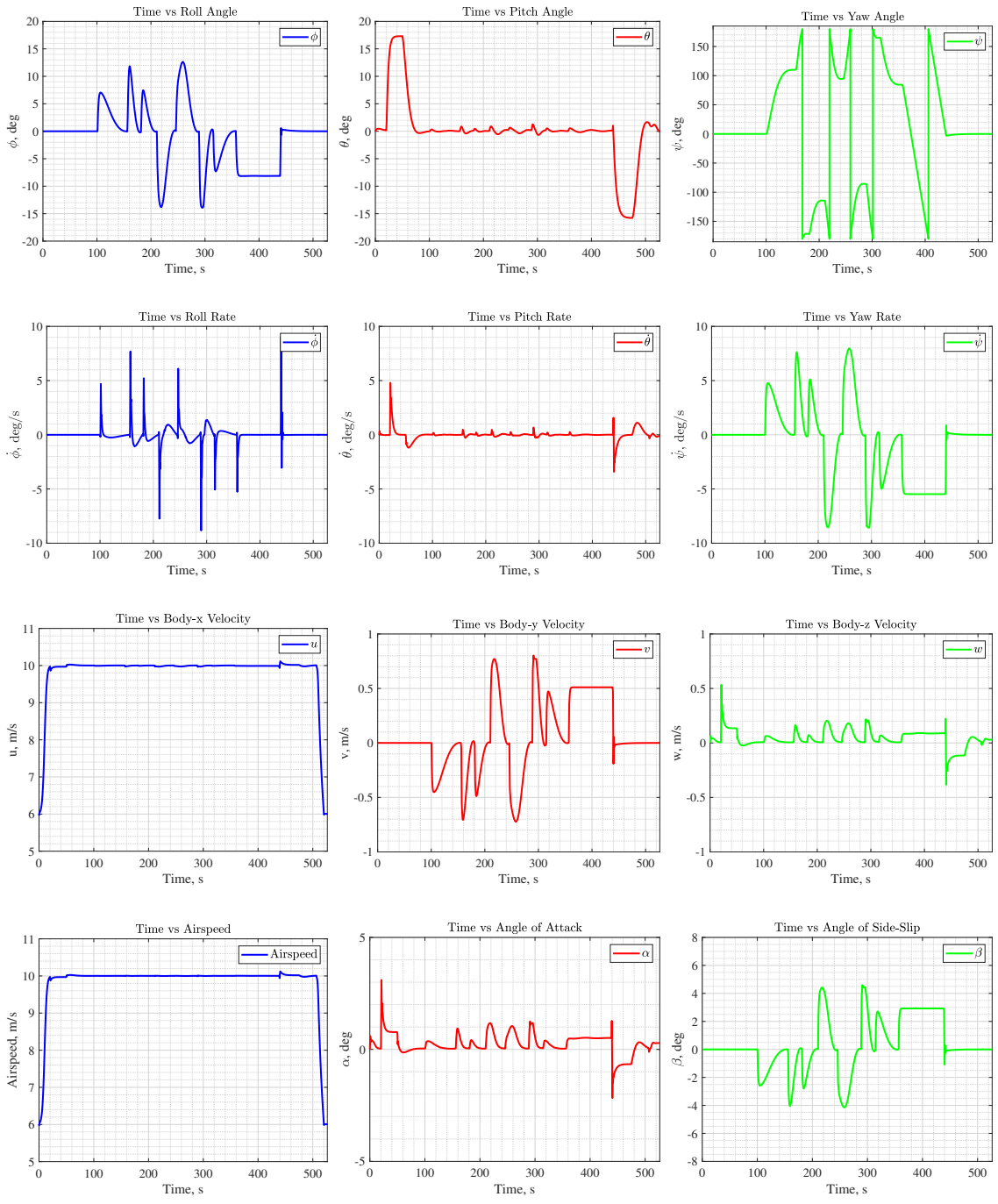

Figure 3.27: Time histories of the airship states for patrolling mission

is carried out, which basically cuts of the motor thrusts and allows drag to slow down the speed.

3.2.1.5.2 Survey Mission Similar to the patrolling mission, the survey mission also employs the waypoint navigation mode as the core element. However, in this scenario, instead of planar waypoints, the mission is constructed with varying elevation waypoints to mimic the surveying mission of an inclined terrain. The mission consists of acceleration, climb, waypoint following, and return-to-base steps as shown with the mission profile of the flight in Figure 3.28.

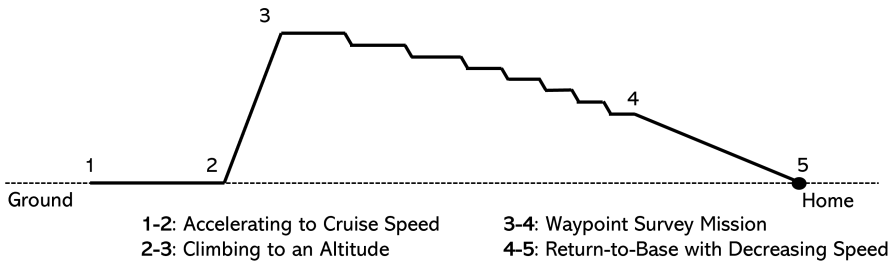

Figure 3.28: Illustration of the survey mission profile

The survey mission begins with the same two initial phases, which are the acceleration and climb steps, as in the patrolling mission. Afterwards, the series of sequential waypoints positioned at decreasing altitudes are followed by the airship in mission mode with the cruise speed. It is worth noting that the narrow turns with altitude change commands are successfully performed in this mission, which differentiates it from the previous scenario. In addition to that, the waypoint mission is followed by the return-to-base autopilot mode, where the vehicle is commanded to head towards the origin with a decreasing airspeed till the minimum speed is reached. The isometric and top views of the simulated trajectory are displayed in Figure 3.29.

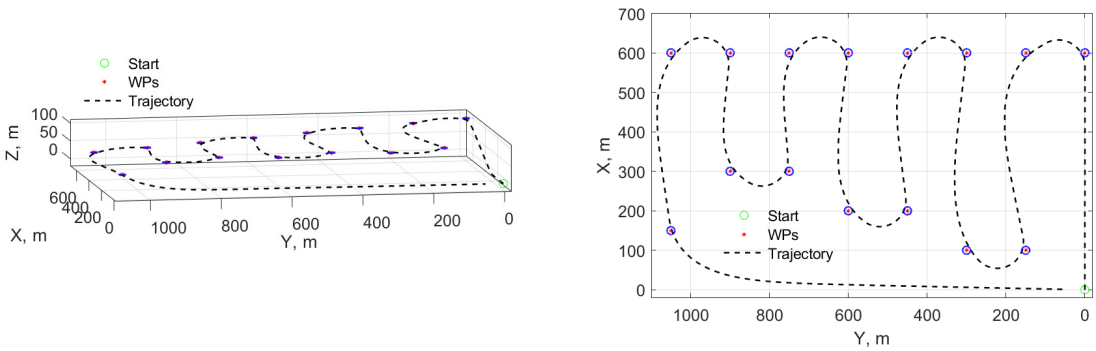

Figure 3.29: Isometric and top views of the survey mission trajectory

The time histories of the airship control inputs and states during the survey mission are given in Figures 3.30 and 3.31. Focusing on the mission mode section of the flight, it is clear that the response of airship is consistent and satisfactory during the altitude change and yaw rate commands with relatively sharp control input corrections. Finally, the return-to-base mode takes place at the end, where the change of airspeed, altitude and heading commands are implemented simultaneously to reach out the home location, which is particularly important to observe the smooth performance of such maneuver since it requires the range of varying trim conditions to work together cleanly.

Remark 3.2.5. *During the scenarios, actuators of the airship are simulated with a first order dynamics having time constants of 0.2 s and 1 s for motors and fin actuators, respectively.*

From the performance of implemented autonomous scenarios, the following undesirable behaviors are viewed. During the heading change maneuver after switching the waypoints for relatively large yaw variations, sharp rolling behavior is observed. During LQR design, instead of using the same penalty weights for all trim conditions,

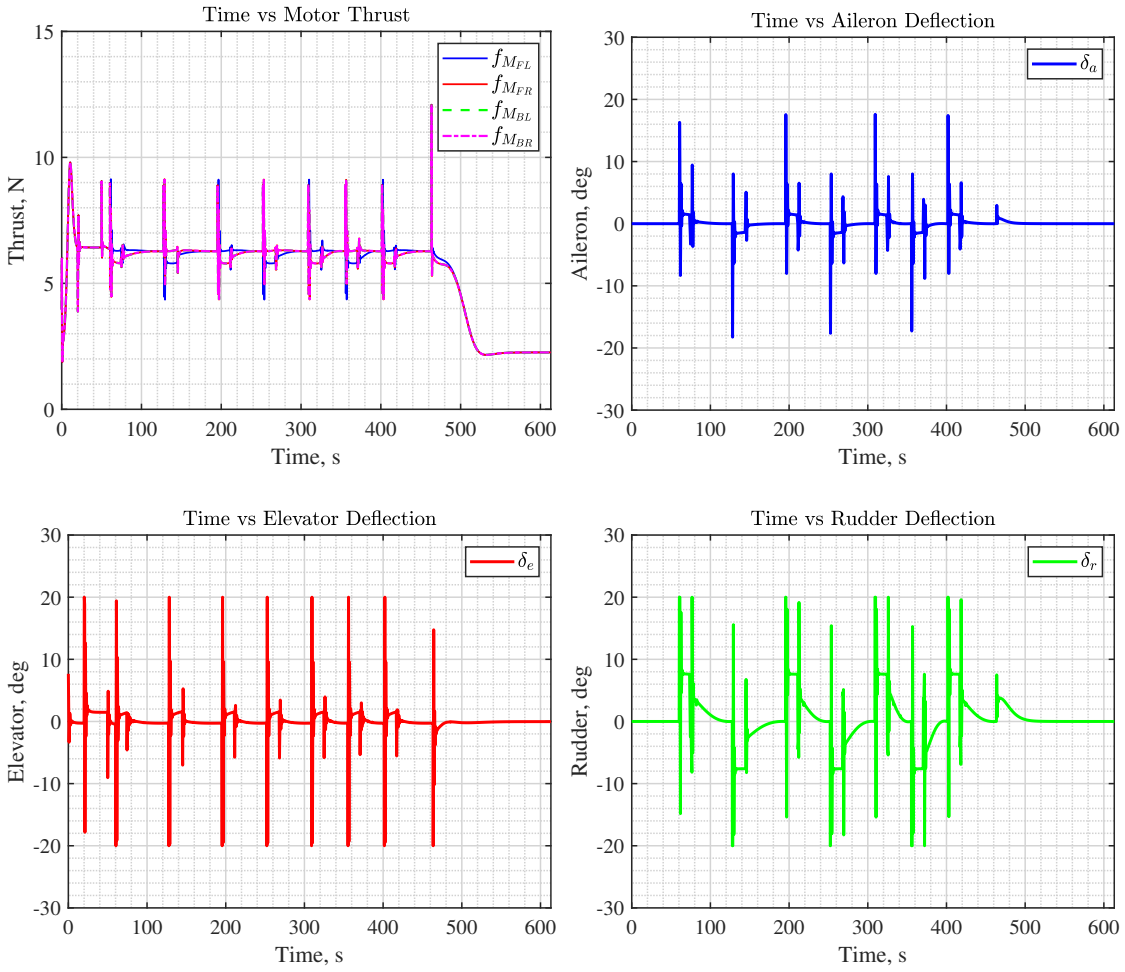

Figure 3.30: Time histories of the airship control inputs for survey mission

various heuristics can be employed to obtain smoother responses to the larger tracking errors. Alternatively, the other smoothing techniques can also be implemented to reduce the effects of such discrete switches.

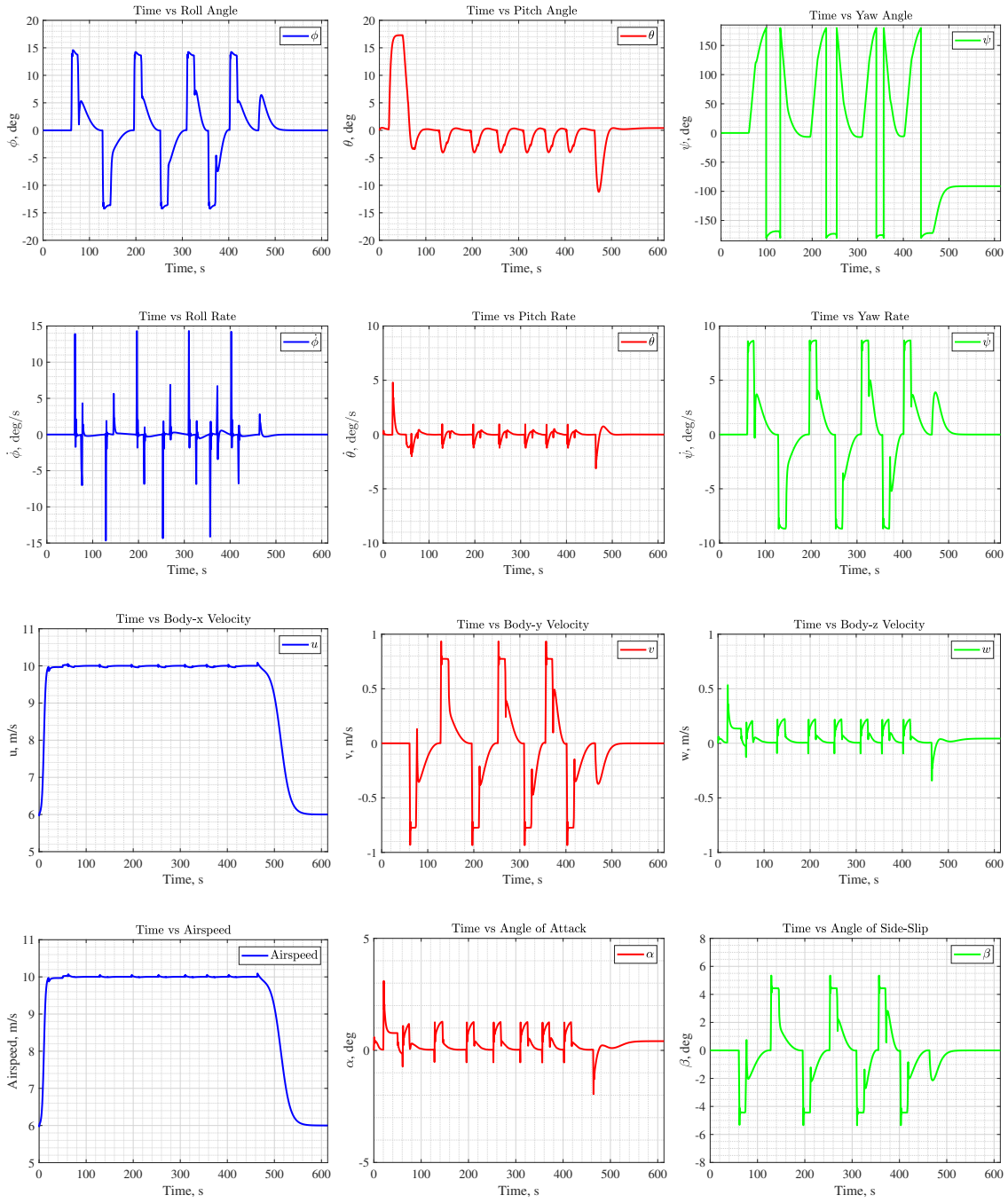

Figure 3.31: Time histories of the airship states for survey mission

3.2.2 Nonlinear Control

In this section, a nonlinear dynamic inversion (NDI) method is utilized for the inner-loop attitude and velocity control of the airship to track a desired trajectory. Firstly, the control affine form of the equations of motion is expressed. Then, benefiting from Lyapunov functions, the feedback linearization of the system is obtained and linear asymptotically stable tracking error functions are derived.

3.2.2.1 Nonlinear Dynamic Inversion

The compact form of the nonlinear equations for the airship dynamic model can be represented by

$$\dot{\boldsymbol{\xi}} = f(\boldsymbol{\xi}) + g(\boldsymbol{\xi}, \boldsymbol{\eta}) \tag{3.18}$$

where $f \in \mathbb{R}^6$, $g \in \mathbb{R}^{6\times 12}$, and the state and control vectors are as follows

$$\boldsymbol{\xi} = [u\ v\ w\ p\ q\ r]^T$$

$$\boldsymbol{\eta} = [f_{M_{FL}}\ f_{M_{FR}}\ f_{M_{BL}}\ f_{M_{BR}}\ \theta_{M_{FL}}\ \theta_{M_{FR}}\ \theta_{M_{BL}}\ \theta_{M_{BR}}\ \psi_{F_{TL}}\ \psi_{F_{TR}}\ \psi_{F_{BL}}\ \psi_{F_{BR}}]^T$$

where individual motor thrust and tilt angle are represented by f_M and θ_M with the subscripts as F for forward, B for backward, L for left, and R for right, which represents the location of motors with respect to the airship body frame origin. Similarly, the rudder deflections are denoted by ψ_F with the subscripts as T for top, B for bottom, and L and R for left and right, respectively.

However, Equation (3.18) is not in a control affine form due to the trigonometric relations between motor thrusts, f_M, and their orientations, θ_M. Applying the below transformation for motor control inputs,

$$\boldsymbol{f}_M = f_M \begin{bmatrix} \cos(\theta_M) \\ 0 \\ -\sin(\theta_M) \end{bmatrix} = \begin{bmatrix} \nu_H \\ 0 \\ \nu_V \end{bmatrix} \tag{3.19}$$

where the horizontal and vertical components of motor forces in the body frame are represented by virtual inputs, ν_H and ν_V. Control affine form of the equations can be obtained as follows,

$$\dot{\boldsymbol{\xi}} = f(\boldsymbol{\xi}) + \bar{g}(\boldsymbol{\xi})\bar{\boldsymbol{\eta}}$$

where the transformed control inputs become

$$\bar{\boldsymbol{\eta}} = [\nu_{H_{FL}}\ \nu_{H_{FR}}\ \nu_{H_{BL}}\ \nu_{H_{BR}}\ \nu_{V_{FL}}\ \nu_{V_{FR}}\ \nu_{V_{BL}}\ \nu_{V_{BR}}\ \psi_{F_{TL}}\ \psi_{F_{TR}}\ \psi_{F_{BL}}\ \psi_{F_{BR}}]^T \tag{3.20}$$

Assumption 3.2.1. *Rudder deflections for the airship are utilized only for the compensation of desired moment to control vehicle attitude. With this assumption and current set of control actuation, the airship becomes an under-actuated system since there is no controlled side force generation. Therefore, the available control authority is limited to the forward and vertical linear accelerations, and the angular acceleration. For this reason, the system is decomposed into the controllable subsystem and internal dynamics.*

The controllable states are $\boldsymbol{\zeta} = [u\ w\ p\ q\ r]^T$ and the reduced system is defined below,

$$\dot{\boldsymbol{\zeta}} = h(\boldsymbol{\xi}) + b(\boldsymbol{\xi})\bar{\boldsymbol{\eta}} \tag{3.21}$$

To design a trajectory tracking controller, we benefited from Lyapunov's direct method. Firstly, the trajectory tracking error is defined as follows,

$$\boldsymbol{e} = \boldsymbol{\zeta}_d - \boldsymbol{\zeta}$$

where the desired state trajectory is denoted by $\boldsymbol{\zeta}_d$. Then, a scalar semi-positive definite Lyapunov candidate function, i.e. $\mathbb{V}_{LFC}(0) = 0$ and $\mathbb{V}_{LFC}(\boldsymbol{e}) > 0$ for any $\boldsymbol{e} \neq 0$, is constructed below,

$$\mathbb{V}_{LFC} = \frac{1}{2}\boldsymbol{e}^T\boldsymbol{e} \tag{3.22}$$

For the systems that have an asymptotically stable tracking behavior, the energy-like candidate function must be monotonically decreasing so that a stable equilibrium state in the sense of Lyapunov can be achieved. The rate of change for Equation (3.22) is obtained by

$$\begin{aligned}\dot{\mathbb{V}}_{LFC} &= \boldsymbol{e}^T\dot{\boldsymbol{e}} \\ &= \boldsymbol{e}^T\left(\dot{\boldsymbol{\zeta}}_d - h(\boldsymbol{\xi}) - \boldsymbol{\mu}\right)\end{aligned} \tag{3.23}$$

where a virtual control input, $\boldsymbol{\mu} \in \mathbb{R}^5$, is defined from Equation. (3.21) as $\boldsymbol{\mu} = b(\boldsymbol{\xi})\bar{\boldsymbol{\eta}}$.

Finally, one of the potential control laws that satisfies the negative definite energy rate condition in Equation (3.23), is selected as follows

$$\boldsymbol{\mu} = \dot{\boldsymbol{\zeta}}_d - h(\boldsymbol{\xi}) + \boldsymbol{K}_{\boldsymbol{\zeta}}\boldsymbol{e} \tag{3.24}$$

where $\boldsymbol{K}_{\boldsymbol{\zeta}} \in \mathbb{R}^{5\times5}$ is a positive definite proportional feedback gain matrix for the state tracking error, which yields an exponentially stable tracking error dynamics, $\dot{\boldsymbol{e}} + \boldsymbol{K}_{\boldsymbol{\zeta}}\boldsymbol{e} = 0$.

Remark 3.2.6. *The internal dynamics of the system, which corresponds to the side velocity v, is investigated by plotting the phase plot for varying side-slip conditions and airspeed in Figure 3.32, where the rudder deflections are kept in neutral position. As can be expected and desired from an airship with stabilizing fins, a stable response with $v\dot{v} < 0$ condition for $v \neq 0$ is shown in this graph, although the side velocity is not controlled by the control inputs. It can be seen that the zero side velocity is the equilibrium state for the internal dynamics.*

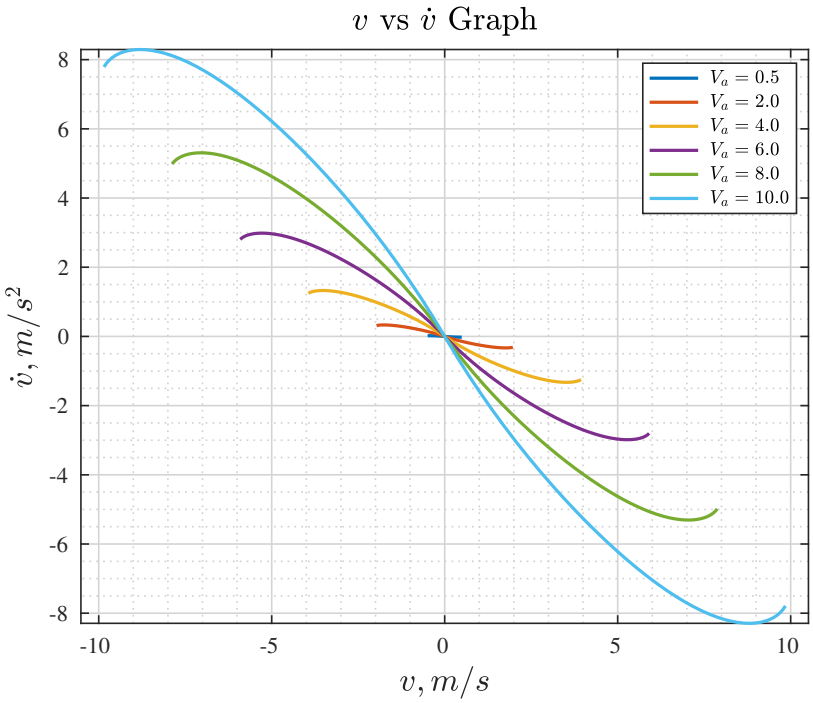

Figure 3.32: Internal dynamics stability analysis by the illustration of v vs $\dot{v}$ phase plot

3.2.2.2 Control Allocation

After obtaining the desired virtual control law in Equation (3.24), the next step is to find the actual control inputs to the actuators of the airship, η, which poses a control allocation problem. Since the aerodynamic control surfaces require a certain level of airflow to sufficiently operate, this problem is investigated under two operating conditions, where the airship is hovering or near hover flight regime with less than a 3 m/s airspeed and the forward flight regime with higher airspeeds, respectively. Hence, individual control allocation strategies are implemented for corresponding flight conditions.

3.2.2.2.1 Hover Flight In hover and near hover conditions, only the thrusters and tilt servo inputs are allocated for control, whereas the rudders are kept in the neutral position. Thus, the control input vector in Equation (3.20) is effectively reduced to only horizontal and vertical virtual motor thrusts, $\bar{\boldsymbol{\eta}}_{hv} = [\nu_{H_{FL}}\ \nu_{H_{FR}}\ \nu_{H_{BL}}\ \nu_{H_{BR}}\ \nu_{V_{FL}}\ \nu_{V_{FR}}\ \nu_{V_{BL}}\ \nu_{V_{BR}}]^T$. The corresponding control allocation problem for this condition is defined as follows

$$\boldsymbol{\mu} = \bar{\boldsymbol{b}}_{hv}(\boldsymbol{\xi})\bar{\boldsymbol{\eta}}_{hv} \tag{3.25}$$

where $\bar{\boldsymbol{b}}_{hv} \in \mathbb{R}^{5\times 8}$ is the control effectiveness matrix for the virtual motor thrusts during the hover flight. Equation (3.25) can be solved by a general Moore-Penrose inverse as

$$\begin{aligned} \bar{\boldsymbol{\eta}}_{hv} &= \bar{\boldsymbol{b}}_{hv}^{\dagger}\boldsymbol{\mu} \\ &= \bar{\boldsymbol{b}}_{hv}^{T}\left(\bar{\boldsymbol{b}}_{hv}\bar{\boldsymbol{b}}_{hv}^{T}\right)^{-1}\boldsymbol{\mu} \end{aligned} \tag{3.26}$$

Finally, using the inverse transformation of Equation (3.19), the individual thrust, f_M, and tilt angle of the motor pods, θ_M, are found from virtual motor thrusts, ν_H and ν_V, as

$$f_M = \sqrt{\nu_H^2 + \nu_V^2} \tag{3.27}$$

$$\theta_M = \text{atan2}(-\nu_V, \nu_H) \tag{3.28}$$

3.2.2.2.2 Forward Flight In the forward flight regime, all control actuations are utilized during control allocation. However, a method similar to daisy chaining algorithm, described in Refs. [94,95], is employed by distributing the desired force and moment between thrusters and rudders while reducing the utilization of tilt servos in the allocation process due to their relatively slow dynamics in general. In this method, first, the moment generation is assigned to the rudders, where the effect of the rudder

drag forces is neglected, and the rudder deflections, $\boldsymbol{\psi}_F = [\psi_{F_{TL}}\ \psi_{F_{TR}}\ \psi_{F_{BL}}\ \psi_{F_{BR}}]^T$, providing the desired torque are found. Then, the aerodynamic forces, including the drag, generated by the deflection of the rudders in the body frame are calculated. Also, the moment acting on the airship due to the rudder drag forces is computed. Finally, the desired forces including the compensation of the rudder forces and moments due to rudder deflections are assigned to the thrusters. The steps for the control allocation in this flight regime is provided below. For given desired force and moment inputs, found in Equation (3.24),

$$\boldsymbol{\mu} = \begin{bmatrix} \mu_x \\ \mu_z \\ \mu_p \\ \mu_q \\ \mu_r \end{bmatrix} = \begin{bmatrix} \boldsymbol{\mu}_f \\ \boldsymbol{\mu}_\tau \end{bmatrix}$$

1. Solve $\boldsymbol{\mu}_\tau = \bar{\boldsymbol{b}}_{\psi_F}(\boldsymbol{\xi})\boldsymbol{\psi}_F$ for rudder deflections, $\boldsymbol{\psi}_F$, satisfying the desired torque, $\boldsymbol{\mu}_\tau \in \mathbb{R}^3$.

$$\boldsymbol{\psi}_F = \bar{\boldsymbol{b}}_{\boldsymbol{\psi}_F}^T \left(\bar{\boldsymbol{b}}_{\boldsymbol{\psi}_F} \bar{\boldsymbol{b}}_{\boldsymbol{\psi}_F}^T\right)^{-1} \boldsymbol{\mu}_\tau$$

   where $\bar{\boldsymbol{b}}_{\boldsymbol{\psi}_F} \in \mathbb{R}^{3\times 4}$ is the control effectiveness matrix for the rudder deflections, neglecting the effect of aerodynamic drag on the body moment.

2. Compute the aerodynamic forces of the rudders in the body frame due to the deflections found in the previous step.

$$\begin{bmatrix} f_{X_{rud}} \\ f_{Y_{rud}} \\ f_{Z_{rud}} \end{bmatrix} = \sum_{i=1}^{4} \boldsymbol{R}_{BF}(\phi_F^i) q_{0_F}^i S_F \left(\Delta C_L(\psi_{F^i})\boldsymbol{e}_2 - \Delta C_D(\psi_{F^i})\boldsymbol{e}_1\right)$$

3. Calculate the moment generated by the rudder drag force. Since it was neglected in the first step, the remaining control inputs need to compensate it.

$$\begin{bmatrix} \tau_{X_{rud}} \\ \tau_{Y_{rud}} \\ \tau_{Z_{rud}} \end{bmatrix} = \sum_{i=1}^{4} \boldsymbol{\rho}_F^i \times \left[-\boldsymbol{R}_{BF}(\phi_F^i) q_{0_F}^i S_F \Delta C_D(\psi_{F^i}) \boldsymbol{e}_1 \right]$$

4. Find the motor thrusts generating the desired forces in the body $x-$ and z-axes while compensating the rudder forces as in Equation (3.26).

$$\bar{\boldsymbol{\eta}}_{hv} = \bar{\boldsymbol{b}}_{hv}^T \left(\bar{\boldsymbol{b}}_{hv} \bar{\boldsymbol{b}}_{hv}^T \right)^{-1} \begin{bmatrix} \mu_x - f_{X_{rud}} \\ \mu_z - f_{Z_{rud}} \\ -\tau_{X_{rud}} \\ -\tau_{Y_{rud}} \\ -\tau_{Z_{rud}} \end{bmatrix}$$

Finally, using Equations (3.27) and (3.28) relations for each pairs of ν_H and ν_V in $\bar{\boldsymbol{\eta}}_{hv}$, the individual motor thrust and tilt angle are found for the airship in the forward flight condition.

Figure 3.33 summarizes the overall control structure of the airship, where the separate subsystems and their feedback loops can be seen clearly. The guidance block takes the waypoint positions from the trajectory generator and the lateral acceleration command from the collision avoidance subsystem, if there is any, and provides the commanded trajectory in terms of ground speed, V_c, heading, ψ_c, yaw rate, $\dot{\psi}_c$, altitude, z_c, and the climb rate, $\dot{z}_c$. Moreover, the airship is commanded to have zero roll and pitch angles at all times, i.e. $\phi_c = \theta_c = 0$. Using rotational kinematics equations and wind velocities, $\boldsymbol{v}_W$, the complete commanded state trajectory, $\boldsymbol{\zeta}_c$, can easily be obtained from the guidance inputs. The desired state trajectory, $\boldsymbol{\zeta}_d$, and its rate of change, $\dot{\boldsymbol{\zeta}}_d$, are found by implementing a first order filter with the dynamics of

$\dot{\boldsymbol{\zeta}}_d = \boldsymbol{\Omega}_{\boldsymbol{\zeta}}(\boldsymbol{\zeta}_c - \boldsymbol{\zeta}_d)$, where $\boldsymbol{\Omega}_{\boldsymbol{\zeta}}$ is the diagonal bandwidth matrix for the corresponding states.

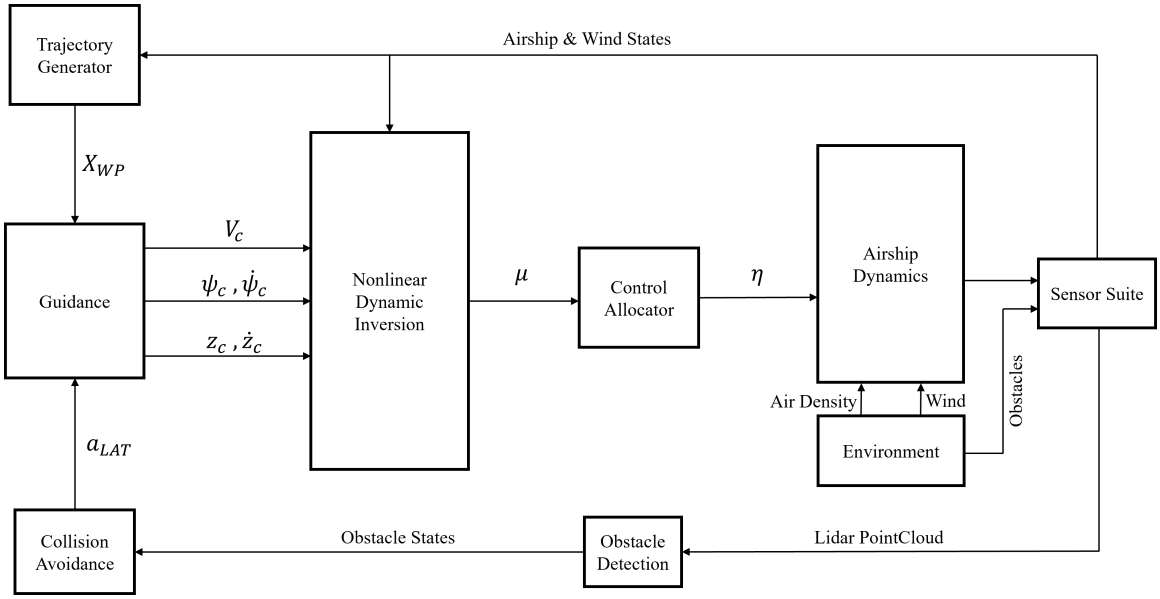

Figure 3.33: The overall NDI control system of the airship

Remark 3.2.7. *The control allocation strategy for the forward flight mode provided above assumes that the actuation in motor tilt mechanism has fast enough dynamics to cope with desired acceleration requirement. However, if an undesired delay in the tilt actuation occurs, this would create an additional delayed dynamics which can cause an unstable behavior. For this reason, the tilt angles of motor pods can be locked at a certain angle such as neutral position where the forces align with body-x axis and necessary guidance strategy can be implemented to adjust the vehicle attitude to guide the airship along the desired trajectory since the effective vertical force cannot be generated with this configuration. Section 3.2.2.3 introduces a total energy control system (TECS) to control airship's pitch angle, total thrust, and climb rate similar to the method implemented in fixed-wing aircraft.*

3.2.2.3 Total Energy Control System Altitude Control

This section introduces a total energy control system (TECS) method to control the airspeed and altitude of the airship smoothly. This concept uses the conservation of energy principle by assuming that for a given total energy, kinetic energy of the aircraft can be converted to potential energy, or vice versa, and only way to change the total energy of the system is through thrust and drag forces. The reference work in [96, 97] have qualitative and quantitative detailed explanations of TECS concept and its implementation in airplanes. In this work, a modified version of Ref. [97] is derived to establish a relation between airspeed, pitch angle, total thrust, and climb rate of the airship so that when the motor pods are locked facing forward, the altitude change maneuver can be smoothly handled.

Total energy of the system is obtain by the sum of potential, E_p, and kinetic, E_k, energy as follows,

$$E_T = E_p + E_k = mgh + \frac{1}{2}mV_T^2$$

where $V_T = \sqrt{u^2 + v^2 + w^2}$ refers to the true airspeed and h is the altitude.

Rate of change of total energy can be derived by

$$\dot{E}_T = mg\dot{h} + mV_T\dot{V}_T$$

Although knowing total energy level of the system provides information about total capability, it does not yield how the energy is distributed among kinetic and potential energies. For this reason, energy distribution quantity, E_D, is defined as

$$E_D = mgh - \frac{1}{2}mV_T^2$$

and the rate of change of energy distribution is obtained below,

$$\dot{E}_D = mg\dot{h} - mV_T\dot{V}_T = 2mg\dot{h} - \dot{E}_T$$

Acceleration in true airspeed can be computed by employing Newton's 2^{nd} law of motion as

$$\dot{V}_T = \frac{F_x \cos(\alpha)\cos(\beta) + F_y \sin(\beta) + F_z \sin(\alpha)\cos(\beta)}{m} \tag{3.29}$$

where F_x, F_y, and F_z are the force components acting along the body axes of airship including controlled and uncontrolled forces.

In order to derive an asymptotically stable response, again, we benefited from a scalar semi-positive definite Lyapunov candidate function below,

$$\mathbb{V} = \frac{1}{2}\tilde{E}_T^2 + \frac{1}{2}\tilde{E}_D^2$$

where $\tilde{E}_T = E_{T_d} - E_T$ and $\tilde{E}_D = E_{D_d} - E_D$.

The rate of change of candidate function is

$$\begin{aligned} \dot{\mathbb{V}} &= \tilde{E}_T \dot{\tilde{E}}_T + \tilde{E}_D \dot{\tilde{E}}_D \\ &= \tilde{E}_T \left(\dot{E}_{T_d} - mg\dot{h} - mV_T \dot{V}_T \right) \\ &+ \tilde{E}_D \left(\dot{E}_{D_d} - 2mgV_T \sin(\gamma) + \dot{E}_T \right) \end{aligned} \tag{3.30}$$

where the relation between flight path angle, climb rate and true airspeed below is used.

$$\sin(\gamma) = \frac{\dot{h}}{V_T}$$

The first part of the equation corresponding to controlling total energy level of the system can be used to compute total commanded net force along body x-axis, F_x^c, utilizing Equation (3.29),

$$F_x^c = -\frac{F_y \sin(\beta) + F_z \sin(\alpha)\cos(\beta)}{\cos(\alpha)\cos(\beta)} + \frac{\dot{E}_{T_d} - mg\dot{h} + K_T \tilde{E}_T}{V_T \cos(\alpha)\cos(\beta)} \tag{3.31}$$

where K_T is a positive scalar for feedback gain. Also, the required change in total motor thrust, ΔT, can be found by

$$\Delta T = F_x^c - F_x$$

On the other hand, by substituting Equation (3.31) in $\dot{E}_T$, the second part of Equation 3.30 corresponding to system's energy distribution can be used to compute commanded flight path angle, γ^c, which controls the climb rate. Furthermore, by assuming a negligible angle of attack, $\alpha \approx 0$, the pitch angle command can be computed by using the relation, $\theta = \gamma + \alpha$.

$$\sin(\gamma^c) = \frac{\dot{E}_{D_d} + \dot{E}_{T_d} + K_T\tilde{E}_T + K_D\tilde{E}_D}{2mgV_T} = \frac{\dot{h}_d}{V_T} + \frac{K_1\tilde{E}_P + K_2\tilde{E}_K}{2mgV_T} \tag{3.32}$$

where $K_1 = K_T + K_D$ and $K_2 = K_T - K_D$ are positive scalar feedback gains for the total energy and energy distribution errors and they are conditioned to be $K_D > K_T$.

Applying the computed commands derived in Equations (3.31) and (3.32), we obtain a negative definite rate of change in Equation (3.30), which proves the stability in the sense of Lyapunov.

$$\dot{\mathbb{V}} = -K_T\tilde{E}_T^2 - K_D\tilde{E}_D^2$$

3.2.2.4 Guidance Laws

This section introduces several autopilot modes, consisting of take-off, landing, waypoint navigation, and collision avoidance phases, that are utilized during a flight mission. The guidance laws corresponding to these modes are formulated below.

3.2.2.4.1 Take-off & Landing Mode In this work, take-off and landing modes both require a stationary waypoint with respect to Inertial frame even though the airship may have relative speed with respect to the surrounding air. Both modes

utilize the same guidance strategy to reach the designated waypoint and keep the airship stationary in Inertial frame at that position. The strategy to guide the airship to a take-off or landing waypoint involves the following steps.

The relative position vector of the waypoint from the current airship location in the body frame, $\boldsymbol{r}_p$, and its unit vector, $\hat{\boldsymbol{r}}_p$, are found by

$$\boldsymbol{r}_p = \boldsymbol{R}_{BI}\left(\boldsymbol{x}_{WP} - \boldsymbol{x}_I\right)$$
$$\hat{\boldsymbol{r}}_p = \frac{\boldsymbol{r}_p}{||\boldsymbol{r}_p||} = \begin{bmatrix} r_{p_x} & r_{p_y} & r_{p_z} \end{bmatrix}^T$$

where $\boldsymbol{x}_I$ and $\boldsymbol{x}_{WP}$ are the inertial positions of the airship and the waypoint, respectively.

The magnitude and direction of the relative position vector, $\boldsymbol{r}_p$, can be employed to generate the necessary guidance commands driving the airship towards the waypoint. Since the side-velocity of the airship in this study is not controlled, resulting in a non-holonomic system, flying towards a certain direction requires the adjustment of heading first so that the inertial velocity vector can be aligned along the desired direction. In addition, the wind speed has to be accounted for while adjusting the heading. Considering the wind speed, represented in the body frame as $[W_u \; W_v \; W_w]^T = \boldsymbol{R}_{BI}\boldsymbol{v}_W$, and the side component of $\hat{r}_p$, the yaw rate command is formulated below,

$$\dot{\psi}_c = \frac{|\dot{\psi}^H_{max}|}{2}\left(\max\left(\min\left(r_{p_y}, 1\right), -1\right) - \max\left(\min\left(\frac{W_v}{\|u^H_{max}\|}, 1\right), -1\right)\right) \tag{3.33}$$

where u^H_{max} and $\dot{\psi}^H_{max}$ represent the maximum allowed forward speed and yaw rate in take-off and landing modes, respectively. While the first term inside the parentheses in Equation (3.33) turns the airship nose towards the waypoint in the $xy-$plane, the second term corrects the attitude towards the direction opposite to the wind. The combined transient effect smoothly guides the heading of airship while compensating

the wind. It is worth noting that as getting closer to the waypoint, $||\boldsymbol{r}_p|| \rightarrow 0$, the heading is getting aligned with the opposite direction of the wind similar to a windsock.

Along with the yaw rate command in Equation (3.33), the airship has to be commanded with a linear velocity to reach the waypoint. A simple approach that adjusts the forward and vertical airspeed components of the airship while compensating the wind velocity is implemented in Equations (3.34)-(3.35).

$$u_c = \max\left(\min\left(r_{p_x} - W_u, |u^H_{max}|\right), 0\right) \tag{3.34}$$

$$w_c = \max\left(\min\left(r_{p_z} - W_w, |w^H_{max}|\right), -|w^H_{max}|\right) \tag{3.35}$$

where w^H_{max} represents the maximum allowed vertical speed in take-off and landing modes. Given that the change in the wind velocity is relatively small, the implementation of velocity and yaw rate commands formulated above results in a smooth position control behavior.

3.2.2.4.2 Waypoint Navigation Mode Apart from take-off and landing phases, an autonomous flight mission requires a mission consisting of certain objectives, which are generally positioned at specific waypoints. Therefore, a waypoint tracking algorithm, adopted from the fixed-wing aircraft waypoint navigation study in Ref. [98], is implemented for the planar waypoint navigation of the airship in this work. Figure 3.34 illustrates the vectors and angles involved with the calculation of the guidance command for the airship traveling from waypoint A to waypoint B on a straight line with a constant speed where P represents the current position of the airship in $xy-$plane. The guidance strategy aims to eliminate the cross track error from the path, denoted by $\boldsymbol{d}$, by finding the yaw rate command to drive the airship to a

reference position at a specific look-ahead distance, L_1, along the straight line path between the waypoints.

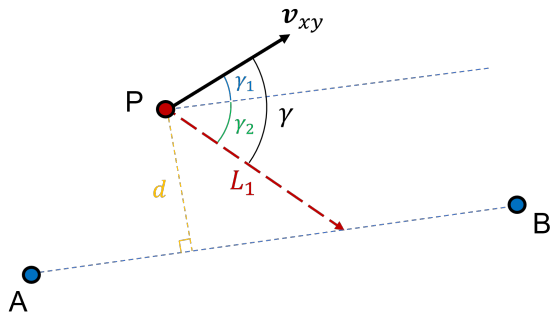

Figure 3.34: Waypoint tracking on a straight line segment

The cross velocity, $\boldsymbol{v}_\perp \in \mathbb{R}^2$, and the velocity parallel to the path, $\boldsymbol{v}_\parallel \in \mathbb{R}^2$, are calculated by using the planar inertial velocity of the airship, $\boldsymbol{v}_{xy}$, and the waypoint vectors as follows,

$$\boldsymbol{v}_\perp = \boldsymbol{v}_{xy} \times \frac{\overrightarrow{AB}}{|\overrightarrow{AB}|} \tag{3.36}$$

$$\boldsymbol{v}_\parallel = \boldsymbol{v}_{xy} \cdot \frac{\overrightarrow{AB}}{|\overrightarrow{AB}|} \tag{3.37}$$

The cross track error from the current position of the airship to the straight line segment between the waypoints are found by Equation (3.38),

$$\boldsymbol{d} = \overrightarrow{AP} \times \frac{\overrightarrow{AB}}{|\overrightarrow{AB}|} \tag{3.38}$$

The angle between the current inertial velocity vector and the desired position vector to the look-ahead reference position is defined by γ and it is composed of the summation of angles γ_1 and γ_2, $\gamma = \gamma_1 + \gamma_2$, which have the below trigonometric relations to Equations (3.36)-(3.38).

$$\gamma_1 = \text{atan2}\left(\boldsymbol{v}_\perp, \boldsymbol{v}_\parallel\right)$$

$$\gamma_2 = \begin{cases} \text{asin}\left(\frac{d}{L_1}\right), & \sin(\frac{-\pi}{4}) \leq \frac{d}{L_1} \leq \sin(\frac{\pi}{4}) \\ -\frac{\pi}{4}, & \frac{d}{L_1} < \sin(\frac{-\pi}{4}) \\ \frac{\pi}{4}, & \sin(\frac{\pi}{4}) < \frac{d}{L_1} \end{cases}$$

where γ_2 angle is constrained between ± 45 degrees to achieve smoother turns during the correction, especially for larger cross track error cases.

Finally, the lateral acceleration required to turn the velocity vector to track the desired position vector is found by the guidance law below,

$$a_{LAT} = k_L \frac{\|\boldsymbol{v}_{xy}\|^2}{L_1} \sin(\gamma)$$

where k_L is the proportional gain to adjust the response of airship to the waypoint tracking on a straight line. The necessary yaw rate command for the airship can be extracted as follows,

$$\begin{aligned} \dot{\psi}_c &= \frac{a_{LAT}}{\|\boldsymbol{v}_{xy}\|} \\ &= k_L \frac{\|\boldsymbol{v}_{xy}\|}{L_1} \sin(\gamma) \end{aligned}$$

Remark 3.2.8. *The waypoint navigation mode employs a proportional (P) controller to regulate the forward speed of airship to the commanded speed between the waypoints. Similarly, a proportional-derivative (PD) controller is utilized for the altitude control.*

3.2.2.5 Simulations Results

In this section, details of the simulation environment, an autonomous waypoint navigation mission scenario, and the simulation results are provided.

3.2.2.5.1 Simulation Environment In order to effectively demonstrate the integration of nonlinear control, control allocation and various guidance modes, we have benefited from a software in the loop process (SITL), PX4-SITL autopilot stack. SITL simulations allow us to investigate how the individual modules of the system, as described in Figure 3.33, collaborate as if how they work in the actual physical system. Moreover, along with PX4-SITL, Gazebo simulation environment is utilized to simulate the dynamics, sensors, actuators, and the environment. In short, a new custom airship airframe is developed in PX4 software stack and it is integrated with Gazebo to run in SITL mode by the use of necessary plugins and custom packages that are developed in Gazebo and the Robot Operating System (ROS), which provides a reliable communication and network between components of the system.

3.2.2.5.2 Mission Map An autonomous mission scenario is constructed with the waypoints shown in Figure 3.35. A flight test aiming for the demonstration of wind effect on the trajectory tracking during the waypoint navigation mission is planned.

The autonomous mission consists of a series of waypoints along a rectangular trajectory displayed on the ground control station mission view in Figure 3.35. The mission requires a take-off item on the lower left corner to the altitude of 25 meters. After reaching to the designated altitude, the remaining waypoints of mission commands a cruise flight with 10 m/s airspeed while tracking straight line trajectories between the waypoints if not obstructed. Finally, the last two items of the mission involve slowing down to 4 m/s and landing maneuver at the start location.

There are two flight cases implemented for the same mission under varying wind conditions. The first flight case represents a flight condition where there is no wind, whereas the second case introduces constant and steady wind blowing from North to

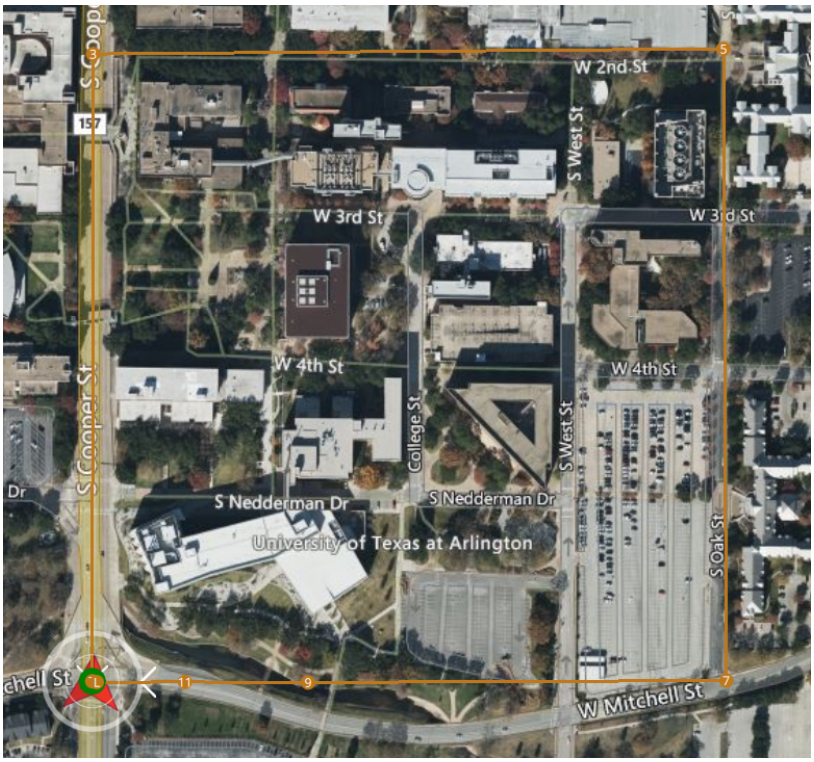

Figure 3.35: Illustration of mission waypoints over QGroundControl (GCS) map view

South direction with the velocity of 4 m/s with respect to the Inertial frame. The airship is expected to carry out the designated flight mission while minimizing the wind effect on the trajectory tracking along the mission waypoints.

In Figure 3.36, the trajectory of airship is compared for both no wind and 4 m/s wind conditions, where the blue and red color depictions are used, respectively. Heading attitude of the airship along the trajectory is also illustrated by plotting an airship shaped marker over the trajectories at various representative timings for a better comparison. As can be seen from the North and South legs of the trajectory in the figure, airship aligns its heading according to the wind vector so that the inertial velocity vector follows the desired tracking response. In addition, since the airship is commanded to travel with constant airspeed, the effect of decreased and increased ground speed due to the wind on various segments of the trajectory, especially during

the turns, are clearly visible. This result establishes a ground to conclude that the overall control and guidance subsystems along with the control allocation method of the airship implemented for this study effectively collaborate and handle the desired varying guidance and control commands.

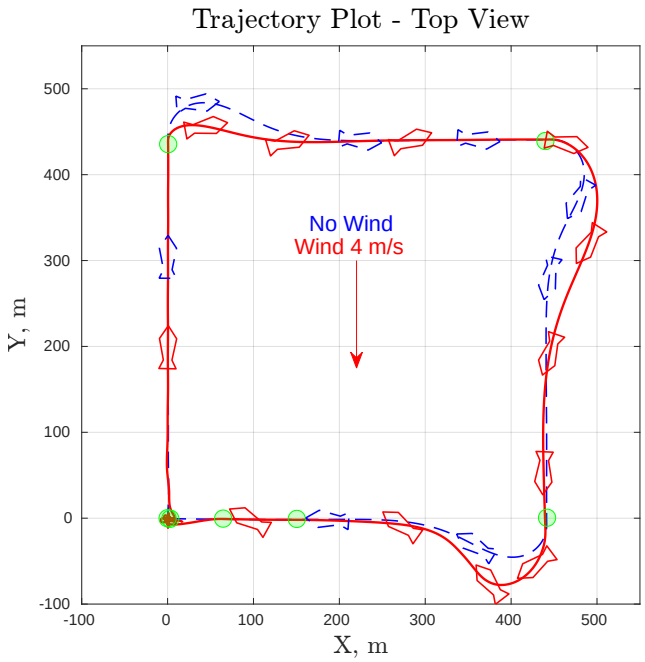

Figure 3.36: Trajectory comparison of the airship for no wind and 4 m/s North wind conditions

Time histories of the states and control inputs of the airship for the 4 m/s wind test condition are plotted in Figure 3.37. The left column in the figure consists of the body velocities, Euler angles, and Euler rates of the airship from top to bottom, while the right column yields the individual control inputs in the order of motor forces, tilt angles, and rudder deflections, consecutively. The naming convention for the control inputs follow the corresponding location of the individual actuators such as FL for the forward left, BR for the backward right, TL for the top left, and so on. The figures include the response of airship during take-off and landing modes, where the

vertical dotted lines are used to distinguish these modes from the waypoint navigation mode. During take-off and landing maneuvers, since the airship has to compensate the wind while ascending or descending to an altitude by keeping the position, some oscillations on the forward speed, attitude, and the controls are observed. Essentially, the lowered control authority for the low airspeed condition and the delayed response of actuators due to their dynamics result in such oscillations, inevitably. On the other hand, the waypoint navigation mode performs a smoother operation over the trajectory where any transient oscillations due to the maneuvers are dampened within acceptable rates. The airship demonstrates a stable response while keeping constant forward cruise speed and the attitude error from the level flight conditions decays rapidly in this mode.

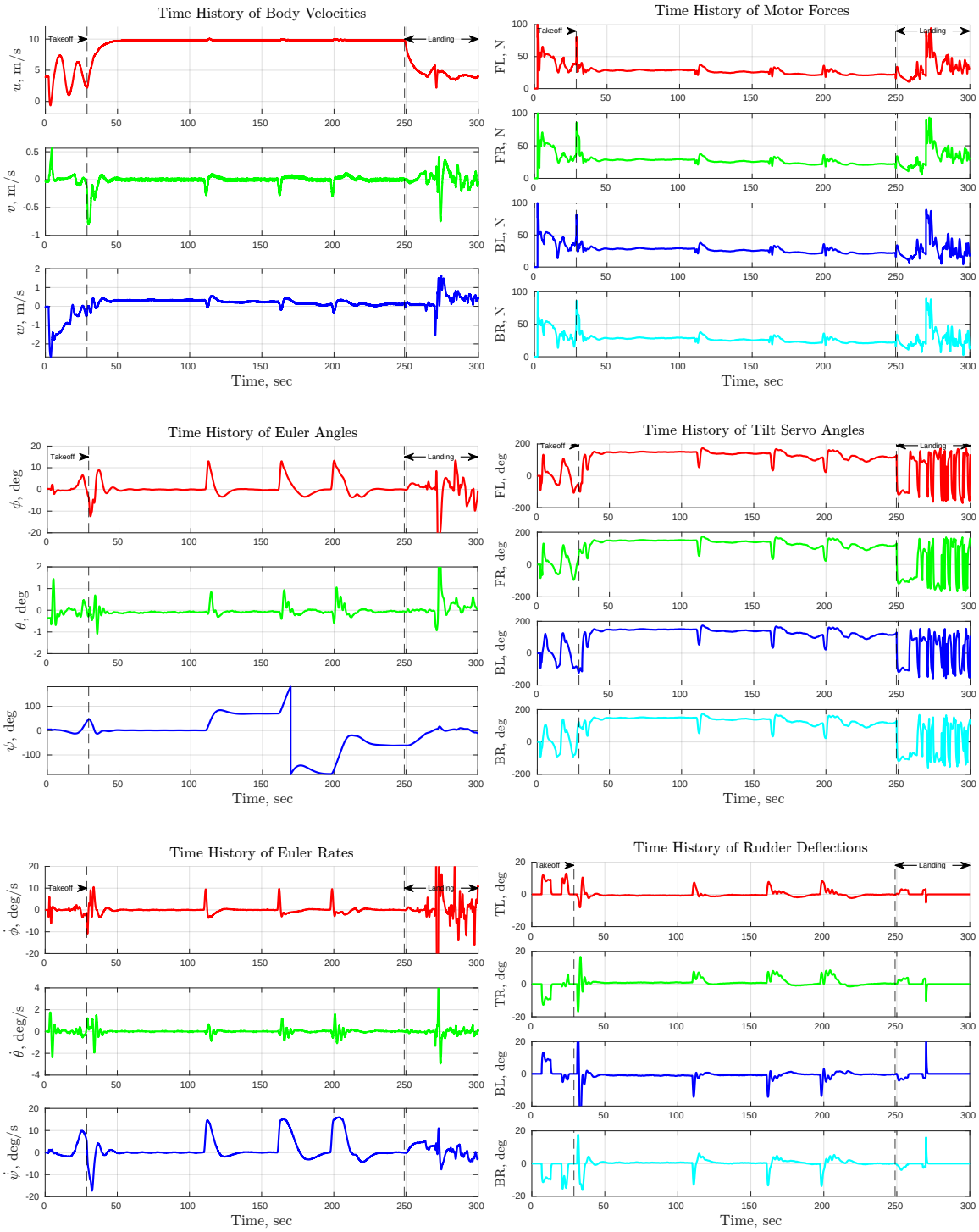

Figure 3.37: Vehicle States (on the left column) and control inputs (on the right column) for the first flight case

3.3 Chapter Summary

This chapter presented the development of linear and nonlinear control strategies for a single multi-rotor with a flexibly suspended payload and airship systems, respectively. Initially, a game theoretic approach is applied for the swing attenuation of the multi-rotor with a slung load system. This approach considers various scenarios based on the cable feedback states available to the controller, including full knowledge of the attitude and velocity of each cable segment, only relative payload attitude with respect to the multi-rotor, and complete lack of knowledge about the cable and payload states. A linear quadratic differential game is then constructed, with the multi-rotor as the minimizing player and the cable and payload swing as the maximizing player. Simulation results indicate that the virtual rigid link method, based on instantaneous relative payload attitude, yields a smoother response than the full state knowledge approach, although slightly slower oscillation damping is observed. This suggests that adequate control of cable and payload swing can be achieved with knowledge of payload's relative position or attitude with respect to the multi-rotor.

Subsequently, the chapter investigated a nonlinear geometric control method for the same system where the payload's relative attitude is known to the controller. This approach uses catenary shape analysis to determine reference position setpoints and desired cable tension, aiding the calculation of control forces and the multi-rotor's desired attitude. A trajectory tracking scenario is successfully demonstrated utilizing this method.

The latter half of the chapter focused on developing a linearized model for airship systems. A gain scheduling technique based on linear-quadratic-regulator (LQR) is designed, using airspeed, yaw rate, and climb rate as scheduling variables, with linear interpolation for smooth transitions. Various autopilot modes are created and tested in simulations, demonstrating effective and smooth mode transitions. Ad-

ditionally, a nonlinear dynamic inversion (NDI) controller is developed for airship attitude stabilization and trajectory tracking. A pseudo-inverse based control allocation method is introduced for different control configurations in hover and forward flight conditions. Finally, autonomous guidance laws for take-off, landing, and waypoint navigation are developed and tested in simulations, considering the full range of airship flight capabilities.

Chapter 4

Cooperative Manipulation and Formation Control using Multiple Aerial Vehicles

In this chapter, cooperation of multiple aerial vehicles are introduced and the cooperating systems are simulated for representative collaboration scenarios.

4.1 Cooperative Aerial Manipulation of a Suspended Payload via Flexible Cables

The nonlinear geometric control approach developed in Section 3.1.2 is extended to accommodate scenarios involving multiple multi-rotors carrying a payload suspended by a flexible cable. In this expanded model, the payload is treated as a rigid body, as depicted in Figure 4.1, illustrating the suspension of the payload via four cooperative multi-rotors.

This work aims to integrate the analytical catenary shape analysis of flexible cables with the cooperative aerial payload manipulation task. Firstly, a geometric control approach is utilized to obtain the desired force and moment for payload to track a given payload trajectory. Then, the distribution of tension forces at the cable attachment points on the payload, which satisfy the desired force and moment, are computed by applying the minimum norm solution based on the attachment geometry. After that, for each tension force at the attachment point which constitutes one of the boundary conditions, the catenary equation is analytically solved, given the known cable mass and length. This solution yields a desired cable shape to achieve the computed loads on the payload. The catenary shape is then exploited to guide individual multi-rotors with relative position and desired thrust information. Finally, a separate geometric control approach is implemented for each multi-rotor that takes

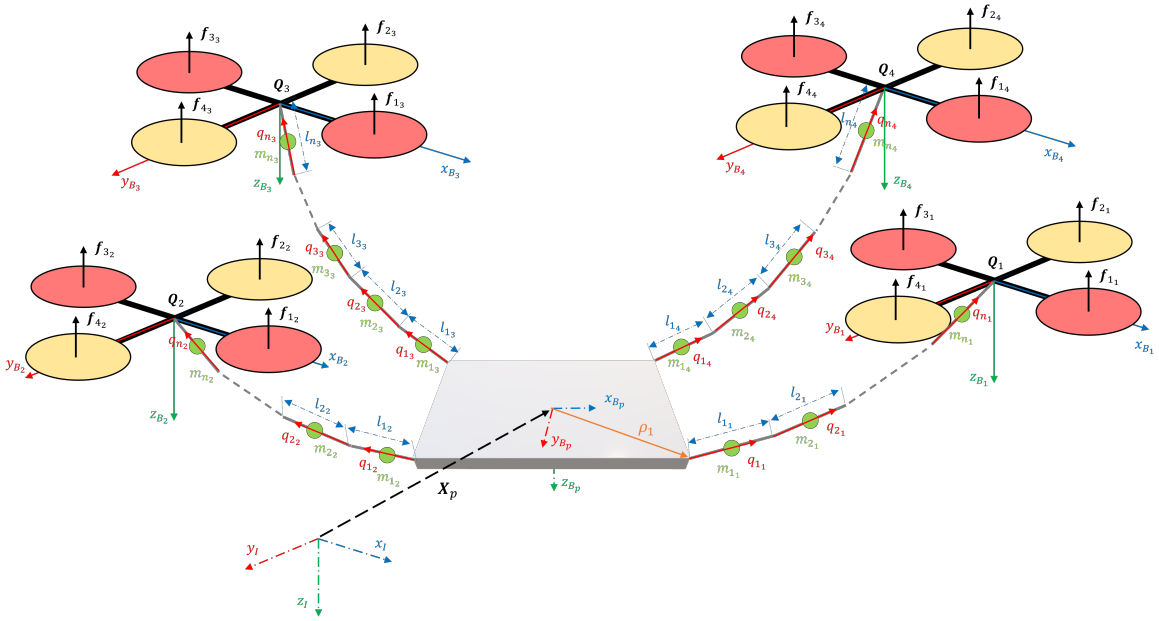

Figure 4.1: Illustration of cooperative multi-rotors with a flexibly suspended payload

this information along with the other desired trajectory states into account to achieve commanded payload trajectory tracking cooperatively.

The main contribution of this work is the integration of catenary analysis to the cooperative manipulation of flexible-cable suspended payload via multi-rotors where the catenary shape information is benefited to assist in guiding individual vehicles during the trajectory tracking task. This work also demonstrates the robustness of developed approach to uncertain states via Monte Carlo simulations where each multi-rotor system independently takes noise corrupted states for both payload and itself to implement necessary guidance and control for stabilization and trajectory tracking. Thus, these results essentially present a successful implementation of distributed control for the cooperative aerial payload manipulation task.

4.1.1 Problem Definition

In this work, a cooperative aerial payload manipulation by utilizing multiple multi-rotors where a rigid payload is suspended via flexible cables under each individual multi-rotor is investigated. The complete system with 4 multi-rotors is illustrated in Figure 4.1. The problem of payload attitude stabilization and trajectory tracking is tackled by providing necessary cable tension forces while applying desired guidance and control efforts to each vehicle. We wish to design a control law for each multi-rotor such that the overall system asymptotically tracks the desired payload position and attitude trajectories that are given as smooth and continuous curves.

The overall system dynamics, derived in Section 2.1.3.2 and in Ref. [84], is provided by the following equations of motion,

$$
\begin{aligned}
&\boldsymbol{M_{00}}\dot{\boldsymbol{v}}_P - \sum_{r=1}^{m}\sum_{i=1}^{n} \boldsymbol{M}_{0i_r}\hat{\boldsymbol{q}}_{i_r}\dot{\boldsymbol{\omega}}_{i_r} - \sum_{r=1}^{m} \boldsymbol{M}_{Q_r}\boldsymbol{R}_P\hat{\boldsymbol{\rho}}_r\dot{\boldsymbol{\omega}}_P \\
&\quad = \sum_{r=1}^{m} \boldsymbol{M}_{Q_r}\boldsymbol{R}_P\hat{\boldsymbol{\omega}}_P\hat{\boldsymbol{\rho}}_r\boldsymbol{\omega}_P + \sum_{r=1}^{m}\sum_{i=1}^{n} \boldsymbol{M}_{0i_r}\left(\boldsymbol{\omega}_{i_r}\cdot\boldsymbol{\omega}_{i_r}\right)\boldsymbol{q}_{i_r} + \boldsymbol{M}_{00}g\boldsymbol{e}_3 - \sum_{r=1}^{m} f_{B_r}\boldsymbol{R}_{Q_r}\boldsymbol{e}_3 \\
&\bar{\boldsymbol{J}}_P\dot{\boldsymbol{\omega}}_P + \sum_{r=1}^{m}\hat{\boldsymbol{\rho}}_r\boldsymbol{R}_P^T\left(\boldsymbol{M}_{Q_r}\dot{\boldsymbol{v}}_P - \sum_{i=1}^{n}\boldsymbol{M}_{0i_r}\hat{\boldsymbol{q}}_{i_r}\dot{\boldsymbol{\omega}}_{i_r}\right) \\
&\quad = \sum_{r=1}^{m}\hat{\boldsymbol{\rho}}_r\boldsymbol{R}_P^T\sum_{i=1}^{n}\boldsymbol{M}_{0i_r}\left(\boldsymbol{\omega}_{i_r}\cdot\boldsymbol{\omega}_{i_r}\right)\boldsymbol{q}_{i_r} - \hat{\boldsymbol{\omega}}_P\bar{\boldsymbol{J}}_P\boldsymbol{\omega}_P + \sum_{r=1}^{m}\hat{\boldsymbol{\rho}}_r\boldsymbol{R}_P^T\left(\boldsymbol{M}_{Q_r}g\boldsymbol{e}_3 - f_{B_r}\boldsymbol{R}_{Q_r}\boldsymbol{e}_3\right) \\
&\boldsymbol{J}_{Q_r}\dot{\boldsymbol{\omega}}_{Q_r} + \hat{\boldsymbol{\omega}}_{Q_r}\left(\boldsymbol{J}_{Q_r}\boldsymbol{\omega}_{Q_r}\right) = \boldsymbol{\tau}_r \\
&\boldsymbol{M}_{ii_r}\dot{\boldsymbol{\omega}}_{i_r} - \hat{\boldsymbol{q}}_{i_r}\sum_{j=1(j\neq i)}^{n}\boldsymbol{M}_{ij_r}\hat{\boldsymbol{q}}_{j_r}\dot{\boldsymbol{\omega}}_{j_r} + \hat{\boldsymbol{q}}_{i_r}\boldsymbol{M}_{0i_r}\left(\dot{\boldsymbol{v}}_P - \boldsymbol{R}_P\hat{\boldsymbol{\rho}}_r\dot{\boldsymbol{\omega}}_P\right) \\
&\quad = \hat{\boldsymbol{q}}_{i_r}\left(\boldsymbol{M}_{0i_r}g\boldsymbol{e}_3 + \sum_{j=1(j\neq i)}^{n}\boldsymbol{M}_{ij_r}\left(\boldsymbol{\omega}_{j_r}\cdot\boldsymbol{\omega}_{j_r}\right)\boldsymbol{q}_{j_r}\right) + \hat{\boldsymbol{q}}_{i_r}\left(-lf_{B_r}\boldsymbol{R}_{Q_r}\boldsymbol{e}_3 + \boldsymbol{M}_{0i_r}\boldsymbol{R}_P\hat{\boldsymbol{\omega}}_P\hat{\boldsymbol{\rho}}_r\boldsymbol{\omega}_P\right)
\end{aligned}
$$

where $\boldsymbol{v}_P, \boldsymbol{\omega}_P \in \mathbb{R}^3$ and $\boldsymbol{R}_P \in \mathrm{SO}(3)$ are linear, angular velocities, and the attitude of payload, respectively. Also, the attitude of each cable segment with length l is defined

in a product of two spheres $\mathrm{S}^2 = \{\boldsymbol{q} \in \mathbb{R}^3 \mid \|\boldsymbol{q}\| = 1\}$ and $\boldsymbol{\omega}$ represents the angular velocity of the segment. $\boldsymbol{\omega}_{Q_r} \in \mathbb{R}^3$, $\boldsymbol{R}_{Q_r} \in \mathrm{SO}(3)$, $f_{B_r} \in \mathbb{R}$ and $\boldsymbol{\tau}_r = [\tau_{x_r}\ \tau_{y_r}\ \tau_{z_r}]^T \in \mathbb{R}^3$ are angular velocity, attitude state, thrust and moment inputs for the multi-rotor r, respectively.

In addition, the computed mass terms are defined by

$$\boldsymbol{M}_{00} = \sum_{r=1}^{m}(m_{Q_r} + \sum_{i=1}^{n} m_{i_r})\boldsymbol{I}_3 + m_P\boldsymbol{I}_3$$

$$\boldsymbol{M}_{0i_r} = \Big(\frac{2(n-i)+1}{2} l m_{i_r} + l m_{Q_r}\Big)\boldsymbol{I}_3$$

$$\boldsymbol{M}_{ij_r} = \begin{cases} \frac{4(n-i)+1}{4} l^2 m_{i_r}\boldsymbol{I}_3 + l^2 m_{Q_r}\boldsymbol{I}_3, \text{ if } i = j \\ \frac{2(n-a)+1}{2} l^2 m_{i_r}\boldsymbol{I}_3 + l^2 m_{Q_r}\boldsymbol{I}_3, \text{ if } i \neq j, \quad (a = \max(i,j)) \end{cases}$$

$$\boldsymbol{M}_{Q_r} = m_{Q_r}\boldsymbol{I}_3 + \sum_{i=1}^{n} m_{i_r}\boldsymbol{I}_3$$

where m_P, m_{Q_r}, and m_{i_r} are masses of payload, multi-rotor r, and the i^{th} link of the cable r. Also, the augmented inertia tensor is found by

$$\bar{\boldsymbol{J}}_P = \boldsymbol{J}_P - \sum_{r=1}^{m} \boldsymbol{M}_{Q_r}\hat{\boldsymbol{\rho}}_r^2$$

where $\boldsymbol{\rho}_r$ is relative position of the attachment point of the cable r on the payload.

Kinematics of the system is provided as follows,

$$\dot{\boldsymbol{x}}_P = \boldsymbol{v}_P$$

$$\dot{\boldsymbol{R}}_P = \boldsymbol{R}_P\hat{\boldsymbol{\omega}}_P$$

$$\dot{\boldsymbol{R}}_{Q_r} = \boldsymbol{R}_{Q_r}\hat{\boldsymbol{\omega}}_{Q_r}$$

$$\dot{\boldsymbol{q}}_{i_r} = \boldsymbol{\omega}_{i_r} \times \boldsymbol{q}_{i_r}$$

where $\boldsymbol{x}_P$ is the payload position in Inertial frame.

4.1.2 Catenary Guided Formation Control Design

The overall steps followed by this control approach are listed below,

1. Desired payload force and moment are found from the given trajectory and current state of the payload.
2. The required force and moment on the payload are distributed among the cable tensions at the cable attachment positions on the payload.
3. Given a desired individual tension force at the payload side end-point, catenary analysis provides the commanded tension force at the other end-point of the cable which also corresponds to the desired multi-rotor position with respect to the instantaneous payload location.
4. A virtual rigid link between the instantaneous position of cable attachment point on the payload and multi-rotor is assumed to capture adequate cable dynamics and can be used to improve the damping of cable oscillations. For this reason, the unit vector pointing along this virtual link, as illustrated in Figure 4.4, and instantaneous angular velocity are estimated continuously.
5. From error between the current virtual link and commanded cable attitude, necessary orthogonal and parallel force components that needed to be applied at the other end of the link are calculated.
6. Finally, given the desired tension force providing the necessary payload acceleration, corrective forces ensuring the cable attitude control, and the catenary guided reference vehicle relative position and payload trajectory, a geometric control approach is implemented for the attitude and trajectory tracking control of each multi-rotor individually.

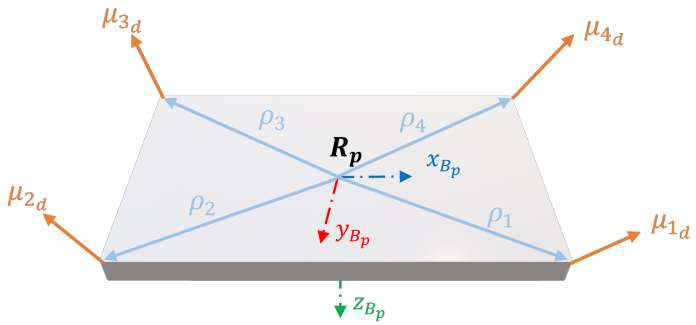

Figure 4.2: Illustration of a desired force distribution along the cable attachment points on the payload

Remark 4.1.1. *This work adopts the approach in Ref. [13] while finding the force distribution among the cable attachment locations and compensating forces and moments due to the rigid body rotation. However, our work incorporates a flexible cable modeling instead of a single link cable model and the catenary guided multi-rotor formation and position control approach.*

4.1.2.1 Payload Position and Attitude Control

Apart from the single multi-rotor suspended point load system, this cooperative system requires an additional step to stabilize and control rigid body attitude. Only way to apply forces and moments on the payload is through suspension cables, and so, there is a need to find the distribution of cable tension forces satisfying the required translational and rotational accelerations, as illustrated in Figure 4.2.

The first step is to find required force and moment, $\boldsymbol{f}_{P_d}$ and $\boldsymbol{\tau}_{P_d}$, on the payload for a given desired trajectory. With the following equations, the desired force and moment on the payload is obtained by

$$\boldsymbol{f}_{P_d} = -\boldsymbol{K}_{\boldsymbol{x}_P}\boldsymbol{e}_{\boldsymbol{x}_P} - \boldsymbol{K}_{\boldsymbol{v}_P}\boldsymbol{e}_{\boldsymbol{v}_P} + m_P\left(\dot{\boldsymbol{v}}_{P_d} - g\boldsymbol{e}_3\right)$$
$$\boldsymbol{\tau}_{P_d} = -\boldsymbol{K}_{\boldsymbol{R}_P}\boldsymbol{e}_{\boldsymbol{R}_P} - \boldsymbol{K}_{\boldsymbol{\omega}_P}\boldsymbol{e}_{\boldsymbol{\omega}_P} + \boldsymbol{J}_P\left(\hat{\boldsymbol{\omega}}_P\boldsymbol{R}_P^T\boldsymbol{R}_{P_d}\boldsymbol{\omega}_P - \boldsymbol{R}_P^T\boldsymbol{R}_{P_d}\dot{\boldsymbol{\omega}}_{P_d}\right)$$

where $\boldsymbol{K}_{\boldsymbol{x}_P}$, $\boldsymbol{K}_{\boldsymbol{v}_P}$, $\boldsymbol{K}_{\boldsymbol{R}_P}$, and $\boldsymbol{K}_{\boldsymbol{\omega}_P}$ are the feedback gains for the position, velocity, attitude, and angular velocity errors, respectively. The state errors are found as,

$$\boldsymbol{e}_{\boldsymbol{x}_P} = \boldsymbol{x}_P - \boldsymbol{x}_{P_d}$$
$$\boldsymbol{e}_{\boldsymbol{v}_P} = \boldsymbol{v}_P - \boldsymbol{v}_{P_d}$$
$$\boldsymbol{e}_{\boldsymbol{R}_P} = \frac{1}{2}\left(\boldsymbol{R}_{P_d}^T\boldsymbol{R}_P - \boldsymbol{R}_P^T\boldsymbol{R}_{P_d}\right)^\vee$$
$$\boldsymbol{e}_{\boldsymbol{\omega}_P} = \boldsymbol{\omega}_P - \boldsymbol{\omega}_P^T\boldsymbol{R}_{P_d}\dot{\boldsymbol{\omega}}_{P_d}$$

4.1.2.2 Load Distribution Among Suspension Cables

Considering the payload geometry and cable attachment points, $\boldsymbol{f}_{P_d}$ and $\boldsymbol{\tau}_{P_d}$ can be represented as follows,

$$\boldsymbol{f}_{P_d} = \sum_{r=1}^{m}\boldsymbol{\mu}_r$$
$$\boldsymbol{\tau}_{P_d} = \sum_{r=1}^{m}\boldsymbol{\rho}_r \times \boldsymbol{R}_P^T\boldsymbol{\mu}_r$$

where $\boldsymbol{\mu}_r$ corresponds to the desired cable tension at the location where cable r is attached to and it is expressed in Inertial frame. Moreover, the relative position

vector $\boldsymbol{\rho}$ is expressed in the payload body frame. These two equations can be written in a matrix form as,

$$\begin{bmatrix} \boldsymbol{I}_3 & \boldsymbol{I}_3 & \dots & \boldsymbol{I}_3 \\ \hat{\boldsymbol{\rho}}_1 & \hat{\boldsymbol{\rho}}_2 & \dots & \hat{\boldsymbol{\rho}}_m \end{bmatrix} \begin{bmatrix} \boldsymbol{R}_P^T \boldsymbol{\mu}_1 \\ \boldsymbol{R}_P^T \boldsymbol{\mu}_2 \\ \vdots \\ \boldsymbol{R}_P^T \boldsymbol{\mu}_m \end{bmatrix} = \begin{bmatrix} \boldsymbol{R}_P^T \boldsymbol{f}_{P_d} \\ \boldsymbol{\tau}_{P_d} \end{bmatrix} \tag{4.1}$$

where the matrix corresponding to the cable attachment locations are defined by

$$\boldsymbol{\Lambda} \triangleq \begin{bmatrix} \boldsymbol{I}_3 & \boldsymbol{I}_3 & \dots & \boldsymbol{I}_3 \\ \hat{\boldsymbol{\rho}}_1 & \hat{\boldsymbol{\rho}}_2 & \dots & \hat{\boldsymbol{\rho}}_m \end{bmatrix}$$

Remark 4.1.2. *It is worth noting that a minimum number of vehicles required to fully define desired force and moment via cable tensions can be obtained from the rank analysis of matrix* $\boldsymbol{\Lambda}$*, in Equation (4.1).*

For $r \geq 3$, there is at least one solution to Equation (4.1) providing desired tension forces, $\boldsymbol{\mu}_d$, if the full rank condition is satisfied. A simple approach utilizing a minimum-norm solution obtained by a generic Pseudo-Inverse can be employed as follows,

$$\begin{bmatrix} \boldsymbol{\mu}_{1_d} \\ \boldsymbol{\mu}_{2_d} \\ \vdots \\ \boldsymbol{\mu}_{m_d} \end{bmatrix} = \begin{bmatrix} \boldsymbol{R}_P & \boldsymbol{0}_3 & \dots & \boldsymbol{0}_3 \\ \boldsymbol{0}_3 & \boldsymbol{R}_P & \dots & \boldsymbol{0}_3 \\ \vdots & \vdots & \ddots & \vdots \\ \boldsymbol{0}_3 & \boldsymbol{0}_3 & \dots & \boldsymbol{R}_P \end{bmatrix} \boldsymbol{\Lambda}^T \left(\boldsymbol{\Lambda} \boldsymbol{\Lambda}^T \right)^{-1} \begin{bmatrix} \boldsymbol{R}_P^T \boldsymbol{f}_{P_d} \\ \boldsymbol{\tau}_{P_d} \end{bmatrix}$$

Remark 4.1.3. *Additional constraints on $\boldsymbol{\mu}_r$ in Equation (4.1) such as minimum or maximum cable tension forces and bounds on unit cable tension directions of can be constructed and the optimization-based numerical solution approaches can be integrated to satisfy these constraints. Also, a collision free relative desired multi-rotor formation can be enforced by utilizing such constraints in each solution step. On the other hand, the other approaches, as in Refs. [11, 65–67] where relative formation control between multi-rotors are also integrated while computing desired tension forces, can be developed.*

4.1.2.3 Catenary Solution for Tension Forces and Cable Shapes

After obtaining the desired force vector $\boldsymbol{\mu}_d$ at each cable attachment point, the catenary analysis is employed to acquire the end-point cable tension and desired catenary shape to sustain the calculated force, which also yields the desired position of the multi-rotor, $\boldsymbol{x}_{Q_d}$, for each vehicle. Figure 4.3 illustrates the required catenary shape to realize the desired payload acceleration.

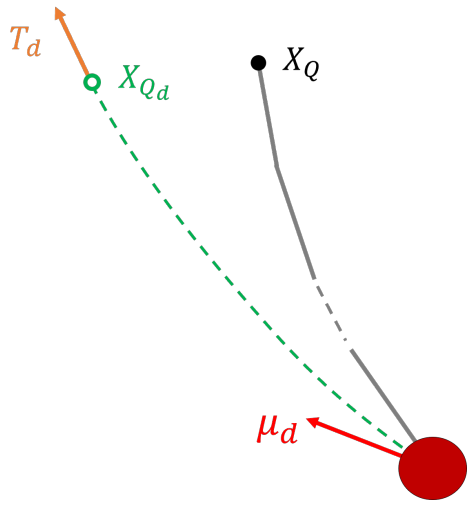

Figure 4.3: Illustration of the desired catenary shape and cable tension computed from desired force vector

4.1.2.4 Estimation of Virtual Rigid Link States

Instead of keeping track of cable shape and states of each segment, which is a non-trivial task, this work assumes an approximate model employing a virtual rigid link between two end-points can be utilized to sufficiently capture the actual cable behavior. Figure 4.4 illustrates the virtual link with length L for a single multi-rotor case.

The virtual link states can be estimated using derivative filters provided that the instantaneous relative position or unit vector along that vector is available. In this work, a second order critically damped filter is utilized to estimate virtual link states, $\boldsymbol{q}_{vir}$ and $\dot{\boldsymbol{q}}_{vir}$. $\boldsymbol{q}_{vir}$ is the unit vector along the virtual link pointing towards the multi-rotor position and $\dot{\boldsymbol{q}}_{vir}$ is the rate of change of this vector in time. From these two states, the angular velocity of the virtual link can be computed by

$$\boldsymbol{\omega}_{vir} = \boldsymbol{q}_{vir} \times \dot{\boldsymbol{q}}_{vir}$$

where $\boldsymbol{q} \times (\boldsymbol{\omega} \times \boldsymbol{q}) = \boldsymbol{\omega}$ and $\boldsymbol{q} \cdot \boldsymbol{\omega} = 0$ identities are used.

Remark 4.1.4. *For practical implementation, the estimation of $\boldsymbol{q}_{vir}$ vector can be obtained by several different methods such as active vision-based and passive beacon-based approaches where a reference point on the payload can be tracked to estimate the relative attitude vector.*

4.1.2.5 Cable Attitude Control

In order to reduce the swing motion of the cable and track the desired cable attitude, virtual link states can be taken into account in the control design. Essentially, there are two goals in this part. The first goal is to eliminate the error between desired and current virtual link attitudes, whereas the second one aims for the compensation of resulting centripetal forces due to the pendulum swing motion of the payload and

cable. The former goal can be achieved by applying a necessary force vector, which is orthogonal to $\boldsymbol{q}_{vir_r}$, to drive the virtual cable to the desired attitude as given in Equation (4.2),

$$\boldsymbol{f}_{\boldsymbol{q}_r}^{\perp} = -\boldsymbol{M}_{Q_r} L \hat{\boldsymbol{q}}_{vir_r} \left(\boldsymbol{K}_{\boldsymbol{q}_r} \boldsymbol{e}_{\boldsymbol{q}_{vir_r}} + \boldsymbol{K}_{\boldsymbol{\omega}_r} \boldsymbol{e}_{\boldsymbol{\omega}_{vir_r}} \right) - \boldsymbol{M}_{Q_r} \hat{\boldsymbol{q}}_{vir_r}^2 \boldsymbol{a}_r \tag{4.2}$$

where subscript r refers to the respective multi-rotor system. The error terms are calculated as below,

$$\boldsymbol{e}_{\boldsymbol{q}_{vir_r}} = \boldsymbol{q}_{vir_{r_d}} \times \boldsymbol{q}_{vir_r}$$

$$\boldsymbol{e}_{\boldsymbol{\omega}_{vir_r}} = \boldsymbol{\omega}_{vir_r} + \hat{\boldsymbol{q}}_{vir_r}^2 \boldsymbol{\omega}_{vir_{r_d}}$$

and utilizing the desired multi-rotor position, found in the previous step, the unit vector along the desired virtual link is obtained by

$$\boldsymbol{q}_{vir_{r_d}} = \frac{\boldsymbol{x}_{Q_{r_d}} - (\boldsymbol{x}_P + \boldsymbol{R}_P \boldsymbol{\rho}_r)}{\| \boldsymbol{x}_{Q_{r_d}} - (\boldsymbol{x}_P + \boldsymbol{R}_P \boldsymbol{\rho}_r) \|}$$

Additionally, $\boldsymbol{a}_r$ represents the linear acceleration component at the cable attachment point of subsystem r relative to the payload's center of gravity, which results from the rotational motion of the payload. This component is calculated as follows,

$$\boldsymbol{a}_r = \boldsymbol{R}_P \hat{\boldsymbol{\omega}}_P^2 \boldsymbol{\rho}_r + \boldsymbol{R}_P \hat{\boldsymbol{\rho}}_r \boldsymbol{J}_P^{-1} \left(\hat{\boldsymbol{\omega}}_P \boldsymbol{J}_P \boldsymbol{\omega}_P \right)$$

To compensate for the centripetal force and to attain the desired acceleration of the cable attachment point, which arises from the relative angular acceleration of the rigid body payload, a feedback force is formulated. This force, parallel to $\boldsymbol{q}_{vir_r}$, is constructed for each vehicle in Equation (4.3),

$$\boldsymbol{f}_{\boldsymbol{q}_r}^{\parallel} = \left(m_{Q_r} + \frac{m_{L_r}}{2} \right) L \left(\boldsymbol{\omega}_{vir_r} \cdot \boldsymbol{\omega}_{vir_r} \right) \boldsymbol{q}_{vir_r} + \boldsymbol{M}_{Q_r} \boldsymbol{q}_{vir_r} \boldsymbol{q}_{vir_r}^T \boldsymbol{a}_r \tag{4.3}$$

where $m_{L_r} = \sum_{i=1}^{n} m_{i_r}$ is the total mass of the cable attached to the r^{th} multi-rotor.

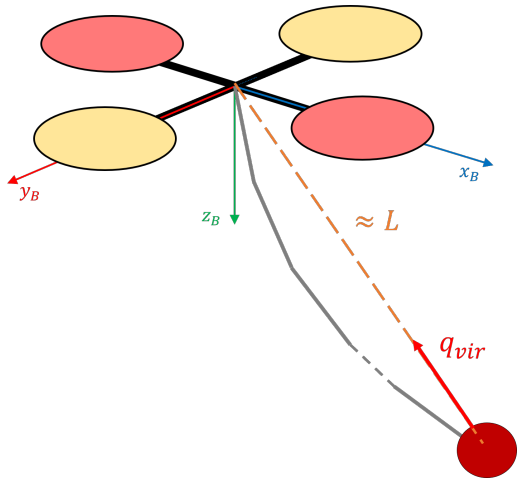

Figure 4.4: Illustration of the virtual rigid link cable connecting multi-rotor to the payload

4.1.2.6 Multi-Rotor Attitude Control

Finally, including all the findings from previous steps, the total net desired force for each multi-rotor that achieves the satisfactory payload trajectory tracking while compensating resultant forces and moments is found below,

$$\boldsymbol{f}_{Q_{r_d}} = \boldsymbol{f}_{r_d} + \boldsymbol{f}_{\boldsymbol{q}_r}^{\perp} + \boldsymbol{f}_{\boldsymbol{q}_r}^{\parallel} - \boldsymbol{K}_{\boldsymbol{x}_Q}\boldsymbol{e}_{\boldsymbol{x}_{Q_r}} - \boldsymbol{K}_{\boldsymbol{v}_Q}\boldsymbol{e}_{\boldsymbol{v}_{Q_r}} + m_{Q_r}\dot{\boldsymbol{v}}_{Q_{r_d}} - m_{Q_r}g\boldsymbol{e}_3 \tag{4.4}$$

where the desired tension force for the system r is $\boldsymbol{f}_{r_d} = \boldsymbol{\mu}_{r_d} - m_{L_r}g\boldsymbol{e}_3$. $\boldsymbol{K}_{\boldsymbol{x}_Q}$ and $\boldsymbol{K}_{\boldsymbol{v}_Q}$ are the feedback gains for multi-rotors' position and velocity errors, which are calculated as below,

$$\boldsymbol{e}_{\boldsymbol{x}_{Q_r}} = \boldsymbol{x}_{Q_r} - \boldsymbol{x}_{Q_{r_d}}$$

$$\boldsymbol{e}_{\boldsymbol{v}_{Q_r}} = \boldsymbol{v}_{Q_r} - \boldsymbol{v}_{Q_{r_d}}$$

Almost globally asymptotically convergent attitude control of each vehicle is provided by the following control law,

$$f_{B_{Q_r}} = -\boldsymbol{f}_{Q_{r_d}} \cdot \boldsymbol{R}_{Q_r}\boldsymbol{e}_3$$

$$\boldsymbol{\tau}_{Q_r} = -\boldsymbol{K}_{\boldsymbol{R}_Q}\boldsymbol{e}_{\boldsymbol{R}_{Q_r}} - \boldsymbol{K}_{\boldsymbol{\omega}_Q}\boldsymbol{e}_{\boldsymbol{\omega}_{Q_r}} + \boldsymbol{\omega}_{Q_r} \times \boldsymbol{J}_Q\boldsymbol{\omega}_{Q_r} - \boldsymbol{J}_Q\left(\hat{\boldsymbol{\omega}}_{Q_r}\boldsymbol{R}_{Q_r}^T\boldsymbol{R}_{Q_{r_c}}\boldsymbol{\omega}_{Q_{r_c}} - \boldsymbol{R}_{Q_r}^T\boldsymbol{R}_{Q_{r_c}}\dot{\boldsymbol{\omega}}_{Q_{r_c}}\right)$$

where the error terms are found by

$$\boldsymbol{e}_{\boldsymbol{R}_{Q_r}} = \frac{1}{2}\left(\boldsymbol{R}_{Q_{r_c}}^T \boldsymbol{R}_{Q_r} - \boldsymbol{R}_{Q_r}^T \boldsymbol{R}_{Q_{r_c}}\right)$$
$$\boldsymbol{e}_{\boldsymbol{\omega}_{Q_r}} = \boldsymbol{\omega}_{Q_r} - \boldsymbol{R}_{Q_r}^T \boldsymbol{R}_{Q_{r_c}} \boldsymbol{\omega}_{Q_{r_c}}$$

and the commanded multi-rotor attitude $\boldsymbol{R}_{Q_{r_c}}$ is computed as follows,

$$\boldsymbol{R}_{Q_{r_c}} = \left[-\frac{\boldsymbol{b}_{3_{r_c}} \times \boldsymbol{b}_{2_{r_c}}}{\|\boldsymbol{b}_{3_{r_c}} \times \boldsymbol{b}_{2_{r_c}}\|}, \quad \frac{\boldsymbol{b}_{3_{r_c}} \times \boldsymbol{b}_{1_{r_d}}}{\|\boldsymbol{b}_{3_{r_c}} \times \boldsymbol{b}_{1_{r_d}}\|}, \quad \boldsymbol{b}_{3_{r_c}}\right]$$

where

$$\boldsymbol{b}_{3_{r_c}} = -\frac{\boldsymbol{f}_{Q_{r_d}}}{\|\boldsymbol{f}_{Q_{r_d}}\|}$$
$$\boldsymbol{b}_{2_{r_c}} = \frac{\boldsymbol{b}_{3_{r_c}} \times \boldsymbol{b}_{1_{r_d}}}{\|\boldsymbol{b}_{3_{r_c}} \times \boldsymbol{b}_{1_{r_d}}\|}$$

and the desired orientation of each multi-rotor can be arbitrarily set by $\boldsymbol{b}_{1_{r_d}}$ unit vector which is used to find the desired projection of body-x axis on the xy-plane.

4.1.3 Simulation Results

In this section, results of a cooperative payload manipulation simulation with the proposed approach are presented for a specified trajectory tracking scenario employing four multi-rotors. The comparisons between catenary guided approach and non-catenary approaches are illustrated and various factors yielding such results are discussed. Furthermore, Monte Carlo simulations are carried out to provide the robustness analysis of proposed approach to uncertainty on the payload and vehicle states.

Following subsection provides various parameters of the system, controller, trajectory, and the other simulation parameters.

4.1.3.1 Simulation Parameters

4.1.3.1.1 System Parameters: Parameters used for multi-rotors, cables, and payload in the simulation are provided in Table 4.1.

Parameter	Value	Parameter	Value
m_Q	1.2 kg	m_P	1 kg
m_L	0.2 kg	L	2 meters
m	4 vehicles	n	5 links
$\boldsymbol{J}_Q$	$\text{diag}([1.367\ 1.367\ 2.586] \times 10^{-2})$		
$\boldsymbol{J}_P$	$\text{diag}([8.35\ 8.35\ 16.67] \times 10^{-2})$		

Table 4.1: System parameters

4.1.3.1.2 Motor Dynamics: A first order dynamics with the time constant of 0.005s is implemented to model the actuator dynamics on rotors. The force and moment due to the rotational speed of an individual rotor, Ω_{M_i}, are calculated by the following equations

$$f_i = k_F \Omega_{M_i}^2$$

$$\tau_z = k_M f_i$$

where k_F and k_M represent the coefficients relating the rotor speed to the force and moment, respectively.

$$k_F = 9.12 \times 10^{-6} \frac{N}{rad^2},\ k_M = 10^{-2} m$$

These coefficients are chosen to provide maximum thrust of 10 Newtons for each motor with full rotational speed of 10000 rpm.

4.1.3.1.3 Payload Trajectory: A desired time-parameterized payload trajectory is defined by the following equations

$$\boldsymbol{x}_{P_d}(t) = \begin{bmatrix} r_{x_d}\sin(\omega_{x_d}t) & r_{y_d}\cos(\omega_{y_d}) - r_{y_d} & r_{z_d}\sin(\omega_{z_d}t) \end{bmatrix}^T$$

where r_{x_d}, r_{y_d} and r_{z_d} correspond to the radius of the curve in x, y and z directions while $\omega_{x_d}, \omega_{y_d}$ and ω_{z_d} refer the angular speed in these axes, respectively. This trajectory defines an infinity (∞) shape in 3D and allows us to illustrate certain maneuvers sufficiently. Table 4.2 lists the parameters used in simulations.

Parameter	Value	Parameter	Value
r_{x_d}	1 m	ω_{x_d}	0.1π rad/s
r_{y_d}	2 m	ω_{y_d}	0.05π rad/s
r_{z_d}	0.5 m	ω_{z_d}	0.1π rad/s

Table 4.2: Trajectory parameters

Moreover, the desired payload heading follows the heading of desired velocity vector without any roll and pitch angle command.

$$\psi_{P_d} = \arctan 2(v_{P_{y_d}}, v_{P_{x_d}}),\ \theta_{P_d} = 0,\ \phi_{P_d} = 0$$

4.1.3.1.4 Control Parameters: Feedback gains used for the simulation are given in Table 4.3 as follows,

Parameter	Value	Parameter	Value
$\boldsymbol{K}_{\boldsymbol{x}_Q}$	$5\boldsymbol{I}_3$	$\boldsymbol{K}_{\boldsymbol{v}_Q}$	$4\boldsymbol{I}_3$
$\boldsymbol{K}_{\boldsymbol{R}_Q}$	$10\boldsymbol{I}_3$	$\boldsymbol{K}_{\boldsymbol{\omega}_Q}$	$4\boldsymbol{I}_3$
$\boldsymbol{K}_{\boldsymbol{q}_r}$	$0.1\boldsymbol{I}_3$	$\boldsymbol{K}_{\boldsymbol{\omega}_r}$	$0.05\boldsymbol{I}_3$
$\boldsymbol{K}_{\boldsymbol{x}_P}$	diag([6 6 10])		
$\boldsymbol{K}_{\boldsymbol{v}_P}$	diag([5 5 5])		

Table 4.3: Controller gains

4.1.3.1.5 State Uncertainties for Monte Carlo Analysis: In order to demonstrate the robustness of developed approach to uncertainties, each vehicle considers independent and unrelated noise corrupted payload and self states during the control input generation. Table 4.4 lists the standard deviations of additive state noises that follow zero mean normal distributions, $w_X \sim N\left(0, \sigma_X^2\right)$ where w_X denotes the noise acting on the state X.

Parameter	Value	Parameter	Value
σ_{ϕ_P}	0.5 deg	σ_{ϕ_Q}	0.1 deg
σ_{θ_P}	0.5 deg	σ_{θ_Q}	0.1 deg
σ_{ψ_P}	0.5 deg	σ_{ψ_Q}	0.1 deg
$\boldsymbol{\sigma}_{\boldsymbol{x}_P}$	diag([5 5 5]) cm		
$\boldsymbol{\sigma}_{\boldsymbol{v}_P}$	diag([1 1 1]) cm/s		
$\boldsymbol{\sigma}_{\boldsymbol{\omega}_P}$	diag([0.05 0.05 0.05]) deg/s		
$\boldsymbol{\sigma}_{\boldsymbol{x}_Q}$	diag([2 2 2]) cm		
$\boldsymbol{\sigma}_{\boldsymbol{v}_Q}$	diag([1 1 1]) cm/s		
$\boldsymbol{\sigma}_{\boldsymbol{\omega}_Q}$	diag([0.05 0.05 0.05]) deg/s		

Table 4.4: Standard deviations of state uncertainties

4.1.3.2 Evaluation Metrics

To evaluate the performance of the payload configuration, the following metric representing a normalized attitude error is utilized,

$$\Psi_P\left(t\right) = \frac{1}{2}\mathrm{Tr}\left[\boldsymbol{I}_3 - \boldsymbol{R}_{P_d}^T \boldsymbol{R}_P\right]$$

The following metric provides a quantitative measure for analyzing and comparing the transient performance of cable motion during the trajectory tracking maneuvers. A more stable and smoother response is indicated by lower average magnitudes of angular velocities in the cable segments, resulting in fewer oscillations.

$$\mathrm{RMS}\left(\boldsymbol{\omega}_{q_r}\right)(t) = \sqrt{\frac{1}{n}\sum_{i=1}^{n}\|\boldsymbol{\omega}_{i_r}\|^2}$$

Furthermore, to demonstrate the smoothness of the control action during trajectory tracking, the root mean square (RMS) of the rotor rotational speeds is employed as follows,

$$\mathrm{RMS}\left(\Omega_M\right)(t) = \sqrt{\frac{1}{4}\sum_{i=1}^{4}\|\Omega_{M_i}(t)\|^2}$$

4.1.3.3 Results and Discussion

To demonstrate the efficacy of our proposed catenary-guided method for cooperative suspended payload manipulation—referred to as 'Method-1' in the subsequent results—we compare it against two other methods that assume a rigid single-link cable. The second method mirrors Method-1's steps, except the part where desired multi-rotor positions are computed by the analytical solution of catenary equations. In this method, since the cable is assumed to be a rigid single-link, the desired multi-rotor position is found by extending a straight line from the base attachment along the $\boldsymbol{\mu}_d$ direction with the known cable length directly. Finally, the third method, as presented in Ref. [13], only considers the parallel and orthogonal force vectors including the gravity compensation in Equation (4.4) while leaving the position, velocity, and acceleration terms out during the computation of vehicle guidance commands. Thus, it highly relies on payload and cable states, which makes it vulnerable to noises on these states. Also, the same virtual cable approximation in the other methods is implemented in the third method to estimate the rigid-link cable states required by the control law.

4.1.3.3.1 Comparison of the Methods: The system initially starts from an hanging equilibrium condition at the origin, $(0, 0, 0)$, where the multi-rotors are hovering and the cables are vertically aligned. In the initial phase of the trajectory, the system accelerates to align with the desired position and velocity, leading to minor initial deviations and oscillations as depicted in the top view of the simulated payload trajectory plots for each method in Figure 4.5. The proposed method swiftly reduces these deviations, achieving convergence to the desired trajectory. In contrast, the second and third methods exhibit larger oscillations and reduced damping.

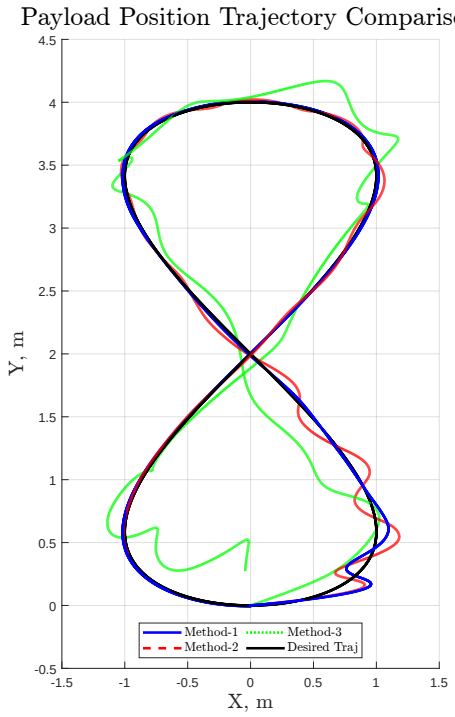

Figure 4.5: Time history of payload position trajectory as seen from the top view

Figure 4.6 illustrates the comparison of payload position tracking for the methods. It is worth noting that during the heading change of the payload, all vehicles has to cooperatively maneuver while keeping desired altitude and cable tension forces.

However, due to the flexible cable implementation and complexity of the actual nonlinear system with delayed response characteristics, during the simultaneous control of payload position and attitude, certain compromise on altitude is recognizable comparing to the horizontal position states for all methods with varying degrees.

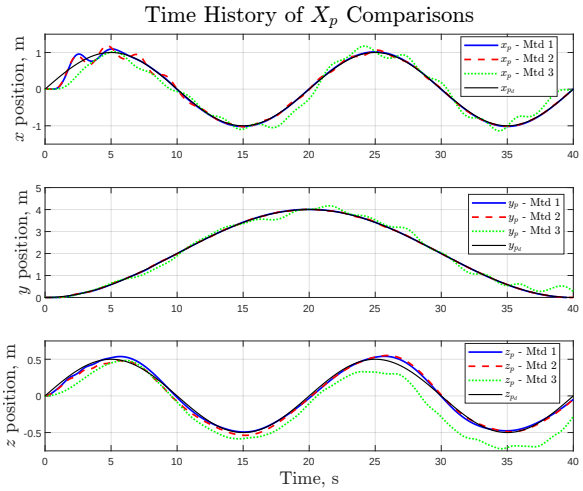

Figure 4.6: Comparison of payload position tracking for different methods (blue: Method-1, red: Method-2, green: Method-3, and black: desired trajectory)

The payload configuration error comparison between the methods is displayed in Figure 4.7. In this figure, contrarily, the first method has a higher error in the tracking of payload configuration. These results suggest that a tighter control of the cable, akin to treating it as a straight link, may result in less deviation from the desired payload configuration. Nonetheless, subsequent analyses of the cable's transient response and multi-rotor control inputs will provide deeper insights into the overall behavior of the system.

Figure 4.8 displays the comparison of root mean square (RMS) of cable angular velocities as time histories for each method. The first method, which accounts for the catenary shape and the effects of cable flexibility, achieves the smoothest response,

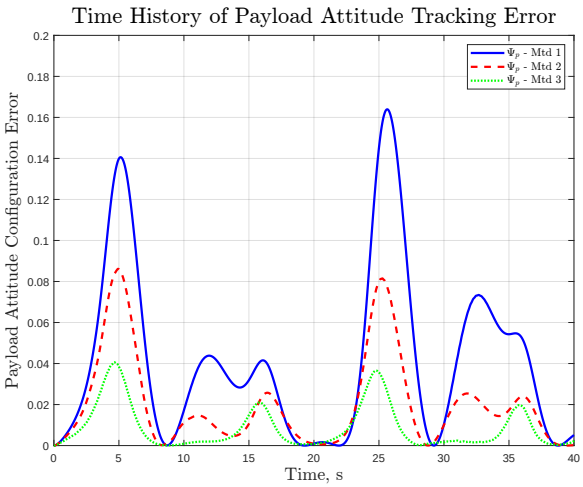

Figure 4.7: Comparison of payload configuration error in time for different methods

indicating improved transient behavior of the cable. In contrast, methods that rely on the single rigid-link cable approximation for guidance and control exhibit persistent oscillations along the cable segments, leading to disturbances in the overall system behavior. The disparity between the actual catenary configuration and the rigid-link approximation contributes to delays and disturbances, potentially destabilizing the system's dynamic response, as evidenced by the performance of the third method.

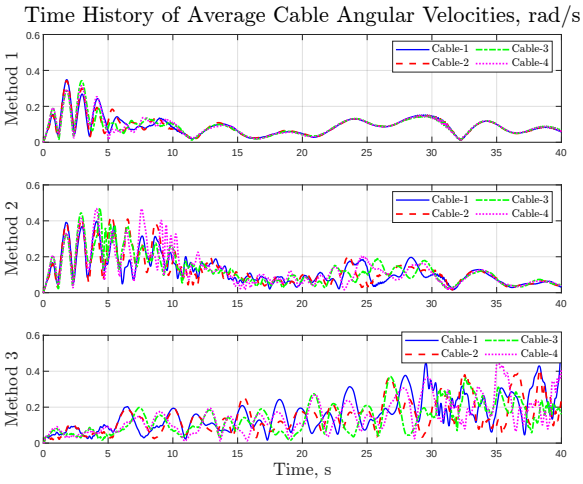

Figure 4.8: Comparison of average (RMS) cable angular velocities for different methods

The control efforts exerted by each vehicle are quantified by the RMS of rotor speeds, as depicted in Figure 4.9. These plots distinctly show the initial acceleration phase followed by a stable convergence in the first method. Conversely, the other two methods display less smooth control responses with more pronounced oscillations, aligning with expectations.

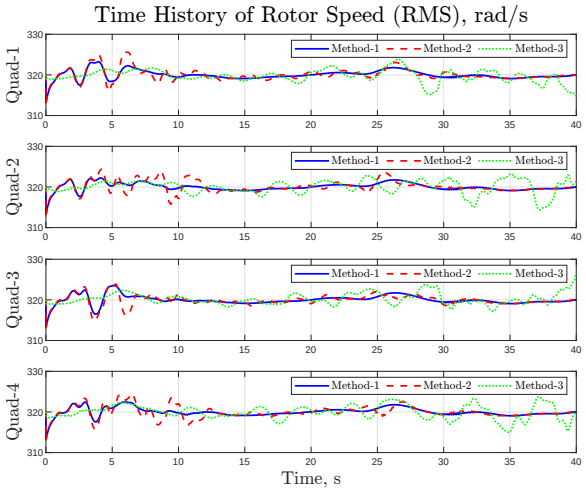

Figure 4.9: Time history of rotor speed RMS values for each multi-rotor

In summary, the results underscore the superiority of the proposed catenary-guided cooperative aerial manipulation method for managing a suspended payload with multiple multi-rotors over the comparative methods that neglect cable flexibility. A video clip illustrating the system's simulated performance along the trajectory is available at the link provided below, [1].

Remark 4.1.5. *The third method is fundamentally designed for a rigid mass-less link and it relies on the fast dynamics of multi-rotors to achieve desired suspension configurations and necessary forces and moments. However, incorporation of flexible cable with certain mass is inherently increased the complexity and characteristic of system*

[1] `https://youtu.be/UvLKmNdKcJo`, (UT Arlington Aerospace Systems Laboratory youtube page)

dynamics. Therefore, finding suitable control gains to stabilize this system sufficiently proves to be quite challenging. Nevertheless, overall performance can be improved with finer tuning and the implementation of disturbance observer and rejection modules, as for the other methods.

4.1.3.3.2 Robustness to Uncertainty: The robustness of the proposed method against uncertain states was evaluated through 1000 Monte Carlo simulations with noise-perturbed states, following the noise characteristics listed in Table 4.4. The results in Figure 4.10 displays the statistical distribution of these trials, marked by the mean and 3σ bounds. The plots on the upper left figure illustrates the payload position error, $\tilde{\boldsymbol{x}} = \boldsymbol{x}_{P_d} - \boldsymbol{x}_P$. In this figure, it is seen that except the initial trajectory catch-up maneuver time period, horizontal payload position errors stay within less than 2 centimeters of the actual track whereas the vertical position tracking errors have seen deviations from the trajectory up to 13cm although the spread of errors are still bounded within 2cm around the mean. Similarly, the plots on the upper right figure denotes the payload velocity tracking error statistical mean and bounds from the simulations. As the horizontal velocity profile is tracked closely, the vertical payload velocity tracking has seen slight departures from the desired track, especially right after sharp corner turning maneuvers at around $t = 5s$ and $t = 25s$. These deviations are more apparent in the attitude error plots in the lower left figure, particularly in payload heading at the aforementioned times, despite adequate roll and pitch tracking. During the payload heading change maneuver, each vehicle has to follow a smooth trajectory that is dictated by the desired catenary tensions assuming the fast dynamics of vehicles allows the close tracking of such a trajectory. Yet, the transient response of the overall system is delayed and relatively slow, especially during altitude and yaw control, due to the flexible nature of the cable, and imposed

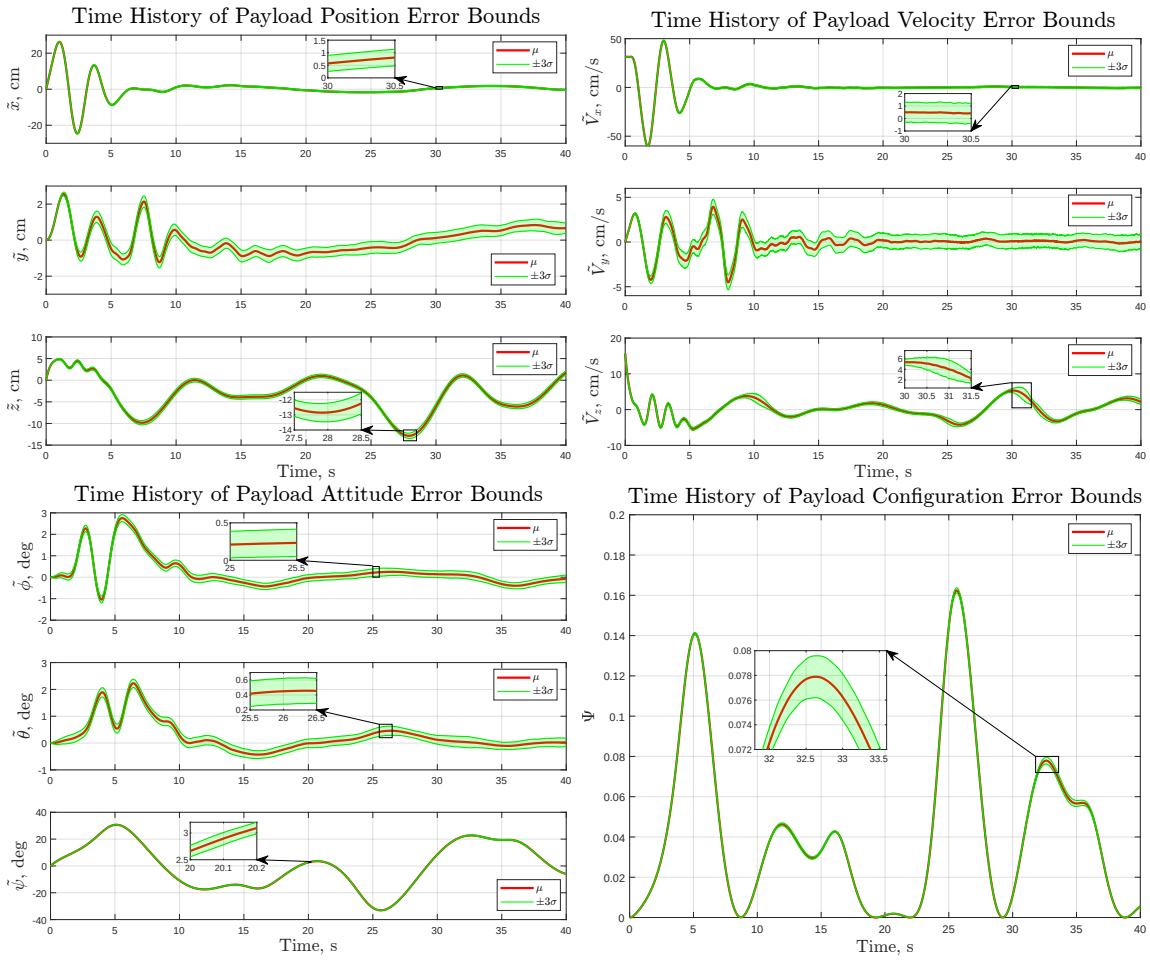

Figure 4.10: The 3σ error bound results from Monte Carlo simulations

latency by the vehicle attitude control and the other control objectives such as position control, velocity matching, and cable attitude control. The configuration error plot on the lower right figure highlights this finding again illustrating the elevated attitude error during sharp maneuver segments mainly due to the yaw angle tracking error.

Figure 4.11 displays the RMS values of rotor speeds for each vehicle during the simulation runs. The plots have consistent mean values without any significant oscillatory behavior along the trajectory. This result provides that the overall system

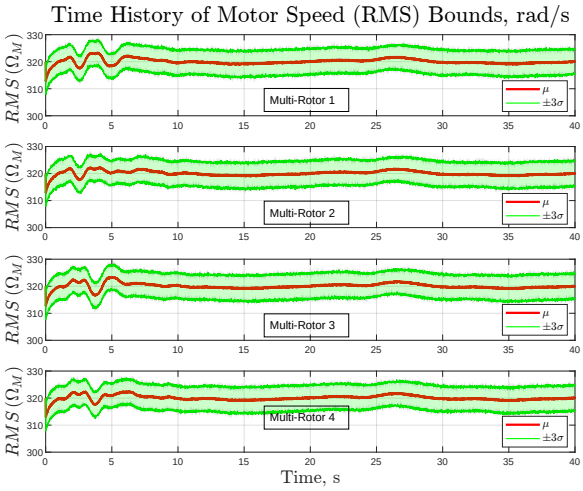

Figure 4.11: Time history of average motor speed bounds from Monte Carlo simulations

response to the uncertain states has enough dampening effect and any disturbance caused by the state uncertainties are not amplified by the cooperative control strategy.

Remark 4.1.6. *The results obtained from Monte Carlo simulations with noise corrupted states demonstrate that each individual vehicle can actually utilize a state estimation of its neighbors and payload, similar to the work in Ref. [38], to generate the control input by itself. Only information to be known is to actual desired trajectory of the payload, which can be encoded in every vehicle. As a result, the proposed method allows us to distribute the cooperative control among vehicles.*

4.2 Cooperative Formation Control of Multiple Multi-Rotors

In the dynamic and evolving field of multi-agent systems, the cooperative formation control of multiple multi-rotors represents a significant step towards achieving advanced aerial capabilities in a variety of applications. This section investigates the dynamics and control mechanisms that enable this complex yet fascinating interaction among multi-rotors. Particularly, a second-order consensus protocol within the framework of multi-agent formations, which play a pivotal role in ensuring synchronized behavior and effective communication among individual units is focused on this research.

Further, this section explores the implementation of an Extended State Observer (ESO) for total disturbance estimation of individual agents. ESO provides a robust framework for accurately predicting and compensating for various uncertainties and disturbances, including factors like wind, air-drag, and unmodeled system dynamics. This not only enhances the stability and reliability of the formation control system but also simplifies the control design process by effectively reducing the dynamics of the agents to a second-order integrator model while maintaining high fidelity in disturbance estimation and compensation. Here, we assumed that the rotational dynamics of the multi-rotor systems are sufficiently fast to reliably follow desired linear acceleration commands without significant lag or error. Therefore, focusing primarily on translational motion of the multi-rotors, overall agent dynamics in the group are represented by a second-order integrator dynamics with uncertainty. This assumption allows for a more streamlined analysis and control design.

The practical aspect of this theoretical framework is demonstrated through the deployment of a simple distributed consensus protocol across various leader-follower graph topologies. This approach is utilized in tracking desired leader trajectories while forming certain formation shapes within the group. The consensus protocol ensures

that all multi-rotors, or agents, in the system converge to a common agreement on the trajectory and formation, despite potential discrepancies in individual perceptions and measurements under certain conditions.

A notable part of this section includes a comparative study demonstrating the effectiveness of ESO in formation tasks with various graph topologies. This study compares several formation tasks executed with and without ESO under conditions like air drag caused by wind.

Overall, this section offers a comprehensive overview of the mechanisms and strategies employed in the cooperative formation control of multiple multi-rotors in this research. By integrating a consensus protocol and an ESO-based disturbance estimation method, we demonstrate a formation control strategy that can be applied in diverse operational scenarios, ranging from surveillance to search-and-rescue operations. Finally, an illustrative scenario symbolizing a real-life search-and-rescue mission is constructed. In this scenario, a group of multi-rotors are transported and deployed to the mission area from an airship. These multi-rotors then execute predefined formation and trajectory tracking tasks during a simulated mission, demonstrating the practical applications of the concepts discussed.

4.2.1 Preliminaries and Problem Formulation

4.2.1.1 Notations

Several mathematical notations are consistently followed in this section. We represent the standard Euclidean norm of a vector $\boldsymbol{x}$ as $||\boldsymbol{x}||$. Maximum and minimum singular values of a matrix $\boldsymbol{M}$ are represented by $\bar{\sigma}(\boldsymbol{M})$ and $\underline{\sigma}(\boldsymbol{M})$, respectively. Moreover, n-dimensional identity matrix is described by $\boldsymbol{I}_n$ and the column vector

consisting of ones is denoted by $\underline{\mathbf{1}}$. In general, the concatenation is illustrated by the underlined vectors or matrices.

4.2.1.2 Graph Theory Basics

A graph is a pair $\mathcal{G} = (\mathcal{V}, \mathcal{E})$ representing the intercommunication among a group of agents. Here, $\mathcal{V} = \{1, 2, \cdots, N\}$ denotes a set of N nodes (or vertices), and $\mathcal{E} \subseteq \mathcal{V} \times \mathcal{V}$ is a set of edges connecting these nodes. We assume the graph does not have self-loops, meaning no node has an edge to itself, and no multiple edges between the same pair of nodes exist. The number of neighbors, denoted as $\|\mathcal{N}_i\|$ of node i, is equal to its in-degree which is calculated by counting the number of incoming edges with arrows towards to the node i from the other nodes. Each edge in the graph is associated with a weight a_{ij}, symbolizing the quality of communication between connected nodes, and it is strictly a non-negative value. A graph is termed 'strongly connected' if there exists a path from any vertex to every other vertex via these edges, as depicted in Figure 4.12. Furthermore, a graph is considered 'balanced' if $a_{ij} = a_{ji}$ for all $(i, j) \in \mathcal{E}_{ij}$, indicating that the edges are undirected.

The graph's structure can be represented by an adjacency or connectivity matrix $\mathcal{A} = [a_{ij}]$, $\mathcal{A} \in \mathbb{R}^{N \times N}$. The edge weights are defined as $a_{ij} = 1$ if there is an edge between nodes i and j, and $a_{ij} = 0$ otherwise. The in-degree of the node i is determined by summing the entries of the ith row in $\mathcal{A}$ as follows,

$$d_i = \sum_{k=1}^{N} a_{ik}$$

and the out-degree of the node is defined with the column sum of A for that node as below,

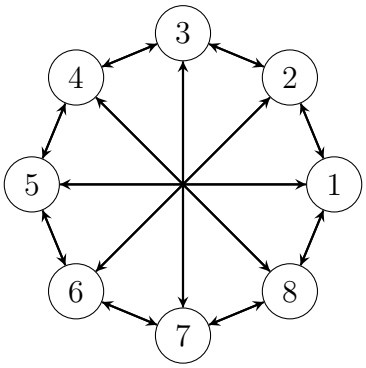

Figure 4.12: Strongly connected graph illustration with 8 nodes

$$d_i^o = \sum_{k=1}^{N} a_{ki}$$

Two other important parameters in graph theory are the diameter and volume of a graph. The diameter of a graph is defined as the longest distance between any two nodes within the graph. The volume of a graph, denoted as Vol$\mathcal{G}$, is the sum of the in-degrees of all its nodes, calculated as

$$\text{Vol}\mathcal{G} = \sum_{i=1}^{N} d_i$$

The graph's structural properties can also be analyzed using the graph Laplacian matrix. This matrix is defined as $\mathbf{L} = \mathcal{D} - \mathcal{A}$, where $\mathcal{D} = diag\{d_i\}$ is the diagonal in-degree matrix. The Laplacian matrix, $\mathbf{L}$, is significant in providing insights into various characteristics of the graph.

Remark 4.2.1. *In the case of a strongly connected and balanced graph, the graph Laplacian matrix is always symmetric. Furthermore, the rank of the Laplacian matrix, denoted as rank*$(\mathbf{L})$*, is equal to* $N-1$*. The second smallest eigenvalue of the graph Laplacian, known as the Fiedler eigenvalue, is particularly significant as it indicates the overall connectivity of the graph, as referenced in Ref. [99].*

4.2.1.3 Problem Formulation

In this section, the focus is on multi-agent formation control using a second-order consensus framework, specifically applied to multiple multi-rotors. Under the assumption that the multi-rotors' rotational dynamics are rapid and that the desired formation control motion does not necessitate high agility from the agents, the analysis concentrates solely on the translational motion of the multi-rotors. This motion is governed by the following equations,

$$\dot{\boldsymbol{x}} = \boldsymbol{v}$$

$$\dot{\boldsymbol{v}} = \boldsymbol{f} - \boldsymbol{u} + \boldsymbol{d}$$

where $\boldsymbol{x} = [x\ y\ z]^T$ and $\boldsymbol{v} = [v_x\ v_y\ v_z]^T$ represent the position and velocity of the vehicle with respect to the Inertial frame, respectively. The term $\boldsymbol{f} \in \mathbb{R}^3$ denotes the known dynamics of the vehicle, which in this case is the gravitational acceleration acting on it, expressed as $\boldsymbol{f} = g\boldsymbol{e}_3$. The virtual control input, $\boldsymbol{u} \in \mathbb{R}^3$, replaces the actual force generation mechanism of the multi-rotor $\boldsymbol{R}_{IB} f_B \boldsymbol{e}_3 / m_Q$, following the fast rotational dynamics assumption made previously. Lastly, $\boldsymbol{d} \in \mathbb{R}^3$ represents the linear acceleration due to total disturbances, which include external disturbances (like air-drag and wind effects), unknown system model inaccuracies, and parametric uncertainties.

In this context, the dynamics of each agent in the multi-rotor formation are modeled as a second-order integrator type with disturbance, as expressed in the following equations,

$$\begin{aligned} \dot{\boldsymbol{x}}_i &= \boldsymbol{v}_i \\ \dot{\boldsymbol{v}}_i &= \boldsymbol{f}_i - \boldsymbol{u}_i + \boldsymbol{d}_i \end{aligned}, \qquad i = 1, 2, \ldots, N \tag{4.5}$$

The objective is to develop a cooperative formation control law that stabilizes the formation and enables it to follow a virtual leader's trajectory. Importantly, the control law must comply with the specified communication graph topology, utilizing only local neighbor information as dictated by this topology.

The dynamics of the virtual leader are defined as,

$$\dot{\boldsymbol{x}}_0 = \boldsymbol{v}_0$$
$$\dot{\boldsymbol{v}}_0 = \boldsymbol{f}_0$$

4.2.2 Second Order Consensus Protocol for Agent Formation

First, local neighborhood tracking errors for position and velocity states are defined for individual agents considering the formation and local communications. The agent dynamics, as detailed in Equation (4.5), are assumed to be uncoupled across the coordinate axes. For simplicity, the derivation is only presented for a single axis. However, using the Kronecker product, $\otimes$, this formulation can be expanded to encompass all three axes.

$$\begin{aligned} e_{x_i} &= \textstyle\sum_{j\in\mathcal{N}_i} a_{ij}\left(x_j - x_i - \Delta_{ji}\right) + g_i\left(x_0 - x_i + \Delta_{0i}\right) \\ e_{v_i} &= \textstyle\sum_{j\in\mathcal{N}_i} a_{ij}\left(v_j - v_i\right) + g_i\left(v_0 - v_i\right) \end{aligned} \tag{4.6}$$

where $e_{x_i} \in \mathbb{R}$ and $e_{v_i} \in \mathbb{R}$ represent the position and velocity tracking errors for the ith agent. The term Δ_{0i} denotes the desired relative position of agent i with respect to the virtual leader in the Inertial frame, which is kept constant. $\Delta_{ji} = \Delta_{0j} - \Delta_{0i}$ represents the desired separation between agents i and j in the formation. Moreover, g_i is the pinning gain indicating the controlled nodes in the graph with $g_i \geq 0$ and $g_i > 0$ for at least one node in the graph. This formulation is crucial for designing a control law that enables each agent to maintain its relative position and velocity

within the formation, based on the information about its neighbors and the virtual leader.

Using the local position and velocity errors, the global error states are derived as follows,

$$\begin{aligned} \underline{\boldsymbol{e}}_x &= -\left(\mathbf{L}+\mathbf{G}\right)\left(\underline{\boldsymbol{x}} - \underline{\mathbf{1}}x_0 - \underline{\boldsymbol{\Delta}}\right) \\ \underline{\boldsymbol{e}}_v &= -\left(\mathbf{L}+\mathbf{G}\right)\left(\underline{\boldsymbol{v}} - \underline{\mathbf{1}}v_0\right) \end{aligned} \tag{4.7}$$

where $\underline{\boldsymbol{e}}_x = [e_{x_1}, \ldots, e_{x_N}]^T$ and $\underline{\boldsymbol{e}}_v = [e_{v_1}, \ldots, e_{v_N}]^T$ represent the global position and velocity error vectors for the entire formation, respectively. The term $\mathbf{L}$ denotes the graph Laplacian, which captures the communication structure and interconnections between agents within the formation. The matrix $\mathbf{G}$, known as the pinning matrix, consist of diagonal entries of node in-degrees, $\text{diag}\{d_1, d_2, \ldots, d_N\}$. Additionally, $\underline{\boldsymbol{\Delta}} = [\Delta_{01}, \Delta_{02}, \ldots, \Delta_{0N}]^T$ is a vector that encapsulates the desired relative positions of each agent with respect to the virtual leader.

Then, differentiating Equations (4.7) and substituting Equations (4.5), the global error dynamics are found as below,

$$\begin{aligned} \dot{\underline{\boldsymbol{e}}}_x &= \underline{\boldsymbol{e}}_v \\ \dot{\underline{\boldsymbol{e}}}_v &= -\left(\mathbf{L}+\mathbf{G}\right)\left(\underline{\boldsymbol{f}} - \underline{\boldsymbol{u}} + \underline{\boldsymbol{d}} - \underline{\mathbf{1}}f_0\right) \end{aligned} \tag{4.8}$$

where $\underline{\boldsymbol{f}}, \underline{\boldsymbol{u}}$ and $\underline{\boldsymbol{d}}$ are the concatenation of corresponding terms for each agent.

To achieve synchronization among agents and leader tracking in the multi-agent system, a simple local control protocol can be implemented as follows,

$$u_i = f_i + \hat{d}_i - k_x e_{x_i} - k_v e_{v_i} \tag{4.9}$$

where $\hat{d}_i$ is the estimated total disturbance for the agent, i.e. $d_i = \hat{d}_i + \tilde{d}_i$. An ESO-based estimation method is further detailed in the subsequent section. The terms $k_x, k_v > 0$ are feedback gains for local neighborhood position and velocity errors.

To analyze the stability of the formation under the chosen control protocol, we can define the state vector $\boldsymbol{z}$ as $\boldsymbol{z} = \left[\underline{\boldsymbol{e}}_x^T \ \underline{\boldsymbol{e}}_v^T\right]^T$,

$$\dot{\boldsymbol{z}} = \underbrace{\begin{bmatrix} \mathbf{0}_N & \boldsymbol{I}_N \\ -\boldsymbol{K}_x\left(\mathbf{L}+\mathbf{G}\right) & -\boldsymbol{K}_v\left(\mathbf{L}+\mathbf{G}\right) \end{bmatrix}}_{\boldsymbol{H}^*} \boldsymbol{z} + \begin{bmatrix} \mathbf{0}_N \\ -\left(\mathbf{L}+\mathbf{G}\right)\left(\underline{\tilde{\boldsymbol{d}}} - \underline{\mathbf{1}} f_0\right) \end{bmatrix} \tag{4.10}$$

where $\boldsymbol{K}_x, \boldsymbol{K}_v \in \mathbb{R}^{N\times N}$ are feedback gain matrices, with diagonal elements corresponding to k_x and k_v, respectively. The term $\underline{\tilde{\boldsymbol{d}}}$ represents the vector of residual errors from the total disturbance estimations.

The matrix $\boldsymbol{H}^*$ is critical for analyzing the system's stability. For the formation to be stable, the gains k_x and k_v need to be chosen such that $\boldsymbol{H}^*$ in Equation 4.10 is a Hurwitz matrix, meaning that all its eigenvalues have negative real parts. Achieving this condition ensures that the formation's error states will converge to zero or a bounded value over time, indicating stable behavior. The sufficient conditions for formation stability can be further explored, as shown in Ref. [99] where an adaptive control technique is employed to approximate external disturbances and system nonlinearities.

Remark 4.2.2. *Investigating the system matrix $\boldsymbol{H}^*$, it can be easily seen that the graph topology and the choice of pinning nodes significantly influence the stability of the formation. Therefore, the selection of control gains needs to take into account the graph's topology.*

The subsequent section illustrates various graph topologies and geometrical formation shapes, such as line, circular, triangle, and square formations. These are depicted in Figure 4.13. Additionally, Table 4.5 provides a detailed examination of the eigenvalues of the graph Laplacians for these formations. The eigenvalues are crucial as they give insights into the formation characteristics, such as connectivity, robustness to disturbances, and the speed of information flow across the formation.

This analysis allows us to understand how different formation shapes and topologies affect the overall system behavior and stability, guiding the selection of appropriate control strategies and gain settings.

	Line	Circle	Triangle	Square	Full Connectivity
$\lambda_1 =$	0	0	0	0	0
$\boldsymbol{\lambda_2 =}$	**0.1522**	**0.5858**	**1.1338**	**1.2679**	**8.0000**
$\lambda_3 =$	0.5858	0.5858	2.1088	1.2679	8.0000
$\lambda_4 =$	1.2346	2.0000	3.2954	2.0000	8.0000
$\lambda_5 =$	2.0000	2.0000	4.2108	4.0000	8.0000
$\lambda_6 =$	2.7654	3.4142	5.3174	4.7321	8.0000
$\lambda_7 =$	3.4142	3.4142	5.6554	4.7321	8.0000
$\lambda_8 =$	3.8478	4.0000	6.2784	6.0000	8.0000
$\text{Vol}\mathcal{G} =$	14	16	28	24	56

Table 4.5: Eigenvalues of various graph Laplacians for the topologies provided in Figure 4.13.

It is expected that an increase in the number of neighbors for each agent should enhance communication quality within the formation. More connected graphs are anticipated to provide faster information transfer among agents, leading to a quicker collective response. The eigenvalues presented in Table 4.5 support this hypothesis. Specifically, the Fiedler eigenvalue, a key metric in graph theory, also known as the graph's algebraic connectivity, is used to measure the speed of interaction among agents within a graph. It is indicative of how well-connected a graph is and higher values suggest better connectivity yielding more efficient information flow across the network. In this context, the line configuration, which exhibits the lowest degree of connectivity compared to other formations, has the lowest Fiedler eigenvalue. This implies slower interactions among agents in the line configuration. Conversely, graph topologies with higher Fiedler eigenvalues, such as square and triangle configurations,

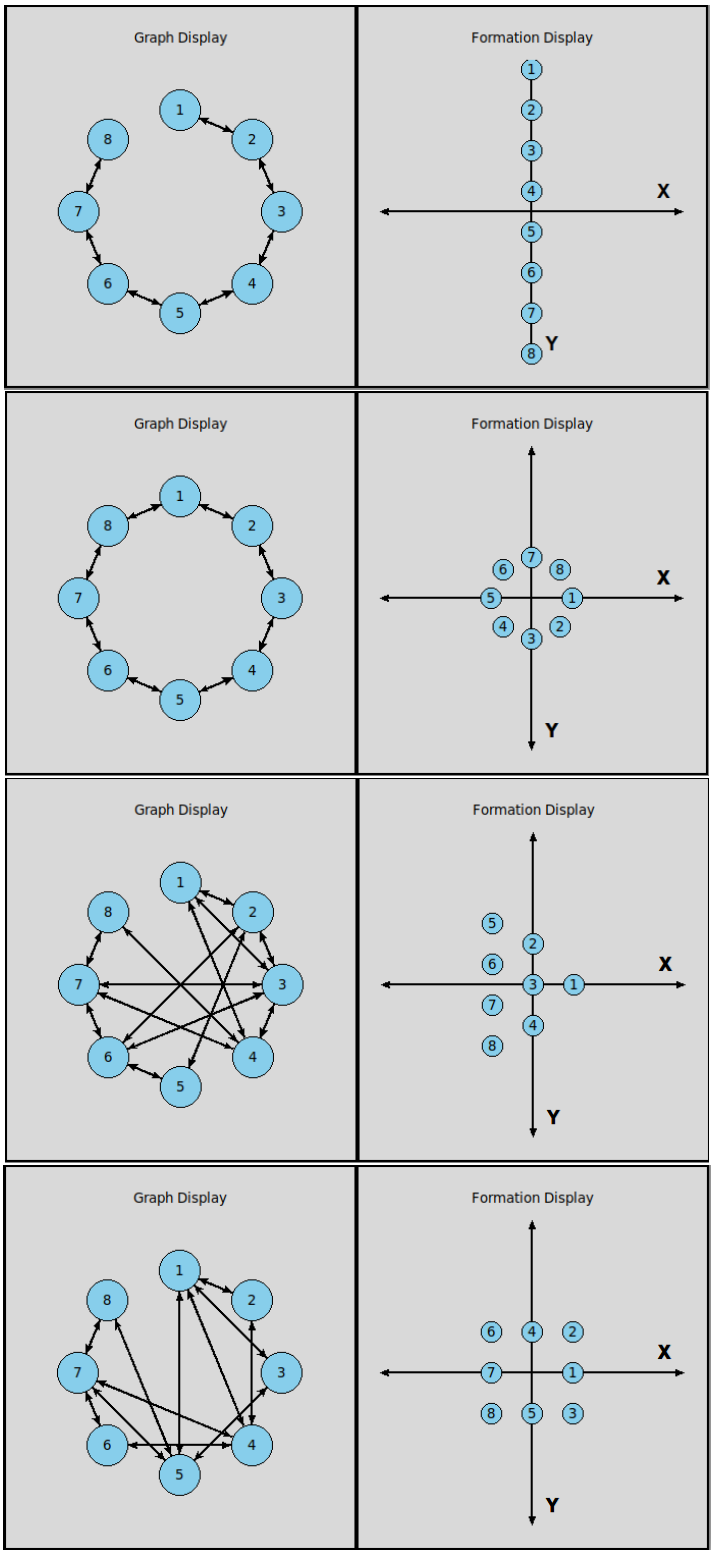

Figure 4.13: Various communication graph topologies and geometrical formation shapes; line, circle, triangle, and square, respectively.

are expected to be more effective for achieving quick convergence of the agents to the desired state or formation. These expectations are validated in simulation results presented in Section 4.2.4.

4.2.3 Extended State Observer Based Total Disturbance Estimation

Consider a second-order single-input-single-output (SISO) nonlinear dynamical system model that is affected by the external disturbance and measurement noise, represented by the following state-space model,

$$\dot{\boldsymbol{x}}(t) = \boldsymbol{A}\boldsymbol{x}(t) + \boldsymbol{b}\left(f(\boldsymbol{x},t) + g(\boldsymbol{x},t)u(t) + d^*(t)\right)$$
$$y(t) = \boldsymbol{c}^T\boldsymbol{x}(t) + w(t)$$

where $\boldsymbol{x} = [x_1\ x_2]^T \in \mathbb{R}^2$ is the state vector of the system. $u \in \mathbb{R}$ denotes the control signal, and $y \in \mathbb{R}$ is the system output. The terms $d^* \in \mathbb{R}$ and $w \in \mathbb{R}$ correspond to the external disturbance and measurement noise, respectively. Additionally, $f \in \mathbb{R}$ describes the controlled system dynamics, while $g \in \mathbb{R}\setminus\{0\}$ represents the control effectiveness. For this system, $\boldsymbol{A} = \begin{bmatrix} 0 & 1 \\ 0 & 0 \end{bmatrix}$, $\boldsymbol{b} = [0\ 1]^T$, and $c = [1\ 0]^T$.

Assumption 4.2.1. *The external disturbance d^* is assumed to be at least first-order continuous and differentiable. It is also bounded within the set $\mathcal{D}_{d^*} \triangleq \{d^* \in \mathbb{R} : |d^*| < r_{d^*}\}$, and and its derivative $\dot{d}^*$ is bounded within $\mathcal{D}_{\dot{d}^*} \triangleq \{\dot{d}^* \in \mathbb{R} : |\dot{d}^*| < r_{\dot{d}^*}\}$, for some positive constants $r_{d^*}, r_{\dot{d}^*} > 0$.*

Assumption 4.2.2. *The measurement noise w is bounded within the set $\mathcal{D}_w \triangleq \{w \in \mathbb{R} : |w| < r_w\}$ for some positive constant $r_w > 0$.*

Given that the state dynamics are unknown, the state-space model can be reformulated to incorporate these assumptions:

$$\dot{\boldsymbol{x}}(t) = \boldsymbol{A}\boldsymbol{x}(t) + \boldsymbol{b}\hat{g}u(t) + \boldsymbol{b}\underbrace{\left(f(\boldsymbol{x},t) + d^*(t) + \left(g(\boldsymbol{x},t) - \hat{g}\right)u(t)\right)}_{d(\boldsymbol{x},t)}$$

$$y(t) = \boldsymbol{c}^T\boldsymbol{x}(t) + w(t)$$

where $d(\boldsymbol{x},t)$ is called the total disturbance and $\hat{g}$ is the constant estimate of g.

Remark 4.2.3. *If the mathematical model of the system is known, the known terms can be moved outside of the total disturbance term and explicitly addressed in the estimator model.*

To implement this, the extended state is defined as $\boldsymbol{z} = \left[\boldsymbol{x}^T d\right]^T \in \mathbb{R}^3$ with the following dynamics,

$$\dot{z}(t) = \underline{\boldsymbol{A}}\boldsymbol{z}(t) + \underline{\boldsymbol{b}}\dot{d}(\boldsymbol{z},t) + \underline{\boldsymbol{d}}\hat{g}u(t)$$

$$y(t) = \underline{\boldsymbol{c}}^T\boldsymbol{z}(t) + w(t)$$

where $\underline{\boldsymbol{b}} = [0\ 0\ 1]^T$, $\underline{\boldsymbol{d}} = [0\ 1\ 0]^T$, and $\underline{\boldsymbol{c}} = [1\ 0\ 0]^T$.

The dynamics of extended state are constructed by using the estimated state $\hat{\boldsymbol{z}} = \boldsymbol{\xi}$ as,

$$\dot{\boldsymbol{\xi}} = \underline{\boldsymbol{A}}\boldsymbol{\xi} + \underline{\boldsymbol{d}}\hat{g}u(t) + \boldsymbol{l}\left(y - \underline{\boldsymbol{c}}^T\boldsymbol{\xi}\right)$$

where $\boldsymbol{l} \in \mathbb{R}^3$ is the observer gain vector, chosen to ensure the desired convergence and stability properties of the observer.

Defining the observer estimation error as $\tilde{\boldsymbol{\xi}} = \boldsymbol{z} - \boldsymbol{\xi}$, error dynamics are obtained as below

$$\dot{\tilde{\boldsymbol{\xi}}} = \underbrace{\left(\underline{\boldsymbol{A}} - \boldsymbol{l}\underline{\boldsymbol{c}}^T\right)}_{\boldsymbol{H}}\tilde{\boldsymbol{\xi}} + \underline{\boldsymbol{b}}\dot{d}(\boldsymbol{z},t) - \boldsymbol{l}w \tag{4.11}$$

Note that in case of constant disturbance without measurement noise, i.e. $\dot{d} = 0$ and $w = 0$, the error dynamics in Equation (4.11) can be effectively controlled. By setting observer gains that makes error system matrix $\boldsymbol{H}$ Hurwitz, an exponentially decaying error dynamics can be achieved. However, for more general case with bounded external disturbance and measurement noise, the stability and boundedness of the system are needed to be shown along with the necessary and sufficient conditions. The sufficient conditions are derived below, but further details on the stability proof can be found in Refs. [80, 100].

Choosing a candidate Lyapunov function $V = \frac{1}{2}\tilde{\boldsymbol{\xi}}^T \boldsymbol{P} \tilde{\boldsymbol{\xi}}$ where $\boldsymbol{P} = \boldsymbol{P}^T > 0$. The rate of change of function V is then computed by

$$\begin{aligned} \dot{V} &= \frac{1}{2}\tilde{\boldsymbol{\xi}}^T \left(\boldsymbol{H}^T \boldsymbol{P} + \boldsymbol{P}\boldsymbol{H}\right) + \tilde{\boldsymbol{\xi}}^T \boldsymbol{P} \underline{\boldsymbol{b}} \dot{d} - \tilde{\boldsymbol{\xi}}^T \boldsymbol{P} \boldsymbol{l} w \\ &= -\frac{1}{2}\tilde{\boldsymbol{\xi}}^T \boldsymbol{Q} \tilde{\boldsymbol{\xi}} + \tilde{\boldsymbol{\xi}}^T \boldsymbol{P} \underline{\boldsymbol{b}} \dot{d} - \tilde{\boldsymbol{\xi}}^T \boldsymbol{P} \boldsymbol{l} w \end{aligned} \tag{4.12}$$

where $\boldsymbol{Q} = \boldsymbol{Q}^T > 0$. Solution to Lyapunov equation $\boldsymbol{H}^T \boldsymbol{P} + \boldsymbol{P}\boldsymbol{H} = -\boldsymbol{Q}$ for chosen $\boldsymbol{Q}$ always exists since $\boldsymbol{H}$ is Hurwitz. Now, we need to show the sufficient conditions that bounded second and third terms on the right hand-side of Equation (4.12) do not overcome the negativity of the first term, which provides the stability.

$$\dot{V} \leq -\frac{1}{2}\underline{\sigma}(\boldsymbol{Q})\|\tilde{\boldsymbol{\xi}}\|^2 + \bar{\sigma}(\boldsymbol{P})\|\tilde{\boldsymbol{\xi}}\| \left(\|\underline{\boldsymbol{b}}\||\dot{d}| + \|\boldsymbol{l}\||w|\right) \tag{4.13}$$

Thus, $\dot{V} < 0$ if and only if

$$\|\tilde{\boldsymbol{\xi}}\| > \frac{2\bar{\sigma}(\boldsymbol{P}) \left(\|\underline{\boldsymbol{b}}\||\dot{d}| + \|\boldsymbol{l}\||w|\right)}{\underline{\sigma}(\boldsymbol{Q})} \tag{4.14}$$

4.2.4 Simulation Results

This section elaborates on the simulation setup utilized to evaluate the formation control strategy for multi-rotor systems. The simulations are implemented using the Gazebo physics simulator, leveraging a custom-built PX4-SITL autopilot software and the Robot Operating System (ROS). This simulation setup allows us to integrate realistic vehicle models, sensor and actuator models, as well as environment models. Two distinct scenarios are considered, each comprising three separate cases, to assess the system's robustness and adaptability under varying conditions, including environmental disturbances and graph topologies.

4.2.4.1 Simulated Scenarios

Scenario 1: Constant Graph Topology Across Various Formation Shapes

In the first scenario, the graph topology is maintained as the fully connected graph for all cases, ensuring maximal communication capability among agents.

- **Case 1 - Baseline Performance Without Wind Disturbance:** The initial case simulates conditions without any wind disturbance, focusing on the baseline performance of the formation control strategy.
- **Case 2 - Impact of Steady Wind without ESO:** This case introduces a wind condition with a magnitude of 30 km/h, blowing towards the positive y direction. Here, the impact of steady wind on formation stability is analyzed without the integration of ESO for disturbance estimation.
- **Case 3 - Integration of ESO under Wind Conditions:** Building upon the previous case, this setup additionally integrates the Extended State Observer (ESO) into each agent for total disturbance estimation, assessing the effectiveness of ESO in mitigating the impact of wind and corresponding air-drag effect on the multi-agent formation.

Scenario 2: Variable Graph Topologies Aligned with Formation Shapes

The second scenario employs variable graph topologies aligned with different formation shapes, as illustrated in Figure 4.13. This scenario tests the adaptability of the system under various communication constraints.

- **Case 1 - Formation Control with Differing Graph Topologies:** Similar to Scenario 1, the first case in this scenario is conducted without wind, focusing on the formation control with differing graph topologies.
- **Case 2 - Wind Conditions with Various Topologies:** This case introduces the same wind conditions as in Scenario 1 (30 km/h, east-to-west), but with varying graph topologies, examining how different communication structures respond to environmental disturbances without the aid of ESO.
- **Case 3 - ESO in Wind Conditions with Various Topologies:** The final case incorporates ESO into agents while maintaining the wind condition. This setup aims to evaluate the combined impact of variable graph topologies and ESO's effectiveness in a wind-affected environment.

The design of these scenarios aims to provide comprehensive insights into the formation control strategy under a range of operational conditions. Scenario 1 establishes a baseline for performance under optimal communication scenarios (fully connected graph), while Scenario 2 introduces more complex and realistic communication constraints. The introduction of wind and the integration of ESO across different cases allow for an in-depth analysis of the strategy's robustness and adaptability to both environmental disturbances and communication limitations.

4.2.4.2 Simulated Multi-Rotor Model

The simulations utilize a multi-rotor model based on DJI F450 quad-rotor, which is comprehensively analyzed in Ref. [101]. This reference provides an in-depth study of the system's parameters, including aerodynamic coefficients, mass and inertia parameters, and other induced effects, identified through a series of exhaustive experiments. Drawing from these findings, this research adopts certain identified parameters and the aerodynamic model of this multi-rotor. The equations of motion for the model are presented as follows,

$$\begin{aligned}
\dot{\boldsymbol{x}} &= \boldsymbol{v} \\
m_Q \dot{\boldsymbol{v}} &= m_Q g \boldsymbol{e}_3 + \boldsymbol{R}_{IB} f_B \boldsymbol{e}_3 \underbrace{-k_d \omega_s \boldsymbol{R}_{IB} \boldsymbol{P} \boldsymbol{v}_{B/W}}_{\boldsymbol{f}_{drag}} \\
\dot{\boldsymbol{R}}_{IB} &= \boldsymbol{R}_{IB} \hat{\boldsymbol{\omega}}_Q \\
\boldsymbol{J}_Q \dot{\boldsymbol{\omega}}_Q &= -\boldsymbol{\omega}_Q \times \boldsymbol{J}_Q \boldsymbol{\omega}_Q + \boldsymbol{\tau} - k_d \omega_s \boldsymbol{R}_{IB} \boldsymbol{P} \boldsymbol{v}_{B/W} \times h \boldsymbol{e}_3
\end{aligned}$$

where $\omega_s = \sum_{i=1}^{4} \omega_{M_i}$ represents the total rotor speed, and $P = \text{diag}\{1,\ 1,\ 0\}$ is used to extract the horizontal components of vehicle's relative velocity. h denotes the positional offset at which the drag force is applied relative to the vehicle's center of gravity.

Furthermore, the control allocation for the multi-rotor is detailed in Equation (3.12), and the modeling of force and moment generation by the rotation of the multi-rotor propellers is outlined in Equation (3.13). The parameters utilized in the simulation model are listed in Table 4.6.

Note that, as provided in Ref. [101], the actual force generation by each individual thruster adheres to the following dynamics,

$$f_i = k_F \omega_i^2 \underbrace{-k_z v_z \omega_i + k_h v_h^2}_{\text{drag related rotor forces}}$$

Parameter	Value	Unit	Parameter	Value	Unit
$J_{Q_{xx}}$	1.3×10^{-2}	kg.m^2	$J_{Q_{xy}}$	-8.8×10^{-5}	kg.m^2
$J_{Q_{yy}}$	1.29×10^{-2}	kg.m^2	$J_{Q_{xz}}$	-6.56×10^{-5}	kg.m^2
$J_{Q_{zz}}$	2.36×10^{-2}	kg.m^2	$J_{Q_{yz}}$	3.98×10^{-5}	kg.m^2
h	0.06	m	L	0.225	m
k_F	1.5×10^{-7}	N/RPM^2	k_M	0.01	m
k_d	1.0587×10^{-5}	N.s/m/RPM	k_z	6.2×10^{-5}	N.s/m/RPM^2
k_h	2.1366×10^{-2}	N.s^2/m^2	$\omega_{M_{max}}$	10×10^4	RPM

Table 4.6: Simulated multi-rotor parameters

where v_h and v_z are the horizontal and vertical components of the relative body velocity. This formulation introduces additional disturbance factors to the previously described vehicle model.

4.2.4.3 Leader Trajectory and Formation Transitions

All simulation cases follow identical commands. Initially, agents are spawned on the ground in a line formation, maintaining a 2-meter separation. Note that among the group, only the first agent (node) is pinned by the leader, having access to the leader's position and velocity states. The leader is then instructed to ascend to an altitude of 10 meters at a steady climb rate of 0.5 m/s, achieved via step velocity input. Once the formation stabilizes at this altitude, the leader progresses forward at a constant speed of 2 m/s. During this phase, the formation undergoes various shape transitions: square, circular, triangular, and finally returning to the same line formation. Following each formation change, a settling period is allowed, its duration dependent on communication strength and convergence behavior.

4.2.4.4 Results and Discussion

Scenario 1 - Constant Graph Topology Across Various Formation Shapes

Case 1 - Baseline Performance Without Wind Disturbance: In the first case of Scenario 1, the performance of multi-rotor formation control is illustrated in Figure 4.14, revealing some insightful dynamics by plotting vehicle positions, velocities and acceleration commands. The vehicle positions within the formation closely follow the desired trajectories with minimal oscillation, indicating a quick convergence to the designated formation shapes. This demonstrates the effectiveness of the consensus control strategy in maintaining formation configuration under no-wind conditions and without employing any disturbance estimator. However, a closer examination of the vehicle velocities reveals mild, yet diminishing oscillations, particularly observable during transitions between formations. These oscillations, though stable, highlight the dynamic nature of the formation's response to changes.

Inspecting the commanded acceleration inputs of the vehicles, more dominant, sharper, yet decaying oscillations are observed. This phenomenon can be attributed to the formation's fully connected graph topology. In such a setup, any perturbation in an agent's position or velocity is not isolated; it echos throughout the entire formation. This interconnectedness means that changes in relative position offsets during transitions impact all the agents repeatedly, even though agents are not in close vicinity, until the oscillations fully decay. The designed asymptotic stability of the formation dynamics ensures that these oscillations are self-limiting, although their presence is an important consideration. This aspect of the formation's behavior underlines the critical role of feedback gains in the system. If adjusted more carefully, these gains could potentially optimize the oscillatory responses, enhancing the formation's stability and responsiveness during transitions. Such refinements could

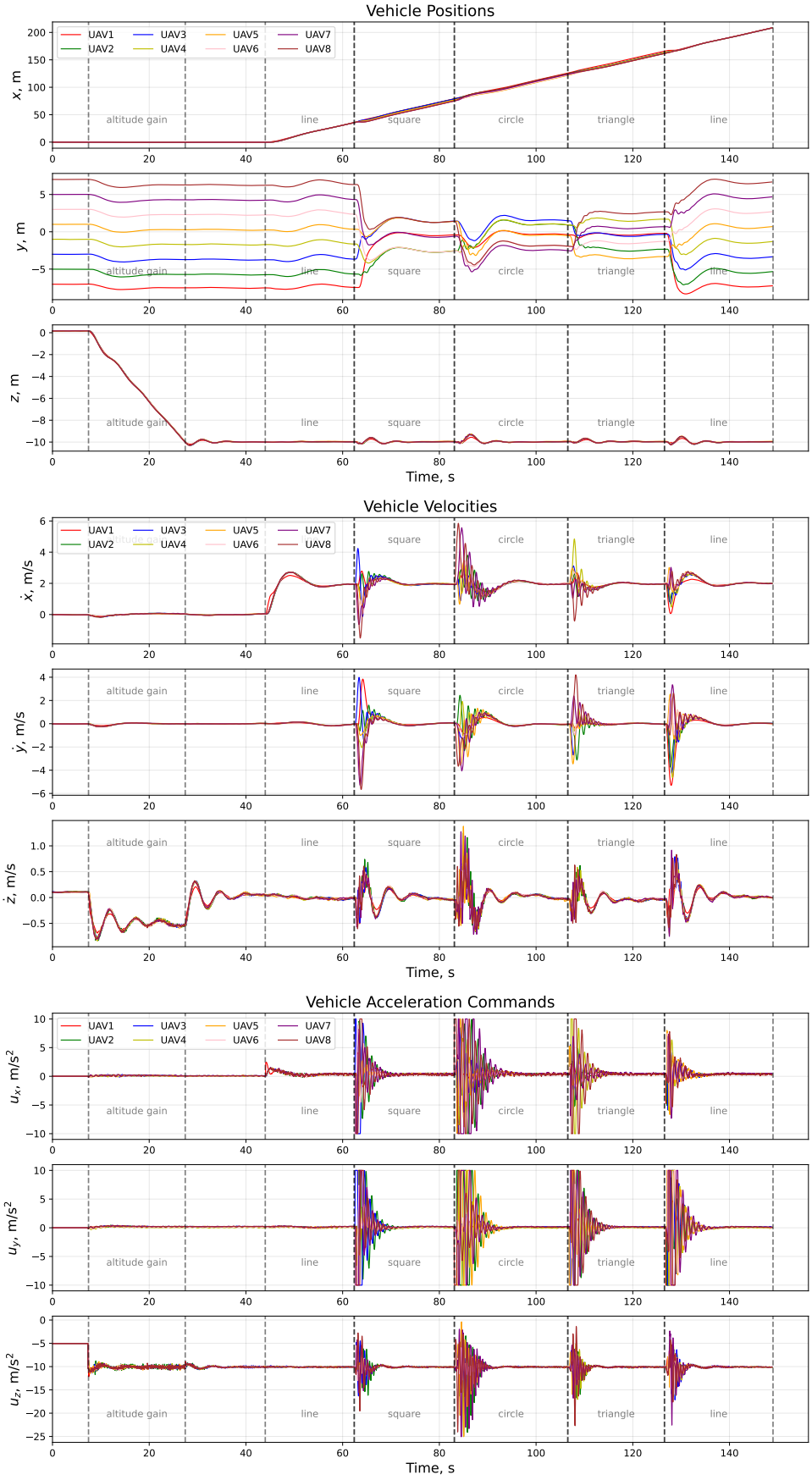

Figure 4.14: Scenario 1 - Case 1 - Position, velocity and acceleration command of vehicles

be crucial for scenarios demanding high precision and rapid adaptability in formation control. Trajectories of each vehicle and the leader is also displayed in Figure 4.15.

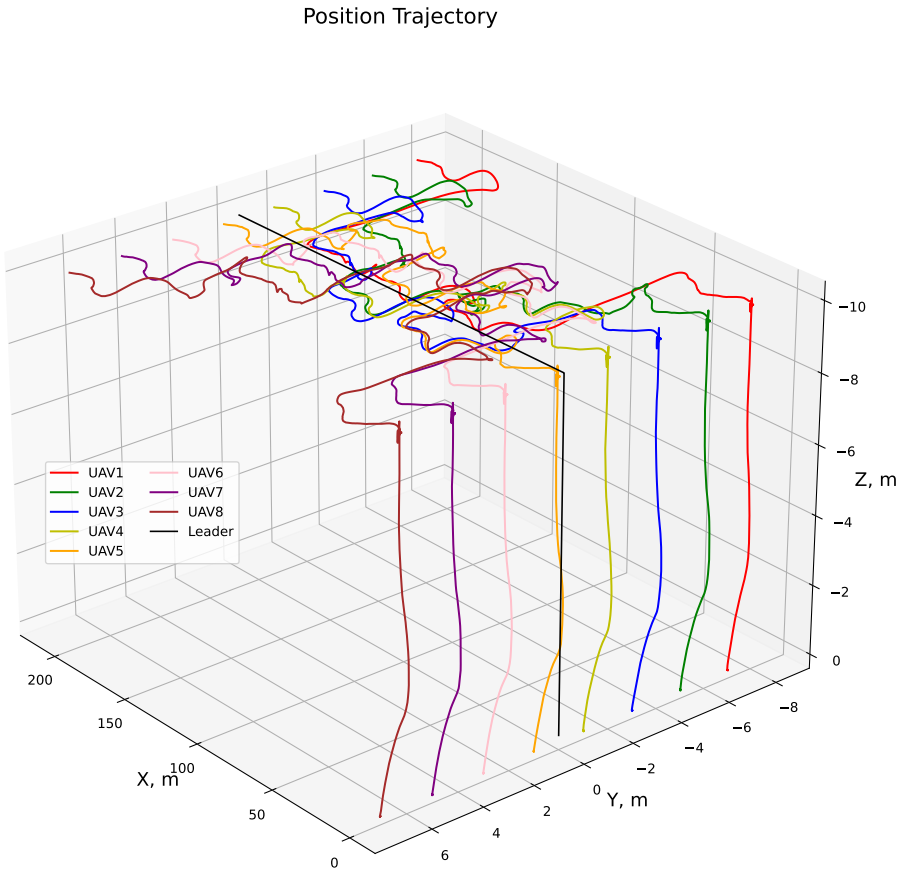

Figure 4.15: Scenario 1 - Case 1 Trajectories (grids are not equally spaced)

Case 2 - Impact of Steady Wind without ESO: The results of the second case are provided in Figure 4.16. The impact of wind on the vehicle positions, when compared with the previous case without wind, is clearly distinguishable. The vehicles are noticeably pushed in the direction of the wind. Despite this, the separation between agents during various formation shapes is largely maintained, with the exception of

node 1, which benefits from direct access to the leader's states. However, in the absence of a mechanism to predict disturbances like wind-caused air drag, the agents in this configuration are unable to proactively account for such external factors. Thus, they react solely to position and velocity errors to preserve desired formation configuration. This reactive approach leads them to stabilize at an arbitrary consensus state, where the external disturbances are balanced by local neighborhood position and velocity error correction forces.

While the introduction of wind results in additional oscillations, the velocity and acceleration commands of individual vehicles remain similar to those in the first case. This similarity indicates that, although the system can withstand and adjust to wind disturbances to some extent, its response is fundamentally reactive, relying on the inherent dynamics of the formation to reach a new equilibrium state under altered environmental conditions. Therefore, the formation control design, originally synthesized for ideal conditions without accounting for disturbance bounds, may be susceptible to such disturbances. This can lead to reduced stability or even destabilization of the entire system, underlining the need for incorporating disturbance estimation and mitigation mechanisms in the control strategy.

Figure 4.17 shows the trajectories of each vehicle and the leader. The effect of wind disturbance is evident during the altitude gain phase where the vertical lines pushed towards left in y-axis.

Case 3 - Integration of ESO under Wind Conditions: The results for this case are provided in Figure 4.18. The most obvious outcome is visible in the vehicle positions, where the effectiveness of the ESO is highlighted comparing to the previous case. The ESO significantly reduces the positional drifts caused by the wind effect. The vehicle positions asymptotically approach the values designated by the formation

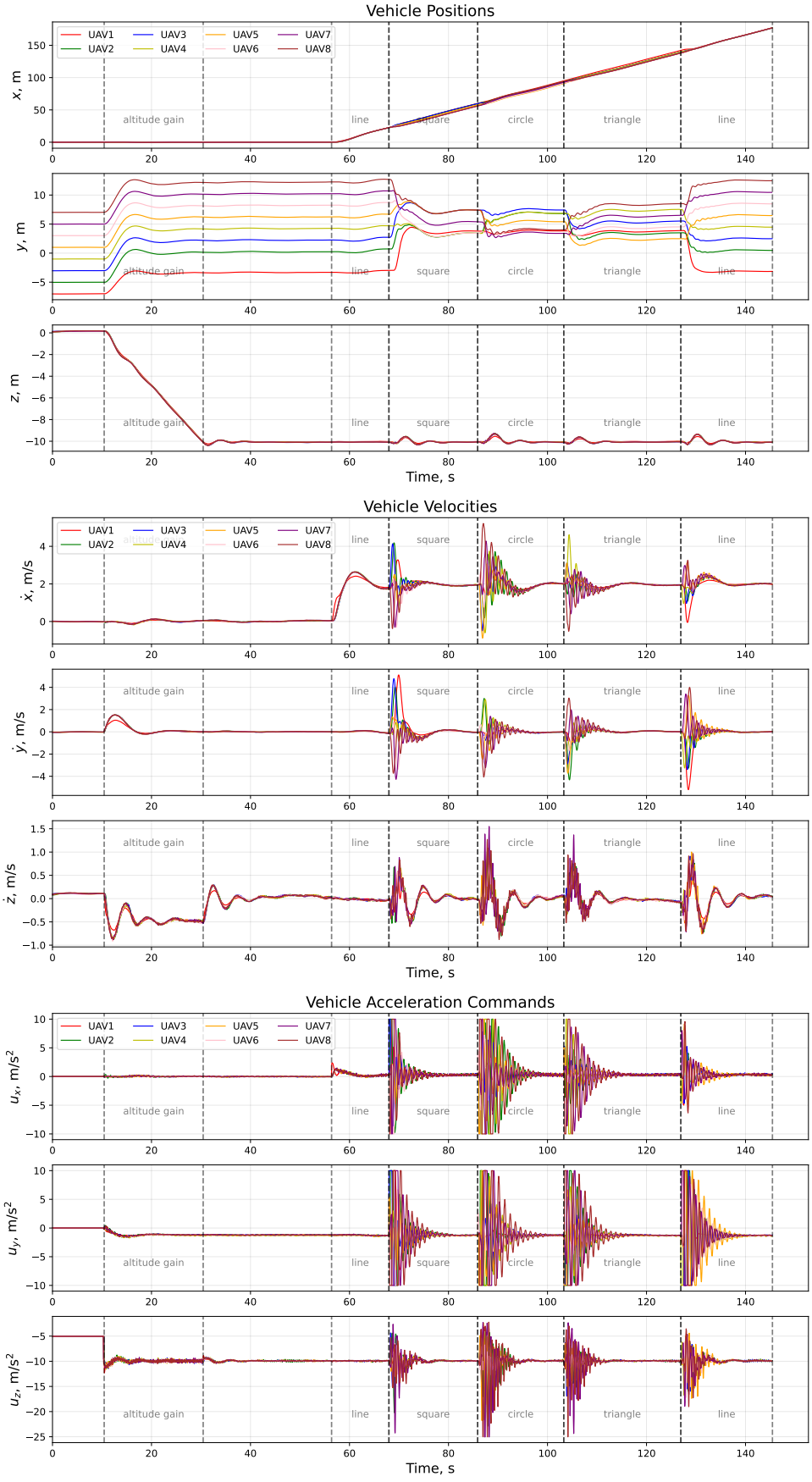

Figure 4.16: Scenario 1 - Case 2 - Position, velocity and acceleration command of vehicles

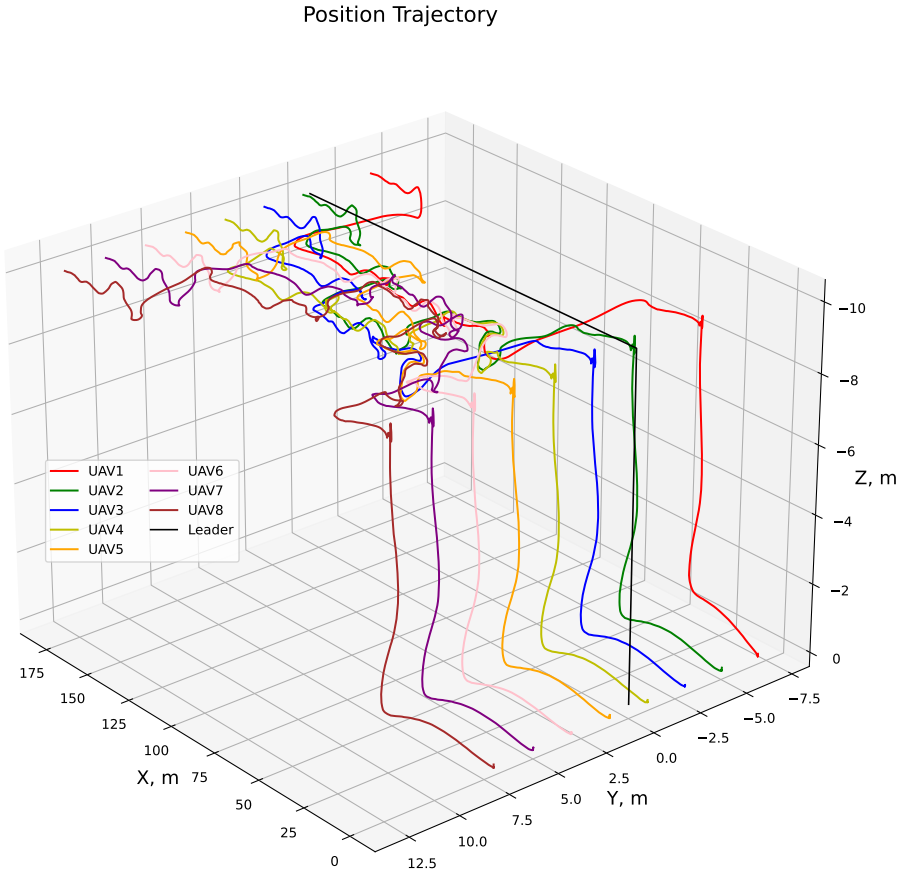

Figure 4.17: Scenario 1 - Case 2 Trajectories (grids are not equally spaced)

configurations, demonstrating ESO's effectiveness. However, when compared to the first case, a transient response to wind effects is still noticeable, especially following formation transitions. This is due to the ESO's own dynamics in estimating the total disturbance, which introduces a lag in the formation's response to external effects. Also, it is worth noting that during transitions, the relative velocity of agents with respect to the wind causes additional drag, leading to slight deviations that are quickly mitigated as well.

Observing the velocity states reveals a more dampened behavior during these transient responses when compared to the previous case. However, in the x component

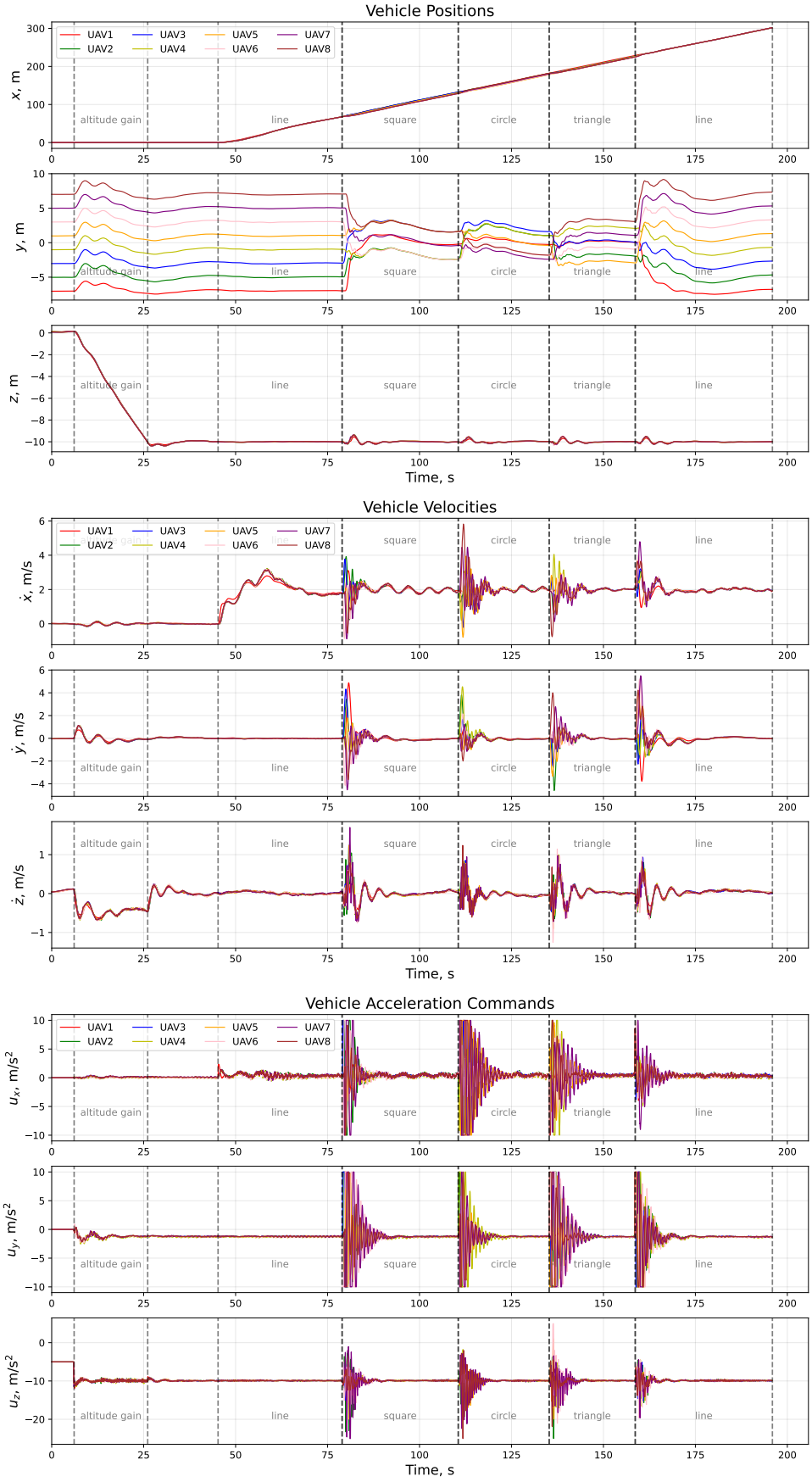

Figure 4.18: Scenario 1 - Case 3 - Position, velocity and acceleration command of vehicles

of vehicle velocities, which aligns with the leader's trajectory direction, low frequency and low magnitude oscillations are observed after transitions, although they slowly decay. This behavior may result from the coupling between the dynamics of the estimator, individual vehicle, and overall formation.

Similarly, a closer look at the vehicle acceleration commands shows a generally more dampened response, particularly in the z component. Furthermore, ESO estimated disturbances for each agent are displayed in Figure 4.19. The y component of these estimates quickly converges to a value reflecting the wind-based air drag disturbance. While low frequency oscillations are present, the x component is also stabilized around a specific value, indicative of drag due to forward velocity. These oscillations, however, require further considerations in adjusting estimator gains and resolving the potential coupling between the estimator and overall formation dynamics.

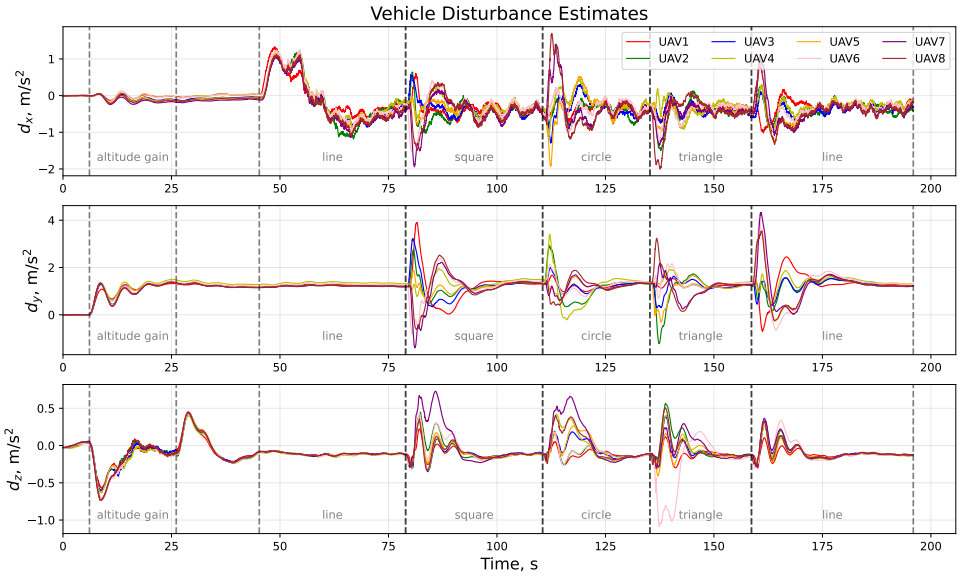

Figure 4.19: Scenario 1 - Case 3 - Total Disturbance Estimate

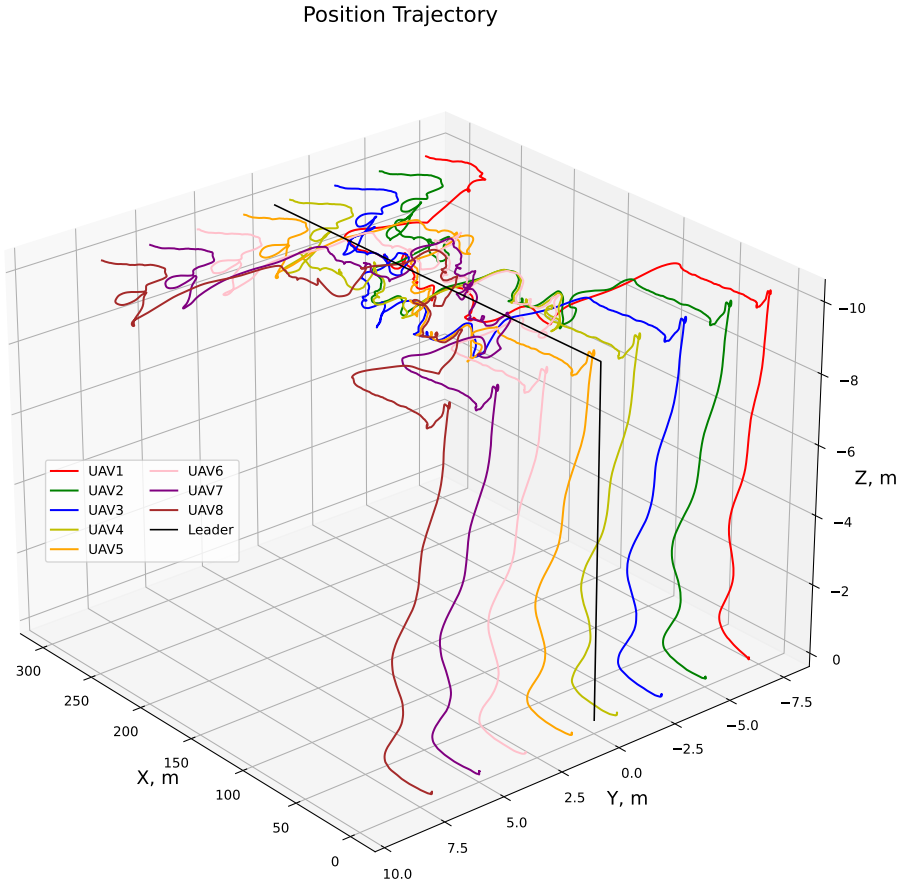

Figure 4.20: Scenario 1 - Case 3 Trajectories (grids are not equally spaced)

Scenario 2 - Variable Graph Topologies Aligned with Formation Shapes

Case 1 - Formation Control with Differing Graph Topologies: The results are illustrated in Figure 4.21. The distinct influence of various graph topologies on formation control is clearly visible, even in the absence of wind. Initially, the system starts in a line formation, which possesses the weakest communication strength among the configurations tested. In this setup, the vehicles, except for the first node, struggle to maintain a close formation. The limited communication, restricted to immediate

neighbors, necessitates longer paths for information propagation, resulting in a laggy response and diminished influence of the leader's trajectory commands.

A notable improvement is observed when the formation switches to a square configuration. The increased connections among agents in this topology lead to a quicker convergence speed. The circular configuration, or 'gossip circle,' though slightly inferior to the square formation, still maintains the desired formation with only minor deviations. The triangular configuration, which has the highest communication volume among the tested topologies, achieves the fastest and most accurate tracking of the desired formation, as anticipated.

Examining the vehicle velocities reveals that the significantly delayed communication in the line topology induces a slow but large response to altitude errors during the altitude gain phase and hover stabilization. Upon transitioning to forward motion, the first node, with direct access to the leader states, reacts the quickest, followed sequentially by its neighbors with a noticeable delay. This delay diminishes significantly in the square configuration, where the response is rapidly propagated through the formation, in contrast to the response observed in the line configuration, which is more spread in time. A similar, even faster response is seen in the triangle configuration.

These observations are supported by the acceleration commands of the vehicles. The stronger the communication between the agents, the sharper and more prompt the commanded accelerations. Interestingly, compared to the fully connected graph of the first case in the previous scenario, the acceleration commands in this scenario are smoother and less oscillatory, potentially contributing to enhanced formation stability.

Trajectories of vehicles and the leader are plotted in Figure 4.22.

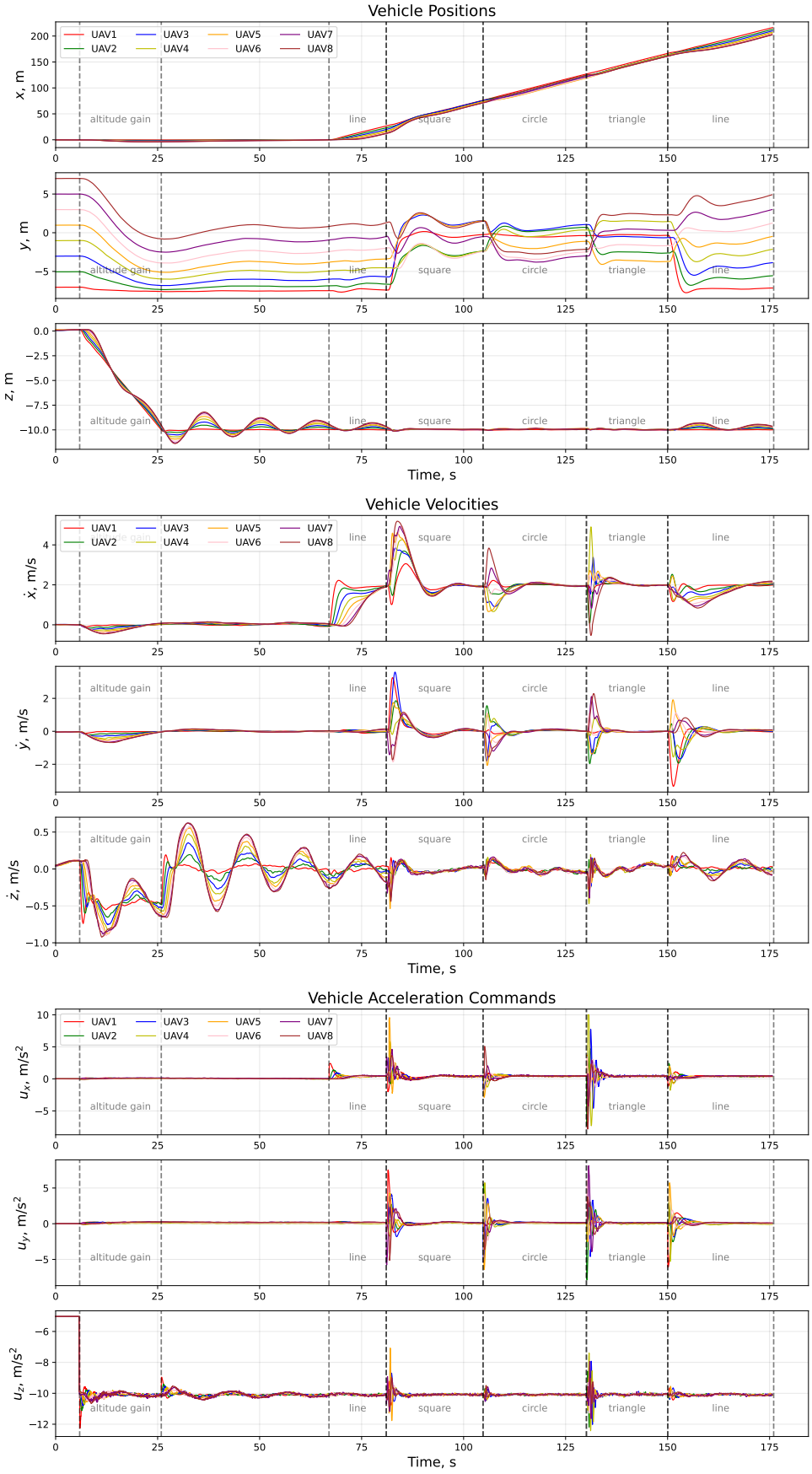

Figure 4.21: Scenario 2 - Case 1 - Position, velocity and acceleration command of vehicles

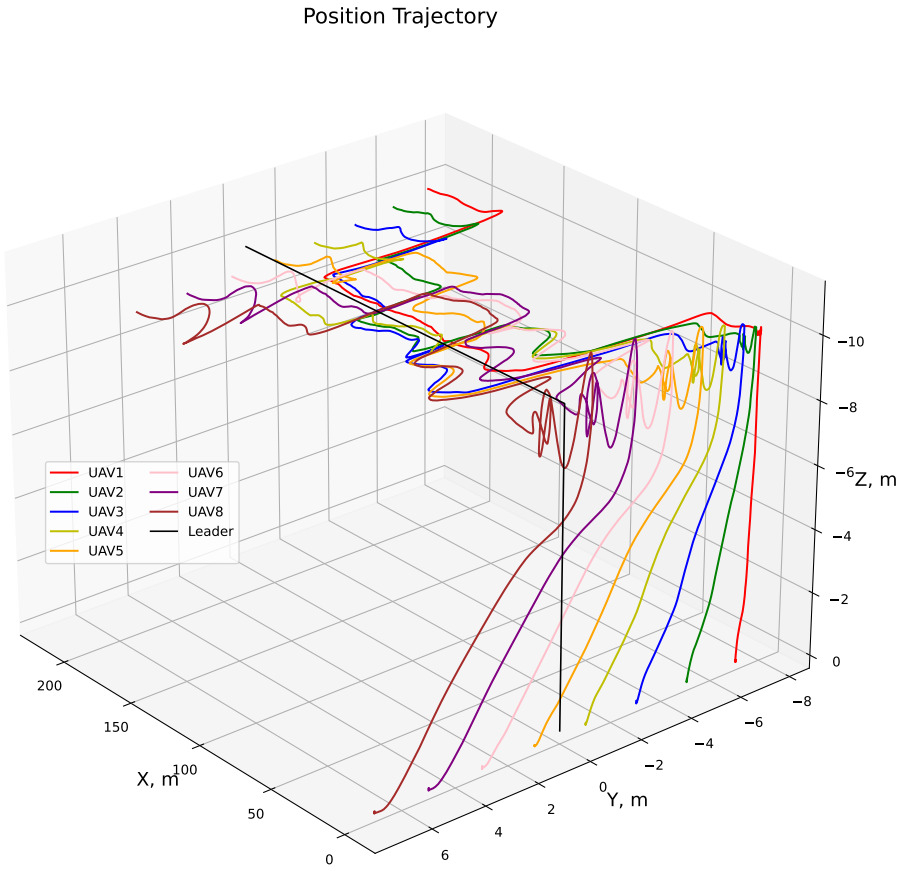

Figure 4.22: Scenario 2 - Case 1 Trajectories (grids are not equally spaced)

Case 2 - Wind Conditions with Various Topologies: Figure 4.23 plots the results for this case. The combined impact of the lack of a disturbance estimator and delayed, weak inter-agent communication becomes particularly dominant, as seen in the line configuration. In this setup, the largest deviation from the desired formation position is observed, highlighting the critical role of effective communication in formation control under wind conditions.

Transitioning to the square configuration brings a noticeable improvement. Despite the rapid convergence seen in this topology, the consensus values achieved are

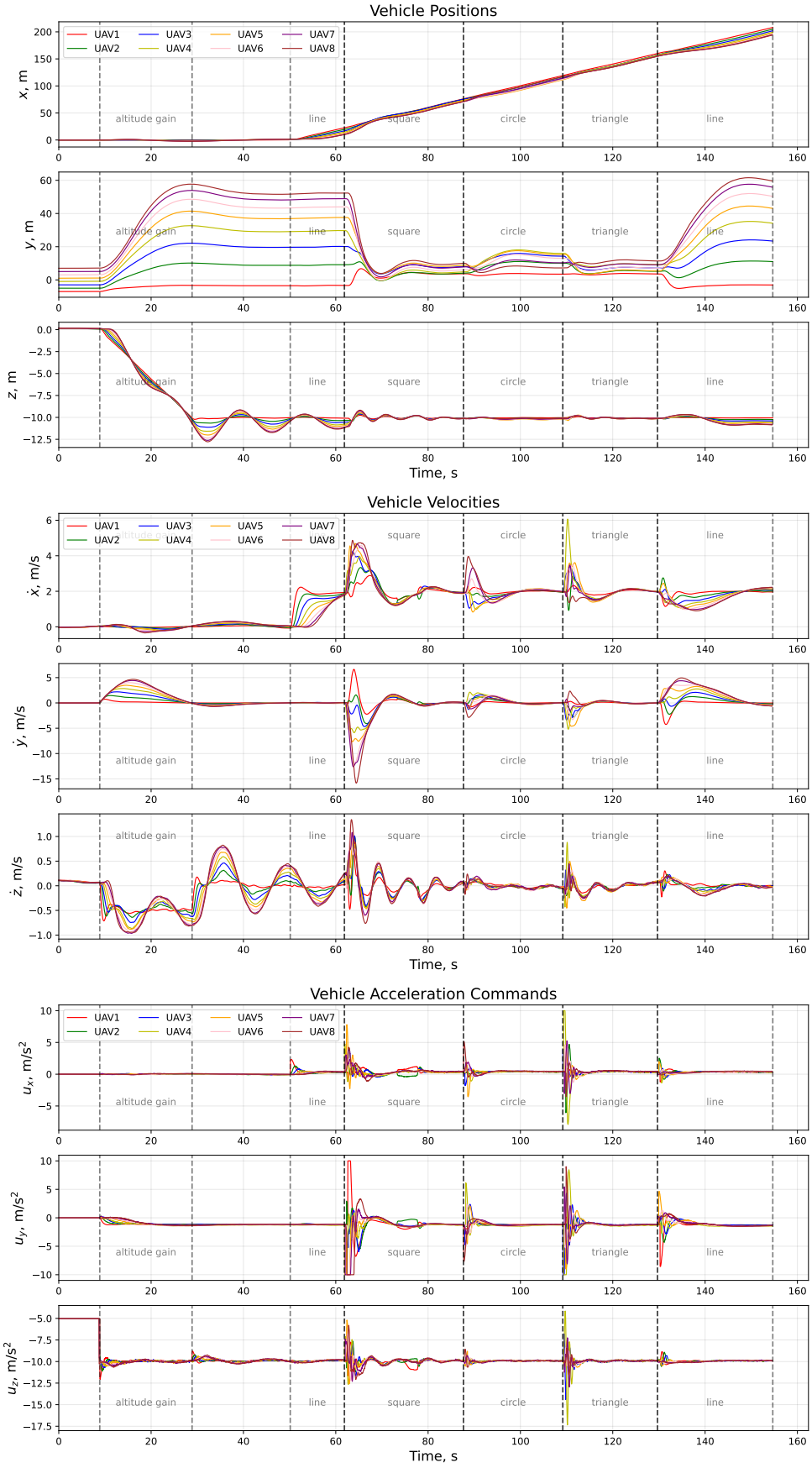

Figure 4.23: Scenario 2 - Case 2 - Position, velocity and acceleration command of vehicles

still not as close to the desired formation as observed in the full connectivity results in Scenario 1. This discrepancy further confirms the influence of communication strength on formation accuracy when we compare the vehicle positions in circular and triangular configurations. The former exhibits larger errors, attributable to its weaker communication links.

Vehicle velocities in this scenario present a less dampened response compared to the second case of Scenario 1. It is observed that high-frequency oscillations after formation transitions are reduced since weaker communication also results in slower information propagation. Despite these limitations, the vehicles exhibit a convergent behavior consistent with the expectations from these graph topologies.

As previously observed, an increase in communication strength leads to sharper and more abrupt acceleration responses. This is particularly visible in the transient behaviors of the agents after transitioning to the square and triangular configurations, where the improved communication provides a more responsive but potentially more volatile control dynamic.

Vehicle trajectories along with the leader are displayed in Figure 4.24.

Case 3 - ESO in Wind Conditions with Various Topologies: Figure 4.25 provides the results of this case. When comparing the results with those of Case 2, we first notice a significant improvement in line configuration, as shown by the vehicle positions aligning more closely with the desired formation. However, there is still a delayed response due to the weaker inter-agent communication. Estimating the total disturbance and proactively mitigating it for each agent has considerably improved formation accuracy, which is also witnessed in other formation configurations. Despite having slightly higher-frequency oscillations, there is a more aggressive convergence in vehicle velocities, compared to the previous case. Additionally, the

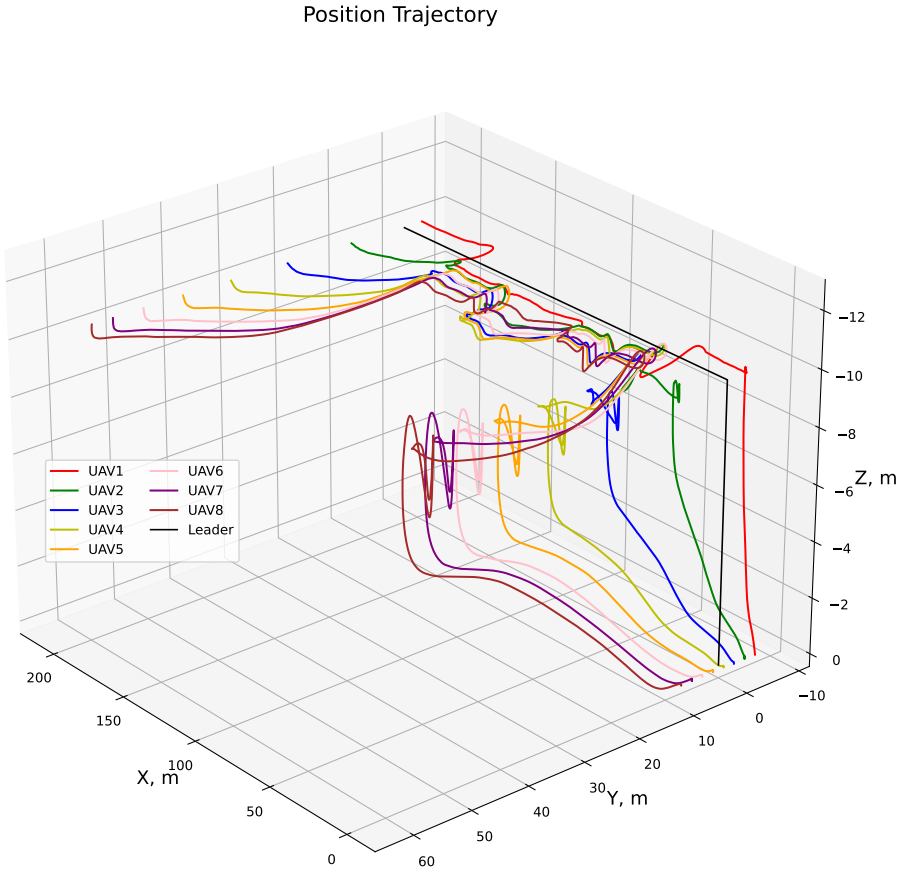

Figure 4.24: Scenario 2 - Case 2 Trajectories (grids are not equally spaced)

velocities in this case remain closer to the desired values. Furthermore, compared to Case 3 of Scenario 1, there is a significant reduction in high-frequency oscillations after the initial phase of each formation transition, along with fewer deviations from the desired values. This enhances the overall stability of the formation. This improvement is even more apparent when examining the vehicle acceleration commands of this case versus those in Scenario 1. We note a substantial decrease in high-frequency acceleration commands, which quickly decay to equilibrium values and maintain a smooth trajectory. This finding is critical, demonstrating the effectiveness of combining ESO integration with slightly sluggish formation dynamics. While ESO effectively

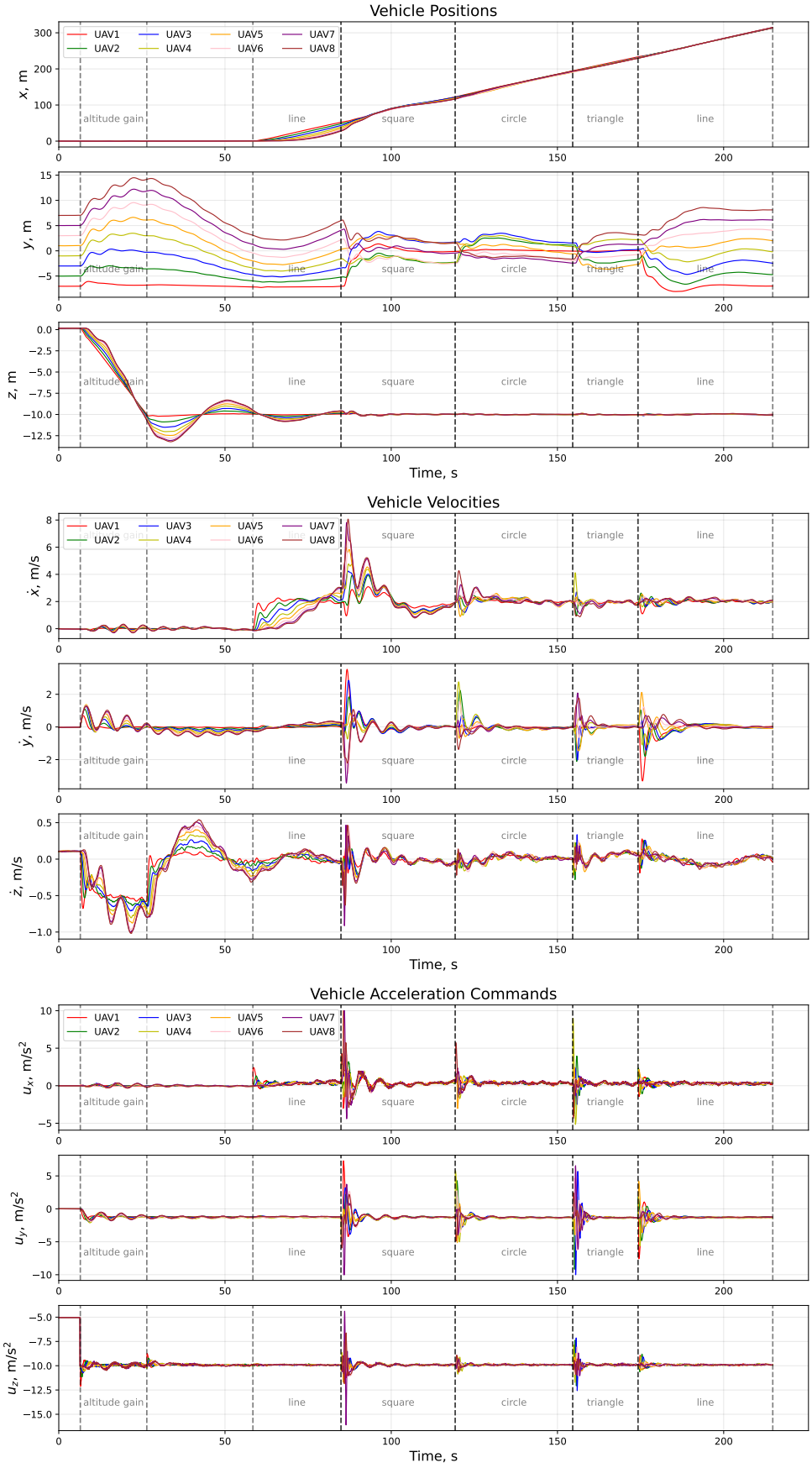

Figure 4.25: Scenario 2 - Case 3 - Position, velocity and acceleration command of vehicles

rejects total disturbances, the slightly sluggish nature of a lightly weaker graph topology, compared to a fully connected graph, acts like a low-pass filter, enhancing the robustness of the formation behavior.

The total disturbance estimation results of the ESO are presented in Figure 4.26. The y-component of the disturbance estimation shows that, while estimating wind disturbance, the transient motion of the agent and additional disturbances are adequately captured. Nevertheless, slight oscillations in the vehicle states are still noticeable, although they are tolerable.

Figure 4.27 depicts the vehicle trajectories along with the leader trajectory.

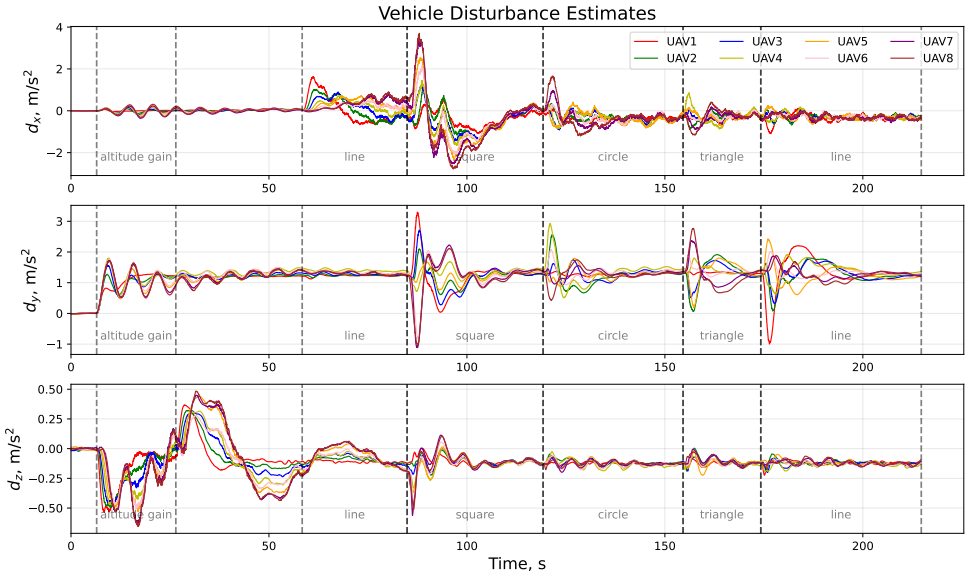

Figure 4.26: Scenario 2 - Case 3 - Total Disturbance Estimate

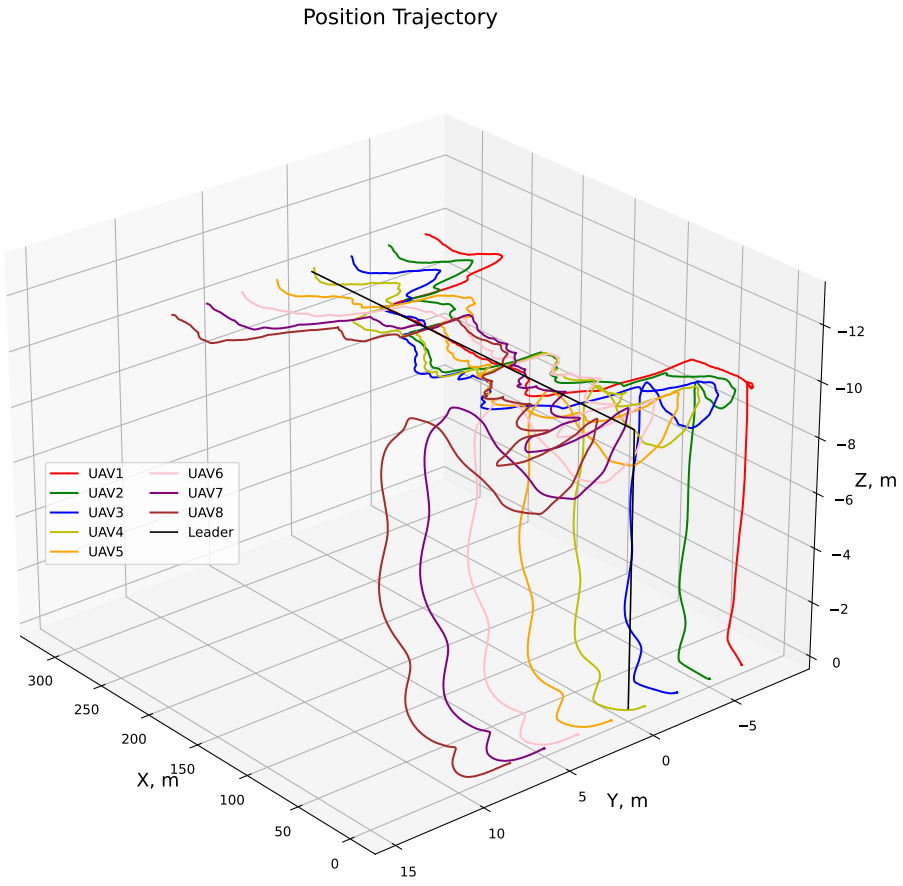

Figure 4.27: Scenario 2 - Case 3 Trajectories (grids are not equally spaced)

4.2.4.5 An Illustrative Real-life Application - Search-and-Rescue Mission

Figure 4.28: Illustrative Scene: A Search-and-Rescue Mission Employing Cooperative Formations of Multi-Rotors, Supported by an Airship for Transportation and Deployment

Description of the Mission Scenario: The scenario illustrated in Figure 4.28 depicts a search and rescue mission assumed to occur in a remote and difficult-to-access location via conventional means, specifically on a sharp mountain surrounded by water in this case. In such emergency situations, aerial support is crucial to effectively search, locate, and respond. To address this, we propose deploying a team of multi-rotors capable of quickly forming various formations to efficiently cover the search area. Given the limitations of these vehicles in traveling long distances, especially when equipped with specialized gear such as cameras, communication devices, and aid kits, we also suggest the use of a larger surrogate aircraft. In this case, an airship is utilized for its ability to effectively transport the multi-rotors to the des-

tination. The airship serves a dual purpose in this scenario. It not only provides physical transportation but also acts as a mobile station, aiming to offer crucial support such as communication, recharging, and other logistical needs to the multi-rotor team. This setup exemplifies both physical and information-level cooperation among multiple UASs.

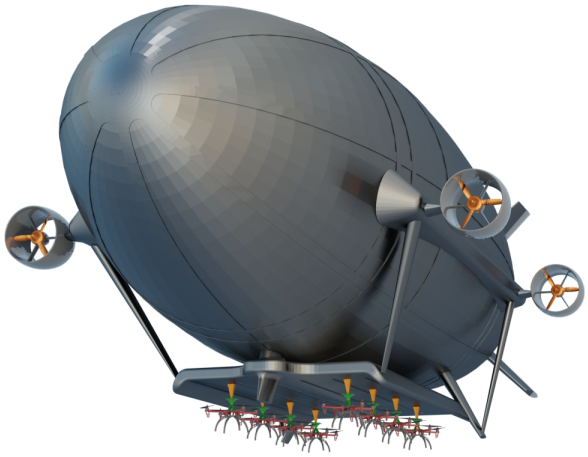

Figure 4.29: Illustration of an airship with a team of multi-rotors attached underneath

In the simulated operation, the airship, with the multi-rotor team attached as shown in Figure 4.29, climbs to a specific altitude from the base station. As the airship navigates toward the mission destination, it begins the sequential deployment of the multi-rotors shortly before arrival. Once all vehicles are deployed, the airship is commanded to loiter near the mission area. The multi-rotors initially form a sparse line formation, moving collectively closer to the mountain for an initial assessment using their onboard cameras. As they approach the mountain, they transition into various formations to thoroughly cover the search areas, focusing on specific spots of interest. The predefined trajectory for the virtual leader position is shown in Figure 4.30.

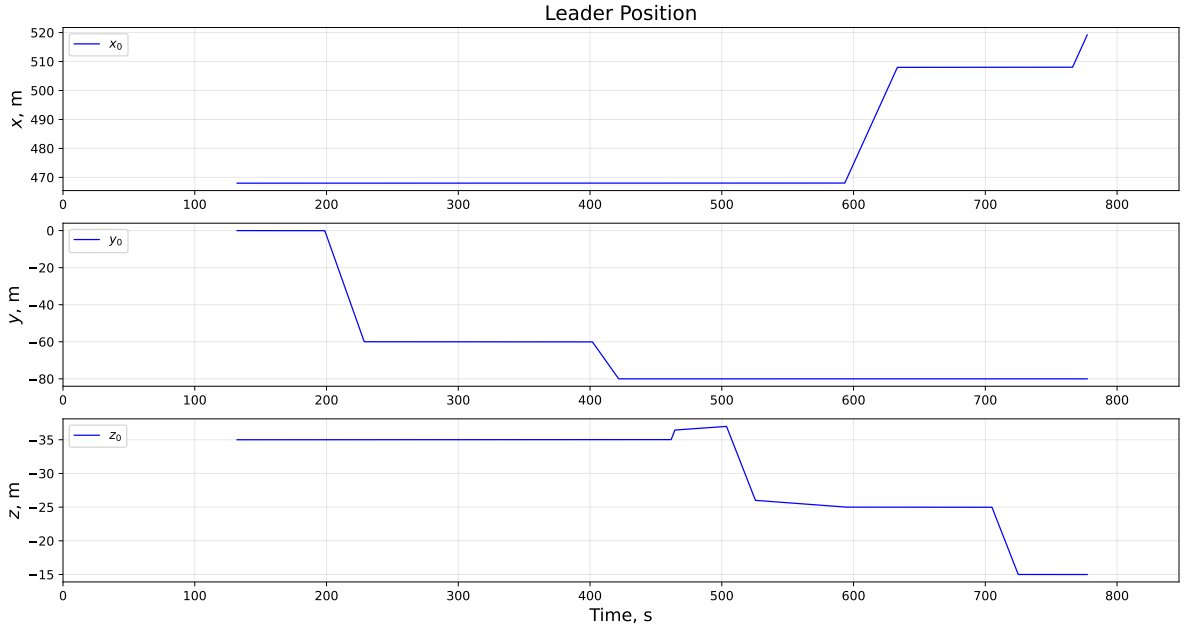

Figure 4.30: Virtual leader trajectory for multi-rotor formations during the search-and-rescue mission

Results:

The 3D trajectories of all vehicles, including the airship, are depicted in Figure 4.31. This graph distinctly illustrates various phases of the mission, including the climbing phase, vehicle deployment, approach towards the target area, and subsequent altitude and formation changes of the vehicles.

Figure 4.32 plots the position and velocity states of each multi-rotor during the execution of the mission. In the plots, the formation shapes are denoted within vertically separated sections. It is worth noting that during both the deployment phase and formation transitions, vehicles quickly recover without suffering extreme oscillations and thus demonstrating the overall stability of the formation.

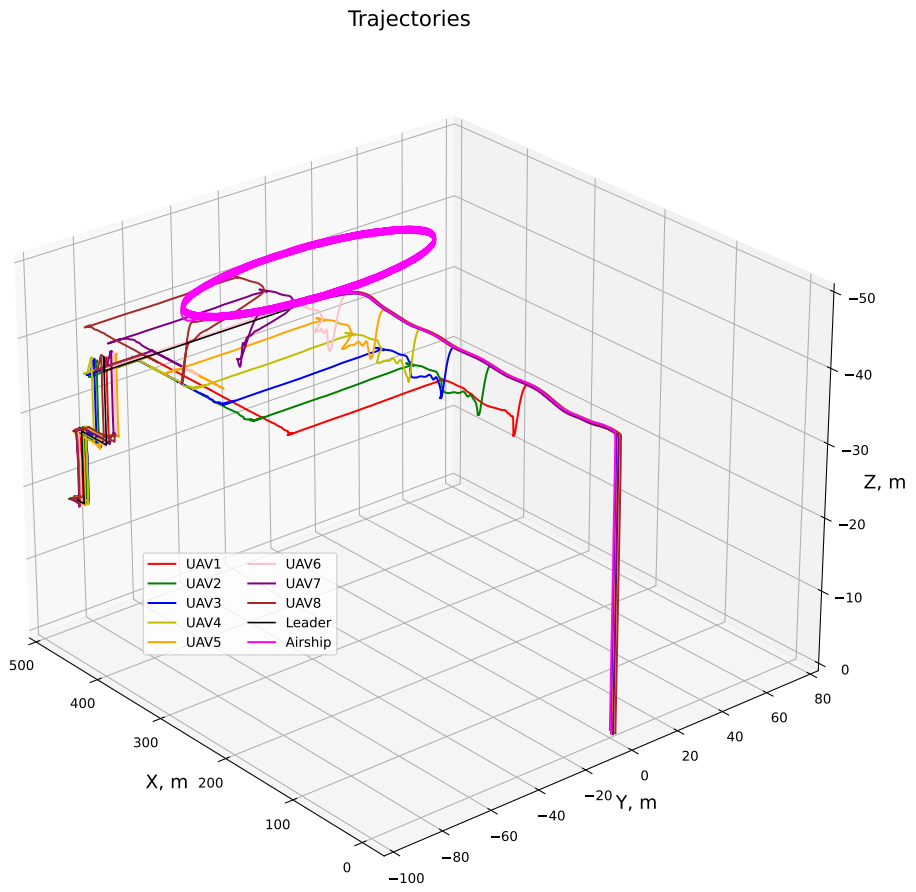

Figure 4.31: Illustration of vehicle trajectories during the mission (grids are not equally spaced)

Acceleration commands for each multi-rotor during the mission are presented in Figure 4.33. We can observe that any oscillations after formation transitions and trajectory commands quickly diminish in magnitude although certain low magnitude oscillations are still present in the commands.

Figure 4.34 shows the total disturbance estimations calculated by the integrated ESO in each multi-rotor. It is worth highlighting that during the deployment process, the accurate estimation of air-drag-induced disturbances significantly improves the vehicles' recovery from the high-velocity air drop from the airship.

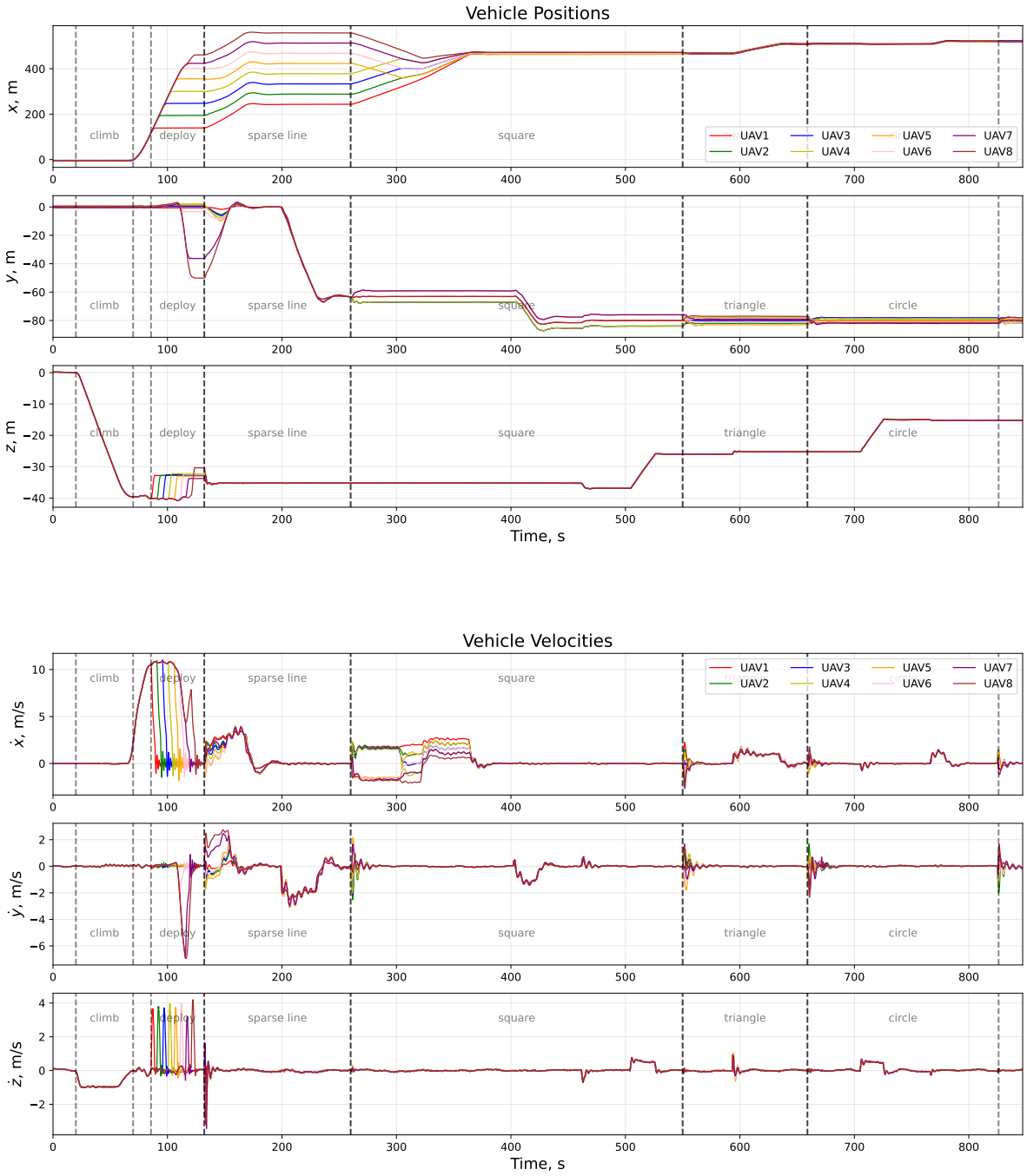

Figure 4.32: Position and velocity states of multi-rotor during the mission

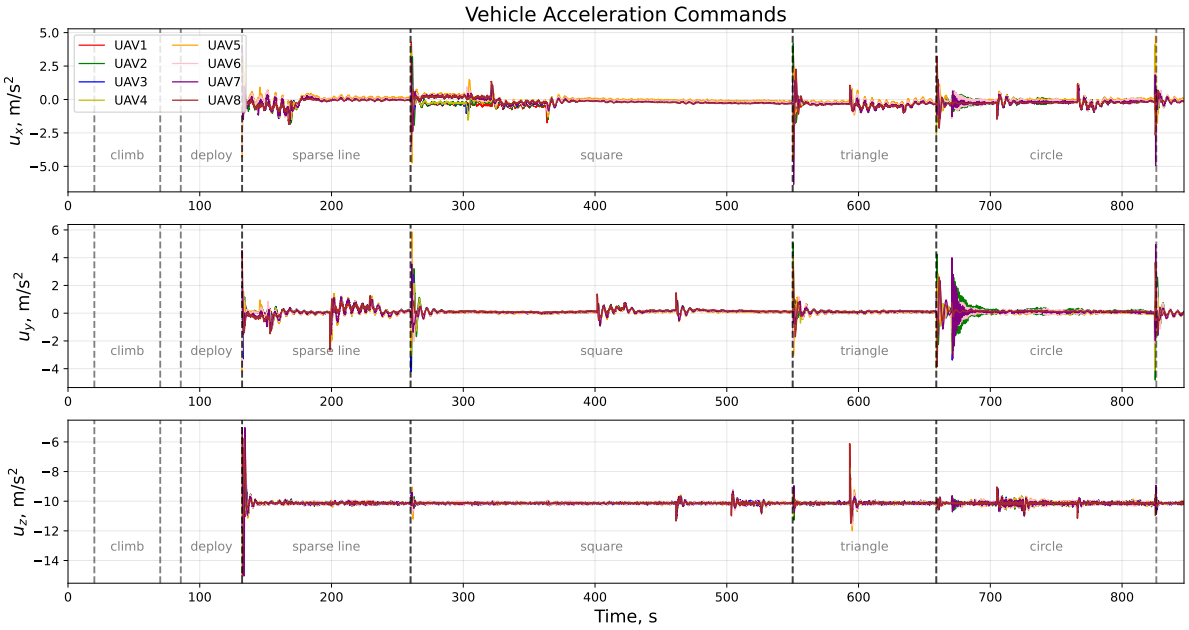

Figure 4.33: Acceleration commands for each multi-rotor during the mission

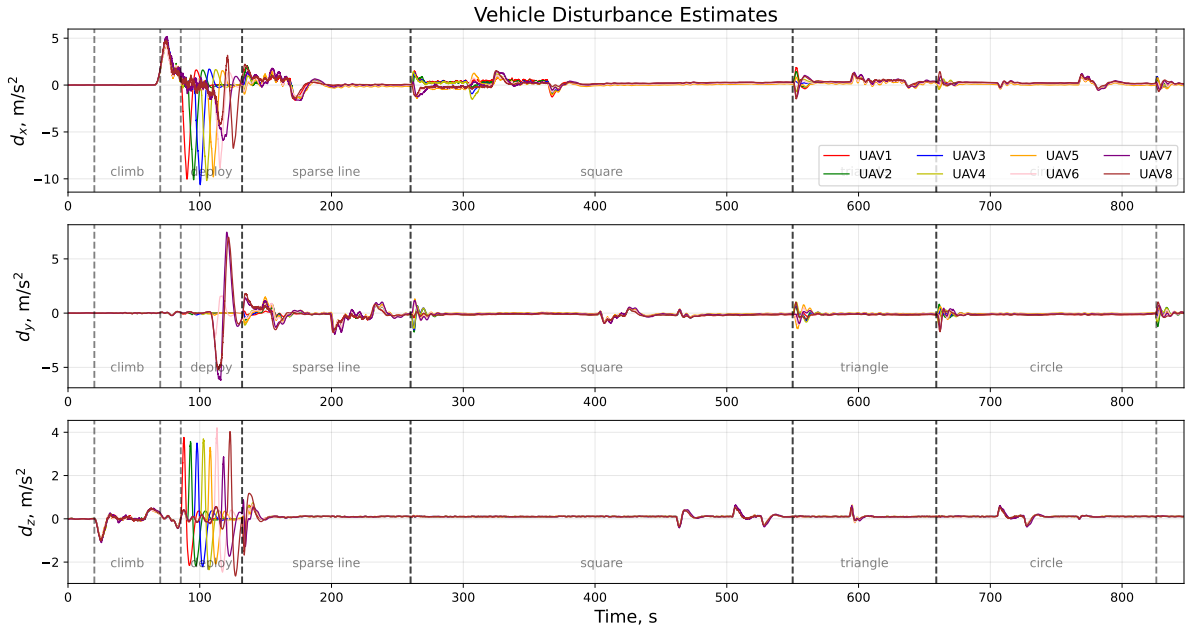

Figure 4.34: Total disturbance estimates from each multi-rotor during the mission

The states of the airship are detailed in Figure 4.35. Here, we observe high-frequency oscillations in speed and angular rate regulations. These oscillations result from the application of higher control gains necessary to accommodate the additional force and moment required after the attachment of the multi-rotors. However, after deployments, these increased gains lead to over-actuation, causing rapid oscillations. Thus, the process of docking and deployment of external payloads to the airship requires further investigation. Future studies could explore an adaptive approach or a dedicated observer, taking into account the limitations and effects of such payload adjustments.

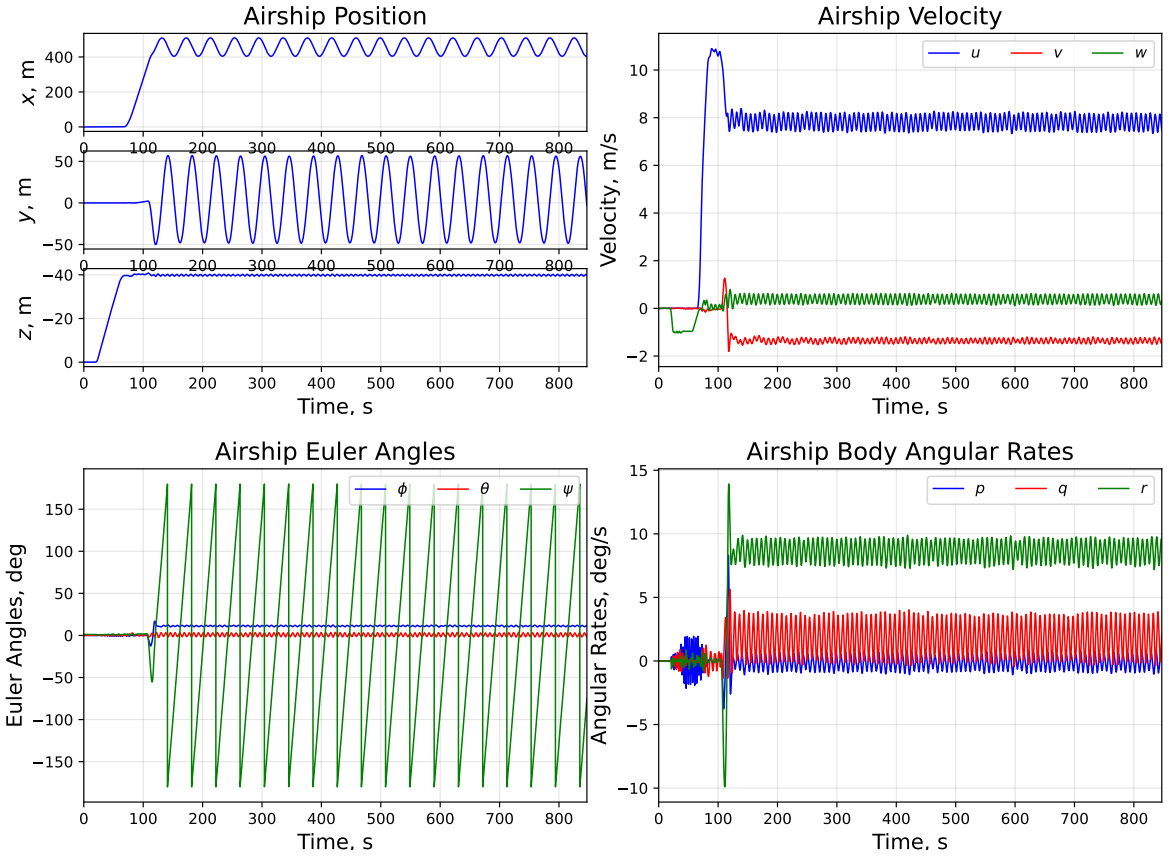

Figure 4.35: States of airship during the mission

General mission overview, including the ground control station, individual camera views of the vehicles, and the simulator environment is shown in Figure 4.36.

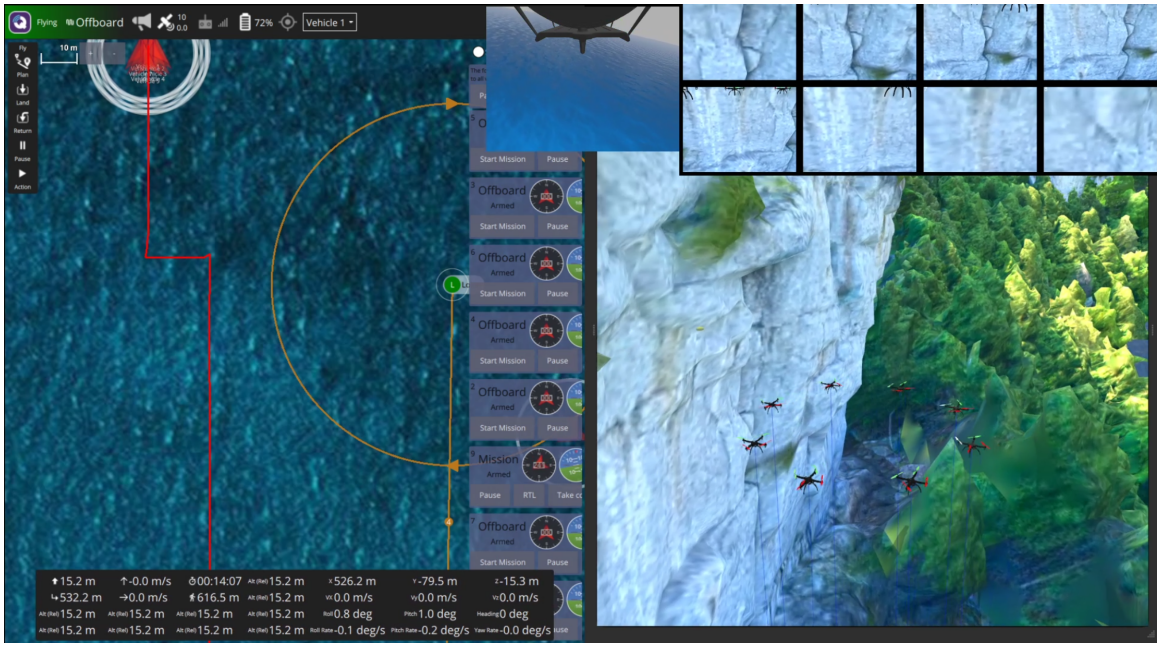

Figure 4.36: Snapshot of the mission view during execution

Remark 4.2.4. *Note that for this scenario, the local neighborhood position errors in Equation (4.6) are saturated to allow long distance separations and transitions.*

4.3 Chapter Summary

This chapter detailed the development of control strategies for both cooperative aerial manipulation and formation tasks involving multiple multi-rotors.

In the first part, the catenary guided nonlinear control approach, as developed in Chapter 3, is extended to scenarios involving cooperative aerial manipulation. Here, multiple multi-rotors suspend a rigid body payload with flexible cables to execute trajectory tracking missions while cooperatively stabilizing the payload's attitude and swing motion. In this work, firstly, desired force and moment on the payload satisfying required accelerations on the commanded trajectory are found. These loads are then distributed among the cable attachment points on the payload using a minimum-norm solution. Following this, the catenary equation is analytically solved, considering the known cable mass and length, to determine the optimal cable shape for achieving the calculated loads. This shape informs the guidance of individual multi-rotors, providing them with relative positioning and thrust requirements. Finally, a separate geometric control approach is applied to each multi-rotor that takes this information along with the other desired trajectory states into account to achieve commanded payload trajectory tracking cooperatively. The efficacy of this method is demonstrated through a simulation where four multi-rotors cooperatively maneuver a rigid rectangular plate suspended by flexible cables. The payload successfully follows an infinity-shaped (∞) trajectory, while maintaining the level attitude and adjusting the heading according to the tangential plane of the commanded trajectory.

The second part studied the dynamics and control of cooperative formation of multiple multi-rotors. It emphasizes a second-order consensus protocol for synchronized behavior and an Extended State Observer (ESO) for accurate disturbance estimation, which is crucial for countering disturbances such as wind and air-drag, enhancing stability and robustness of the overall formation. Practical implementa-

tion is demonstrated through a distributed second-order consensus protocol applied for various leader-follower graph topologies, focusing on trajectory and formation convergence. A comparative study illustrated the effectiveness of ESO in different formation tasks and graph topologies, particularly under wind-induced air drag. This part is concluded by highlighting the application of these strategies in a simulated search-and-rescue mission, demonstrating the potential use cases of these concepts in real-world scenarios.

Chapter 5

Summary and Closing Remarks

In this dissertation, we have studied the cooperative behavior of groups of Uncrewed Aerial Systems (UAS), particularly focusing on physical and information-level cooperation for tasks such as aerial payload manipulation and cooperative formation. The study has developed system models, guidance and control methods, and conducted necessary analyses, following the outlined objectives and problem specifications.

Chapter 2 established extensive mathematical models for cooperative aerial manipulation and formation tasks, focusing on multi-rotor systems with flexibly suspended payloads and airship systems. The modeling process began with individual subsystems, including a flexible cable model, a single multi-rotor with a slung load with point mass suspended via a flexible cable, and a comprehensive airship dynamical model. Then, it continued modeling cooperative multi-rotors with a rigid-body payload suspended via flexible cables. A key contribution was introducing analytical catenary analysis to validate the flexible cable model's applicability as a flexible suspension mechanism. Another significant contribution was the development of a momentum and structure-preserving Lie group variational integrator. This tool addressed the challenges of numerical inaccuracies and instabilities in simulating these highly nonlinear and complex payload manipulation systems, demonstrating superior stability and accuracy over traditional ODE-based solvers. Therefore, a foundation for more robust and reliable simulations, essential for controlling and operating these complex systems, is established.

In Chapter 3, the focus shifted towards developing control strategies for single multi-rotor systems with suspended payloads and airships, respectively. A linear-quadratic-tracker (LQT) based control approach was employed, utilizing a game-theoretic framework for swing attenuation of the payload and flexible suspension cable. This framework considered various scenarios based on the available cable feedback states, ranging from complete knowledge of each cable segment's attitude and velocity to having no information about the cable and payload states. The virtual rigid link method, based on instantaneous relative payload attitude, demonstrated a smoother response compared to the full state knowledge approach. This suggests that effective attenuation of cable and payload swing is achievable with limited knowledge of the payload and cable suspension subsystem. Additionally, a nonlinear geometric control method was explored, incorporating catenary shape analysis to determine reference position setpoints and desired cable tension for multi-rotor position and attitude control. This method successfully demonstrated trajectory tracking. The chapter also studied developing a linearized model for airship systems, designing a gain scheduling technique based on LQT controllers with airspeed, yaw rate, and climb rate as scheduling variables. Various autopilot modes were developed and tested, showing effective and smooth mode transitions during representative mission scenarios. Furthermore, a nonlinear dynamic inversion (NDI) controller was developed for airship attitude stabilization and trajectory tracking, employing a pseudo-inverse based control allocation method for different control configurations in hover and forward flight conditions. Finally, autonomous guidance laws for take-off, landing, and waypoint navigation were developed and tested, considering the full range of airship flight envelope.

Chapter 4 extended the catenary guided nonlinear control approach to cooperative aerial manipulation scenarios. Multiple multi-rotors were employed to suspend a

rigid body payload with flexible cables, executing trajectory tracking missions while cooperatively stabilizing the payload's attitude and swing motion. Firstly, the desired force and moment on the payload to provide required accelerations on the commanded trajectory were found. Then, these loads were distributed among the cable attachment points using a minimum-norm solution. Following that, the analytically solution of catenary equation was utilized to determine the optimal cable shape for achieving the calculated loads. This informed the guidance of individual multi-rotors, providing them with relative positioning and thrust requirements. A geometric control approach was applied to each multi-rotor, integrating this information with other desired trajectory states for effective payload trajectory tracking. The effectiveness of this method was demonstrated through a simulation where four multi-rotors cooperatively maneuvered a rigid rectangular plate suspended by flexible cables, successfully following an infinity-shaped trajectory while maintaining level attitude and adjusting the heading according to the commanded trajectory. In addition, based on a series of Monte Carlo simulations, a robustness analysis was conducted, highlighting certain disturbance rejection characteristics of the cooperative system. The chapter also addressed the dynamics and control of cooperative formation of multiple multi-rotors, emphasizing a second-order consensus protocol for synchronized behavior and an Extended State Observer (ESO) for accurate disturbance estimation. This was crucial for countering disturbances such as wind and air-drag, thus, enhancing the stability and robustness of the overall formation. A series of test cases and scenarios were demonstrated, focusing on trajectory and formation convergence under various conditions. These included scenarios using a fully connected graph, varying graph topologies with changing formations, and steady wind conditions. In some cases, ESO was integrated to assess its impact. A comparative study illustrated the effectiveness of ESO in different formation tasks and graph topologies, especially under

conditions of wind-induced air drag. The chapter concluded by highlighting the application of these strategies in a simulated search-and-rescue mission. This simulation involved using an airship as a surrogate aircraft, which transported and deployed the multi-rotors to the mission area and then remained nearby as a support station, while the multi-rotors executes predefined formation and trajectory tracking tasks. Hence, the potential real-world applications of these concepts were demonstrated.

References

[1] K. Sreenath, T. Lee, and V. Kumar, "Geometric control and differential flatness of a quadrotor uav with a cable-suspended load," in 52nd IEEE Conference on Decision and Control, 2013, pp. 2269–2274.

[2] K. Sreenath, N. Michael, and V. Kumar, "Trajectory generation and control of a quadrotor with a cable-suspended load - a differentially-flat hybrid system," in 2013 IEEE International Conference on Robotics and Automation, 2013, pp. 4888–4895.

[3] T. Lee, M. Leok, and N. H. McClamroch, "Dynamics and control of a chain pendulum on a cart," 2012 IEEE 51st IEEE Conference on Decision and Control (CDC), pp. 2502–2508, 2012.

[4] F. A. Goodarzi, D. Lee, and T. Lee, "Geometric stabilization of a quadrotor uav with a payload connected by flexible cable," in 2014 American Control Conference, 2014, pp. 4925–4930.

[5] P. Kotaru, G. Wu, and K. Sreenath, "Differential-flatness and control of quadrotor(s) with a payload suspended through flexible cable(s)," in 2018 Indian Control Conference (ICC), 2018, pp. 352–357.

[6] F. A. Goodarzi, "Autonomous aerial payload delivery with quadrotor using varying length cable," in 2016 International Conference on Advanced Mechatronic Systems (ICAMechS), 2016, pp. 394–399.

[7] J. Zeng, P. Kotaru, and K. Sreenath, "Geometric control and differential flatness of a quadrotor uav with load suspended from a pulley," in 2019 American Control Conference (ACC), 2019, pp. 2420–2427.

[8] C. Gabellieri and A. Franchi, "Differential flatness and manipulation of elasto-flexible cables carried by aerial robots in a possibly viscous environment," in 2023 International Conference on Unmanned Aircraft Systems (ICUAS). United States: IEEE, Jun. 2023, pp. 963–968.

[9] P. Kotaru, G. Wu, and K. Sreenath, "Dynamics and control of a quadrotor with a payload suspended through an elastic cable," in 2017 American Control Conference (ACC), 2017, pp. 3906–3913.

[10] S. Tang and V. Kumar, "Mixed integer quadratic program trajectory generation for a quadrotor with a cable-suspended payload," in 2015 IEEE International Conference on Robotics and Automation (ICRA), 2015, pp. 2216–2222.

[11] T. Lee, K. Sreenath, and V. Kumar, "Geometric control of cooperating multiple quadrotor uavs with a suspended payload," in 52nd IEEE Conference on Decision and Control, 2013, pp. 5510–5515.

[12] C. Meissen, K. Klausen, M. Arcak, T. I. Fossen, and A. Packard, "Passivity-based formation control for uavs with a suspended load," IFAC-PapersOnLine, vol. 50, no. 1, pp. 13 150–13 155, 2017, 20th IFAC World Congress. [Online]. Available: https://www.sciencedirect.com/science/article/pii/S2405896317328380

[13] T. Lee, "Geometric control of multiple quadrotor uavs transporting a cable-suspended rigid body," in 53rd IEEE Conference on Decision and Control, 2014, pp. 6155–6160.

[14] G. Wu and K. Sreenath, "Geometric control of multiple quadrotors transporting a rigid-body load," in 53rd IEEE Conference on Decision and Control, 2014, pp. 6141–6148.

[15] F. A. Goodarzi and T. Lee, "Dynamics and control of quadrotor uavs transporting a rigid body connected via flexible cables," in 2015 American Control Conference (ACC), 2015, pp. 4677–4682.

[16] ——, "Stabilization of a rigid body payload with multiple cooperative quadrotors," Journal of Dynamic Systems, Measurement, and Control, vol. 138, no. 12, 08 2016.

[17] J. Simo, N. Tarnow, and K. Wong, "Exact energy-momentum conserving algorithms and symplectic schemes for nonlinear dynamics," Computer Methods in Applied Mechanics and Engineering, vol. 100, no. 1, pp. 63–116, 1992. [Online]. Available: https://www.sciencedirect.com/science/article/pii/0045782592901152

[18] J. E. Marsden and M. West, "Discrete mechanics and variational integrators," Acta Numerica, vol. 10, pp. 357 – 514, 2001.

[19] M. West, "Variational integrators," PhD dissertation, California Institute of Technology, 2004.

[20] E. Hairer, G. Wanner, and C. Lubich, Symplectic Integration of Hamiltonian Systems. Berlin, Heidelberg: Springer Berlin Heidelberg, 2006, pp. 179–236. [Online]. Available: https://doi.org/10.1007/3-540-30666-8_6

[21] T. Lee, N. McClamroch, and M. Leok, "A lie group variational integrator for the attitude dynamics of a rigid body with applications to the 3d pendulum," in Proceedings of 2005 IEEE Conference on Control Applications, 2005. CCA 2005., 2005, pp. 962–967.

[22] T. Lee, M. Leok, and N. H. McClamroch, "Lie group variational integrators for the full body problem," Computer Methods in Applied Mechanics and Engineering, vol. 196, no. 29, pp. 2907–2924, 2007. [Online]. Available: https://www.sciencedirect.com/science/article/pii/S0045782507000758

[23] H. Lamb, The Inertia-coefficients of an Ellipsoid Moving in Fluid, ser. Great Britain Advisory Committee for Aeronautics. ACA/R & M-623. H.M. Stationery Office, 1918.

[24] M. M. Munk, Aerodynamics of Airships. Berlin, Heidelberg: Springer Berlin Heidelberg, 1936, pp. 32–48. [Online]. Available: https://doi.org/10.1007/978-3-642-91484-3_2

[25] S. P. Jones and J. D. DeLaurier, "Aerodynamic estimation techniques for aerostats and airships," Journal of Aircraft, vol. 20, no. 2, pp. 120–126, 1983. [Online]. Available: https://doi.org/10.2514/3.44840

[26] S. Gomes and J. Ramos, "Airship dynamic modeling for autonomous operation," in Proceedings. 1998 IEEE International Conference on Robotics and Automation (Cat. No.98CH36146), vol. 4, 1998, pp. 3462–3467 vol.4.

[27] W. Department, Airship Aerodynamics, U.S. Department of Transportation, Federal Aviation Administration. [Online]. Available: https://www.faa.gov/regulations_policies/handbooks_manuals/aviation/media/airship_aerodynamics.pdf

[28] J. Mueller, M. Paluszek, and Y. Zhao, "Development of an aerodynamic model and control law design for a high altitude airship," in AIAA 3rd "Unmanned Unlimited" Technical Conference, Workshop and Exhibit, 2004.

[29] J. Waishek, A. Dogan, and Y. Bestaoui, "Comprehensive characterization of airship response to wind and time varying mass," in AIAA Atmospheric Flight Mechanics Conference, 2010.

[30] M. Wasim and A. Ali, "Estimation of airship aerodynamic forces and torques using extended kalman filter," IEEE Access, vol. 8, pp. 70 204–70 215, 2020.

[31] M. Bisgaard, A. la Cour-Harbo, and J. Dimon Bendtsen, "Adaptive control system for autonomous helicopter slung load operations," Control Engineering

Practice, vol. 18, no. 7, pp. 800–811, 2010, special Issue on Aerial Robotics. [Online]. Available: https://www.sciencedirect.com/science/article/pii/S0967066110000341

[32] I. Palunko, P. Cruz, and R. Fierro, "Agile load transportation : Safe and efficient load manipulation with aerial robots," IEEE Robotics & Automation Magazine, vol. 19, no. 3, pp. 69–79, 2012.

[33] M. E. Guerrero, D. A. Mercado, R. Lozano, and C. D. García, "Ida-pbc methodology for a quadrotor uav transporting a cable-suspended payload," in 2015 International Conference on Unmanned Aircraft Systems (ICUAS), 2015, pp. 470–476.

[34] A. R. Godbole and K. Subbarao, "Nonlinear control of unmanned aerial vehicles with cable suspended payloads," Aerospace Science and Technology, vol. 93, p. 105299, 2019. [Online]. Available: https://www.sciencedirect.com/science/article/pii/S1270963818325185

[35] G. Wu and K. Sreenath, "Variation-based linearization of nonlinear systems evolving on $so(3)$ and $\mathbb{S}^2$," IEEE Access, vol. 3, pp. 1592–1604, 2015.

[36] R. P. Jain, "Transportation of cable suspended load using unmanned aerial vehicles: A real-time model predictive control approach," MS thesis, 08 2015.

[37] M. Guo, D. Gu, W. Zha, X. hua Zhu, and Y. Su, "Controlling a quadrotor carrying a cable-suspended load to pass through a window," Journal of Intelligent & Robotic Systems, vol. 98, pp. 387–401, 2020.

[38] G. De La Torre, E. Theodorou, and E. N. Johnson, "Autonomous suspended load operations via trajectory optimization and variational integrators," Journal of Guidance, Control, and Dynamics, vol. 40, no. 2, pp. 278–291, 2017. [Online]. Available: https://doi.org/10.2514/1.G001769

[39] S. Tang, V. Wüest, and V. Kumar, "Aggressive flight with suspended payloads using vision-based control," IEEE Robotics and Automation Letters, vol. 3, no. 2, pp. 1152–1159, 2018.

[40] S. Dai, T. Lee, and D. S. Bernstein, "Adaptive control of a quadrotor uav transporting a cable-suspended load with unknown mass," in 53rd IEEE Conference on Decision and Control, 2014, pp. 6149–6154.

[41] S. Tan, B. Nagabhushan, S. Tan, and B. Nagabhushan, Robust heading-hold autopilot for an advanced airship, 1997. [Online]. Available: https://arc.aiaa.org/doi/abs/10.2514/6.1997-1488

[42] R. Hun, A. Tiwari, and N. K. Sinha, "Design and simulation of autopilot control system for stratospheric airship," IFAC-PapersOnLine, vol. 49, no. 1, pp. 712–717, 2016, 4th IFAC Conference on Advances in Control and Optimization of Dynamical Systems ACODS 2016. [Online]. Available: https://www.sciencedirect.com/science/article/pii/S2405896316301409

[43] J. Nakpiam, O. Daskiran, C. Elliott, and A. Dogan, "Airship waypoint navigation in the presence of wind," in AIAA Atmospheric Flight Mechanics Conference, 2012.

[44] G. Atmeh and K. Subbarao, "Guidance, navigation and control of unmanned airships under time-varying wind for extended surveillance," Aerospace, vol. 3, no. 1, 2016.

[45] R. C. do Valle, L. L. Menegaldo, and A. M. Simões, "Smoothly gain-scheduled control of a tri-turbofan airship," AIAA Journal of Guidance, Control, and Dynamics, vol. 38, no. 1, pp. 53–61, 2015.

[46] J. R. Azinheira, A. Moutinho, and E. C. de Paiva, "Airship hover stabilization using a backstepping control approach," Journal of Guidance, Control,

and Dynamics, vol. 29, no. 4, pp. 903–914, 2006. [Online]. Available: https://doi.org/10.2514/1.17334

[47] A. Moutinho and J. Azinheira, "Stability and robustness analysis of the aurora airship control system using dynamic inversion," in Proceedings of the 2005 IEEE International Conference on Robotics and Automation, 2005, pp. 2265–2270.

[48] A. S. Marton, "Control architecture for the navigation system of robotic airship using incremenntal controllers," PhD dissertation, UNIVERSIDADE ESTADUAL DE CAMPINAS, 2021.

[49] A. Moutinho, "Modeling and nonlinear control for airship autonomous flight," PhD dissertation, 12 2007.

[50] E. C. de Paiva, F. Benjovengo, and S. S. Bueno, "Sliding mode control for the path following of an unmanned airship," IFAC Proceedings Volumes, vol. 40, no. 15, pp. 221–226, 2007, 6th IFAC Symposium on Intelligent Autonomous Vehicles. [Online]. Available: https://www.sciencedirect.com/science/article/pii/S1474667016346651

[51] Y. Yang, J. Wu, and W. Zheng, "Positioning control for an autonomous airship," AIAA Journal of Aircraft, vol. 53, no. 6, pp. 1638–1646, 2016.

[52] H. S. Vieira, E. C. de Paiva, S. K. Moriguchi, and J. R. H. Carvalho, "Unified backstepping sliding mode framework for airship control design," IEEE Transactions on Aerospace and Electronic Systems, vol. 56, no. 4, pp. 3246–3258, 2020.

[53] G. C. Avenant, "Autonomous flight control system for an airship," MS thesis, 03 2010.

[54] C.-S. Park, H. Lee, M.-J. Tahk, and H. Bang, "Airship control using neural network augmented model inversion," in Proceedings of 2003 IEEE Conference on Control Applications, 2003. CCA 2003., vol. 1, 2003, pp. 558–563 vol.1.

[55] O. Daskiran, B. Huff, and A. Dogan, Low Speed Airship Control using Reinforcement Learning and Expert Demonstrations. [Online]. Available: https://arc.aiaa.org/doi/abs/10.2514/6.2017-0934

[56] W.-X. Zhou, P.-F. Zhou, Y.-Y. Wang, and D.-P. Duan, "Planar path following nonlinear controller design for an autonomous airship," Proceedings of the Institution of Mechanical Engineers, Part G: Journal of Aerospace Engineering, vol. 233, no. 5, pp. 1879–1899, 2019.

[57] B. Nie, Z. Liu, T. Guo, L. Fan, H. Ma, and O. Sename, "Design and validation of disturbance rejection dynamic inverse control for a tailless aircraft in wind tunnel," Applied Sciences, vol. 11, p. 1407, 02 2021.

[58] D. Mellinger, M. Shomin, N. Michael, and V. R. Kumar, "Cooperative grasping and transport using multiple quadrotors," in International Symposium on Distributed Autonomous Robotic Systems, 2010.

[59] R. Ritz and R. D'Andrea, "Carrying a flexible payload with multiple flying vehicles," in 2013 IEEE/RSJ International Conference on Intelligent Robots and Systems, 2013, pp. 3465–3471.

[60] N. Michael, J. Fink, and V. Kumar, "Cooperative manipulation and transportation with aerial robots," Autonomous Robots, vol. 30, no. 1, pp. 73–86, 01 2011, copyright - Springer Science+Business Media, LLC 2011; Last updated - 2015-08-29. [Online]. Available: https://login.ezproxy.uta.edu/login?url=https://www.proquest.com/scholarly-journals/cooperative-manipulation-transportation-with/docview/822061365/se-2

[61] Z. Li, J. Erskine, S. Caro, and A. Chriette, "Design and control of a variable aerial cable towed system," IEEE Robotics and Automation Letters, vol. 5, no. 2, pp. 636–643, 2020.

[62] D. Sanalitro, H. J. Savino, M. Tognon, J. Cortés, and A. Franchi, "Full-pose manipulation control of a cable-suspended load with multiple uavs under uncertainties," IEEE Robotics and Automation Letters, vol. 5, no. 2, pp. 2185–2191, 2020.

[63] J. Gimenez, D. C. Gandolfo, L. R. Salinas, C. Rosales, and R. Carelli, "Multi-objective control for cooperative payload transport with rotorcraft uavs," ISA Transactions, vol. 80, pp. 491–502, 2018. [Online]. Available: https://www.sciencedirect.com/science/article/pii/S0019057818302192

[64] L. Qian and H. H. T. Liu, "Robust control study for tethered payload transportation using multiple quadrotors," Journal of Guidance, Control, and Dynamics, vol. 45, no. 3, pp. 434–452, 2022. [Online]. Available: https://doi.org/10.2514/1.G006173

[65] G. Li and G. Loianno, "Nonlinear model predictive control for cooperative transportation and manipulation of cable suspended payloads with multiple quadrotors," 2023.

[66] S. Sun and A. Franchi, "Nonlinear mpc for full-pose manipulation of a cable-suspended load using multiple uavs," 2023.

[67] J. Geng and J. W. Langelaan, "Cooperative transport of a slung load using load-leading control," Journal of Guidance, Control, and Dynamics, vol. 43, no. 7, pp. 1313–1331, 2020. [Online]. Available: https://doi.org/10.2514/1.G004680

[68] K. Sreenath and V. R. Kumar, "Dynamics, control and planning for cooperative manipulation of payloads suspended by cables from multiple quadrotor robots," in Robotics: Science and Systems, 2013.

[69] P. Kotaru and K. Sreenath, "Multiple quadrotors carrying a flexible hose: dynamics, differential flatness and control," IFAC-PapersOnLine, vol. 53, no. 2, pp. 8832–8839, 2020, 21st IFAC World Congress. [Online]. Available: https://www.sciencedirect.com/science/article/pii/S2405896320318061

[70] S. H. Nair, R. N. Banavar, and D. Maithripala, "Control synthesis for an underactuated cable suspended system using dynamic decoupling," in 2019 American Control Conference (ACC), 2019, pp. 2645–2650.

[71] R. Olfati-Saber and R. Murray, "Consensus problems in networks of agents with switching topology and time-delays," IEEE Transactions on Automatic Control, vol. 49, no. 9, pp. 1520–1533, 2004.

[72] P. Lin, "Robust h_∞ consensus analysis of a class of second-order multi-agent systems with uncertainty," IET Control Theory & Applications, vol. 4, pp. 487–498(11), March 2010. [Online]. Available: https://digital-library.theiet.org/content/journals/10.1049/iet-cta.2008.0492

[73] Z. Li, "Global h_∞ consensus of multi-agent systems with lipschitz non-linear dynamics," IET Control Theory & Applications, vol. 6, pp. 2041–2048(7), September 2012. [Online]. Available: https://digital-library.theiet.org/content/journals/10.1049/iet-cta.2011.0555

[74] A. Das and F. L. Lewis, "Cooperative adaptive control for synchronization of second-order systems with unknown nonlinearities," International Journal of Robust and Nonlinear Control, vol. 21, no. 13, pp. 1509–1524, 2011. [Online]. Available: https://onlinelibrary.wiley.com/doi/abs/10.1002/rnc.1647

[75] L. Xu and Y. Li, "Distributed robust formation tracking control for quadrotor uavs with unknown parameters and uncertain disturbances," Aerospace, vol. 10, no. 10, 2023. [Online]. Available: https://www.mdpi.com/2226-4310/10/10/845

[76] Z. Ding, "Consensus disturbance rejection with disturbance observers," IEEE Transactions on Industrial Electronics, vol. 62, no. 9, pp. 5829–5837, 2015.

[77] X. Wang, G. Wang, S. Li, and K. Lu, "Composite sliding-mode consensus algorithms for higher-order multi-agent systems subject to disturbances," IET Control Theory & Applications, vol. 14, no. 2, pp. 291–303, 2020. [Online]. Available: https://ietresearch.onlinelibrary.wiley.com/doi/abs/10.1049/iet-cta.2019.0644

[78] O. Mechali, L. Xu, X. Xie, and J. Iqbal, "Theory and practice for autonomous formation flight of quadrotors via distributed robust sliding mode control protocol with fixed-time stability guarantee," Control Engineering Practice, vol. 123, p. 105150, 2022. [Online]. Available: https://www.sciencedirect.com/science/article/pii/S0967066122000570

[79] C. Wang, "Robust cooperative control of multi-agent systems : a prediction and observation prospective," Boca Raton, Florida, 2021.

[80] Q. Zheng, L. Q. Gaol, and Z. Gao, "On stability analysis of active disturbance rejection control for nonlinear time-varying plants with unknown dynamics," in 2007 46th IEEE Conference on Decision and Control, 2007, pp. 3501–3506.

[81] Y. Huo, Y. Lv, X. Wu, and Z. Duan, "Fully distributed consensus for general linear multi-agent systems with unknown external disturbances," IET Control Theory & Applications, vol. 13, no. 16, pp. 2595–2609, 2019. [Online]. Available: https://ietresearch.onlinelibrary.wiley.com/doi/abs/10.1049/iet-cta.2018.6457

[82] M. Ran, Q. Wang, and C. Dong, "Active disturbance rejection consensus control of uncertain high-order nonlinear multi-agent systems," Transactions of the Institute of Measurement and Control, vol. 42, no. 3, pp. 604–617, 2020. [Online]. Available: https://doi.org/10.1177/0142331219878605

[83] M. Ran, Q. Wang, C. Dong, and L. Xie, "Active disturbance rejection control for uncertain time-delay nonlinear systems," Automatica, vol. 112, p. 108692, 2020. [Online]. Available: https://www.sciencedirect.com/science/article/pii/S0005109819305552

[84] U. C. Kaya and K. Subbarao, "Momentum Preserving Simulation of Cooperative Multirotors With Flexible-Cable Suspended Payload," Journal of Dynamic Systems, Measurement, and Control, vol. 144, no. 4, p. 041007, 01 2022. [Online]. Available: https://doi.org/10.1115/1.4053343

[85] U. Kaya and K. Subbarao, "Simulation of autonomous airship operations with integrated autopilot modes for practical scenarios," in AIAA AVIATION 2022 Forum, June 2022.

[86] U. C. Kaya, A. kashyap, K. Subbarao, and A. Chakravarthy, Nonlinear Control of an Autonomous Airship with Collision Avoidance Capability. [Online]. Available: https://arc.aiaa.org/doi/abs/10.2514/6.2023-0491

[87] U. C. Kaya and K. Subbarao, Catenary Guided Cooperative Aerial Manipulation of a Cable Suspended Payload via Multi-Rotors.

[88] Z. R. Manchester and M. A. Peck, "Quaternion variational integrators for spacecraft dynamics," Journal of Guidance, Control, and Dynamics, vol. 39, no. 1, pp. 69–76, 2016. [Online]. Available: https://doi.org/10.2514/1.G001176

[89] T. Lee, M. Leok, and N. H. McClamroch, "Discrete control systems," 2007.

[90] A. Nikhilraj, H. Simha, and H. Priyadarshan, "Optimal energy trajectory generation for a quadrotor uav using geometrically exact computations on se(3)," IEEE Control Systems Letters, vol. 3, no. 1, pp. 216–221, 2019.

[91] N. Nordkvist and A. K. Sanyal, "A lie group variational integrator for rigid body motion in se(3) with applications to underwater vehicle dynamics," in 49th IEEE Conference on Decision and Control (CDC), 2010, pp. 5414–5419.

[92] J. Schultz, K. Flaßkamp, and T. D. Murphey, "Variational Integrators for Structure-Preserving Filtering," Journal of Computational and Nonlinear Dynamics, vol. 12, no. 2, 12 2016, 021005. [Online]. Available: https://doi.org/10.1115/1.4034728

[93] T. Lee, M. Leok, and N. H. McClamroch, "Geometric tracking control of a quadrotor uav on se(3)," in 49th IEEE Conference on Decision and Control (CDC), 2010, pp. 5420–5425.

[94] T. I. Fossen, T. A. Johansen, and T. Perez, "A survey of control allocation methods for underwater vehicles," in Underwater Vehicles, A. V. Inzartsev, Ed. Rijeka: IntechOpen, 2009, ch. 7.

[95] M. W. Oppenheimer, D. B. Doman, and M. A. Bolender, "Control allocation," in The Control Handbook, 2nd Ed. CRC press, 2011, ch. 8.

[96] "Energy management: Mastering altitude and airspeed control," in Airplane Flying Handbook. United States Department of Transportation, Federal Aviation Administration, 2021, ch. 4, pp. 1–19. [Online]. Available: https://www.faa.gov/regulations_policies/handbooks_manuals/aviation/airplane_handbook

[97] M. E. Argyle and R. W. Beard, "Nonlinear total energy control for the longitudinal dynamics of an aircraft," in 2016 American Control Conference (ACC), 2016, pp. 6741–6746.

[98] S. Park, J. Deyst, and J. How, "A new nonlinear guidance logic for trajectory tracking," in AIAA Guidance, Navigation, and Control Conference and Exhibit, 2004.

[99] F. L. Lewis, H. Zhang, K. Hengster-Movric, and A. Das, "Cooperative control of multi-agent systems : optimal and adaptive design approaches," Dordrecht, 2014.

[100] K. Łakomy and R. Madonski, "Cascade extended state observer for active disturbance rejection control applications under measurement noise," ISA Transactions, vol. 109, pp. 1–10, 2021. [Online]. Available: https://www.sciencedirect.com/science/article/pii/S0019057820303815

[101] T.-L. Liu, "Optimal aggressive constrained trajectory synthesis and control for multi-copters," PhD dissertation, The University of Texas at Arlington, 2023.

Biographical Statement

Uluhan Cem Kaya was born in Kayseri, Turkey, in 1992. He received his Bachelor of Science degree in Aerospace Engineering from Middle East Technical University, Turkey, in 2015, followed by a Master of Science degree in Aerospace Engineering from the University of Texas at Arlington (UTA), in Spring 2019. In Fall 2019, he continued to pursue his Ph.D. in Aerospace Engineering at the same institution. During his academic journey, he was assigned to Graduate Teaching Assistant (GTA) and Graduate Research Assistant (GRA) roles in various occasions. As a GTA from 2016 to 2020, he actively contributed to the Unmanned Vehicle Systems Development Courses at UTA. He was also integral part of various research projects in UTA as GRA. These are "Safe Task-Aware Autonomous Resilient Systems (STAARS)" sponsored by National Science Foundation (2017-2019), and "Lighter than Air Hybrid Electric Orb for Urban Air Mobility" sponsored by Galaxy Unmanned Systems (GUS) LLC (2020-2023).

In addition to his academic pursuits, he gained practical experience through Aerospace Engineering internships at GUS in the Summers of 2021 and 2022. He then transitioned to the role of Flight Control Systems Engineer at the same company, starting in May 2023. His skills and research encompass expertise in Engineering and Robotics, including modeling, simulation and control of autonomous systems. He has gained proficiency in various simulation environment, including Gazebo, Robot Operating System (ROS), Simulink, and developed strong programming skills in C++, Python, Matlab, and LaTeX.

Upon completing his Ph.D., he will continue his position in Galaxy Unmanned Systems LLC as a Flight Control Systems Engineer.